

Ph.D. Thesis

**Biomagnetic Sensing with Nitrogen-Vacancy
Centers in Diamonds**



Department of Physics
Technical University of Denmark

Luca Troise

Supervisor: Professor Ulrik Lund Andersen
Co-Supervisor: Associate Professor Alexander Huck
Co-Supervisor: Associate Professor Kirstine Berg-Sørensen

November 2021

Abstract

The Nitrogen vacancy (NV) center is a novel solid-state sensor for detecting magnetic fields with high sensitivity and high spatial resolution at room temperature. Such a magnetometer has potential applications in a variety of fields, including biomedicine, neuroscience, and nanoscale magnetic resonance microscopy. In this thesis, we demonstrate advances in biomagnetic sensing using an NV magnetometer with sensitivity of $50 \text{ pT}\sqrt{\text{Hz}}$ in the low frequency range. Our experiments show the first magnetic measurements of optogenetically activated action potential in mammalian muscle tissue. We show that these measurements can be performed in an unshielded laboratory and that the biological signal can be easily recovered by digital signal processing techniques. In addition, we present the development of a miniaturized diamond NV magnetometer with nanotesla sensitivity, suitable for detecting a variety of low-level magnetic fields. Finally, we show the steps towards spatially resolving biomagnetic fields in a proof-of-principle experiment using a camera with an integrated lock-in amplifier.

Resumé

Nitrogen-Vacancy (NV) centeret i diamant er en nyskabende sensor, der kan måle magnetiske felter med høj sensitivitet og høj rumlig opløsning ved stue temperatur. Denne magnetsensor har potentielle anvendelser i mange forskellige felter, inklusiv biomedicin, neurovidenskab og nanoskala magnetisk resonans mikroskopi. I denne afhandling demonstrerer vi fremskridt inden for biomagnetisk målinger, hvor vi anvender en NV magnetsensor med en sensitivitet på $50 \text{ pT}\sqrt{\text{Hz}}$ i lav frekvensområdet. Vores eksperimenter er de første magnetiske målinger af et optogenetisk aktiveret aktionspotentialer i muskelvæv fra et pattedyr. Vi viser at disse magnetiske målinger kan laves i et laboratorium, som ikke er magnetisk afskærmet og at det biologiske signal let kan gendannes ved hjælp af digitale signal behandlingsteknikker. Yderligere præsenterer vi udviklingen af en miniaturiseret NV diamant magnetsensor med nanotelsa sensitivitet, som er i stand til at måle svage magnetfelter fra en række forskellige kilder. Til sidst viser vi vigtige fremskridt imod et proof-of-principle eksperiment, der kan måle biomagnetiske signaler med rumlig opløsning, hvor vi anvender et kamera med en integreret lock-in forstærker.



Acknowledgements

I would like to thank my supervisors, Professor Ulrik Lund Andersen, Associate Professor Alexander Huck, and Associate Professor Kirstine Berg-Sørensen for their guidance and wisdom during the last three years of my life.

I'm thankful to Jim for transmitting his work dedication and his invaluable lab experience to me.

I am grateful to Nikolaj for being an incredibly kind person to work with and for his patience in answering my never-ending questions about biology.

Thank you Josh, my back-to-back office mate for the infinite conversations about privacy policies.

I would like to thank Teresa for urging me not to use paper cups and be more eco-friendly (I still do it, secretly).

Thanks to Rasmus for his kindness and assistance with translating the abstract of this thesis into Danish.

I'm really thankful to Tine, one of the most valuable workers in our group.

Thank you my friends, Iyad, Maxime, Angelo, Dino, Adnan and Deepak, without you I would not have made it this far.

I'm grateful to all the people that have been part of QPIT in the last three years.

I want to thank my parents and family for always being there for me, despite the thousands of kilometers between us.

My deepest thanks go to my dog, for breaking my laptop the week before handing in this thesis.

Thank you Carolina, for making me smile every day.

“In this terrifying world, all we have are the connections that we make”

Contents

| | |
|---|----------|
| Abstract | ii |
| Resumé | iii |
| Acknowledgements | v |
| 1 Introduction | 1 |
| 1.1 Magnetic field sensing | 2 |
| 1.2 Magnetometers and their characteristics | 3 |
| 1.3 Highly-sensitive magnetometers | 4 |
| 1.4 Thesis Structure | 6 |
| 1.5 List of Publications | 7 |
| 2 Magnetometry With Nitrogen-Vacancy Centers | 9 |
| 2.1 Nitrogen-Vacancy centers | 10 |
| 2.1.1 Optically Detected Magnetic Resonance | 10 |
| 2.1.2 Ground State Hamiltonian | 12 |
| 2.2 Magnetic Field Sensing Techniques | 13 |
| 2.2.1 Ramsey measurements and spin control | 14 |
| 2.2.2 Pulsed and continuous-wave ODMR | 15 |
| 2.3 Diamond Synthesis | 18 |

vi

| | | |
|----------|---|-----------|
| 2.3.1 | Generation of NV centers | 18 |
| 2.4 | Applications for biological measurements | 19 |
| 3 | Experimental Framework | 21 |
| 3.1 | Sensor Characteristics | 22 |
| 3.1.1 | Diamond Sample | 22 |
| 3.1.2 | Sensor Geometry | 22 |
| 3.2 | Optical Pumping | 24 |
| 3.3 | Control and Detection | 25 |
| 3.3.1 | Three-Frequency Drive Scheme | 25 |
| 3.3.2 | Microwave Power Optimization | 26 |
| 3.3.3 | Lock-In Detection | 27 |
| 3.4 | Biological Measurements | 30 |
| 3.4.1 | Optogenetics | 30 |
| 3.4.2 | Data Recording | 31 |
| 3.5 | Data Post-Processing and Analysis | 34 |
| 3.5.1 | Notch Filters and Spectral Whitening | 34 |
| 3.5.2 | Low-pass Filter | 37 |
| 3.5.3 | Epoching and Detrending | 38 |
| 4 | Nanotesla sensitivity magnetic field sensing using a compact diamond nitrogen-vacancy magnetometer | 41 |
| 4.1 | Introduction | 41 |
| 4.2 | Publication | 41 |
| 5 | Optimization of a Diamond Nitrogen Vacancy Centre Magnetometer for Sensing of Biological Signals | 47 |
| 5.1 | Introduction | 47 |
| 5.2 | Publication | 48 |

| | | |
|-----------|---|------------|
| 6 | Detection of biological signals from a live mammalian muscle using an early stage diamond quantum sensor | 61 |
| 6.1 | Introduction | 61 |
| 6.2 | Publication | 62 |
| 7 | Laser stimulation of muscle activity with simultaneous detection using a diamond colour centre biosensor | 75 |
| 7.1 | Introduction | 75 |
| 7.2 | Publication | 76 |
| 8 | High speed microcircuit and synthetic biosignal widefield imaging using nitrogen vacancies in diamond | 115 |
| 8.1 | Introduction | 115 |
| 8.2 | Publication | 116 |
| 9 | Sensing of Action Potentials from Corpus Callosum in Mice | 129 |
| 9.1 | Introduction | 129 |
| 9.2 | Preliminary Investigation | 131 |
| 10 | Summary and Outlook | 133 |
| | Bibliography | 137 |

Chapter 1

Introduction

Magnetism was most probably first observed by the ancient Greeks in a form of the mineral magnetite known as lodestone, which possessed the incredible ability to attract iron. The word magnet itself comes from the Greek term *magnētis lithos*, “the Magnesian stone”. In 1820, the Danish physicist Hans Christian Ørsted discovered that if a wire carrying electrical currents is placed near a compass needle, the needle will rotate perpendicular to current flow [1]. A decade later, the English scientist Michael Faraday would discover that a changing magnetic field could induce a current in a nearby circuit [2]. These two important discoveries were included in the equations that govern electromagnetism, Maxwell’s equations.

We know now that magnetic fields can be generated by magnets, electric currents or by time-varying electric fields. Everyday technologies make use of magnetic fields or magnetic materials, for instance, computer hard drives that store data by creating small magnetic domains or industrial electromagnetic cranes that are used for lifting heavy metal objects.

Electric currents deriving from biological processes, such as neurons firing in the brain or muscular contractions, are also able to induce weak magnetic fields. The field of biomagnetism is documenting the existence of these elusive signals that can give crucial information on the underlying processes in biological systems and in a wide range of clinical diagnostic situations.

1.1 Magnetic field sensing

Magnetic field induction can be described in classical terms by the Maxwell-Faraday law [3] that relates time-varying magnetic fields to spatially-varying electric fields:

$$\nabla \times \mathbf{E} = -\frac{\partial \mathbf{B}}{\partial t} \quad (1.1)$$

Where \mathbf{B} and \mathbf{E} represents the magnetic field (or magnetic flux density) and the electric field respectively. The Standard International (SI) defines the Tesla (T) as the unit for magnetic B-field, where 1 Tesla corresponds to the field intensity generating one newton (N) of force per ampere (A) of current per meter of conductor.

As illustrated in Fig. 1.1, compared to the Earth’s static magnetic field, which at its surface ranges from 25 to 65 μT , brain magnetic fields strengths are measured to be between 8 and 9 orders of magnitude smaller. Moreover, magnetic noise generated by electrical devices and moving magnetic objects, encountered in a typical laboratory environment, is usually a thousand times stronger than any magnetic signal induced by the activity of neurons within the brain [4, 5]. As such, in order to sense the really weak biomagnetic signals, very sensitive *magnetometers*¹ are needed

By using magnetometers, we can determine the magnetic flux density at the point in space in which they are located. For instance, the field generated by a magnetic dipole’s perturbation usually decays in strength with a factor of $1/r^3$, where r is the distance from the source. Thus, distance plays a crucial role in the ability to sense.

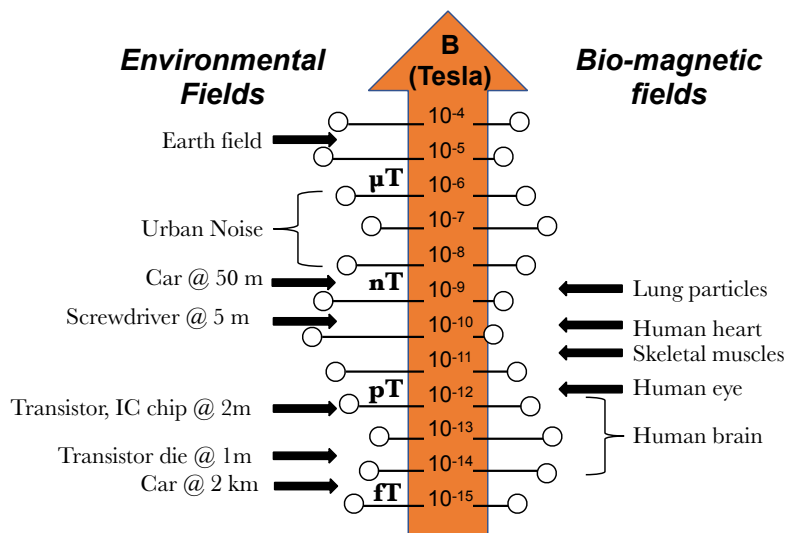


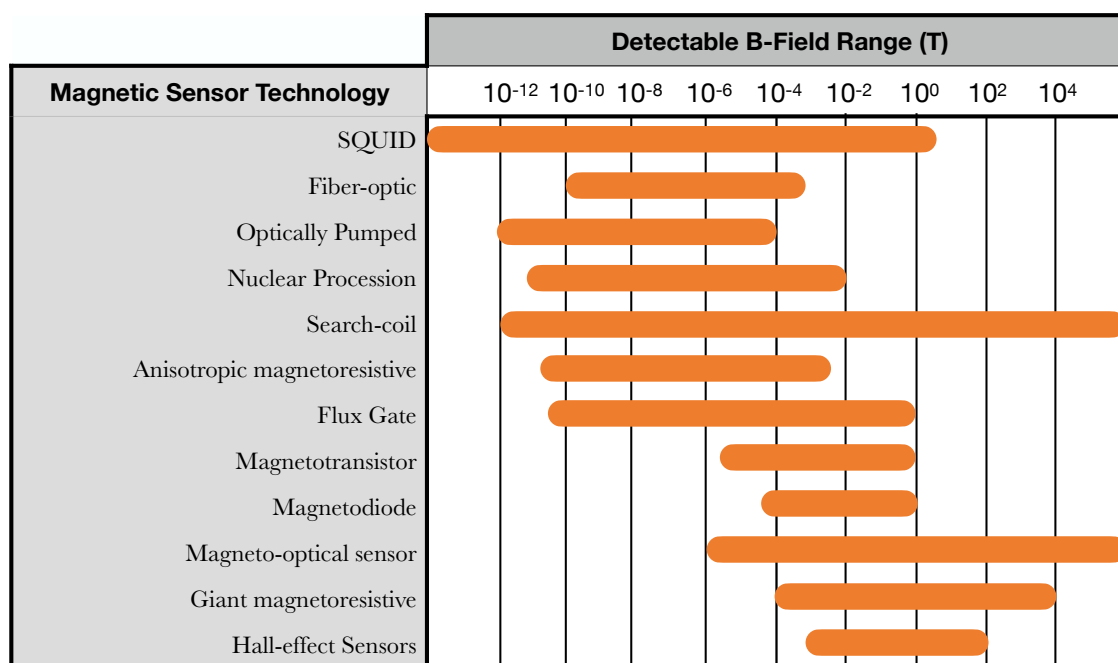
Figure 1.1: Magnetic field sources and strengths. Adapted from [4]

¹The terms “Magnetometer” and “Magnetic Sensor” can assume slightly different meanings [6], however, for the purpose of this work they will be used interchangeably.

1.2 Magnetometers and their characteristics

In general, magnetometers fall into two categories that can differ greatly in terms of their functionality and operation:

- **Scalar magnetometers**, that measure only the magnitude of the field passing through the sensor. Some quantum magnetometers, such as *proton precession* magnetometers, are an example of this [6].
- **Vector magnetometers**, which are sensitive to the strength of different field components of the B-field. For instance, *fluxgate* magnetometers can measure the strength of any component of the Earth's field just by orienting the sensors along the direction of the desired component [7].



1

Table 1.1: Range of detectable field amplitudes for different magnetic sensor technologies. Adapted from [8].

One of the most important parameter used to describe both vector and scalar magnetometers is the sensor's **transfer function**. It can be defined as the frequency-dependent function $H(\omega)[V/T]$ used to convert the input (magnetic field) to the output (voltage). Another important parameter is the **intrinsic noise level** of the sensor and can be represented as an amplitude spectral density (ASD) in terms of frequency-normalized magnetic field units (T/\sqrt{Hz}). The latter can be computed by dividing

the Fourier transform of the output voltage of the sensor by the transfer function $H(\omega)$ [9].

Directly related to the noise level is the **sensitivity** of a sensor. It can be defined as the smallest change in magnetic field (magnitude or magnetic field components) that can be detected and it is expressed in the same units as the noise level. The dynamic range instead, can be defined as the ratio between the maximum and minimum field strengths detectable by the magnetometer. The sensitivity and the **dynamic range** of magnetometers can also be used as a method of classification. The magnetometers which measure magnetic fields in the $< 0.1 \mu\text{T}$ range are considered *high-sensitivity* magnetometers, while those which measure fields in the $0.1 \mu\text{T}$ - 1mT and $>1 \text{mT}$ ranges are considered *medium-sensitivity* and *low-sensitivity* magnetometers respectively [9]. In Table 1.1, different types of magnetometers are shown with their average dynamic ranges.

When magnetic sensors are placed into fields that are spatially inhomogeneous, they produce a signal proportional to the mean-field value over an effective area or volume, that is dependent upon the geometry of the sensor. Several sensors are encapsulated for cryogenic or wiring necessity, this can create dead volumes around the sensor and therefore limit their **spatial resolution**. The overall spatial resolution for a square or circular planar sensor tightly depends on the ratio $s = r_0/\sqrt{A}$ where r_0 is the mean source-sensor distance and A is the active sensor area. For $s \ll 1$ the main limiting factor is the size of the sensor while for $s \gg 1$, the source-sensor distance becomes predominant [10].

1.3 Highly-sensitive magnetometers

Measuring signals with magnetometers that achieve sub-nanotesla sensitivity involves dealing with extremely noisy environments. To counteract environmental magnetic noise, a typical solution that can be adopted is to shield the sensor with a high magnetic permeability material (e.g. Mu-Metal). Typically, nanotesla-level shielding is used in fundamental physics experiments and in biomagnetic measurements like neural imaging [11]. Practical measurements can be far more hostile than working in controlled and magnetically shielded laboratories; background noise in hospitals, airports, cars or spacecrafts can be many orders of magnitude higher than the strength of the signal of interest. Aside from having high signal-to-noise ratio, modern magnetometers are required to work under harsh physical conditions such as high levels of radiation [12], vibrations and extreme pressures [13] and temperatures [14]. It is also important to address the safety and bio-compatibility of sensors for use in biomagnetic studies and diagnostic: very hot vapor cells or cryogenically cooled devices cannot be placed in direct contact with living tissues or cells without damaging the sample.

SQUIDS

Traditionally, the predominant technology for measuring human biomagnetic field has been liquid-helium cooled superconducting quantum interference device (SQUID) magnetometers. SQUIDS are high-sensitivity vector magnetometers, with common noise levels of $3 \text{ fT}/\sqrt{\text{Hz}}$ in commercial instruments and as low as $0.3 \text{ fT}/\sqrt{\text{Hz}}$ in experimental environments [15]. Josephson Junctions are at the core of a SQUID and consist of two superconductors coupled by an insulating barrier (also known as S-I-S junctions). Direct current (DC) and radio frequency (RF) are the two main types of SQUID: DC SQUIDS operate with two Josephson junctions placed in a superconducting loop; RF SQUIDS works with only one [16].

The most well-known application of SQUID sensors for biomagnetic measurements is the Magnetoencephalography (MEG) [17], a non-invasive diagnostic test that maps the magnetic fields induced electric currents in the brain (Fig. 1.2). To maintain superconductivity, commercial MEG instruments are usually operated at 4.2 K with liquid helium cooling (low T_c SQUID). High-temperature SQUID sensors relying on liquid nitrogen cooling have also been developed starting from the late 1980's, but they have not been employed in commercial MEG systems because their reliability and noise levels have not yet reached the levels available with low T_c sensors [4].



Figure 1.2: Person undergoing a MEG with SQUID array sensors. From United States Department of Health and Human Services.

SERFs

The Spin Exchange Relaxation Free (SERF) atomic magnetometer was originally proposed by the Romalis Lab at Princeton University in 2002 [18]. Atomic magnetometers work by detecting changes in atom energy levels caused by external magnetic fields. Typically, a near-resonant pump laser is used to excite atoms to high energy states, which undergo Larmor spin precession. This precession, which is sensitive to external magnetic fields, can induce a change in the optical absorptive and dispersive properties of atoms, which can be measured by monitoring the intensity of transmitted light [19]. The SERF magnetometer is an atomic magnetometer that adopts alkali metals and a pump-probe optical scheme. It operates in the so-called SERF regime in which the high temperature and high density of atoms is able to overcome the decoherence induced by the spin-exchange interaction [20]. Although the degree of heating depends on the employed alkali atoms, the necessity of having highly saturated vapor density requires a minimum working temperature of 373 K [21]. Sensitivities up to $0.16 \text{ fT}/\sqrt{\text{Hz}}$ with narrow bandwidth have been reported using SERF magnetometers in a gradiometer arrangement [22] and recent developments for MEG applications have also seen the creation of multi-channel SERF sensors with sensitivity of $10 \text{ fT}/\sqrt{\text{Hz}}$ and sensing volumes of 12 mm^3 [23].

NV-Centers in Diamonds

A novel alternative for high-spatial resolution magnetic-field detection is sensors based on nitrogen vacancy (NV) centers in diamond [24]. NV centers are paramagnetic defects that can be optically polarized and read out, and exhibit impressive coherence properties even at room temperature [25]. While single NV-centers confined in the crystal lattice can be used for detection of weak magnetic fields with nanoscale spatial resolution [26, 27], sensing with high density of NV centers enables ultra-high sensitivity at the cost of reduced spatial resolution [28]. Although the overall sensitivity is still inferior to that of SQUIDs and SERF magnetometers, the high spatial resolution, the biocompatibility and possibility of working at room temperature makes NV centers in diamond a very promising tool for biosensing.

1.4 Thesis Structure

This work is structured as follows. Chapter 2 gives a brief summary of some basic properties of the Nitrogen-Vacancy center, its properties, and its applications for biosensing. Chapter 3 presents an overview of the experimental setups and methods for measuring biomagnetic fields that were implemented in this Ph.D. project. Chapters 4-8 include the published and submitted results while Chapter 9 describes ongoing pursuits. Finally, a summary of this work and an outlook are presented in the last chapter.

1.5 List of Publications

The work presented in this thesis has been published or submitted in the following publications:

1. Webb, J. L., Clement, J. D., Troise, L., Ahmadi, S., Johansen, G. J., Huck, A., & Andersen, U. L. (2019). Nanotesla sensitivity magnetic field sensing using a compact diamond nitrogen-vacancy magnetometer. *Applied Physics Letters*, 114(23), 231103.
Personal contribution: Experiments, data collection and data analysis.
2. Webb, J. L., Troise, L., Hansen, N. W., Olsson, C., Wojciechowski, A. M., Achard, J., ... & Andersen, U. L. (2021). Detection of biological signals from a live mammalian muscle using an early stage diamond quantum sensor. *Scientific reports*, 11(1), 1-11.
Personal contribution: Methodology, experiments, data collection, data analysis and manuscript writing.
3. Webb, J. L., Troise, L., Hansen, N. W., Achard, J., Brinza, O., Staacke, R., ... & Andersen, U. L. (2020). Optimization of a Diamond Nitrogen Vacancy Centre Magnetometer for Sensing of Biological Signals. *Frontiers in Physics*, 8, 430.
Personal contribution: Methodology, experiments, data collection and data analysis.
4. Webb, J. L., Troise, L., Hansen, N. W., Frellsen, L. F., Osterkamp, C., Jelezko, F., ... & Andersen, U. L. (2021). High speed microcircuit and synthetic biosignal widefield imaging using nitrogen vacancies in diamond. *arXiv preprint arXiv:2107.14156*.
Personal contribution: Methodology, experiments and data collection.
5. Troise, L., Hansen, N. W., Olsson, C., Webb, J. L., ... & Andersen, U. L. (2021). Laser stimulation of muscle activity with simultaneous detection using a diamond colour centre biosensor. (Submitted)
Personal contribution: Methodology, experiments, data collection, data analysis and manuscript writing.

Chapter 2

Magnetometry With Nitrogen-Vacancy Centers

Nitrogen vacancy (NV) centers in diamonds as magnetic field sensors were first proposed in 2008 by Taylor et al. [24] and Degen [29] and shortly after demonstrated with single NVs [26, 27] as well as ensembles [28]. NV center magnetometers have been successfully applied in condensed matter physics [30], neuroscience and fundamental biology [31, 32], along with nuclear magnetic resonance [33, 34] and geoscience [35]. Not limited only to measurements of magnetic fields, NV centers have been also employed as sensors for other physical quantities such as pressure [36], temperature [37] and electric fields [38, 39].

NV centers magnetometry can provide many advantages over SQUID and atomic magnetometers, including superior ease of use and a higher spatial resolution. These novel sensors are capable of detecting broadband signals from DC up to 100 kHz [40], operating as high frequency magnetometers in the MHz range [41] or several GHz for relaxometry measurements [42]. No cryogenics, vacuum systems, or strong magnetic fields are required for this highly biocompatible sensor [43–46] that can be employed over ambient temperatures and pressures and require only $\sim 10^{-3}$ T bias fields. By virtue of these properties, NV sensors can be placed at distances of ~ 1 nm from field sources, providing nanometer-scale spatial resolution for applications such as magnetic field imaging.

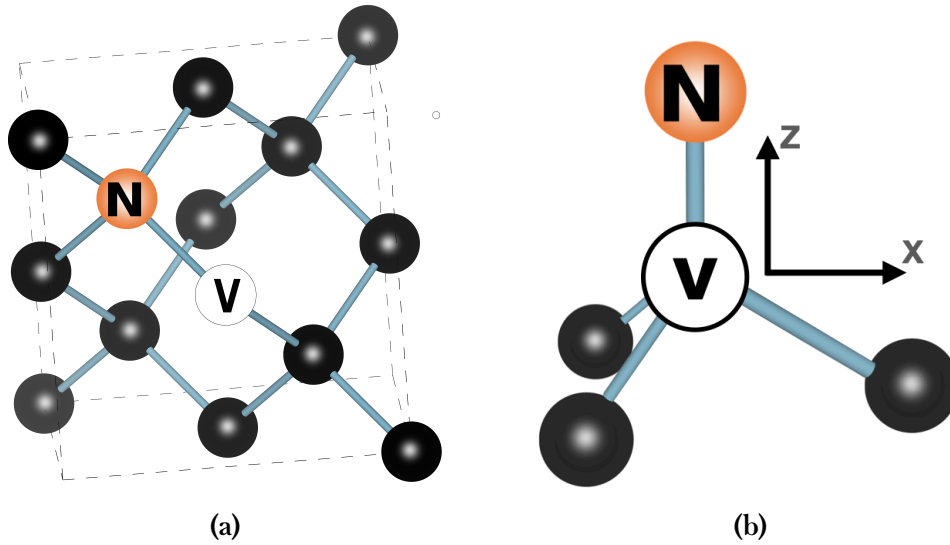


Figure 2.1: a) Diamond lattice containing an NV center. b) C_{3v} symmetry of an NV center.

2.1 Nitrogen-Vacancy centers

Diamond is the hardest naturally occurring material known. A significant proportion of available diamonds is used in industrial applications, and the demand for this material is continuously growing. Along with hardness, diamond has several impressive chemical, physical, and mechanical characteristics such as high thermal conductivity, high electrical resistivity, broad optical transparency, resistance to chemical corrosion, and biological compatibility.

Perfect diamond crystals are transparent, but certain contaminants in natural and artificial diamonds can affect their color and other properties. For instance, diamonds with high nitrogen levels (>10 ppm) tend to have a yellow-brown color, while diamonds with Boron impurities (>1 ppm) appear blue [47]. These imperfections in the crystal lattice, also called color centers, are very common; they can be attributed to lattice irregularities and to substitutional or interstitial impurities. Nitrogen, boron and hydrogen atoms are among the most commonly found diamond impurities, however, this chapter will address the Nitrogen-Vacancy (NV) color center, which is the building block of our solid-state magnetometer.

2.1.1 Optically Detected Magnetic Resonance

The NV center is a point defect in the diamond lattice consisting of a single substitutional nitrogen atom adjacent to a carbon vacancy and its symmetry axes lie along the four $[111]$ crystallographic directions (Fig. 2.1a). This implies that an NV center has a C_{3v} symmetry and it's spatially invariant under two rotations by 120° and 240° (about the z-axis), three vertical reflections and the identity operation (Fig. 2.1b).

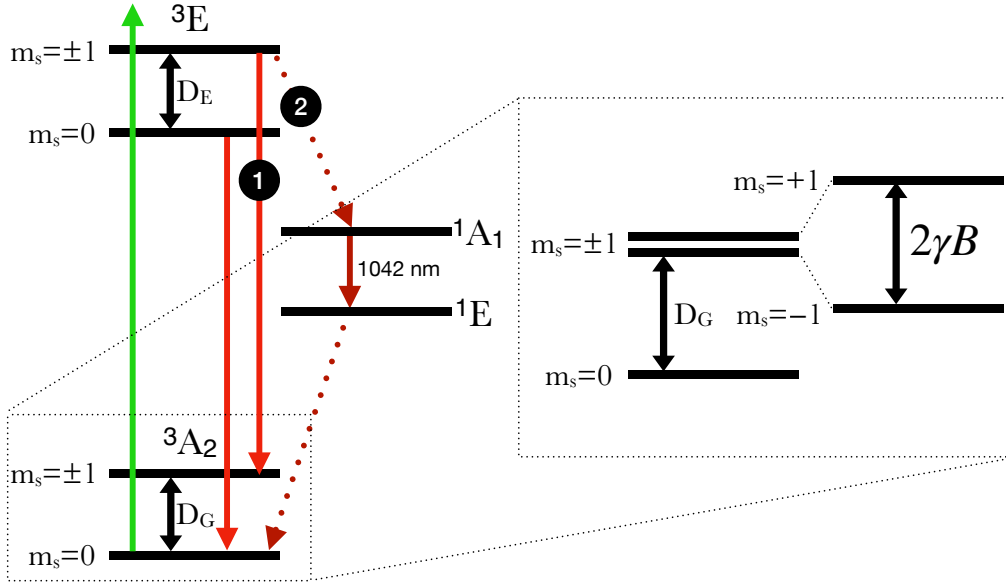


Figure 2.2: Simplified energy level structure for NV⁻ center in diamond. D_G and D_E represent the spin-triplets zero-field splitting energy of the ground state and excited respectively. The degenerate $m_s = \pm 1$ spin states are subject to Zeeman splitting in the presence of an external magnetic field B . Under green laser illumination and with a microwave field at the D_G frequency, electron decay can occur radiatively (1) or via IR emission (2), leading to a magnetic field sensitive variation in red fluorescence emission.

Although NV centers can assume three potential charge states (NV⁻, NV⁺, NV⁰), it is the negatively charged NV⁻ that is most useful for magnetometry and sensing applications¹.

Six electrons contribute to the NV⁻ electronic structure, namely three electrons from the neighboring carbon atoms, two from the nitrogen atom, and one is an unpaired electron from a donor in the lattice.

The NV center has 4 experimentally observed electronic states: two spin-triplet states consisting of a ground state 3A_2 and an excited state 3E , and two-singlet shelving states. Two additional singlet states are predicted, possibly within the diamond conduction band [48, 49]. As shown in Fig. 2.2, the zero-field splitting energies between the spin levels $m_s = 0$ and $m_s = \pm 1$ are $D_G = 2.87$ GHz for the ground state and $D_E = 1.42$ GHz for the excited state. The transition between the ground and the excited state can be excited optically in the wavelength range between 450 nm and 637 nm while the fluorescence emission has a wavelength ranging from 637 to 800 nm [50]. This optical transition is mainly spin-conserving: electrons starting in the $m_s = 0$ state are trapped between two $m_s = 0$ states due to spin conservation, whereas electrons in the

¹For the purposes of this work the NV⁻ will be simply addressed as NV

$m_s = \pm 1$ state will eventually undergo the $m_s = 0$ cycling transition.

On account of that, electrons excited by a pump laser can decay in two possible ways: (1) spin-preserving radiative decay (637 nm) between the triplet states (bright state) or (2) non-radiative decay/infrared emission (dark state) via singlet shelving states. If an external microwave (MW) field is applied to the NV center at the D_G frequency, while optically exciting the NV center, a population transfer between the $m_s = 0$ and $m_s = \pm 1$ occurs and it can be optically read out as a drop in fluorescence emission. The percentage variation in the fluorescence is commonly called *contrast* and by varying the frequency of the MW field it is possible to characterize this resonance in a process called *Optically Detected Magnetic Resonance* (ODMR) spectroscopy. The average contrast can be up to 30% for single NVs and 1-2% for NV ensembles. More recent reports have demonstrated ODMR contrasts up to 30% with perfectly aligned (>99%) shallow NV ensembles [51].

When an external magnetic field is applied to the NV center, the ground state $m_s = \pm 1$ is no longer degenerate due to the Zeeman effect (insert of Fig. 2.2). It follows that the splitting between the $m_s = +1$ and $m_s = -1$ levels is directly proportional to the strength of the magnetic field, which can now be read out optically. The relation that links the energy splitting and the magnetic field strength B is given by $2\gamma_e B$ where γ_e is the gyromagnetic ratio and $|\gamma_e/2\pi| = 28.025 \text{ Hz/nT}$ [52]. In this case, the ODMR spectrum appears as two separate resonance peaks given by the two spin transitions $m_s = 0 \Leftrightarrow m_s = -1$ and $m_s = 0 \Leftrightarrow m_s = +1$.

Nitrogen has two stable isotopes, ^{14}N and ^{15}N with a natural abundance of 99.64% and 0.36% respectively [53]. The variation in the nuclear spins of nitrogen isotopes results in two types of NV centers with different hyperfine structures.

2.1.2 Ground State Hamiltonian

The NV center's ground state Hamiltonian in the presence of an external magnetic field can be simplified as it follows:

$$\mathcal{H}_{NV} = \mathcal{H}_B + \mathcal{H}_N + \mathcal{H}_E \quad (2.1)$$

Where \mathcal{H}_B describes the external B field interaction with the electron spin and the zero-field energy D_G , \mathcal{H}_N is the result of the hyperfine interaction between the nitrogen's nuclear spin and the NV electron spin and \mathcal{H}_E describes the interaction with electric fields and crystal strain [54, 55]. For magnetic sensing applications, however, the latter term can be neglected except in extreme cases, such as in the presence of a strong electric field or a highly strained diamond lattice.

Assuming a coordinate system with the internuclear NV direction being parallel to the z -axis (Fig. 2.1b), with $\mathbf{S} = (S_x, S_y, S_z)$ being the electronic spin operator, \mathcal{H}_B can be represented as:

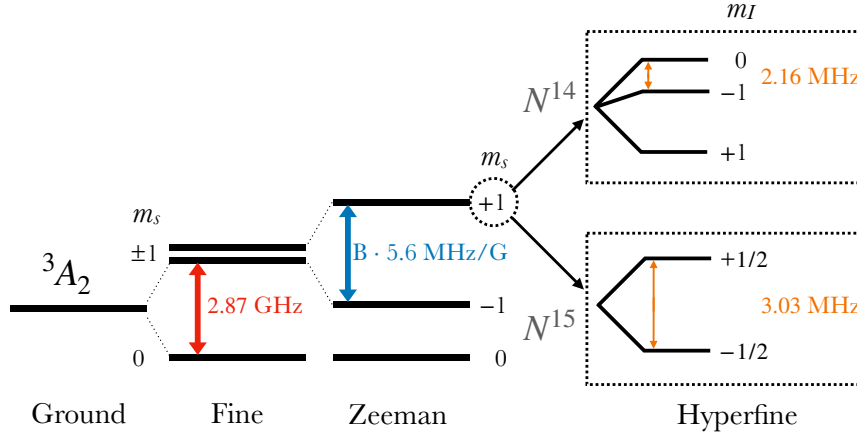


Figure 2.3: Fine, Zeeman and hyperfine structures of the NV⁻ ground state. As a result of the hyperfine structure, the $m_s=0$ to $m_s=\pm 1$ transitions are split into three resonances separated by 2.16 MHz for the ^{14}N nuclei and 3.03 MHz for the ^{15}N nuclei.

$$\mathcal{H}_B/h = D_G S_z^2 + \frac{g_e \mu_B}{h} (\mathbf{B} \cdot \mathbf{S}) \quad (2.2)$$

Where h is Planck's constant, μ_B represents the Bohr magneton, g_e the electronic g-factor for NV. The hyperfine interaction (Fig. 2.3) with the nitrogen nuclear spin can be described as:

$$\mathcal{H}_N = A_{\parallel} S_z I_z + A_{\perp} (S_x I_x + S_y I_y) + Q[I_z^2 - I(I+1)/3] - \gamma_I (\mathbf{B} \cdot \mathbf{I}) \quad (2.3)$$

With A_{\parallel} and A_{\perp} being the axial and transverse hyperfine coupling parameters, Q is the electric quadrupole parameter, γ_I is the nitrogen's nuclear gyromagnetic ratio and $\mathbf{I} = (I_x, I_y, I_z)$ is the atomic spin of nitrogen (spin-1 for and spin- $1/2$ for ^{15}N).

2.2 Magnetic Field Sensing Techniques

Magnetic sensing techniques can be divided in two large categories based on the bandwidth of the fields of interest: DC broadband sensing and AC sensing (Table 2.1). While DC-low frequency sensing protocols are used to sense static and low frequency fields (up to ~ 100 kHz), AC sensing can be used to detect fields up to ~ 10 MHz [56]. Recent NMR studies have also demonstrated sensing up to ~ 100 MHz with AC protocols [57]. Although both AC and DC sensing are fundamentally limited by the spin projection noise arising from quantum mechanical uncertainty, the NV relaxation times and shot noise have a greater impact on sensor performance. In this section,

some of the more common sensing techniques with NV centers will be reviewed together with their strengths and limitations.

| | Broadband DC Sensing | AC Sensing |
|----------------------|--|---|
| Sensing Techniques | Ramsey, cw-ODMR, pulsed ODMR | Hahn Echo, Dynamical Decoupling (DD) |
| Bandwidth | 0 to ~100 kHz (pulsed ODMR) 0 to ~10 kHz (cw-ODMR) | Center Frequency from ~1 kHz to 10 MHz, bandwidth <10 kHz |
| Relevant Relaxation | Inhomogenous spin dephasing T_2^* | Longitudinal Relaxation T_1 , homogenous spin decoherence T_2 |
| Sensing Applications | Biocurrent detection, magnetic imaging of minerals, imaging of magnetic nanoparticles in biological systems, vibration and temperature sensing | Single biomolecule and protein detection, nanoscale nuclear magnetic resonance, nanoscale electron spin resonance, noise spectroscopy |

Table 2.1: Overview of the operational regimes of broadband DC and AC sensing protocols in diamonds using NV^- ensembles. Adapted from [55].

2.2.1 Ramsey measurements and spin control

The Ramsey interferometry method [58] is a way of detecting slowly changing magnetic fields by taking advantage of the spin properties of NV centers. As shown in Fig. 2.4a, after initializing the spin states with a laser pulse to the $|0\rangle$ ($m_s=0$) state, it is possible to coherently drive the spin population in a superposition of the $|0\rangle$ and $|1\rangle$ ($m_s=+1$) states by applying a resonant MW field. This causes the spin population to oscillate with an angular frequency Ω_R called the Rabi frequency. The MW field is applied only as a short pulse (known as $\pi/2$ pulse) for the duration of $\pi/2\Omega_R$. The first MW pulse is followed by spin precession for a time τ , during which a phase that depends on external magnetic fields accumulates. A second MW pulse of the same duration is then applied to project the spin population in the $|1\rangle$ state. Lastly, the spin state is read optically with a pump laser pulse.

One of the main advantages of Ramsey magnetometry is that the accumulated phase and therefore the field sensitivity increases with the interrogation time τ . As τ increases, other effects come into play that tend to reduce contrast, such as decoherence, dephasing and spin-lattice relaxation. Those effects are governed respectively by the three relaxation times T_2 , T_2^* and T_1 . T_2^* is primarily caused by static inhomogeneities in the external magnetic field or by the intrinsic defects in the spin system.

An exponential decay envelope with characteristic time T_2^* occurs when a series of Ramsey measurements is performed by varying the free precession interval τ (red dashed line in Fig. 2.4b). Static inhomogeneities in an external magnetic field or defects in the spin system are major causes of T_2^* , inducing spin ensembles to precess at different Larmor frequencies. For interrogation times $\tau \sim T_2^*$, the T_2^* limited sensitivity of a Ramsey measurement can be expressed as:

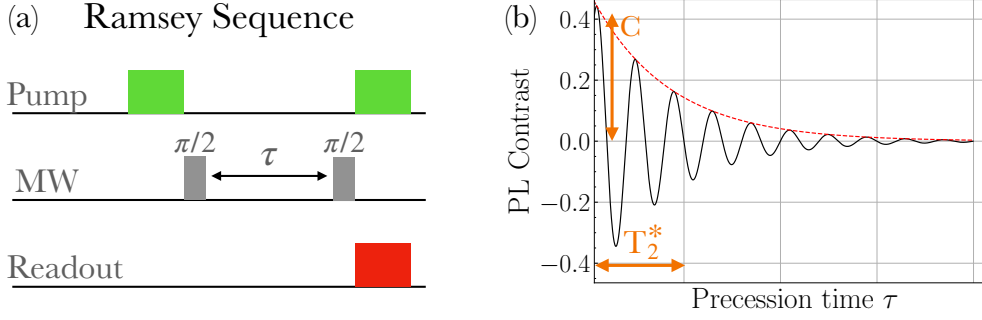


Figure 2.4: a) Diagram of Ramsey pulsed protocol. b) Ideal representation of Ramsey fringes observed by varying the precession time τ , with contrast C and exponential decay associated to T_2^* . Adapted from [55]

$$\eta_{\text{Ramsey}} \approx \frac{\hbar}{g_e \mu_b} \frac{1}{\sqrt{N T_2^*}} \quad (2.4)$$

where N represents the number of interrogated spins [28]. For larger spin ensembles, the spin initialization and readout times can be orders of magnitude longer than the precession time, highly limiting the measurement bandwidth and the sensitivity.

By adding a π pulse in between the $\pi/2$ pulses it is possible to overcome the dephasing given by static inhomogeneities. In this protocol, known as the Hahn-Echo sequence [59], phase accumulated within the first half of free-precession is cancelled by phase accumulated within the second half. The relevant relaxation time in this case is the spin-spin relaxation time T_2 and is due to time-varying fields that affect the coherence of the spin ensemble. For NV centers T_2 can exceed T_2^* by orders of magnitude [60]. Inherently insensitive to both static and slow variations in magnetic field, the Hahn-Echo sequence is most suitable for measurements of AC fields. For detection of higher frequency AC fields in the GHz range, T_1 limited relaxometry measurements allow phase-insensitive detection with limited bandwidth [42].

2.2.2 Pulsed and continuous-wave ODMR

Pulsed ODMR

The pulsed ODMR technique is closely related to the Ramsey sequence, with the main difference being that the resonant MW pulse is applied throughout the interrogation time τ (Fig. 2.5a). Variations in the external magnetic field cause the ODMR resonance to detune from the driving MW field, which results in changes in fluorescence intensity [61]. Compared to Ramsey measurement, the pulsed ODMR scheme introduces linewidth broadening due to the longer duration of the resonant pulse. Hence, the final resonance profile can be described as a Lorentzian curve given by a convolution of the MW broadening effect and the dephasing time T_2^* . If the interrogation time is set to $\tau \approx T_2^*$, a good approximation for the pulsed ODMR linewidth can be

expressed as $\Delta\nu \approx 1/\pi T_2^*$ [61].

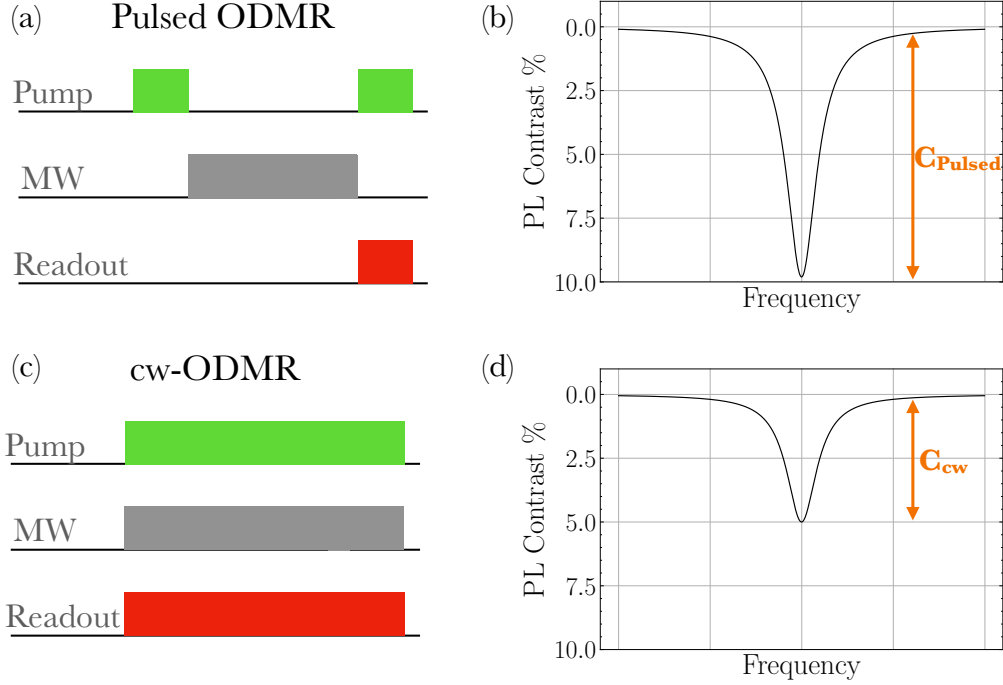


Figure 2.5: a) Diagram of cw-ODMR protocol. b) Ideal representation of cw-ODMR resonance with contrast C_{cw} . c) Diagram of pulsed ODMR sensing protocol. d) Ideal representation of pulsed ODMR resonance with contrast C_{pulsed} . Adapted from [55].

Continuous-wave ODMR

The continuous-wave optically detected magnetic resonance (cw-ODMR) is the most straightforward DC to low-frequency (<10 kHz) magnetometry scheme with NV centers; it does not require pulsed MW fields, pulsed excitation and expensive arbitrary waveform generators (AWGs) [28, 32, 40]. The cw-ODMR consists of a continuous optical and MW drive with simultaneous optical readout (Fig. 2.5a).

The most common way of employing cw-ODMR for magnetic field detection consists in:

1. Applying an external magnetic field to split ODMR resonances in accordance with the four different NV crystallographic directions.
2. Tuning the MW field at frequency corresponding to the steepest slope $|dI/df|^{\text{max}}$ of the resonance in the direction of interest. Where I and f represent the red fluorescence intensity and the MW frequency respectively Fig. 2.6.
3. Monitoring the changes in output fluorescence ΔI , directly proportional to external field variations for the Zeeman effect.

Except in extreme cases of applications that require very low laser intensity, the shot-noise limited sensitivity of a typical cw-ODMR measurement can be expressed as:

$$\eta_{cw} \approx \frac{4}{3\sqrt{3}} \frac{h}{g_e \mu_b} \frac{\delta\nu}{C_{cw} \sqrt{R}} \quad (2.5)$$

where $\delta\nu$ and C_{cw} are the resonance linewidth and contrast and R is photon count rate [61].

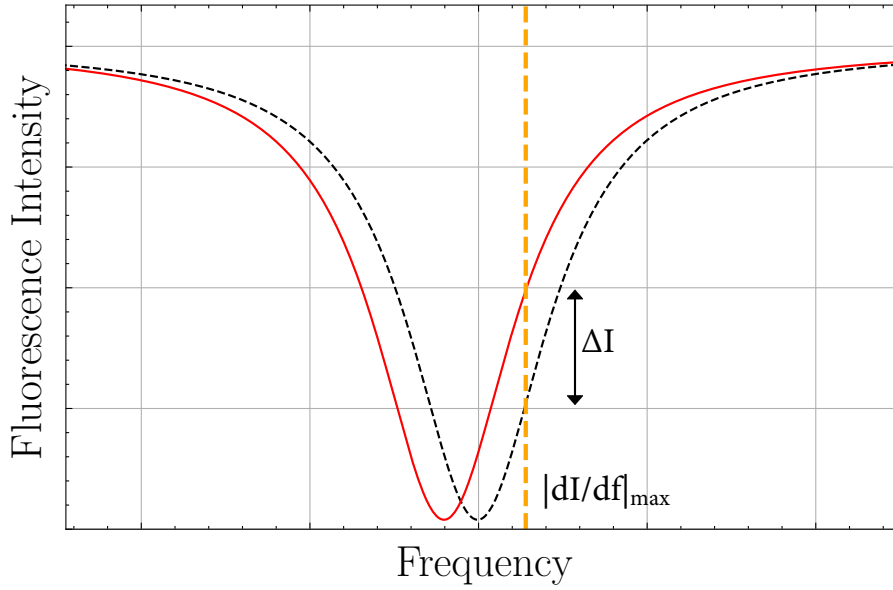


Figure 2.6: Continuous wave ODMR detection of magnetic field induced resonant shift. The frequency shift between ODMR curves can be detected as a change in the output fluorescence ΔI at the point of maximum slope $|dI/df|_{\max}$.

To achieve the highest sensitivity, choosing the right measurement protocol is crucial. Large NV ensembles are needed for maximizing bulk sensitivity in the shot-noise limited regime as well as for high spatial resolution wide-field microscopy. Depending upon the sensing scheme used, effects such as strain across the NV ensemble, causing inhomogeneous broadening, and amplitude variations in the MW drive can impact sensitivity differently. A recent study from our group [62], has demonstrated that for large NV ensembles in the low-frequency (<10 kHz) sensing range, cw-ODMR can outperform pulsed sensing schemes. This effect is particularly evident in cases in which a large inhomogeneous broadening and large MW field amplitude variations are present. Furthermore, Ramsey pulsed schemes can severely limit measurement bandwidth due to the long polarization and readout times associated with NV ensembles. These characteristics make cw-ODMR ideally suited for broadband biological measurements [55].

2.3 Diamond Synthesis

Diamond hosts a wide variety of color centers that are suitable for quantum technologies due to their outstanding optical and spin properties [63–65]. Material science and engineering techniques have been instrumental in the fabrication of specially designed and engineered synthetic crystals that have enabled diamond to be used as a platform for a wide variety of applications. Two different techniques are available to manufacture synthetic diamond crystals: High-Pressure-High-Temperature (HPHT) and Chemical Vapor Deposition (CVD).

HPHT

Traditionally, the most common method for synthesizing diamonds has been HPHT, which is based on recreating the natural conditions of diamond formation in a controlled environment. During HPHT synthesis, carbon-rich materials are compressed at pressures >5 GPa and heated above 1250 °C. The yellow color of diamonds grown by HPHT is usually due to the high amounts of nitrogen impurities, up to a few hundred parts per million (ppm), that originate from the atmosphere or growth media [66]. The concentration of nitrogen impurities can be reduced by adding a metal catalyst that extracts nitrogen from the carbon source during the growth process. Recently, HPHT with less than 5 parts per billion (ppb) of nitrogen has been produced [67].

CVD

CVD is the most common method for growing diamonds with high quality NV centers [68]. Chemical vapor deposition involves placing a small diamond seed inside a sealed chamber and subjecting it to temperatures around 800 Celsius. The chamber is filled with a carbon-rich gas mixture (mainly of hydrogen and methane) and the gases are ionized into plasma with microwaves or lasers. The ionization process breaks down the molecular bonds and carbon atoms attach on the surface of the diamond seed, allowing homoepitaxial growth of the substrate.

In comparison to HPHT, CVD allows greater control over the growth chamber environment, resulting in highly pure diamonds. Furthermore, CVD growth uses lower pressures than atmospheric pressure and requires lower temperatures than HPHT. Possible disadvantages of CVD include maintaining constant growth conditions for longer periods of time when creating thicker crystals. Variations in these conditions, especially temperature, can cause undesirable effects such as crystal strain, vacancies clusters and polycrystalline growth that can highly affect the overall quality of the diamond [69].

2.3.1 Generation of NV centers

Despite the fact that natural NV concentrations are sufficient for certain applications, most uses require doped diamond layers with optimized concentrations.

High concentrations of nitrogen can be introduced by ion (N^+) implantation or during CVD growth [70], high N-to-NV⁻ conversion efficiency instead can be obtained from high-energy irradiation and subsequent annealing ($\geq 800^\circ\text{C}$) [71].

Irradiation can be carried out with different types of particles such as Helium atoms, protons and electrons, thereby resulting in the creation of single vacancies (GR1) [72]. It is usually preferable to irradiate with electrons or protons rather than heavier particles due to their longer stopping range, which allows for a more uniform creation of vacancies [28]. Following irradiation, annealing is a vital step to improve the N/NV ratio and the coherence properties of the sample. Heating the crystal at temperatures in the range of 800°C - 1000°C , allows the vacancies to diffuse in the lattice and be captured by substitutional nitrogens. By annealing simultaneously to irradiation, it is possible to associate vacancies with nearby nitrogen atoms more easily and avoid the formation of vacancy clusters [73].

2.4 Applications for biological measurements

Magnetic fields play an important role in biological systems, both within the realm of basic sciences as well as technological applications. Quantitative measurements with sub-cellular resolution of neural activity are critical for understanding how the brain processes information. Many different approaches have proven successful so far, including voltage-sensitive fluorescent dyes [74] and microelectrode arrays (MEAs) [75]. Nevertheless, many of these techniques suffer from low sensitivity, cytotoxicity, bleaching or inadequate temporal and spatial resolution.

A considerable amount of work has been dedicated in the direction of incorporating nanodiamonds (NDs) probes containing NV centers within biological tissues and cells [31, 76, 77]. For instance, ferritin (iron-containing proteins found in many organisms) was detected by NDs with sensitivities approaching single molecule detection threshold [78].

In 2012, Hall et al. proposed a non-invasive and biocompatible action potential (AP) detection method based on NV magnetometry, showing the possibility of non-invasive widefield imaging of planar neuron activity with high spatial and temporal resolution [79]. Following the work of Jensens et al. with atomic magnetometers [80], the first experimental demonstration of in vivo AP detection with NV centers in diamonds was realized by Barry et al. in 2016 [32]. The magnetic field associated with the propagating AP in a marine worm (*Myxicola infundibulum*) and squid (*Loligo pealeii*) was detected in a widefield setup with a temporal resolution of $32\ \mu\text{s}$. By using a specimen-to-sensor distance of about $10\ \mu\text{m}$, the non-invasive measurement could be conducted for a long period of time ($>24\text{h}$) with little to no impact on the biological samples.

Magnetometry using NV-based techniques is expected to be a pivotal technique in

the coming years since it doesn't require fluorescent labels, it's non-invasive, and it can be applied to a wide range of systems, from cells to intact organisms. Several technical challenges associated with this technique need to be overcome, for instance, sensitivity needs to be improved to reach sub pico-tesla levels without sacrificing the high spatial resolution [81].

Chapter 3

Experimental Framework

Our first experimental attempt to create an NV diamond magnetometer for biological applications has seen the development of a miniaturized sensor (described in Chapter 4). Such magnetometer, with dimensions $11 \times 7 \times 7 \text{ cm}^3$ exhibited a sensitivity of $7 \text{ nT}/\sqrt{\text{Hz}}$ over a bandwidth of 125 Hz by using a diamond cut at the Brewster angle (67°). The limited sensitivity of this miniaturized detector was suitable for the detection of magnetic fields arising from e.g. electrical power systems, but it could not detect the extremely small fields generated from biological tissues.

There have therefore been multiple attempts to build a high-sensitivity detector that could measure magnetic fields in the sub-nanotesla range. The methods presented in this chapter refer to the last configuration that has been used to successfully sense the magnetic fields generated by optogenetically triggered action potentials in mice. By employing a cw-ODMR scheme in a wide-field microscopy setup, this configuration allowed a bulk sensitivity of $50 \text{ pT}/\sqrt{\text{Hz}}$ with a bandwidth of $\sim 10 \text{ kHz}$ limited only by relaxation time T_2^* .

In parallel to the evolution of sensing experiments, methods have been developed to spatially resolve biomagnetic signals in a wide-field configuration. With a lock-in amplifier camera, proof-of-principle spatial resolution has been demonstrated for the recovery of AC fields generated in micro-scale circuits. The details of these experiments are described in Chapter 8.

3.1 Sensor Characteristics

3.1.1 Diamond Sample

The diamond used in this work was an electronic-grade single crystal (Element Six) of dimensions $2 \times 2 \times 0.5 \text{ mm}^3$ and $[100]$ oriented. A $20 \text{ }\mu\text{m}$ thick ^{12}C purified layer was overgrown (LSPM, Paris) with CVD to achieve a concentration of 5 ppm of ^{14}N . The diamond was then proton irradiated at 2.25 MeV and annealed at $800 \text{ }^\circ\text{C}$ for 4 hours. The final NV density in the doped layer was estimated to be between 0.1 and 1 ppm allowing an ODMR linewidth of $\sim 1 \text{ MHz}$ and a contrast of $\sim 3\%$.

3.1.2 Sensor Geometry

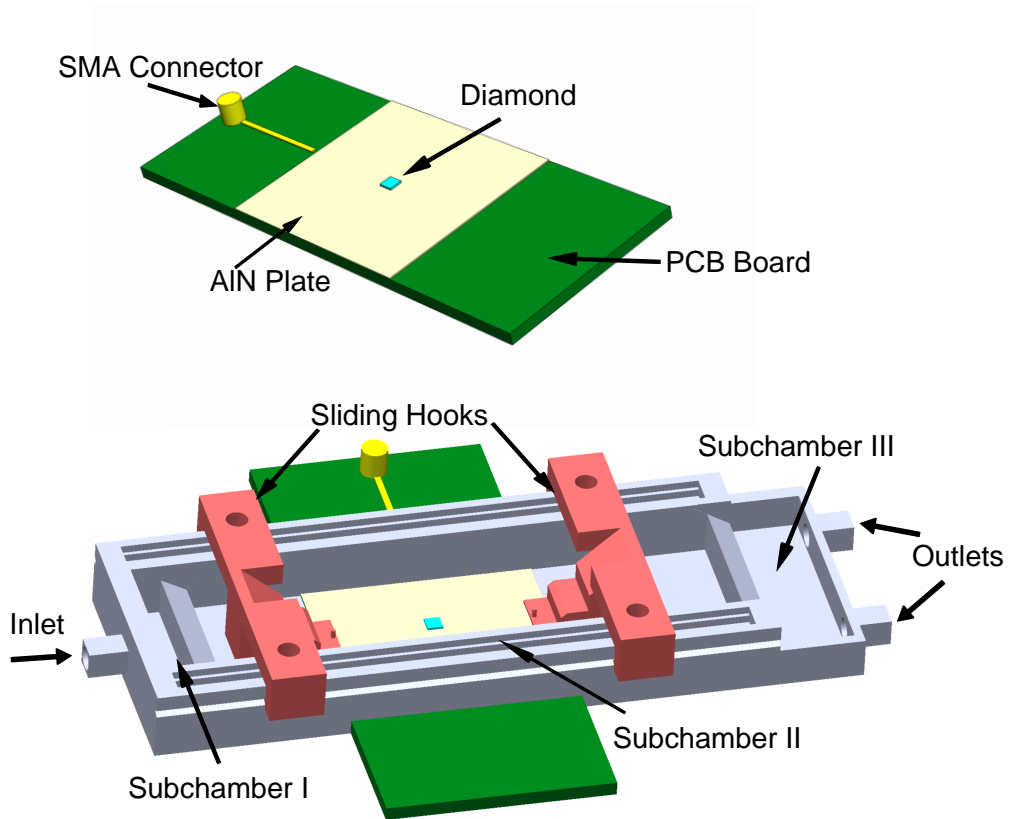


Figure 3.1: 3D Schematics of the sensor geometry. The diamond is placed in a hole in the center of an AlN plate placed on top of a MW resonator. This structure is placed below a 3D printed sample chamber consisting of three subchambers.

A laser-cut aluminum nitrate heat sink plate with dimensions of $3 \times 3 \times 0.05 \text{ cm}$ was used to mount the diamond. The diamond was inserted and glued in the hole in the center of the plate using watertight aquarium silicone. As shown in Fig. 3.1(top), the aluminum nitride (AlN) plate was positioned on top of a custom-built broadband resonator fabricated on a PCB circuit board [82]. The board presented a hole in

the center allowing light excitation and collection from the bottom surface of the diamond.

For the purpose of experimenting on biological samples, a custom 3D-printed plastic chamber for holding a bath solution was designed Fig. 3.1(bottom). The solution was pumped into the chamber via peristaltic pump (Pharmacia P-3). The chamber was composed of three communicating subchambers. The first one (I) was serving as flux and air-bubbles dampener to minimize the movement of the sample. The second subchamber (II) was used as a sample holder, and the third (III) was used as an overflow well for keeping a constant volume of solution in subchamber II. The combined volume for subchambers I and II was $\sim 74 \times 20 \times 7 \text{ mm}^3$. Attached to the chamber, two 3D-printed plastic sliders terminating with a platinum-iridium hook were used for stretching and positioning the biological samples on the diamond. The chamber was glued with silicone on top of the AlN plate and, being fully accessible from above, it allowed easy introduction and manipulation of biological sample and probe electrodes.

A layer of $16 \mu\text{m}$ thick household aluminum foil was placed with the most reflective side facing the top surface of the diamond (Fig. 3.2). By reflecting both green pump light and red fluorescence back in the diamond, the aluminum allowed an increase in fluorescence collection of $\sim 2x$. Moreover, it prevented heat and light damage to the biological sample even with 2 W of pump laser power. The aluminum foil was attached to the chamber by a $50 \mu\text{m}$ thick layer of Kapton tape that also served as an electrical insulator for the diamond. It has been demonstrated that polyimide, the polymer composing Kapton tape, has a high degree of biocompatibility and it allows in-vivo measurements for long periods of time [83]. While the sample-to-sensor distance increased due to the tape layer, the resulting $\sim 70 \mu\text{m}$ of separation were taken also as a precaution against sample damage.

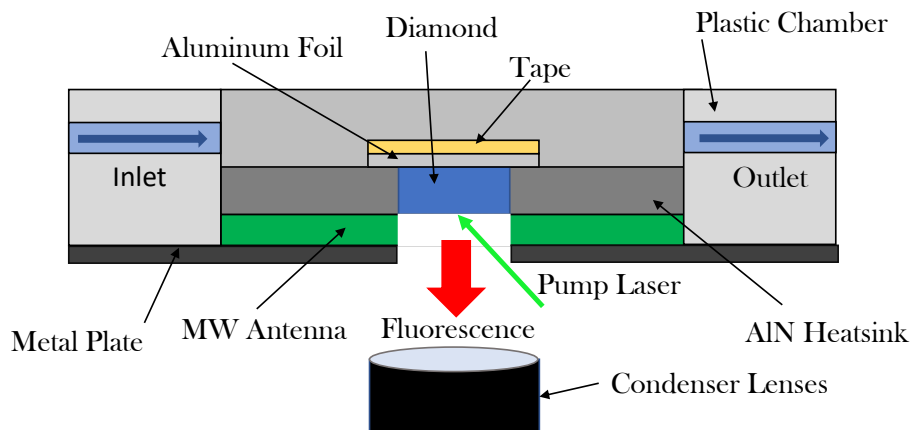


Figure 3.2: Side view schematic of the sensor. Green light is coupled to the diamond through Brewster angle illumination while red fluorescence is collected from the bottom with a condenser lens.

3.2 Optical Pumping

Using a cw-ODMR scheme, NV centers were optically pumped with up to 2 W of 532 nm green laser (Coherent Verdi G5). Fig. 3.3 shows a schematic of the optics utilized for NV excitation and fluorescence detection. A polarizing beam splitter (PBS) and half-wave plate (HWP) were used to control the amount of laser power entering the setup. Using an a-coated $f=400\text{mm}$ lens, the diamond was illuminated from below at the diamond Brewster's angle (67°) [32]. The beam waist at the diamond was estimated to be $\sim 200\ \mu\text{m}$. As the transmitted power is polarization dependent at the Brewster's angle, laser light was linearly polarized using another set of PBS and HWP. The same PBS was also used to split the green laser light into a reference beam, necessary for balanced detection. Neutral density (ND) filters were used to decrease the power of the reference beam and avoid detector saturation.

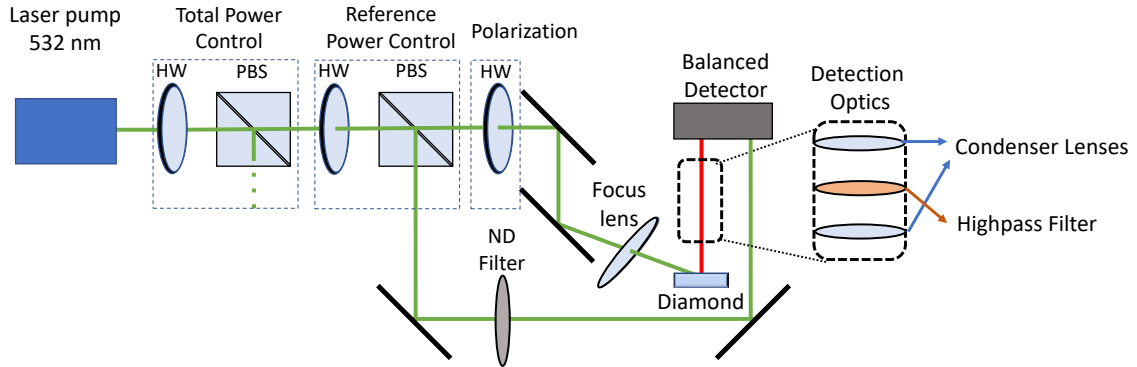


Figure 3.3: Schematics of the optical setup. Balanced detection is achieved by splitting a reference beam from the laser pump with a PBS.

NV fluorescence was collected from the bottom surface of the diamond using a 12 mm diameter condenser lens (Thorlabs ACL1210) placed in a vertically translating beam tube. Red light was reflected in the xy -plane by using a 45° fixed mirror (not shown in the figure) and filtered from green light with a high-pass optical filter (Thorlabs FEL0600). Using the same type of condenser lens as earlier, filtered light was focused onto the photodiode. In the present study, a Nirvana 2007 balanced photodetector (New Focus Inc.) was used. Typically, with balanced detection, a reduction of one order of magnitude in the output fluorescence noise level was observed.

3.3 Control and Detection

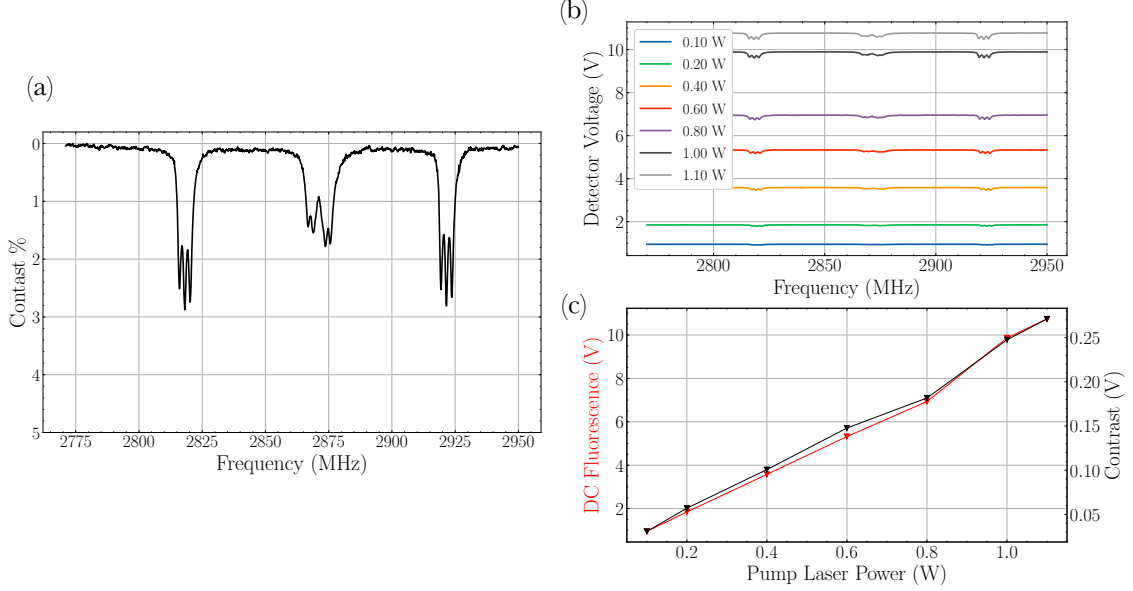


Figure 3.4: a) cw-ODMR in a (100) alignment obtained by detecting the red fluorescence while sweeping the MW frequency. b) ODMR traces with varying pump laser power up to detector input saturation (10.7 V). c) Scaling of fluorescence intensity and absolute contrast with varying laser power.

To split the NV resonance along the defect axes and optimize sensitivity in a chosen direction, two rare-earth (Neodymium) magnets were aligned parallel to the (110) direction in the diamond providing a mT scale offset field (Fig. 3.4a). By measuring the output voltage of the photodetector, it was possible to determine the maximum laser pump power corresponding to the detector input saturation. As illustrated in Fig. 3.4b with power input of 1.1 W, the detector produced a saturation voltage of 10.7 V corresponding to ~ 3 mW of red fluorescence. Fluorescence intensity and contrast increased linearly with varying input laser power up to the detector saturation (Fig. 3.4c).

3.3.1 Three-Frequency Drive Scheme

A three-frequency drive scheme was used to generate the MW field and boost sensitivity [84]. The signal produced by two radio-frequency (RF) generators (Stanford SG394) was mixed using an RF mixer and amplified (Minicircuits ZHL-16W-43+). As depicted in Fig. 3.5, the first signal generator (labeled “Main”) was employed to drive the transition in the triplet ground state between the $m_s=0$ and $m_s=\pm 1$ with a carrier frequency in the range of 2.7-3 GHz, frequency modulated in the 20-40 kHz range with a modulation deviation of ~ 0.5 MHz. The second generator (labeled “Aux”) was used to drive the hyperfine coupling with the ^{14}N nuclear spins. The latter generator produced a sinusoidal signal whose frequency matched the hyperfine

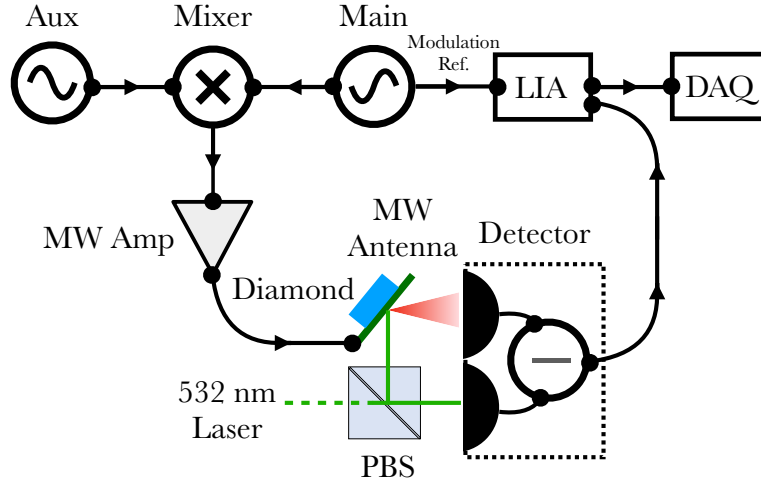


Figure 3.5: Schematics of the MW and detection apparatus. A frequency modulated signal from the Main generator is mixed with a 2.16 MHz signal and delivered to the MW resonator after amplification. The output from the balanced detector is demodulated and amplified with the LIA by using a modulation reference signal and finally digitised.

constant $A_{\parallel} = 2.16$ MHz introduced in the previous chapter. The amplified signal was fed to the microwave resonator.

Finally, the output voltage from the detector was demodulated and amplified using a lock-in amplifier (LIA, Stanford SR850) and a reference modulation signal. To digitise the demodulated signal, a digital acquisition card (DAQ, NI PCI-6221) was used with acquisition rate of 80 kSa/s.

3.3.2 Microwave Power Optimization

For ODMR measurements, the optimal MW power was defined as the combination of MW powers from both Main and Aux signal generators that produced the largest ODMR slope. The optimal power for MW antennas is affected not only by the properties of diamonds, but also by a number of factors such as the antenna geometry, the pump laser power, cabling losses, and the type of solution or sample laying onto the diamond sensor, that could affect the near-field coupling.

To find the optimal power, a LabVIEW script was implemented that allowed to independently sweep the MW powers of the two signal generators for each ODMR measurement. The maximum slope of an ODMR measurement was defined as $|dV/d\omega|_{max}$ where V is the lock-in voltage and ω represents the frequency expressed in MHz. Fig. 3.6c shows examples of $dV/d\omega$ measurements for different MW power

combinations with 1.1 W of pump laser power and with $\sim 10 \text{ mm}^3$ of deionized (DI) water were present in the solution chamber. In this example the optimal power combination was found to be (10,-8) dBm for Main and Aux respectively (Fig. 3.6d). The optimized ODMR measurement with three-frequency drive allowed a larger ODMR contrast (Fig. 3.6a) leading to an increase in sensitivity of up to three times compared to a single-frequency drive measurement (Fig. 3.6b).

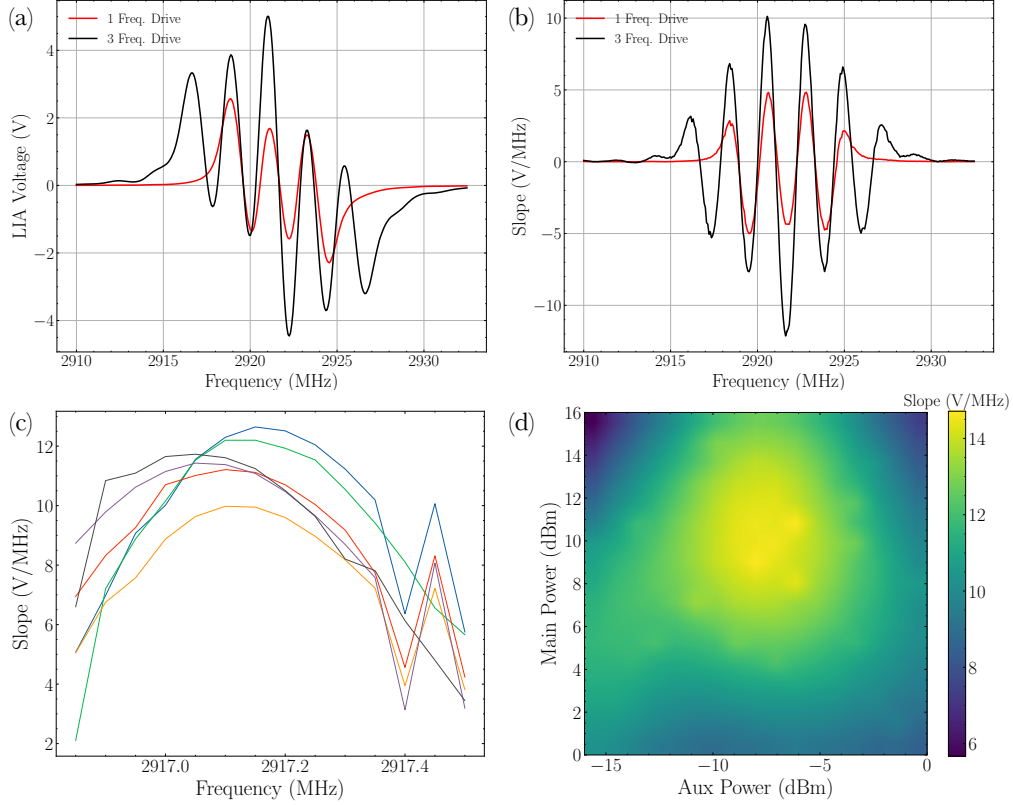


Figure 3.6: a) Comparison of ODMRs obtained by using a single-frequency drive and a three-frequency drive scheme. b) Derivatives of the ODMR signals shown in a). The three-frequency drive scheme shows a slope ~ 3 larger compared to the single-drive. c) Slope measurements with a three-frequency drive scheme obtained by varying the MW powers of the two signal generators. d) Heat map of the maximum ODMR slopes obtained with varying MW powers.

3.3.3 Lock-In Detection

Lock-in detection were implemented to measure ODMR away from noisy DC frequencies. Lock-in amplifiers [85] must receive a reference modulation signal V_{ref} from a signal generator in order to demodulate the input signal V_{sig} :

$$V_{sig} = A_{sig} \sin(\omega_{sig} t + \theta_{sig})$$

$$V_{ref} = A_{ref} \sin(\omega_{ref} t + \theta_{ref})$$

The LIA, after amplifying the input signal, multiplies it by the modulation reference using phase-sensitive detection (PSD). The output signal in this case is simply the product of two sine waves.

$$\begin{aligned} V_{LIA} &= A_{sig}A_{ref}\sin(\omega_{sig}t + \theta_{sig})\sin(\omega_{mod}t + \theta_{ref}) \\ &= 1/2A_{sig}A_{ref}\cos[(\omega_{sig} - \omega_{ref})t + \theta_{sig} - \theta_{ref}] - \\ &\quad 1/2A_{sig}A_{ref}\cos[(\omega_{sig} + \omega_{ref})t + \theta_{sig} + \theta_{ref}] \end{aligned}$$

If the signal frequency is the same as the reference frequency, after low-pass filtering the high frequency components, the LIA output signal is directly proportional to the input signal amplitude :

$$V_{LIA} = 1/2A_{sig}A_L\cos(\theta_{sig} - \theta_{ref})$$

By tuning of the reference signal phase θ_{ref} , it is possible to remove phase difference, resulting in a lock-in output signal that depends directly on the input signal.

$$V_{LIA} = 1/2V_{sig}V_{ref}$$

In order to reject unwanted parts of the spectrum, Lock-in amplifiers have traditionally set the low-pass filter bandwidth by adjusting the time constant. As an approximation, the lock-in filter transfer function can be represented with the RC filter model:

$$H(\omega) = \frac{1}{1 + i\omega\tau}$$

With $\tau = 1/(2\pi f)$, where f is the -3 dB frequency of the filter. **Fig. 3.7a** shows a series of Amplitude Spectral Density (ASD) measurements from the lock-in output voltage with varying time constant. With smaller time constants, bandwidth can be increased at the expense of increased high-frequency noise. For the purpose of detecting the induced magnetic field from action potentials, the time constant was set to $30 \mu\text{s}$, allowing a bandwidth of ~ 3 kHz.

By tuning the MW field to the frequency corresponding to the highest ODMR slope, NV centers become susceptible to external magnetic fields. This is reflected in the ASD shown in **Fig. 3.7b**, where noise peaks generated by external magnetic noise sources are present. It is important to note that away from noisy DC components (>10 Hz), the noise floor has a constant value of $50 \text{ pT}/\sqrt{\text{Hz}}$. This value can be interpreted as the sensor's sensitivity η , for which only signal components with amplitudes $>\eta$ can be detected in a single-shot measurement. The overall noise floor is the sum of different contributions originating from the electronic equipment, laser technical

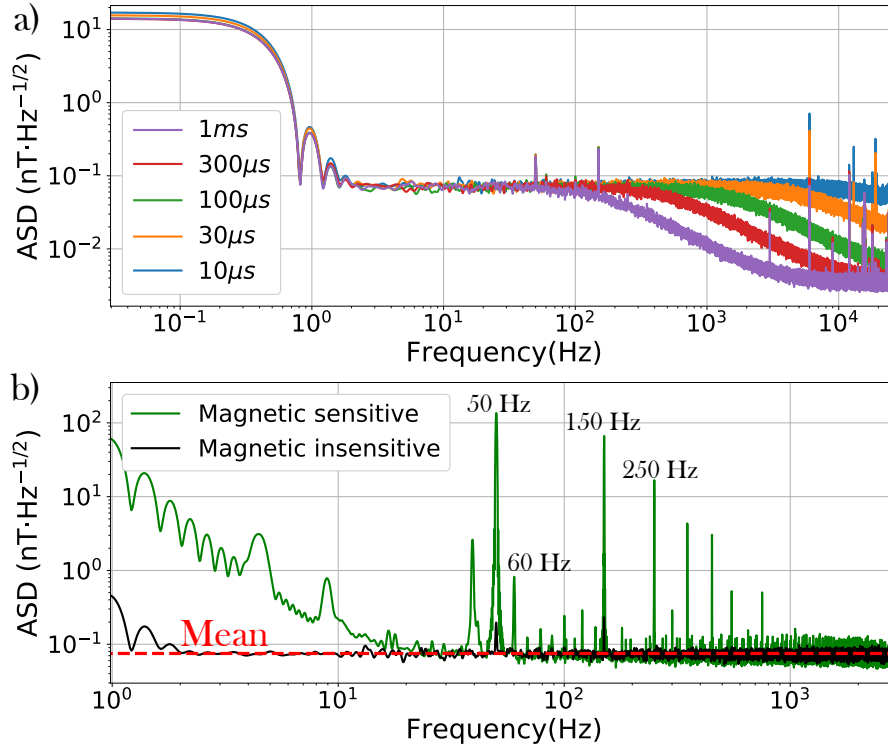


Figure 3.7: a) ASDs in magnetic units from the LIA output with varying lock-in time constant. b) Comparison of noise spectra with MW frequency tuned on the ODMR resonance (Magnetic Sensitive) and away from the resonance (Magnetic Insensitive) with a mean noise floor value of $50 \text{ pT}/\sqrt{\text{Hz}}$.

noise and the shot noise. Based on the previously mentioned figures, the shot-noise limited sensitivity in the low frequency regime was estimated to be in the range of $10\text{-}20 \text{ pT}/\sqrt{\text{Hz}}$. Due to the imperfect rejection of laser technical noise, achieving shot-noise limited sensitivity is very difficult.

While maintaining maximum sensitivity without saturating, the diamond sensor was able to measure ambient background noise up to the kHz frequency range. The maximum detectable field amplitude of the sensor was estimated to be $\sim 35 \mu\text{T}$, assuming an ODMR linewidth of 1 MHz. Compared to the amplitude of the largest noise components, 200 nT for 50 Hz and 70 nT for 150 Hz, this is more than two orders of magnitude higher. Other than mains harmonics, many broad and narrow-band noise peaks are observed. These noise components are produced by heat and water pumps, compressors, and the lock-in amplifier (60 Hz, USA-made).

The ASDs were computed from 60s time-traces using the Welch's method with a Hanning window, segment length of 3.5 s and 50% overlap. The relevant methods utilized in this work for filtering the noise components and retrieving the signals of interest will be described in the last section of this chapter.

3.4 Biological Measurements

3.4.1 Optogenetics

A novel technology, called optogenetics, makes use of genetic targeting of specific proteins in conjunction with optical techniques to enable noncontact stimulation of action potentials (APs) in specific neurons or tissues [86, 87]. Light-triggered activation of AP can be achieved by introducing a gene derived from the alga *Chlamydomonas reinhardtii* that encodes the protein Channelrhodopsin-2 (ChR2), a light-activated cation channel (Fig. 3.8a). By delivering blue light with pulses with an intensity that exceeds the depolarization threshold, this technique enables the triggering of consistent and highly reproducible AP responses even with long pulse trains.

In this work, experiments were conducted using a combination of NV-center magnetometry and optogenetic technology on mice in which ChR2 was expressed by fast-twitch muscle fibers in the extensor digitorum longus (EDL) muscles.

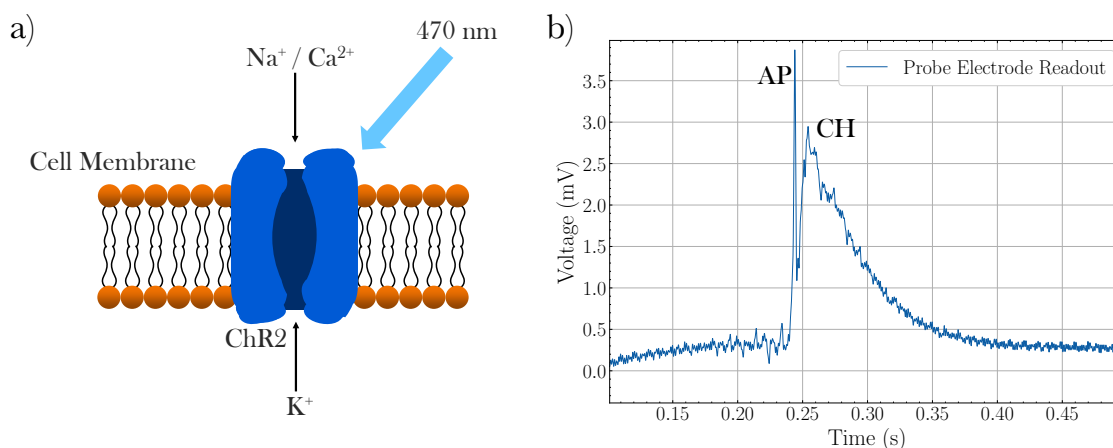


Figure 3.8: a) Sketch of optogenetically triggered action potential. By shining blue light onto the muscle tissue, the ChR2 channels open and trigger APs by allowing Na^+ ions to enter the cell. b) Preliminary recordings of optogenetically induced action potentials measured with probe electrodes on genetically modified mouse muscle. The two features labeled as AP and CH represent the action potential and the ChR2 response to the light stimulus.

Optogenetic stimulation of compound action potentials (synchronous APs from multiple cells) in EDL muscles was tested with probe electrodes recording in a preliminary study, conducted under the same environmental conditions used for the magnetometry experiments. Fig. 3.8b shows an example of these preliminary recordings. Two features were clearly distinguishable in the measured signal, the first one (labeled AP) is to be attributed to the compound action potential of the muscle fibers. The second (labeled CH), can be associated with intrinsic response from the Channelrodopsin. Further investigation of these features is carried out in Chapters 6 and 7.

3.4.2 Data Recording

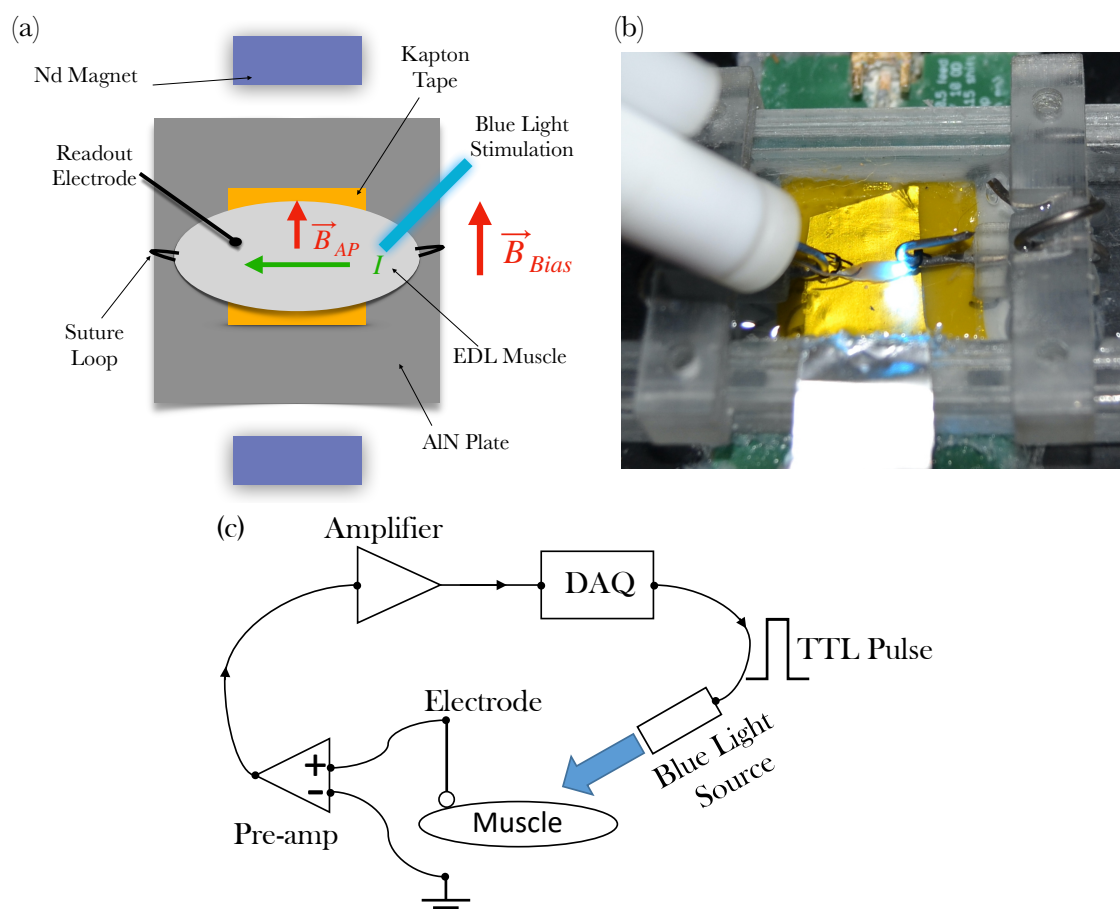


Figure 3.9: a) Top view schematic of biological measurement. Compound action potentials are triggered in the mouse muscle with blue light stimulation. The muscle is aligned perpendicularly to the direction of the magnetic bias field. b) Photograph of the setup sketched in a). c) Diagram of the blue light stimulation and probe electrode apparatus.

A holding chamber containing oxygenated ACSF (Artificial cerebrospinal fluid) solution was used to maintain EDL muscles after the dissection. To minimize the presence of external pathogens that could shorten the lifespan of the samples, the sample chamber described in Section 3.1 and the silicon tubing used to pump the ACSF solution were cleaned using diluted household bleach.

After rinsing the bleach with deionized water, oxygenated ACSF solution was pumped in the sample chamber using the peristaltic pump in a closed loop configuration. The temperature of the solution in the chamber was typically measured between 30-35 °C, taking into account the pump laser and microwaves heating effects.

The muscle was positioned on top of the diamond sensor in the bath solution by gently stretching the suture loops with the two adjustable hooks. The long side of the

muscle was positioned perpendicular to the bias field's direction, so that stimulated electric currents associated with APs would produce a magnetic field parallel to the sensing direction (Fig. 3.9a,b).

A silver wire coated with AgCl was used as a probe electrode to detect the electrophysiological response. The latter will be hereinafter referred to as “electric signal” to avoid confusion with the optical readout from the NV-centers, labeled as “magnetic signal”. The probe electrode was placed on the muscle surface through a micromanipulator, that allowed micrometer control over the electrode's movement.

The electric signal was first amplified through a differential headstage pre-amplifier (Fig. 3.9c), also placed on the micromanipulator. The pre-amplifier measured the voltage difference between the probe electrode and a ground electrode, positioned in the bath solution. Subsequently, the signal was further amplified with a voltage amplifier (Axon Cyberamp 320) and digitized using the previously mentioned DAQ card .

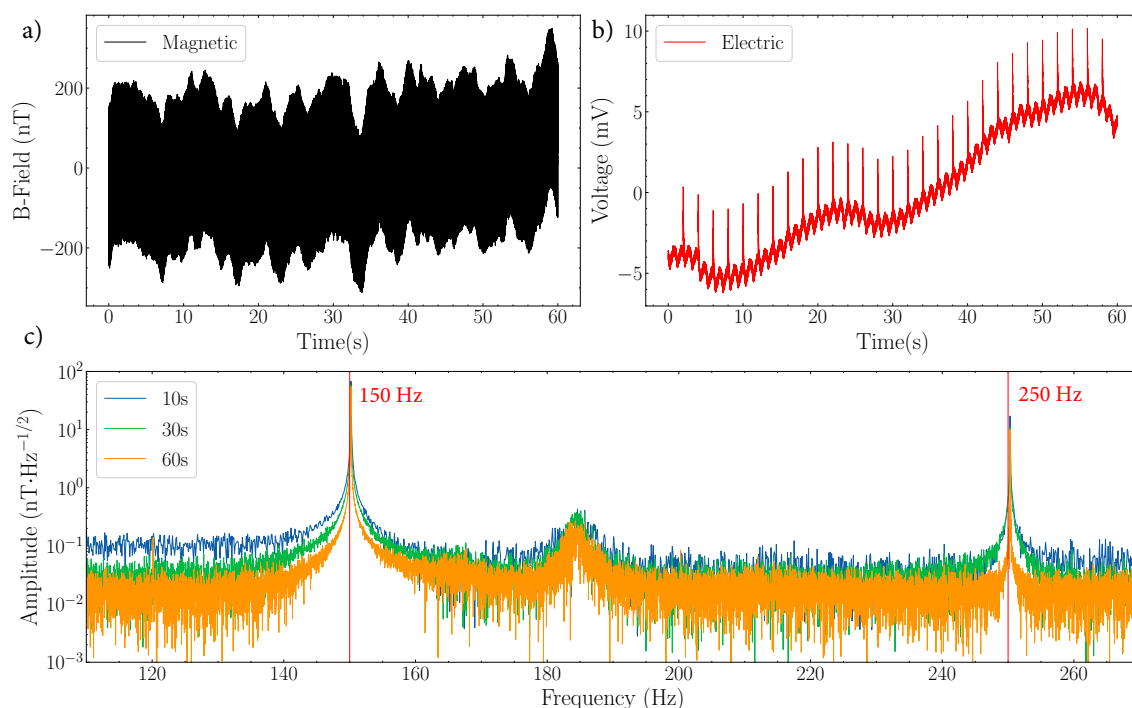


Figure 3.10: a) Example of a 60s time-trace recorded by digitizing the lock-in output voltage during a biological measurement. b) Probe electrode time-trace recorded simultaneously to a). The features that appear with a 0.5 Hz frequency correspond to the biological response from the mouse muscle. c) ASDs obtained by varying the length of the same time-trace. Noise peaks appear broader with shorter time-traces.

Two sets of experiments were performed by varying the light source used for optogenetic stimulation: the first involving the use of 470nm LEDs (Thorlabs' M470F3) and the second involving 488 nm laser (OdicForce Ltd.). In both sets of experiments, the light sources were activated using a 5ms TTL pulse generated from the DAQ card.

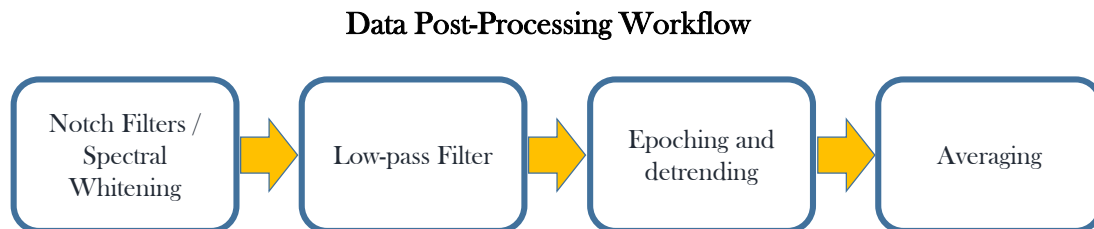
In order to avoid photoelectric effect artifacts, blue light was free-space coupled onto the muscle surface in a location that maximized the light spot-probe electrode distance and at the same time ensured that the AP signal propagated in only one direction.

For both light sources, the optimal blue light power was defined as the minimum power that maximized the muscle's AP response. To avoid damages to the biological sample, light power was initially set at a low level (5 mW) and was then gradually increased until the maximized response was observed. Typically, blue light optimal power was found to be between 20 and 50 mW. A train of pulses with 5 ms length and with a frequency of 0.5 Hz was used for optical stimulation. These values were chosen based on the preliminary experiments conducted by our collaborators.

A frequency resolution of 0.017 Hz was achieved by recording both magnetic and electric signals as time-traces of 60 seconds (**Fig. 3.10a,b**), which was necessary to correctly identify and remove noise peaks generated by environmental sources. An example of Fourier transforms using only the first 10s and 30s of a time trace rather than the entire 60s can be seen in **Fig. 3.10c**. As a result of the shorter segment length, the mains noise peaks appear broader in the frequency spectrum due to the lower frequency resolution. This effect can pose problems when designing sharp notch filters to extract biological signals that are buried in the noise. Due to the large amount of points (60s x 2 x 80000 kSa/s) required to be recorded simultaneously and the limited RAM of the computer, longer time-traces (>60s) could not be recorded. The recorded magnetic and electric signals were stored as compressed binary files before post-processing and analysis, that will be explained in detail in the next section of this chapter.

3.5 Data Post-Processing and Analysis

In this section, it is demonstrated how simple digital signal processing techniques can be used to recover target signals in an unshielded laboratory where external noise sources produce disturbances that are orders of magnitude larger. The post-processing and analysis of data are carried out using a Python v3.0 environment. The recovery of the biological signal can be divided in four steps, as depicted in diagram below. The first step includes the removal of magnetic correlated noise that appears in the noise spectrum as well-defined peaks. The second step involves the removal of high-frequency components with the use of a low-pass filter. Third, the time-traces are divided into smaller windows (epochs) and low-frequency drift is removed. Finally, averaging of the epochs is carried out in the last step.



Caption

3.5.1 Notch Filters and Spectral Whitening

As previously shown in Fig. 3.7, the two largest noise peaks in the magnetic spectrum, both in width and amplitude, could be seen at 50 Hz and 150 Hz: the fundamental mains frequency produced by equipment transformers. Other noise peaks produced by lab equipment or building infrastructures (heat pumps, high-current cabling and compressors) appear in the frequency spectrum as narrowband or broad noise peaks with lower amplitudes. To be able to measure biological signals, it is crucial to attenuate these correlated noise components in time-traces.

For this goal, two different strategies have been applied. The first one (I) involved the identification of noise peaks in the frequency spectrum and subsequent filtering with very steep (brick-wall) notch filters. The second (II) involved spectral whitening, a procedure that has been widely used in many applications that include detection of gravitational waves [88, 89] and radars [90]. Both strategies were applied with the intention of removing all correlated noise while at the same time minimizing the distortions introduced by frequency domain filtering. A direct comparison of the resulting signals obtained with these two methods is shown at the end of the section.

(I) Automatic Peak Removal

To be able to correctly remove the noise peaks in the spectral domain, recording of 30 to 60 minutes of pure-noise time-traces were carried out. This allowed for

identification of noise peaks that were not related to sample response.

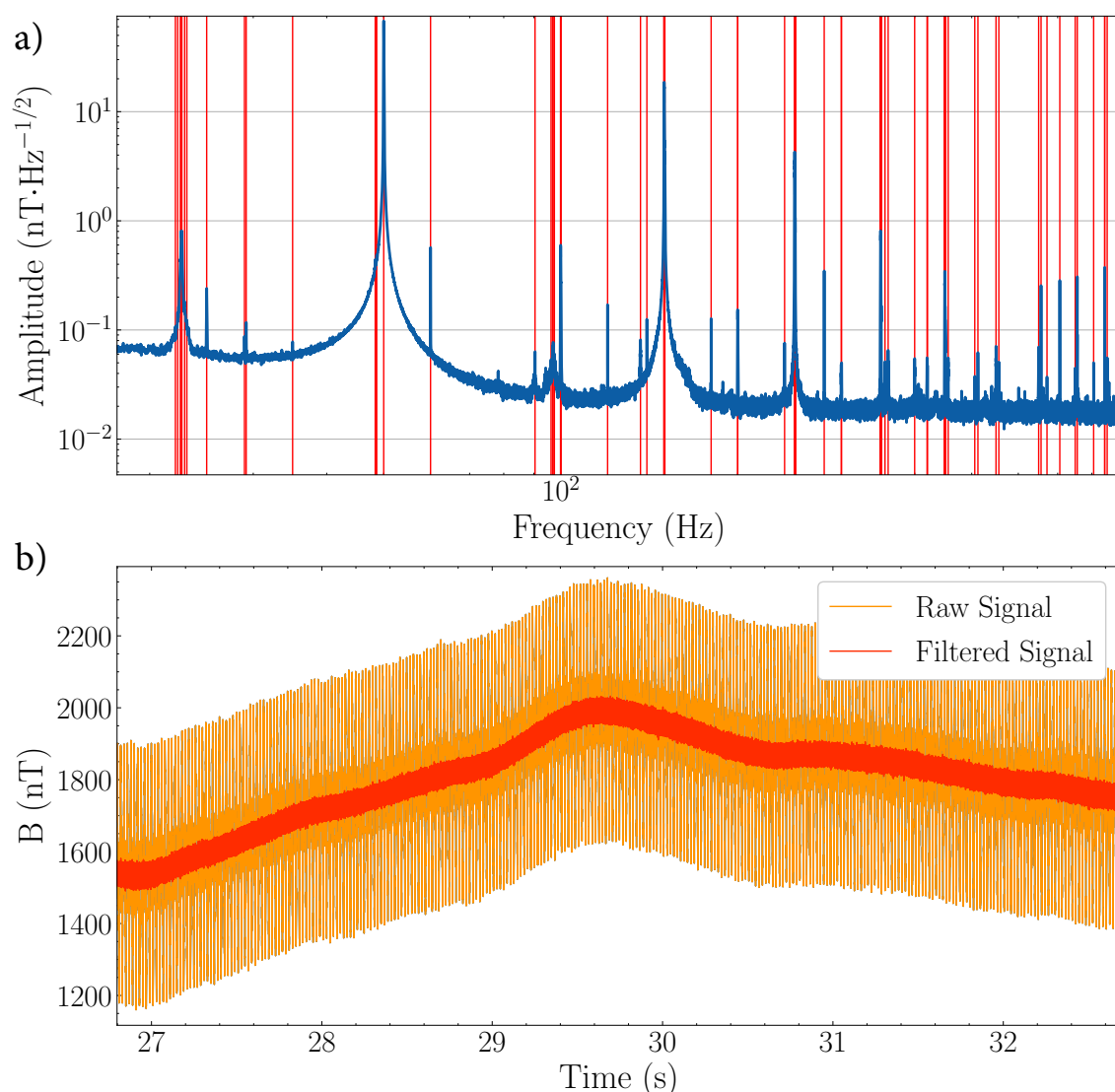


Figure 3.11: a) Amplitude spectral density of a 60s magnetic time trace. The red vertical lines indicate the noise peaks detected by the peak-finder algorithm. b) Comparison of the same magnetic time-trace before and after removing the correlated noise peaks.

An example of amplitude spectral density averaged over 30 minutes is illustrated in **Fig. 3.11a**, and its peaks are identified using Scipy's peak-finder function. The only parameter used in the peak-finder function was the peak prominence, defined as the vertical distance between the peak and its lowest contour line (noise-floor). As output of the peak-finder function both the positions f_i and the estimated half-widths w_i of the noise peaks were given. Peaks positions and peaks widths were used to compute a comb filter transfer function with brick-wall attenuation:

$$H(\omega) = \begin{cases} -10 \text{ dB} & \omega \in f_i \pm w_i \\ 0 \text{ dB} & \text{Otherwise} \end{cases} \quad (3.1)$$

Since brick-wall filters are known to produce ringing effects in the time-domain due to their infinite order [91], $H(\omega)$ was convolved with a gaussian window to smooth the sharp frequency cut-off. The smoothed transfer function was again convolved with the recorded time-traces to allow the attenuation of frequency peaks. It was difficult for the peak-finder function to identify the widths of the main peak frequencies (50 and 150 Hz) due to their wide frequency distribution. To correct this, two additional 5th order Butterworth notch filters were also applied at those frequencies. **Fig. 3.11b** shows an example of the same time time-trace before and after convolving with the filter transfer function.

Since the averaged noise spectrum was recorded before the actual biological measurement, this technique was applied under the assumption that the noise spectrum would remain somewhat unchanged for the duration of the measurement. Generally, this assumption has proven correct; except during measurements on particularly cold days in which the variable load of the building's heat pumps would shift the frequency position of some of the noise components.

(II) Spectral Whitening

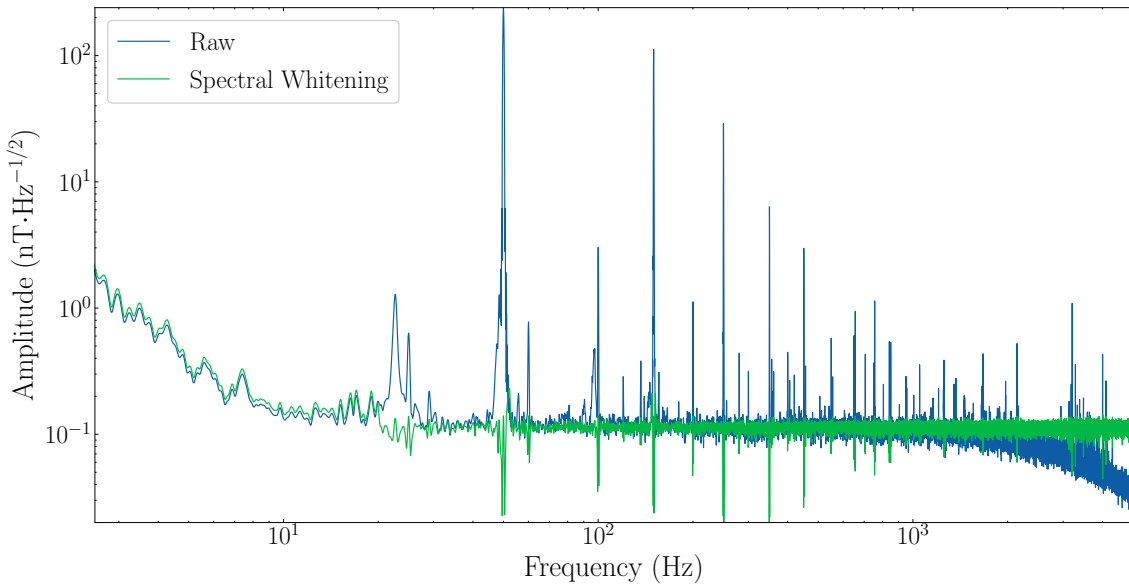


Figure 3.12: Comparison of ASDs from 60s magnetic time-traces before and after applying the spectral whitening filter in the 20Hz - 5kHz range.

To avoid the use of fixed filter widths and ringing artifacts deriving from very sharp filters, spectral whitening was implemented as a substitutional method for correlated noise removal. To implement spectral whitening, a Linear Time-Invariant (LTI) filter was computed for each of the recorded 60s time-traces with the following transfer

function:

$$H(\omega) = S_{xx}^{-1/2}(\omega) \quad (3.2)$$

Where S_{xx} is the PSD of the time trace calculated with Welch's modified periodogram method using Python's Matplotlib library. The double-sided PSD was computed using a Hanning window and two input parameters: segment length and segment overlap. The optimization of these parameters for spectral whitening is explained in detail in the Supplementary Information in Chapter 7.

As illustrated in Fig. 3.12, spectral whitening correctly removes all the correlated noise in the signal by flattening the noise spectrum. Two factors are worth noticing when implementing this procedure. The first is that the PSD which is used to generate the transfer function might contain frequency components from the biological target signal that are above the noise floor. In this case, spectral whitening would attenuate these components together with the correlated noise. In our specific situation, this is avoided due to the SNR of the target signal being $\ll 1$. The second factor is that the original units of the signal (Tesla) are lost when convolving with the transfer function. This occurs because the Fourier Transform of the signal is effectively divided by the square root of the power spectral density that has the same units. To recover the Tesla units of the signal, the spectral whitening transfer function can be modified as:

$$H(\omega) = \sqrt{\frac{k}{S_{xx}(\omega)}} \quad (3.3)$$

Where k is the mean value of the PSD in the bandwidth of interest. The recovery of the units in our case could be achieved with a good degree of accuracy if the PSD was reasonably flat in the whitened bandwidth.

3.5.2 Low-pass Filter

To determine the low pass cutoff frequency for filtering the high-frequency components from magnetic time-traces without distorting the biological signal, the electric signal from the probe electrodes was used as a reference. This is due to the fact that the magnetic biological signal can be recovered only after filtering and averaging and therefore has an unknown bandwidth. For this reason, the electrical response was used as a good approximation of the underlying magnetic signal. Fig. 3.13a shows an example of the averaged electric signal coming from optogenetic stimulation of an EDL muscle. The latter was split into two segments of 0.5 s of length each. The first segment contained only noise coming from the detection apparatus while the second segment contained the triggered biological signal and noise. By separately computing the ASDs of these two segments (Fig. 3.13b), the differences between the two spectra gave a clear indication that the bandwidth of the biological signal lay in the 0-1 kHz range. This can also be illustrated by computing the spectrogram of the electric

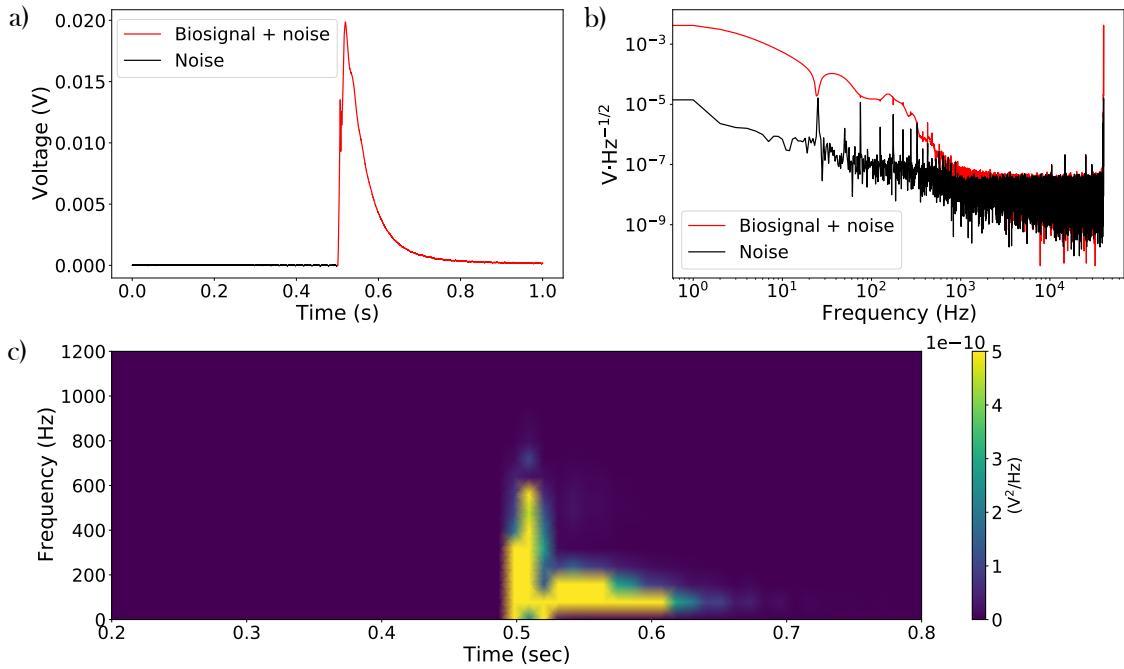


Figure 3.13: a) Electrical probe readout from a mouse muscle stimulation. The signal is divided in two segments of 0.5s each, the first half consists of only noise (black) while the second consists of noise and triggered biological response. b) ASDs of the two signals shown in a) the bandwidth of the biological response can be inferred by their difference. c) Spectrogram of the 1s time-trace shown in a).

signal (**Fig. 3.13c**); after the triggering of the action potential at 0.5s, bright patches corresponding to frequency components up to ~ 700 Hz are visible.

Using this two methods, the low-pass filter cutoff frequency for the magnetic time trace could be safely estimated to be in the range between 700 Hz and 1 kHz.

3.5.3 Epoching and Detrending

Before averaging the magnetic signal, epochs of 1 s centered on the stimulation trigger were extracted from the 60 seconds time-traces. **Fig. 3.14a** and **Fig. 3.14b** show an example of epochs extracted from the electric and magnetic signal respectively.

Due to laser power fluctuations, an accentuated baseline drift is present in the magnetic epochs. To avoid the distorting effect of high-pass filters, the drift was removed by using the robust detrending method [92]. According to this, an epoch is fitted with a high order polynomial after masking the time-interval in which the biological signal should be present. The fit is subsequently subtracted to the epoch to remove the slow drift. In this example, the epochs were masked in the time interval between the stimulation trigger at 0.5 s and 0.8 s and fitted using a 10th order polynomial. The resulting detrended signals are shown in **Fig. 3.14c**.

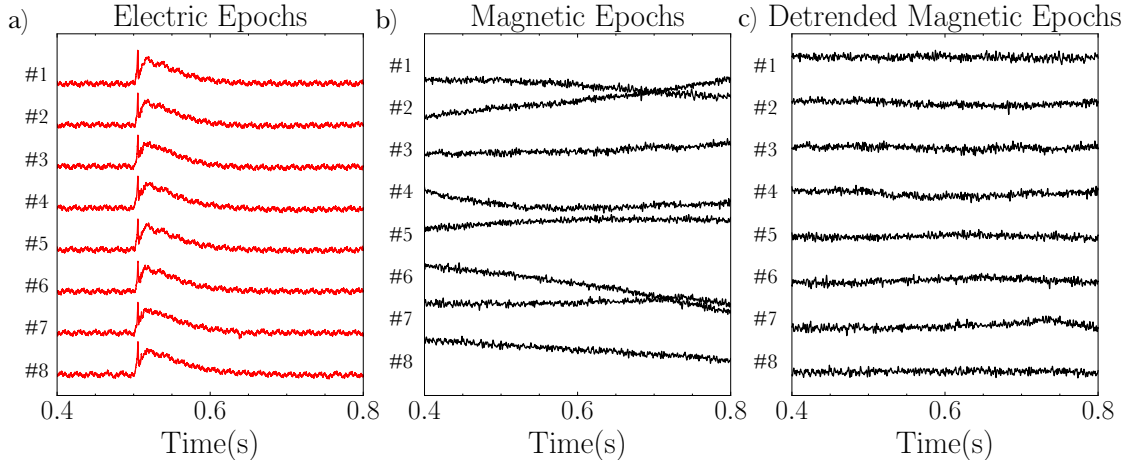


Figure 3.14: a) Example of probe electrode epochs extracted from 60s time-traces. b) Magnetic epochs with low-frequency drift. c) Magnetic epochs after drift removal with the robust detrending algorithm.

In this example, after removing the baseline drift, 22×10^3 magnetic epochs recorded over a period of ten hours were averaged. This resulted in a final RMS noise level as low as 10 pT (**Fig. 3.15a**). To confirm that the resulting noise after the post-processing is uncorrelated and random, the scaling of noise standard deviation with varying number of averaged epochs was fit with a $1/\sqrt{N}$ function, where N represents the number of epochs averaged. **Fig. 3.15b** and **Fig. 3.15c** show a direct comparison of the same averaged magnetic signal recovered using the two different methods illustrated in Section 3.5.1 with good agreement between them.

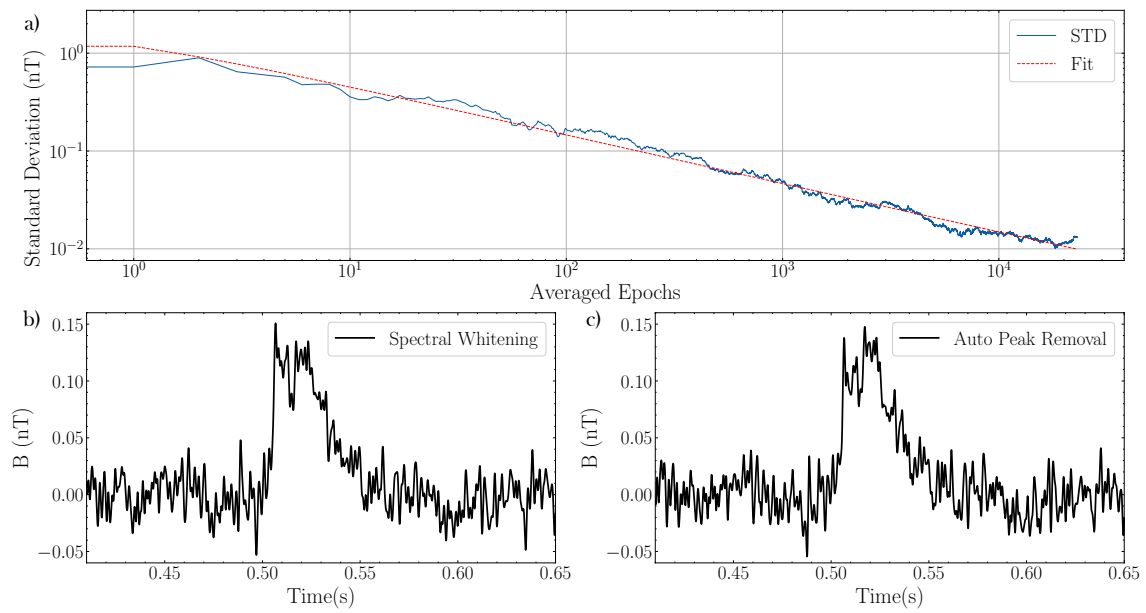


Figure 3.15: a) Noise scaling (STD) with varying number of averaged epochs. The curve is fit with a $1/\sqrt{N}$ function. b) Averaged magnetic epoch obtained with the automatic peak removal algorithm. c) Averaged magnetic epoch obtained with the spectral whitening method.

Chapter 4

Nanotesla sensitivity magnetic field sensing using a compact diamond nitrogen-vacancy magnetometer

4.1 Introduction

The development of a miniaturized diamond NV magnetometer is presented in this chapter. With a compact sensor head of dimensions $11 \times 7 \times 7 \text{ cm}^3$, efficient fluorescence collection is achieved by bringing the diamond into direct contact with an optical filter and a photodiode. The diamond used in this work has sides cut at 67° , the diamond Brewster angle, in order to optimize transmission of 532 nm pump light. A second cut at 22.7° directs the beam throughout the diamond's width to maximize the number of excited NVs. With a sensitivity of $7 \text{ nT}/\sqrt{\text{Hz}}$ close to the shot-noise limit, this flexible method for NV magnetometry is not limited to laboratory applications.

4.2 Publication

This section was published in Applied Physics Letters with the title of “Nanotesla sensitivity magnetic field sensing using a compact diamond nitrogen-vacancy magnetometer” as follows:

Nanotesla sensitivity magnetic field sensing using a compact diamond nitrogen-vacancy magnetometer



Cite as: Appl. Phys. Lett. **114**, 231103 (2019); doi: 10.1063/1.5095241

Submitted: 8 March 2019 · Accepted: 30 May 2019 ·

Published Online: 13 June 2019



View Online



Export Citation



CrossMark

James L. Webb, Joshua D. Clement, Luca Troise, Sepehr Ahmadi, Gustav Juhl Johansen, Alexander Huck, ^{a)} and Ulrik L. Andersen ^{b)}

AFFILIATIONS

Center for Macroscopic Quantum States (bigQ), Department of Physics, Technical University of Denmark, Fysikvej 309, 2800 Kgs. Lyngby, Denmark

^{a)}Electronic mail: alexander.huck@fysik.dtu.dk

^{b)}Electronic mail: ulrik.andersen@fysik.dtu.dk

ABSTRACT

Solid state sensors utilizing diamond nitrogen-vacancy (NV) centers are a promising sensing platform that can provide high sensitivity and spatial resolution at high precision. Such sensors have been realized in bulky laboratory-based forms; however, practical applications demand a miniaturized, portable sensor that can function in a wide range of environmental conditions. Here, we demonstrate such a diamond NV magnetic field sensor. The sensor head fits inside a $11 \times 7 \times 7$ cm³ 3D-printed box and exhibits sub-10 nT/ $\sqrt{\text{Hz}}$ sensitivity over a 125 Hz bandwidth. We achieve efficient fluorescence collection using an optical filter and diode in contact with the diamond, which is cut at the Brewster angle to maximize the coupling of 532 nm pump light. We discuss the potential of this flexible approach to achieve sub-nT/ $\sqrt{\text{Hz}}$ shot noise limited sensitivity suitable for detection of a wide range of low-level magnetic fields, particularly those from electrical power systems and from biological sources.

© 2019 Author(s). All article content, except where otherwise noted, is licensed under a Creative Commons Attribution (CC BY) license (<http://creativecommons.org/licenses/by/4.0/>). <https://doi.org/10.1063/1.5095241>

Quantum sensing using nitrogen-vacancy (NV) centers in diamond has attracted widespread interest in recent years due to the extraordinary high sensitivity and high precision sensory capability of materials under ambient conditions.¹ Sensing of electric fields,² temperature,³ strain fields,⁴ and pressure⁵ has been demonstrated. In particular, research has focused on detection of magnetic fields with a high spatial resolution down to the nanoscale^{6–8} and on samples in environmental conditions that cannot be addressed by alternative solid state magnetometers.

The sensing mechanism is based on electron spin resonance via optical detection of fluorescence from an ensemble of NV centers which is sensitive to local magnetic and electric fields, in addition to the background conditions (e.g., temperature). The sensor sensitivity depends on various parameters, in particular, the number of active NV centers and the spin coherence time T_2^* . These parameters depend on diamond type and the growth method: high pressure high temperature vs chemical vapor deposition, the isotopic composition of the diamond (purified ¹²C vs ¹³C), and the defect nitrogen isotope.⁹

Numerous studies on NV based sensors have focused on increasing the sensitivity via higher photon collection efficiency,^{10–12} using novel excitation schemes,^{13,14} optimized measurement protocols,¹⁵ and diamond structures.¹⁶ Most realizations have been large, bulky setups allowing for maximum optimization and sensitivity in a fixed position. However, as sensor sensitivity now approaches a stage where new interesting applications become possible (e.g., in biodiagnostics), it is of great importance to design and develop miniaturized and movable versions. Recent work has been dedicated to the development of rugged, stable, transportable, and miniaturized diamond sensors to realize such applications.^{17–19}

In this article, we present the design and construction of such a miniaturized, handheld diamond magnetic field sensor based on readily available off-the-shelf and 3D printed components. Using a specially cut and coated (but commercially available) diamond sample combined with a cheap microwave (MW) antenna, an optical filter, and a photodiode, we demonstrate a compact NV excitation and fluorescence collection strategy which in turn enables the construction of a

compact hand-held magnetometer head, coupled to an external microwave and laser source. We show that such a sensor can achieve $7 \text{ nT}/\sqrt{\text{Hz}}$ sensitivity over a bandwidth of 125 Hz, highly suitable for low field, low frequency sensing applications. A NV magnetometer measures external magnetic fields through the Zeeman shift of its spin-triplet 3A ground state ($m_s = 0, \pm 1$), as shown in Fig. 1. A magnetic field induces an energy shift in the ground triplet state of $m_s \gamma_e B_z$, where B_z is the magnetic field along an NV symmetry axis and γ_e is the gyromagnetic ratio (28 Hz/nT). A measurement of the $m_s = \pm 1$ NV ground state energy shift thus reveals information about the strength of the magnetic field along an NV axis.

The field-induced energy shift in the triplet is measured using the technique of optically detected magnetic resonance (ODMR), where the NV centers are both optically excited and driven by a microwave (MW) source. When driven with MW frequency corresponding to the spin splitting of the triplet state, relaxation can occur via a singlet state, as shown in Fig. 1. This results in a detectable dip in red $\approx 637 \text{ nm}$ fluorescence output at a frequency that depends on the Zeeman shift and hence the magnetic field. Intersystem crossing from the singlet shelving state to the $m_s = 0$ triplet ground state polarizes the spins in the $m_s = 0$ ground state. Under optical pumping with green laser light, this completes a loop that allows continuous detection of the ODMR fluorescence dip.²⁰ Detection of ODMR can be via a pulsed scheme, using a Ramsey or spin-echo sequence⁹ or, as in this work, a simpler, robust continuous wave (CW) approach with constant laser and MW power.

There are two primary obstacles to achieving high sensitivity in an NV-based sensor. First, it is necessary to efficiently excite the NV centers. The low NV center absorption cross section requires a high

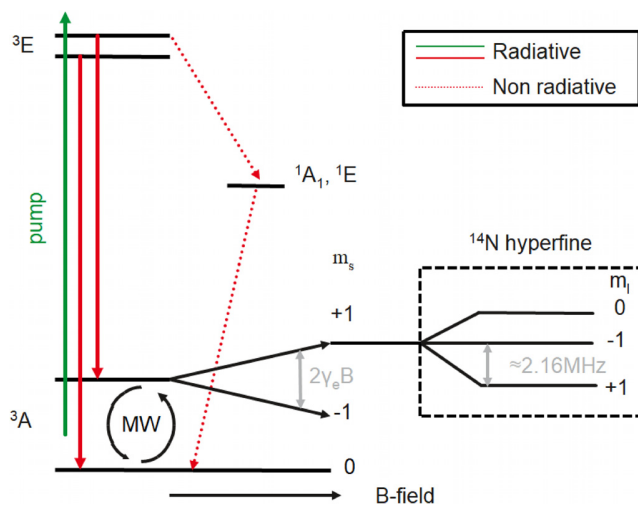


FIG. 1. NV energy level scheme. The NV center is optically pumped at 532 nm into the excited triplet state 3E and decays back into the ground state 3A with fluorescent red emission. For the $m_s = 0$ sublevel, emission occurs within the triplet only. For the $m_s = \pm 1$ levels, intersystem crossing into a singlet state 1E can lead to decay nonradiatively (or via 1042 nm infrared emission) via the singlet ground state 1A . This results in a dip in fluorescence output. By transferring the populations between $m_s = 0$ and $m_s = \pm 1$, through absorption of resonant MWs at $\approx 2.8 \text{ GHz}$, dependent on the Zeeman shift of the 3E levels, this drop in fluorescence can be directly observed (ODMR). The electronic transitions are hyperfine split by the ^{14}N nuclear spin.

power pump laser, pump trapping,¹³ or an optical cavity.²¹ Second, fluorescence light must be efficiently captured, despite the high refractive index of diamond meaning much of it is trapped by total internal reflection. Different schemes to maximize fluorescence collection include using a parabolic collection lens,¹² collection at the diamond edges,⁷ and using a dielectric antenna.¹¹

In this work, we have addressed these two challenges by using an approach with angled cut diamond end facets that allow a high power, tightly collimated pump beam to travel laterally through the entire diamond width. This is outlined schematically in Fig. 2(a). In addition, we maximize the collection of this light by attaching (using immersion oil) a photodiode to the front surface of the diamond after a thin optical filter while reflective coating the back.

The simplified and compact setup design is presented in Fig. 2(b). We used a commercially available single crystal diamond, grown via chemical vapor deposition with the natural ^{13}C content, with dimensions of $6 \times 6 \times 1.2 \text{ mm}^3$ from Element 6. The sample had $[^{14}\text{N}] < 1 \text{ ppm}$, and the natural $[^{14}\text{NV}]$ concentration was determined to be $\approx 0.2 \text{ ppb}$.²¹ We used a p-polarized pump laser (Cobolt 05-01) with a maximum power of 0.5 W at 532 nm, which can be fiber coupled into the sensor head. The pump beam was collimated to a mode field diameter of approximately $45 \mu\text{m}$ and focused on one of the edge cut facets of the diamond. The two edge facets for the 532 nm pump beam were cut by Almax easyLab to the Brewster angle of $67^\circ \pm 0.1^\circ$, respectively, facilitating efficient entry of the pump beam into the

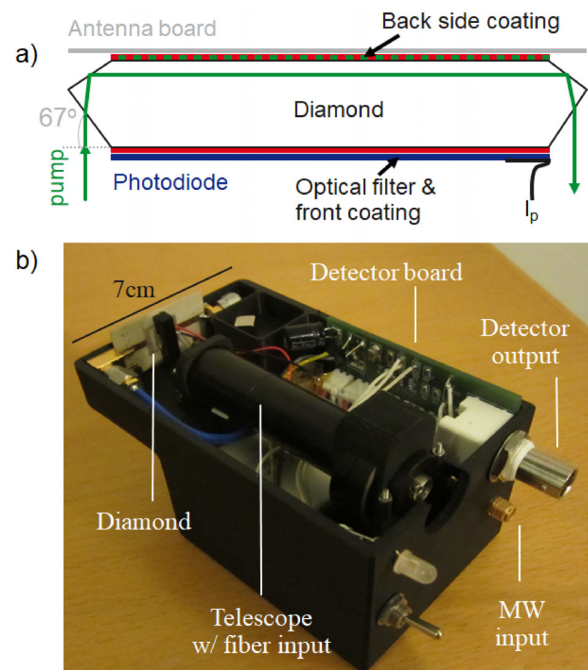


FIG. 2. (a) Schematic of the specially cut diamond crystal, optical coatings and filter, attached photodiode, and MW antenna. We use two cut surfaces, one at the diamond Brewster angle (67°) to ensure maximum transmission of a beam perpendicular to the diamond front surface and a second cut at 22.7° to direct the beam laterally through the entire width of the diamond, exciting the maximum number of NV centers as possible and exiting at an identically cut facet on the opposite side. (b) Labeled photograph of the opened handheld sensor head.

diamond. We estimate the pump beam to propagate inside at least the full width of the diamond (≈ 6 mm). As indicated in Fig. 2, the back side of the diamond was coated with a highly reflective (HR, $R > 99\%$) coating covering the spectrum 500–800 nm, while the front side was HR ($R > 99\%$) coated for 532 nm and antireflective coated ($R < 1\%$) for 600–800 nm. We attach a 550 nm long pass optical filter (Thorlabs FELH0550, cut to size) before the photodiode to reject stray pump light.

The diamond was mounted onto a printed circuit board with a MW split-ring resonator²² with a diamond loaded design resonance frequency of 2.89 GHz confirmed by a S_{11} reflection measurement. Microwaves were delivered from an external source (Stanford SG380 with Minicircuits ZHL-16W-43+ amplifier) at a 500 kHz width frequency modulation at 33.3 kHz. For the magnetic field measurements, we applied a MW drive with three frequency components separated by the ^{14}N hyperfine frequency of $f_{hf} = 2.16$ MHz to boost sensitivity.²¹

For optical detection, we used photodiodes (PDB-C160SMCT-ND, Advanced Photonix), 15 V battery reverse biased. The photodiode responsivity was $R_{532\text{nm}} = 0.2$ A/W at 532 nm and $R_{637\text{nm}} = 0.37$ A/W at 637 nm. By using a small polarizing beam splitter and half-wave plate, we sampled a fraction of the 532 nm pump laser beam and directed this onto a secondary, identical photodiode in a balanced detection scheme in order to perform common mode rejection (CMR) of pump laser technical noise. The resulting signal was passed into a lock-in amplifier (Stanford Research 850), external to the sensor head, locked to the MW modulation frequency (33.3 kHz), with output digitized by an external analog-to-digital converter (NI-DAQ 6221) allowing precise detection of the ODMR spectrum. We consider that in an updated design, these components could be readily incorporated in the sensor head.

We optimized our setup by first measuring the DC photocurrent I_{pc} directly using an ammeter from the primary photodiode on the diamond as a function of pump laser power from 30 mW up to 0.5 W. We also measured the amplitude spectral density (ASD) of the detected modulated ($f_m = 33.3$ kHz) fluorescence signal using only the primary photodiode and by CMR via balanced detection. This was done by a fast-Fourier transform of a 1 s signal digitized at 125 kSa/s, taking the average level up to the -3 dB filter roll-off imposed by the lock-in time constant (1 ms). The ASD as a function of I_{pc} can be seen in Fig. 3 alongside the shot noise level, calculated from the DC photocurrent, and the electronic noise floor. We define the electronic noise floor as the noise level from the detection electronics with zero pump and ambient illumination. The single and balanced photodiode data therefore include this electronic noise. The measurements demonstrate the dominance of technical noise from the pump laser over all other sources of noise. CMR of technical noise was able to reduce the noise level by $> \times 10$ vs single diode detection. Using CMR, we were able to obtain near shot noise limited fluorescence detection, the difference being due to the limitations of our manual (optical) balancing scheme. We measured photocurrent to scale linearly with pump power, indicating better photodetection sensitivity at high power (due to the scaling of shot noise with the root of laser power). Using maximum laser power (0.5 W), we then measured the ODMR spectrum from the diamond. In order to resolve the ^{14}N hyperfine structure, we use a fixed offset field ≈ 1 mT from two rare earth magnets. The optical magnetic resonance spectrum was recorded by sweeping the MW frequency, measuring the modulated photovoltage using a lock-in amplifier. The

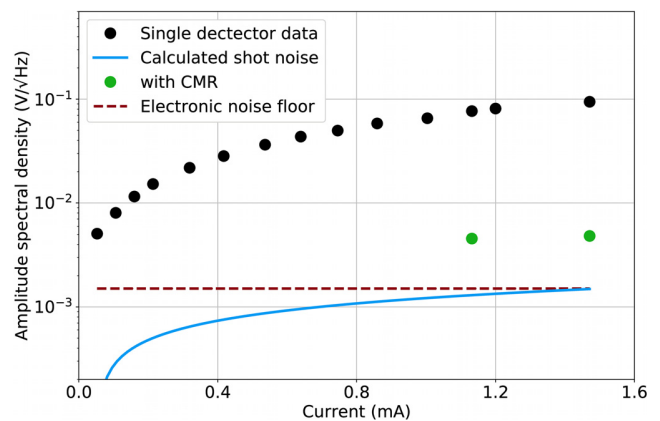


FIG. 3. Mean amplitude spectral density of the optical signal over the 125 Hz sensing bandwidth, plotted as a function of photocurrent, I_{pc} for a single photodetector (the primary photodiode on the diamond), at 330 mW and 0.5 W for two photodetectors in a balanced configuration to reject common mode noise (with CMR). We also plot the shot noise for a single detector calculated from $I_{pc} (\times \sqrt{2})$ for CMR and the electronic noise floor.

plotted spectrum in Fig. 4 arises from the deliberate permanent magnet alignment along one of the four $\langle 111 \rangle$ NV axes and clearly shows the ^{14}N hyperfine splitting. By a linear fit to the ODMR spectrum, we determine a slope of $25 \mu\text{V}/\text{Hz}$ corresponding to 0.7 mV/nT assuming a shift of 28 Hz/nT. This slope was optimized by repeating the ODMR spectrum as a function of MW drive power. The optimum power prior to amplification was 4 dBm and -2 dBm for the main and 2.16 MHz drive, respectively, giving ≈ 6 W from the amplifier. We note importantly no saturation of the ODMR contrast with laser power, an issue that can limit NV sensor sensitivity.²³ With the sensitivity determined from the ODMR spectrum, we measured magnetic sensitivity as a function of magnetic field frequency, again by fast-

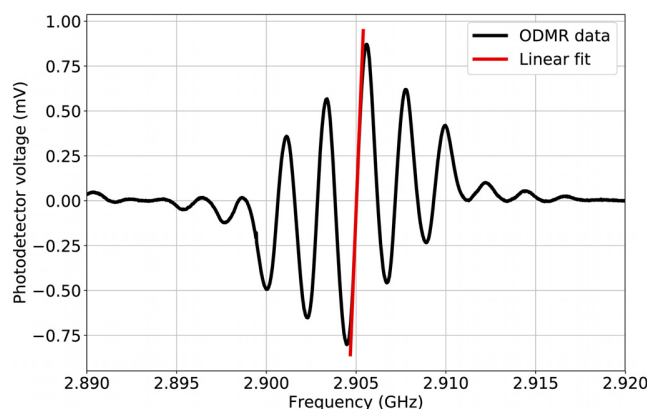


FIG. 4. Optically detected magnetic resonance (ODMR) spectrum, recorded as a function of MW drive frequency with CMR on. We observe the $m_s = 0 \leftrightarrow +1$ electron spin transition and hyperfine splitting arising from ^{14}N . By a linear fit to the slope of the ODMR spectrum, we determined the relation between signal voltage and frequency shift to be $25 \mu\text{V}/\text{Hz}$, from which we determined the magnetic field sensitivity using the relation $\gamma_e B_z$, assuming $\gamma_e = 28$ Hz/nT.

Fourier transform of 1 s of digitized signal at 125 kSa/s. The magnetic noise density spectrum is plotted in Fig. 5. We compare sensitivity with CMR on and off and at MW drive frequencies of 2.905 GHz and 2.908 GHz, corresponding to the points of maximum (least) magnetic field sensitivity as determined from the maximum slope (peak) of the ODMR spectrum. We plot the ultimate electronic noise floor, defined by our amplifier and analog-to-digital converter, located at $\approx 2 \text{ nT}/\sqrt{\text{Hz}}$.

The amplitude spectrum shows a noise floor of $\approx 150 \text{ nT}/\sqrt{\text{Hz}}$ without CMR and $\approx 7 \text{ nT}/\sqrt{\text{Hz}}$ with CMR turned on. This highlights how essential rejection of laser technical noise is in diamond magnetometry. When magnetically sensitive, we observed peaks primarily at 50 Hz and 150 Hz. Such peaks were not observed when at a magnetically insensitive drive frequency (2.908 GHz). These frequencies correspond clearly to direct detection of the magnetic field produced by nearby electrical transformers: the strong 3rd harmonic at 150 Hz is a frequency component of the transformer magnetic field produced by magnetic hysteresis in the transformer core. Were we detecting spurious mains electrical noise, the 2nd harmonic at 100 Hz would also be strongly present. Peaks at 60 Hz and higher harmonics were traced to inbuilt components in United States-purchased equipment.

Based on the detected photocurrent, we calculate the total optical power detected by the primary photodiode to be 3.6 mW. This corresponds to an estimated shot noise limited sensitivity of $\approx 3 \text{ nT}/\sqrt{\text{Hz}}$. The absorption cross section at 532 nm for a single ^{14}NV center is reported²⁴ to be $\sigma_{\text{NV}} = 3.1 \times 10^{-15} \text{ mm}^2$. Taking a NV density of $6.4 \times 10^{13} \text{ cm}^{-3}$, a NV quantum efficiency of $\eta \approx 0.9$,²⁵ and a propagation length inside the diamond of 6 mm, the fluorescence power from the ensemble is 0.53 mW at the maximum pump power (0.5 W). This is significantly lower than the measured fluorescence power of 3.6 mW. This illustrates that the majority of the photocurrent is due to leakage of pump light past the filter and into the photodiode. It also highlights the minimal single pass absorption of the pump light by our diamond with this level of NV defects. Such absorption can be enhanced by

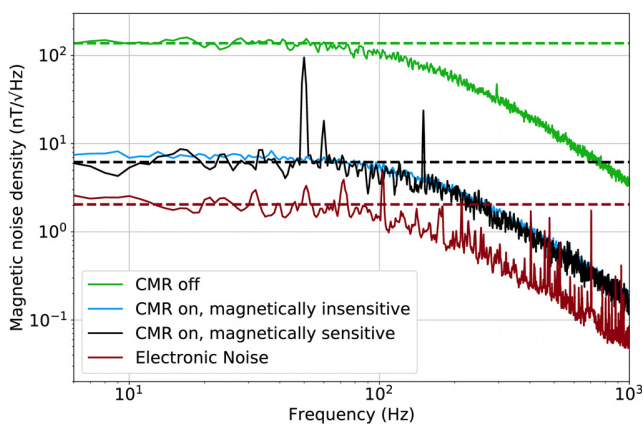


FIG. 5. Magnetic noise frequency spectrum at 0.5 W pump power, plotted as ASD in $\text{nT}/\sqrt{\text{Hz}}$. We show the noise density without balanced detection (CMR off), with CMR on and the detector magnetically sensitive (2.905 GHz) and insensitive (2.908 GHz). We also show the electronic limit (pump off). We observe a mean noise floor of $7 \text{ nT}/\sqrt{\text{Hz}}$ when rejecting laser technical noise. We observe the same high frequency peaks at 400–1 kHz on all data, from the power supplies and cooling fans. Only when magnetically sensitive do we clearly observe 50/150 Hz peaks from mains transformer field.

boosting defect density via optimized doping, irradiation, and annealing or by use of an optical cavity around the diamond.²⁵

Our current design has potential to be improved to subnanotesla sensitivity and in compactness and size. The primary limitation of our sensor head size was the internal focusing optics, which could be further miniaturized. Increasing the NV concentration in combination with ^{12}C purification has been shown to improve ODMR contrast and reduce linewidth.⁹ Leakage of pump light, in a wide range of incidence angles, proved difficult to fully reject in our sensor using available commercial filters. Further improvement in filter composition and structure is required in this geometry. Moving the filter away from the diamond surface to narrow the incidence angle of scattered pump light would help, but at the expense of sensor miniaturization. An ideal filter rejecting all pump light reduces the shot noise by approximately a factor of 2–3. Electronic balancing of the detection and CMR would reduce our electronic noise floor. In the shot noise limit, simply increasing laser power would improve sensitivity (3.3 W pump power has been demonstrated²⁶). We note that our bandwidth is not imposed by the physics of our sensor and could easily be increased in order to detect higher frequency fields, limited only by relaxation time T_2^* . A noise source not considered here is temperature variation, dependent on heat dissipation and the local environment. It has been demonstrated that such temperature effects can be efficiently corrected by driving simultaneously at both the $m_s = \pm 1 \text{ MW}$ resonances.²⁷

Several recent efforts have been made to produce a miniaturized NV magnetometer as an integrated package,^{18,19} with onboard light and MW sources, of sensitivity in the 30–100 $\text{nT}/\sqrt{\text{Hz}}$ range. We show that to achieve subnanotesla level sensitivity may require pump power of the order of several Watts for a millimeter-scale diamond with a sufficiently large NV ensemble at currently achievable NV defect densities and levels of material strain. This factor suggests that having a sensor head(s) into which laser and MWs can be coupled (a setup common in, e.g., medical devices) may be preferable for high sensitivity operation, since it may be difficult to generate enough power at low electronic noise in an integrated package within the sensor head.

The level of sensitivity we demonstrate in this work should permit many new applications. We particularly highlight applications in sensing of weak (nanotesla, picotesla scale) magnetic fields from biological sources, such as living tissue or samples in solution. This can be difficult for alternative techniques, e.g., unencapsulated magnetoresistive sensors, relying on electrical readout. Biocompatibility of diamond allows high proximity with a sample, assisting field detection given the rapid (cubic) drop in field strength with distance. Competing techniques may need to be positioned relatively far (many millimeters) from the sample. Of particular interest is sensing of bioelectric signals by their magnetic field that cannot otherwise be easily accessed by electrical probes (for example, magnetoencephalography of the brain) where current magnetometers—superconducting quantum interference (SQUID) devices or recently demonstrated atomic vapor cells²⁸—are expensive and cumbersome and have poor spatial resolution.

High spatial resolution in diamond NV sensors can be readily achieved by imaging fluorescence with a camera and has been demonstrated elsewhere in, e.g., geological samples²⁹ and magnetic bacteria to the micrometer scale.³⁰ Biological signals are typically observed in the hundreds of hertz to low-kilohertz frequency range, over which we demonstrate excellent sensitivity in this work. Other low frequency

magnetic signals of interest include diagnostics of mains power systems (transformers, motors) operating at DC or single/three phase 50/60 Hz.

In conclusion, we have developed a diamond magnetometer with a handheld sensing head, with a sensitivity of $7 \text{ nT}/\sqrt{\text{Hz}}$ and an ultimate noise floor of $3 \text{ nT}/\sqrt{\text{Hz}}$. We demonstrate robust, flexible sensing using diamond NV centers which is not limited to fixed benchtop applications. We discuss a route to achieving $\text{sub-nT}/\sqrt{\text{Hz}}$ sensitivity through improvements in the NV-concentration, optical filtering, and detection and by implementing pulsed measurement schemes.

We gratefully acknowledge Kristian H. Rasmussen and Aleksander Tchernavskij for support in fabrication and electronic design. This project was financially supported by the Innovation Fund Denmark (EXMAD project and Qubiz center) and the Novo Nordisk foundation (bioQ project).

REFERENCES

- ¹J. M. Taylor, P. Cappellaro, L. Childress, L. Jiang, D. Budker, P. R. Hemmer, A. Yacoby, R. Walsworth, and M. D. Lukin, *Nat. Phys.* **4**, 810 (2008).
- ²F. Dolde, H. Fedder, M. W. Doherty, T. Noebauer, F. Rempp, G. Balasubramanian, T. Wolf, F. Reinhard, L. C. L. Hollenberg, F. Jelezko, J. Wrachtrup, and T. Nöbauer, *Nat. Phys.* **7**, 459 (2011).
- ³V. M. Acosta, E. Bauch, M. P. Ledbetter, A. Waxman, L.-S. Bouchard, and D. Budker, *Phys. Rev. Lett.* **104**, 070801 (2010).
- ⁴M. E. Trusheim and D. Englund, *New J. Phys.* **18**, 123023 (2016).
- ⁵M. W. Doherty, V. V. Struzhkin, D. A. Simpson, L. P. McGuinness, Y. Meng, A. Stacey, T. J. Karle, R. J. Hemley, N. B. Manson, L. C. Hollenberg, and S. Praver, *Phys. Rev. Lett.* **112**, 047601 (2014).
- ⁶P. Maletinsky, S. Hong, M. S. Grinolds, B. Hausmann, M. D. Lukin, R. L. Walsworth, M. Loncar, and A. Yacoby, *Nat. Nanotechnol.* **7**, 320 (2012).
- ⁷D. Le Sage, L. M. Pham, N. Bar-Gill, C. Belthangady, M. D. Lukin, A. Yacoby, and R. L. Walsworth, *Phys. Rev. B* **85**, 121202 (2012).
- ⁸K. Jensen, V. M. Acosta, A. Jarmola, and D. Budker, *Phys. Rev. B* **87**, 014115 (2013).
- ⁹L. Rondin, J.-P. Tetienne, T. Hingant, J.-F. Roch, P. Maletinsky, and V. Jacques, *Rep. Prog. Phys.* **77**, 056503 (2014).
- ¹⁰L. Marseglia, J. P. Hadden, A. Stanley-Clarke, J. P. Harrison, B. Patton, Y.-L. D. Ho, B. Naydenov, F. Jelezko, J. Meijer, P. R. Dolan, J. M. Smith, J. G. Rarity, and J. L. O'Brien, *Appl. Phys. Lett.* **98**, 133107 (2011).
- ¹¹D. Riedel, D. Rohner, M. Ganzhorn, T. Kaldewey, P. Appel, E. Neu, R. Warburton, and P. Maletinsky, *Phys. Rev. Appl.* **2**, 064011 (2014).
- ¹²T. Wolf, P. Neumann, K. Nakamura, H. Sumiya, T. Ohshima, J. Isoya, and J. Wrachtrup, *Phys. Rev. X* **5**, 041001 (2015).
- ¹³H. Clevenson, M. E. Trusheim, C. Teale, T. Schröder, D. Braje, and D. Englund, *Nat. Phys.* **11**, 393 (2015).
- ¹⁴L. Bougas, A. Wilzewski, Y. Dumeige, D. Antypas, T. Wu, A. Wickenbrock, E. Bourgeois, M. Nesladek, H. Clevenson, D. Braje, D. Englund, and D. Budker, *Micromachines* **9**, 276 (2018).
- ¹⁵V. M. Acosta, E. Bauch, A. Jarmola, L. J. Zipp, M. P. Ledbetter, and D. Budker, *Appl. Phys. Lett.* **97**, 174104 (2010).
- ¹⁶G. Balasubramanian, P. Neumann, D. Twitchen, M. Markham, R. Kolesov, N. Mizuochi, J. Isoya, J. Achard, J. Beck, J. Tissler, V. Jacques, P. R. Hemmer, F. Jelezko, and J. Wrachtrup, *Nat. Mater.* **8**, 383 (2009).
- ¹⁷G. Chatzidrosos, A. Wickenbrock, L. Bougas, N. Leefter, T. Wu, K. Jensen, Y. Dumeige, and D. Budker, *Phys. Rev. Appl.* **8**, 044019 (2017).
- ¹⁸F. M. Strner, A. Brenneis, J. Kassel, U. Wostradowski, R. Rlver, T. Fuchs, K. Nakamura, H. Sumiya, S. Onoda, J. Isoya, and F. Jelezko, *Diamond Relat. Mater.* **93**, 59 (2019).
- ¹⁹M. I. Ibrahim, C. Foy, D. Kim, D. R. Englund, and R. Han, in *2018 IEEE Symposium on VLSI Circuits* (2018), pp. 249–250.
- ²⁰G. M. H. Thiering and A. Gali, *Phys. Rev. B* **98**, 085207 (2018).
- ²¹S. Ahmadi, H. A. El-Ella, J. O. Hansen, A. Huck, and U. L. Andersen, *Phys. Rev. Appl.* **8**, 034001 (2017).
- ²²K. Bayat, J. Choy, M. Farrokh Baroughi, S. Meesala, and M. Loncar, *Nano Lett.* **14**, 1208 (2014).
- ²³A. Dréau, M. Lesik, L. Rondin, P. Spinicelli, O. Arcizet, J.-F. Roch, and V. Jacques, *Phys. Rev. B* **84**, 195204 (2011).
- ²⁴T.-L. Wee, Y.-K. Tzeng, C.-C. Han, H.-C. Chang, W. Fann, J.-H. Hsu, K.-M. Chen, and Y.-C. Yu, *J. Phys. Chem. A* **111**, 9379 (2007).
- ²⁵S. Ahmadi, H. A. R. El-Ella, A. M. Wojciechowski, T. Gehring, J. O. B. Hansen, A. Huck, and U. L. Andersen, *Phys. Rev. B* **97**, 024105 (2018).
- ²⁶J. M. Schloss, J. F. Barry, M. J. Turner, and R. L. Walsworth, *Phys. Rev. Appl.* **10**, 034044 (2018).
- ²⁷A. M. Wojciechowski, M. Karadas, C. Osterkamp, S. Jankuhn, J. Meijer, F. Jelezko, A. Huck, and U. L. Andersen, *Appl. Phys. Lett.* **113**, 013502 (2018).
- ²⁸E. Boto, N. Holmes, J. Leggett, G. Roberts, V. Shah, S. S. Meyer, L. D. Muñoz, K. J. Mullinger, T. M. Tierney, S. Bestmann, G. R. Barnes, R. Bowtell, and M. J. Brookes, *Nature* **555**, 657 (2018).
- ²⁹D. R. Glenn, R. R. Fu, P. Kehayias, D. Le Sage, E. A. Lima, B. P. Weiss, and R. L. Walsworth, *Geochem., Geophys., Geosyst.* **18**, 3254, <https://doi.org/10.1002/2017GC006946> (2017).
- ³⁰D. Le Sage, K. Arai, D. R. Glenn, S. J. Devience, L. M. Pham, L. Rahn-Lee, M. D. Lukin, A. Yacoby, A. Komeili, and R. L. Walsworth, *Nature* **496**, 486 (2013).

Chapter 5

Optimization of a Diamond Nitrogen Vacancy Centre Magnetometer for Sensing of Biological Signals

5.1 Introduction

Sensing biosignals is a powerful tool for clinical diagnosis and fundamental research. Standard electrophysiology techniques typically rely on invasive probe sensors that show poor spatial resolution and limited access to deep tissues. In the current chapter, we present advances in the biomagnetic sensing field using a bio-compatible NV diamond magnetometer with sensitivity of $100 \text{ pT}/\sqrt{\text{Hz}}$. With a solid-state sensor that can operate at room temperature and in an unshielded environment, this setup is suitable for a variety of different ex vivo systems, including brain slices or mammalian muscles. A discussion of the challenges of achieving such measurements is given, including the filtering of external magnetic noise and temperature stability. Additionally, the steps toward improving sensitivity using pulsed magnetometry schemes are presented along with the steps towards wide-field NV imaging of biological signals.

5.2 Publication

This section was published in *Frontiers in Physics* with the title of “Optimization of a Diamond Nitrogen Vacancy Centre Magnetometer for Sensing of Biological Signals” as follows:



Optimization of a Diamond Nitrogen Vacancy Centre Magnetometer for Sensing of Biological Signals

James L. Webb^{1*}, Luca Troise¹, Nikolaj W. Hansen², Jocelyn Achard³, Ovidiu Brinza³, Robert Staacke⁴, Michael Kieschnick⁴, Jan Meijer⁴, Jean-François Perrier², Kirstine Berg-Sørensen⁵, Alexander Huck¹ and Ulrik Lund Andersen¹

¹ Department of Physics, Center for Macroscopic Quantum States (bigQ), Technical University of Denmark, Kongens Lyngby, Denmark, ² Department of Neuroscience, Copenhagen University, Copenhagen, Denmark, ³ Laboratoire des Sciences des Procédés et des Matériaux, CNRS, Université Paris 13, Sorbonne Paris Cité, Paris, France, ⁴ Division Applied Quantum System, Felix Bloch Institute for Solid State Physics, University of Leipzig, Leipzig, Germany, ⁵ Department of Health Technology, Technical University of Denmark, Kongens Lyngby, Denmark

OPEN ACCESS

Edited by:

Carlo Manzo,
Universitat de Vic-Universitat Central
de Catalunya, Spain

Reviewed by:

Liam Terres Hall,
The University of Melbourne, Australia
Takeshi Ohshima,
National Institutes for Quantum and
Radiological Science and Technology,
Japan
Anne Fabricant,
Helmholtz Institute Mainz, Germany

*Correspondence:

James L. Webb
jaluwe@fysik.dtu.dk

Specialty section:

This article was submitted to
Biophysics,
a section of the journal
Frontiers in Physics

Received: 23 December 2019

Accepted: 28 August 2020

Published: 19 October 2020

Citation:

Webb JL, Troise L, Hansen NW, Achard J, Brinza O, Staacke R, Kieschnick M, Meijer J, Perrier J-F, Berg-Sørensen K, Huck A and Andersen UL (2020) Optimization of a Diamond Nitrogen Vacancy Centre Magnetometer for Sensing of Biological Signals. *Front. Phys.* 8:522536. doi: 10.3389/fphy.2020.522536

Sensing of signals from biological processes, such as action potential propagation in nerves, are essential for clinical diagnosis and basic understanding of physiology. Sensing can be performed electrically by placing sensor probes near or inside a living specimen or dissected tissue using well-established electrophysiology techniques. However, these electrical probe techniques have poor spatial resolution and cannot easily access tissue deep within a living subject, in particular within the brain. An alternative approach is to detect the magnetic field induced by the passage of the electrical signal, giving the equivalent readout without direct electrical contact. Such measurements are performed today using bulky and expensive superconducting sensors with poor spatial resolution. An alternative is to use nitrogen vacancy (NV) centers in diamond that promise biocompatibility and high sensitivity without cryogenic cooling. In this work we present advances in biomagnetometry using NV centers, demonstrating magnetic field sensitivity of ~ 100 pT/ $\sqrt{\text{Hz}}$ in the DC/low frequency range using a setup designed for biological measurements. Biocompatibility of the setup with a living sample (mouse brain slice) is studied and optimized, and we show work toward sensitivity improvements using a pulsed magnetometry scheme. In addition to the bulk magnetometry study, systematic artifacts in NV-ensemble widefield fluorescence imaging are investigated.

Keywords: diamond, biosensing and bioimaging, NV center in diamond, magnetic field, sensing

1. INTRODUCTION

Many biological processes generate electrical signals, for example synaptic transmission and muscular contraction. Such signals give key information on the functioning on biological systems, either for clinical diagnostic purposes (such as electrocardiography) or for fundamental understanding of processes and structure. Measuring these signals is typically performed using electrical probes carefully positioned in the desired region. This however poses difficulties if this region is not easily accessible, such as inside the brain, or where signals must be highly spatially resolved. An alternative approach is to measure the magnetic field produced when these signals propagate as electrical current. Existing techniques for this, such as magnetoencephalography (MEG) or magnetocardiography (MCG) are limited by reliance on superconducting quantum

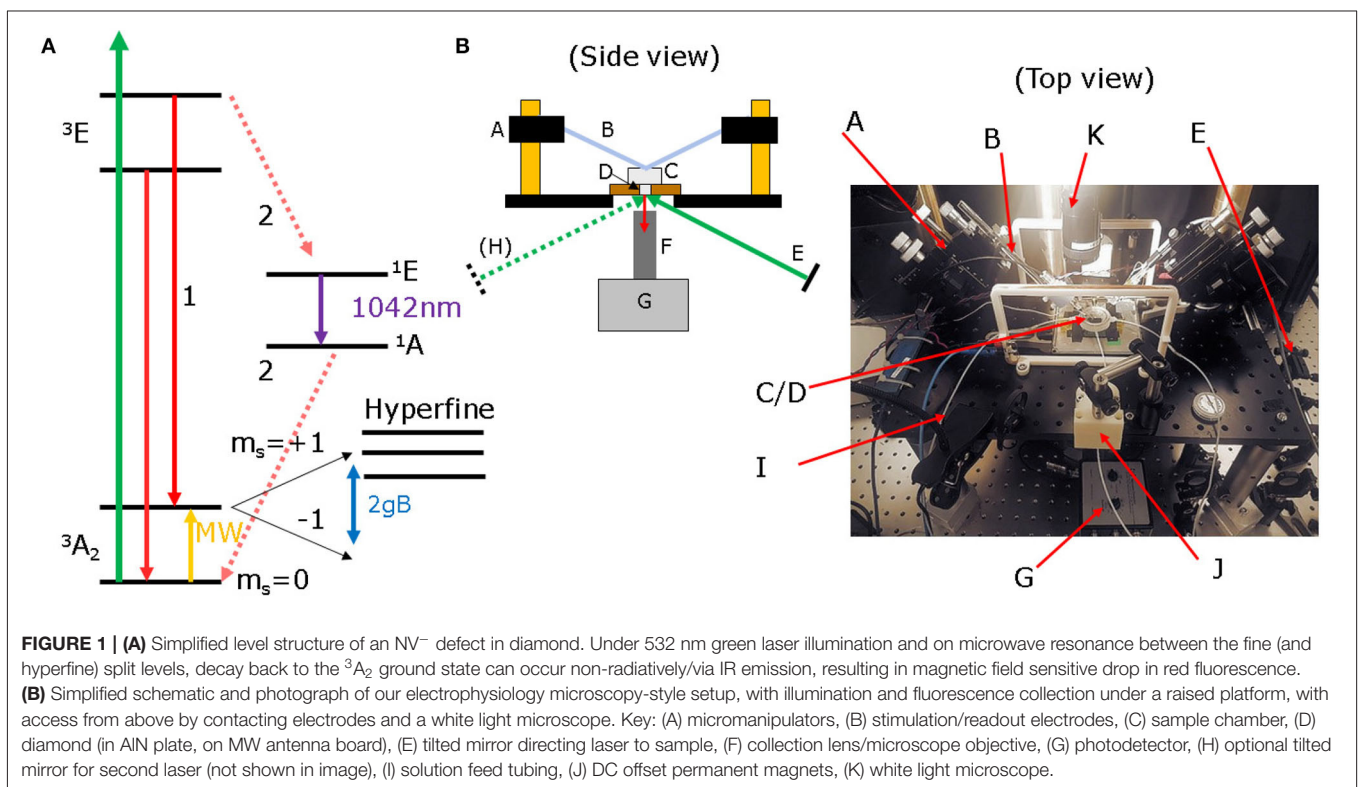
interference device (SQUID) systems [1]. These suffer a number of disadvantages including the need for an expensive magnetically shielded room and bulky cryogenic cooling, increasing the sample-sensor distance and resulting in weaker magnetic field at the sensor and poor spatial resolution.

A number of technologies are currently being researched in an effort to replace SQUIDs and overcome these difficulties, including microelectromechanical (MEMs) sensors [2], sensors based on magnetoresistive effects for magnetomyography [3] and in particular atomic (optically pumped) magnetometers for which cryogen-free MEG has recently been demonstrated [4]. Another alternative in the solid state is to sense magnetic fields using nitrogen vacancy (NV) centers in diamond [5]. Such defects, specifically the NV^- center, have an electronic structure that results in magnetic field dependent variation in fluorescence output under illumination with resonant microwaves (MW) and 532 nm green laser light. Although as yet the sensitivity to magnetic field of NV sensors is worse than SQUIDs or atomic magnetometers, they have a number of advantages well-suited to biosensing. They operate under ambient conditions, from DC to kHz+ bandwidth needed for ms-timescale biological signals and in close proximity (or even within [6]) cells or tissue, due to the excellent biocompatibility of diamond. The high density of such defects in the material also makes possible imaging of biological signals near the optical diffraction limit with micrometer scale resolution, in a way not possible by competing techniques. Finally, the high dynamic range of NV sensors means they can be operated without extensive magnetic shielding from ambient magnetic noise (e.g., from 50/60 Hz mains) and unlike atomic

magnetometers, they do not require shielding from the Earth's magnetic field to achieve maximum sensitivity.

Figure 1A shows the simplified level structure of an NV^- defect in diamond used for such sensing. Electrons excited by a 532 nm pump laser can decay in two ways. The most likely, labeled (1) is directly in the triplet state between ground $^3\text{A}_2$ and excited ^3E state. However, if microwaves (MW) are applied on resonance between the ground $m_s = 0$ $^3\text{A}_2$ state and its fine $m_s = \pm 1$ (and hyperfine) split levels (2.8 GHz) followed by pump excitation, decay back to the ground state can occur through process (2), via singlet shelving states ^1A , ^1E and non-radiative processes/weak infrared emission peaking at 1,042 nm [7]. This leads to a drop in fluorescence output on microwave resonance of up to 30% for a single NV, or 1–2% for a large NV ensemble [8]. This process is termed ODMR: optically detected magnetic resonance. The $m_s = \pm 1$ states can be Zeeman split by a magnetic field, which shifts the resonance frequency, allowing detection of the field amplitude by monitoring fluorescence output. A 1 nT field produces a shift of 28 Hz when the field is aligned along an NV axis and shifts down to a few Hz can be detected within 1 s of acquisition time, corresponding to the picotesla level fields expected from biological signals.

Biosensing can cover bulk magnetometry, collecting all emitted fluorescence from a diamond and aiming for maximum overall sensitivity. It also covers widefield imaging magnetometry, aiming for realtime imaging of magnetic field at high resolution using a microscope objective and a camera. It can also cover scanning magnetometry using single or few NVs, via confocal microscopy, a scanning NV tip or nanodiamonds



within a biological sample [9]. In this work we focus only the first two areas, bulk and widefield sensing. An excellent up to date summary of the field in general is given in the recent work by Barry et al. [10].

To date, bulk magnetometry biosensing has proved challenging. Barry et al. [11] demonstrated detection of single neuron action potentials from a marine worm, with excellent $15 \text{ pT}/\sqrt{\text{Hz}}$ low frequency sensitivity. Few groups have yet to replicate this level of sensitivity, let alone on a biological specimen. We note a distinction between DC-low frequency sensitivity and the typically significantly better AC ($>10 \text{ kHz}$) sensitivity achievable using pulsed dynamical decoupling techniques, where $10 \text{ pT}/\sqrt{\text{Hz}}$ has been demonstrated [12–14]. These frequencies are however too high for detection of many biological signals in the sub-kHz range. The best reported low frequency/DC sensitivities are typically worse [15–17] with few-nT/ $\sqrt{\text{Hz}}$. Vector magnetometry has also been demonstrated in the DC-low frequency range, important since magnetic fields from complex biosystems may not be easily directed along a single sensitive NV axis [18, 19].

For widefield imaging, a goal is to image the field from biological signals (such as neuron action potentials) [20, 21]. However, the pixel imaging sensitivity is on the order of $250 \text{ nT}-2 \mu\text{T}/\sqrt{\text{Hz}}$, as yet insufficient for imaging pT-level fields [22]. Biosensing imaging work has therefore focused on samples which have a strong magnetic field due to the presence of ferromagnetic material [23–25]. Several works have studied magnetic microbeads, the tracking of which can have applications in biology [26]. The majority of work however has focused on imaging non-biological samples with far stronger magnetic fields, such as geological samples [27], vortices in superconductors [28], and ferromagnetic nanowires [29].

In this work we present experimental measurements using bulk magnetometry and widefield sensing. We demonstrate a magnetometer setup with $100 \text{ pT}/\sqrt{\text{Hz}}$ sensitivity which is designed and optimized for measurements of magnetic field from biological samples. We show the setup, in an inverted microscope geometry, is also well-suited for widefield imaging. We discuss the adaptations and considerations required for biological magnetometry and the potential limitations and pitfalls in terms of sample damage and imaging artifacts. Finally, we discuss the future prospects for these methods, with reference to our measurements using pulsed magnetometry.

2. MATERIALS AND METHODS

Our NV magnetometer setup is pictured in a schematic and photograph in **Figure 1B**. We use an inverted microscope geometry, where laser excitation and light collection is performed with the diamond held on a raised platform, above a microwave antenna board and below a custom-3D printed bath chamber for holding a biological sample (C and D, **Figure 1**), with the solution fed via capillary tubes (I) from a peristaltic pump. This configuration has developed from typical electrophysiology microscopy setups. The setup allows a test sample to be placed directly above the diamond, with easy access to the sample from

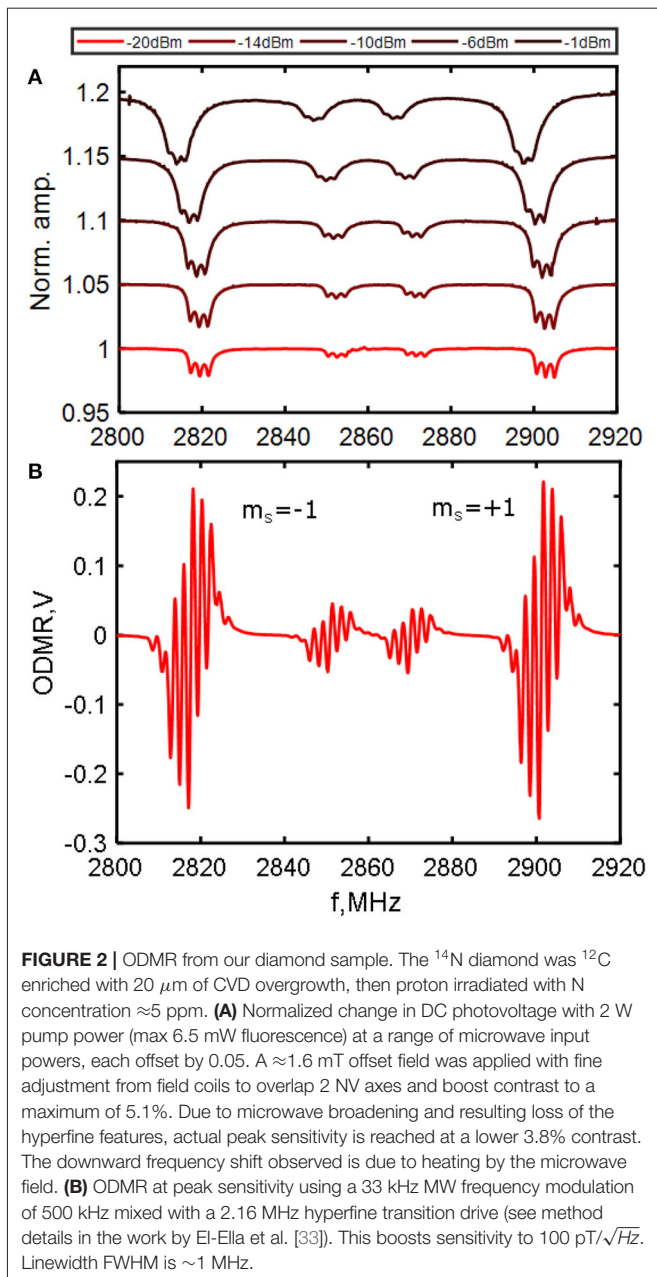
above, allowing the entry of stimulating electrodes using 2-axis adjustable micromanipulators (A,B) and a white light microscope (K) for positioning the electrodes and sample examination.

Fluorescence from the diamond can be collected from beneath the platform (F), using either a microscope objective or a condenser lens in a beam tube. Via a mirror, this is then directed to the photodetector (G), placed below and in front of the raised platform. Using a beamsplitter, a reference beam is also supplied to the detector for noise rejection. Pump light is supplied from a tilted mirror (E) to the right of the setup at Brewster's angle for diamond (67.5°) to maximize coupling into the diamond (light can also be supplied from the left using a second tilted mirror (H) from a second laser if required). Polarization of the pump light is controlled using a polarizing beamsplitter and half wave plate. Alternatively, both pump illumination and fluorescence collection can happen through the same lens using a dichroic mirror and optical filter to split the red/green components. This allows a focused beam to be supplied for imaging. In order to split the defect energy levels, optimize sensitivity in a single on-NV axis direction and obtain good contrast and sensitivity, a mT scale DC offset field is provided by two neodymium permanent magnets (J) placed in front and behind the sample chamber along with field coils for applying test signals. To switch between bulk sensing and imaging, minimal simple adaptation is required: the condenser lens/beamtube (F) is replaced with a microscope objective using the same screw fitting and the balanced photodetector (G) replaced with a suitable camera.

2.1. Diamond Material

Careful selection of exposure dose, ^{12}C isotopic purification to remove the negative effects of ^{13}C spins [30, 31] and understanding the role of strain [32] are key to maximizing sensitivity by achieving narrow microwave resonance linewidths and high fluorescence contrast (change in output between microwaves on/off). In this work we use a diamond (grown at LSPM, Paris) with a $20 \mu\text{m}$ CVD-grown ^{12}C purified layer, doped with 5 ppm nitrogen-14, carefully irradiated using H^+ ions (at U. Leipzig) and subsequently annealed at 800°C . **Figure 2** shows ODMR for our ^{12}C purified diamond. The linewidth FWHM, proportional to the dephasing time T_2^* [34], is on the order of 1 MHz, as compared 10–50 MHz for high density and unpurified samples.

Peak sensitivity balances high NV number (high brightness) and ODMR contrast and linewidth. Brighter samples with higher NV density tend to have a lower contrast and broader linewidth and those with high contrast and narrow linewidths tend to be low in brightness. Further discussion of the sensitivity limitations, including the effects of laser line narrowing and microwave power broadening are given in the work by Dreau et al. [35]. Our diamond has a linewidth comparable to the better diamonds in literature (FWHM $\leq 1 \text{ MHz}$), contrast of 1–2% at maximum field sensitivity and total fluorescence collection of 5–6 mW at 2 W of pump power. Based on these values, a simple estimate based on realistic collection efficiencies gives a shot noise limited sensitivity to DC and low frequency fields on the order of $10\text{--}20 \text{ pT}/\sqrt{\text{Hz}}$.



2.2. Laser Coupling and Light Collection

A factor critical to good performance in diamond NV magnetometry is coupling laser light in at Brewster's angle for diamond. This produces significant improvements in fluorescence generation by both coupling more pump light into the diamond and increasing internal reflection of the pump light, illuminating more NV centers [36]. This also has the additional benefit of minimizing damaging pump laser leakage into any biological sample. This configuration, used for all experiments in this work, is achieved in our setup using a tilted mirror, directing the light in from the right hand side of the setup. Using an extra dichroic mirror, our setup also allows pump light to

be directed through a microscope objective, with light incident perpendicular to the sample. Due to the limited field of view, this however can lead to saturation in the ODMR amplitude and reduction in contrast and sensitivity at higher power. For imaging we therefore use a microscope objective just for fluorescence collection. For the Brewster's angle configuration, we rotated the polarization of the incident light using a half wave plate to ensure maximum transmission into the diamond.

Our setup was also designed to utilize more than one laser beam incident on the diamond at the correct angle, using an additional tilted mirror to the left hand side of the setup. Although laser light from two separate sources is not coherent, both beams can be sampled into the reference of a balanced photodetector in order to effectively reject the technical noise from both lasers simultaneously. This permits using two lower cost DPSS 1–2 W lasers in combination to achieve greater sensitivity, as compared to having to purchase a single, high power, high stability laser. For imaging, our collection efficiency was limited by the numerical aperture of the objective. For bulk magnetometry, we used an aspheric condenser lens (Thorlabs, antireflective coated) to maximize fluorescence collection.

2.3. Detection and Sensing Limitations

Sensing with an NV center ensemble is fundamentally limited by shot noise from the strong fluorescence background originating from transition directly from excited ^3E to ground $^3\text{A}_2$ triplet state and the low 1–3% change in fluorescence level on microwave resonance. This is the difficult task of detection of a small dip in brightness on a large bright background with a consequently high shot noise level. This shot noise limited regime means sensitivity improves with the square root of the number of NV centers (larger ensemble) and by high pump laser power (up to the order of Watts). In order to address the NV^- defects and reach these power levels, we used a 532 nm DPSS laser (Coherent Verdi) of maximum power output 2 W. We note that the majority of the fluorescence produced is trapped within the diamond by its high refractive index.

In practice, reaching this shot noise limited regime is difficult due to laser technical noise and electrical readout noise. In our setup, we rejected laser technical noise using a balanced photodetector (Newport Nirvana) or by sampling the input laser beam and digitally subtracting it from the fluorescence signal [19]. The majority of our electrical readout noise originates primarily from the transimpedance amplifiers within the detector and the choice of photodiode. For the balanced detector, we used the inbuilt photodiodes, with bandwidth limited by the electric balance feedback circuit to 100 kHz. For the alternative sampling and subtraction method, we chose a photodetector with a larger area photodiode and higher capacitance (Thorlabs DET100) to ensure maximum fluorescence detection, at the cost of higher noise. Detection bandwidth was 10 MHz, more than sufficient for kHz signal detection.

For the majority of this work sensing was performed by supplying microwaves frequency modulated at 33 kHz with 500 kHz modulation width. This modulation could then be detected in the collected fluorescence from the diamond and the ODMR spectrum recovered by sweeping microwave frequency and

performing detection using a lock-in amplifier. Once the ODMR spectrum had been obtained, a fixed microwave frequency was used corresponding to the point of maximum slope and thus giving the maximum response to any magnetic field induced change in fluorescence output. We used a three-frequency drive method as outlined in El-Ella et al. [33]. Measurements were performed using a continuous wave method with constant microwave and laser power.

In the section *Pulsed Measurement* of this work, short microwave and laser pulses were instead used for sensing, measuring the change in output on the readout laser pulse with and without a prior microwave pulse. Pulses were generated from a TTL pulse generator (Spincore Pulseblaster) and fed to fast RF switches (Minicircuits) and an acousto-optic modulator (Isomet). The objective of the pulsed scheme was to reduce microwave power broadening effects and enhance ODMR contrast [5, 8].

2.4. Measurement Environment

In order to maintain optimum sensitivity, it is necessary to well control the environment in proximity to the diamond. This is difficult to achieve in practice due to the need to hold biological samples in solution that can vary in volume or composition over time, due to movement (particularly muscle tissue) and due to changes in temperature, all of which can shift the optimum microwave frequency and power required to maximize magnetometer sensitivity.

The efficiency of microwave coupling to the diamond can be considerably affected by having a water or other solution in close proximity. This is particularly critical for antennas with a narrow resonance, such as wire loops [37]. To counter this, we fabricated a custom-designed broadband antenna on a PCB board to be placed adjacent to the diamond. Using this antenna, we could reoptimize MW power (often by several orders of magnitude) after a stable carbogenated solution level sufficient to hold the specimen within was reached. Typically a depth of 0.5–1 cm was used, defined by the need to fully cover and contain within the solution a biological sample, such as a tissue slice or a mouse muscle. In order to maintain sensitivity, it was critical to keep a constant solution level and constant flow (provided by a peristaltic pump), avoiding shifts in the MW resonance. Stabilization of the level could be passively achieved by careful custom chamber design for the pumping rate required, by manually constricting a section of tubing to reduce inflow or by controlling the rate of inflow or outflow using needle valves in the feed and return piping. These could either be manually operated or controlled from a level sensor on the chamber. If necessary to fully inhibit sample movement, inhibitor chemicals as butanedione monoxime (BDM) (dissected tissue) or local anesthetic (living specimen) could be introduced to the solution feed and pumped to the sample.

Another factor was gradual thermal drift, caused by microwave or (as previously discussed) laser heating. Thermal drift could, over the course of minutes, push the optimum microwave resonance frequency away from the setpoint frequency, reducing sensitivity. To correct for this, we designed automated software to perform an ODMR sweep every few

measurements, with the computer automatically determining the point of maximum field sensitivity and maintaining the microwave frequency at this point. This could alternatively be performed continuously by keeping the frequency at a point that maximized the strength of a low frequency (111 Hz) signal applied to test coils aligned with the field sensitive axis.

2.5. Sample-Diamond Separation

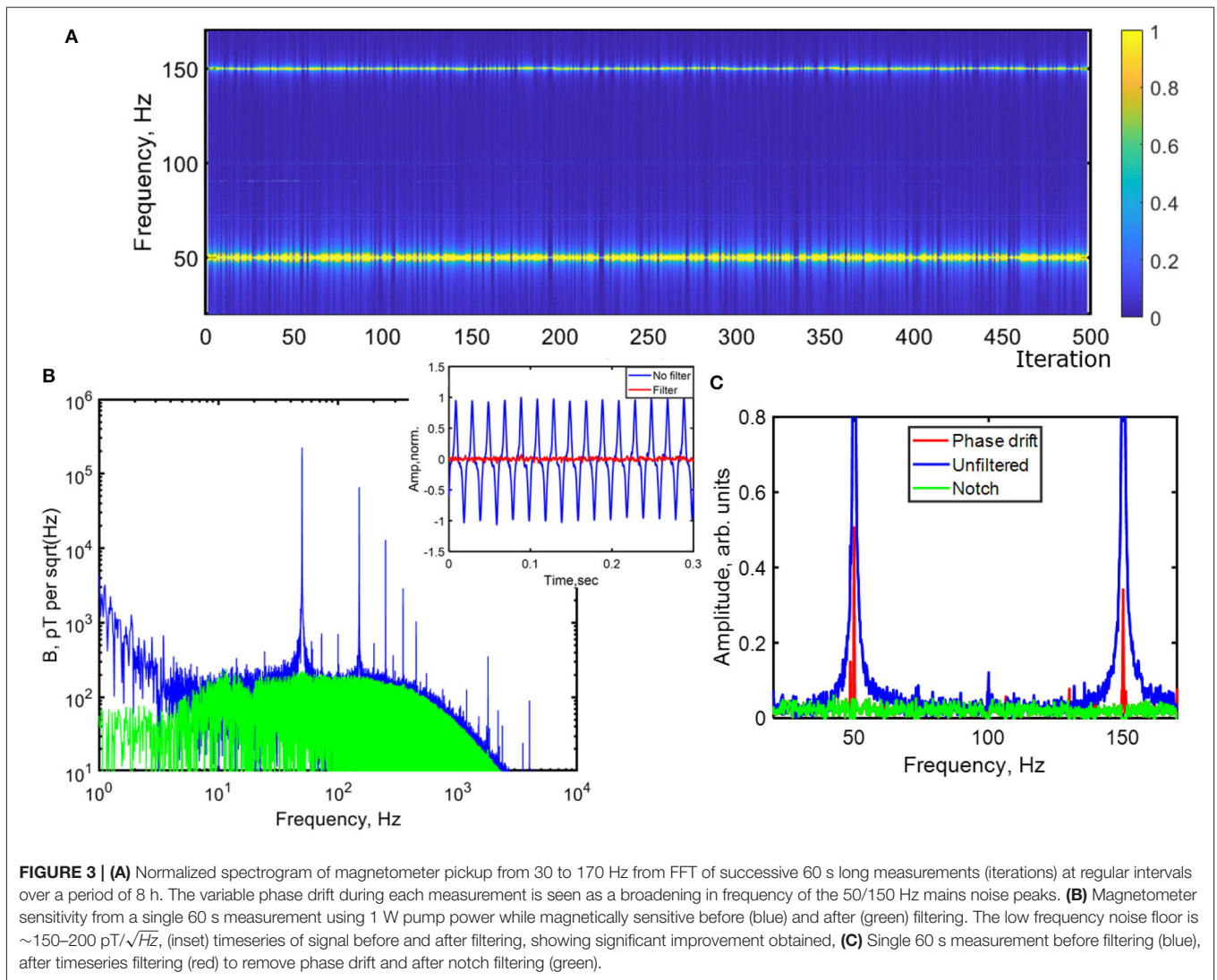
Since magnetic field strength drops as the inverse of distance (current carrying wire approximation) or the cube of the distance (magnetic dipole approximation), only a small difference in separation between diamond and biological sample (order of μm [22]) can make a significant difference in signal detection strength. This poses particular challenges for biological systems, where the tissue generating the signal may unavoidably be many millimeters from the sample (such as within muscle or under bone) or cannot be directly in thermal contact with a diamond heated by a laser beam. In our setup, we used a reflector/insulator layer above the diamond (aluminum foil/Kapton tape) to keep the sample as close to the diamond as possible while minimizing heat transport from diamond to sample. We also found that samples could float from the surface away from the diamond. Using a Pt and nylon harp (standard equipment for electrophysiology) helped stop this without disrupting the DC offset magnetic field. We also used Ti hooks and electrodes to hold the sample onto the diamond, with care taken not to damage the sample.

2.6. Stimulating Electrode Type and Design

In order to stimulate a biological response, our setup was configured to use standard electrophysiology probes attached to micromanipulators, which could supply current pulses to the sample. In electrophysiology experiments, only the electrical performance of the test electrodes is important and no offset magnetic field is used. This means many types of electrical stimulation electrodes that can be purchased contain magnetizable steel, often in the outer sheath of concentric-type electrodes. Such electrodes become magnetized in the DC offset field, which disrupts the field close to the diamond, significantly reducing magnetometer performance. To avoid this problem we developed an alternative, which was to use custom-made electrodes using Pt/Ir wire with a glass or plastic outer sheath. We found similar electrodes could be made from biocompatible, non-ferrous Ti or W wire (Cu was not biocompatible unless coated with Au or Ag/AgCl).

2.7. Averaging

Due to the weakness of biological signals, it is necessary to repeat the signal N times and then average, with improvement in sensitivity proportional to $1/\sqrt{N}$. This however places considerable demands on a biological sample, for example due to fatigue in a muscle, due to damage induced in the tissue by repeated stimulation or due to thermal degradation. We found that a bath of carbogenated (5% carbon dioxide, 95% oxygen) solution allowed the sample to survive for many hours, permitting many thousands of stimulations and averages.



3. RESULTS

3.1. Magnetic Noise

In any practical laboratory or clinical setting, there will be substantial magnetic field generation from mains transformers in equipment and in building wiring. This occurs primarily at the fundamental mains frequency (European 50 Hz or North American 60 Hz) and the 3rd harmonic (150 or 180 Hz) arising from magnetic hysteresis in the transformer, but also at higher harmonics and at multiples of three phase frequencies. Such low frequency fields are difficult to shield against, requiring full mu-metal enclosure, impractical for processing of biological samples, or extremely costly fully shielded rooms into which feeding piping or cabling is equally hard. Active cancellation, by using field coils to generate a counter field to the noise, can reduce it but this is hard to achieve for multi-axis sensing at a small 1–2 mm diamond, at kHz bandwidth and operating at sub-nT/ $\sqrt{\text{Hz}}$ sensitivity. The majority of commercially available systems cannot achieve these levels of field cancellation.

The alternative we present here is for the magnetically sensitive signal from the diamond magnetometer to be processed and filtered by Fast Fourier Transform (FFT) methods. This requires not only effective filtering but minimal filtering, since many biological signals have frequency components in the 10–500 Hz range and any strong filtering here will distort or remove the desired signal entirely. Such a filter must adapt to any drift in mains frequency and be able to capture any transient noise (such as from a fan or pump turning on and off). Further, it must counter phase drift in the mains supply, which acts to spread the mains noise across a wider frequency range.

In **Figure 3** we demonstrate how effective this can be. Magnetometer data was collected for 60 s in order to give good frequency discrimination. Low frequency and DC drift arising from laser power fluctuations is first removed by a highpass filter at 10 Hz. Next, a 50 Hz zero phase pure sine wave is correlated with a readout of the fundamental mains frequency obtained from tapping input to a transformer, in order to obtain a time series of the phase drift over the measurement period. A slight

constant phase shift can be added to this signal to account for any phase shift due to inductive effects, then normalized and subtracted from the magnetic readout. This process could be repeated several times to remove multiple (additive) sources of noise with different phase. It can then be repeated at 150, 250 Hz, or other strong harmonics of mains. Consequently, the phase drift broadening is removed in the frequency domain. Narrow notch or bandstop filters can then be used, centered on the noise frequencies, to remove any remaining noise components (Figure 3C). Any high frequency RF noise could then be removed by a final lowpass filter at 5–10 kHz. The overall effect in the data is a reduction in noise by orders of magnitude, down to the electrical and optical noise floors (inset, Figure 3B).

The ability to remove strong background magnetic noise components is key to allowing diamond NV sensing to be used in an ordinary lab or clinical environment without extensive and costly magnetic shielding for applications in research and medical diagnosis (e.g., magnetocardiography). This work complements our recent work on a flexible handheld magnetometer, containing the diamond, focusing optics and electronic components [38].

3.2. Laser Heating

In order to optimize sensitivity in NV center experiments limited by fluorescence shot noise, high laser powers of the order of several Watts are required. This presents a challenge of focusing a high power visible laser beam onto a mm-size diamond while remaining within the $\leq 37^\circ\text{C}$ range from most biological processes. We found that sudden changes in temperature, such as from fast ramping of the laser to high power, would damage biological samples. Heat must be dissipated from the diamond while minimizing the distance between diamond and sample, to maximize magnetic field strength at the diamond. Samples often cannot be placed directly on a metal heatsink, as this would short out any conduction paths and potentially interfere with the microwave or DC magnetic offset fields.

Figure 4 shows the effect of slow ramping the laser power on the electrical readout on the local field potential evoked in the CA1 region of the hippocampus in a slice preparation of a mouse brain. Placing the sample directly onto the diamond surface, heated by the pump laser, was found to cause rapid damage or death to the slice. By using a metal foil layer as heatsink and to reflect stray laser light back into the diamond and thinner Kapton tape as electrical insulation, it was possible to ramp the laser slowly to high power while keeping the sample alive, with the signal strength slightly improving through gradual heating to a more optimal temperature for biological processes ($35\text{--}37^\circ\text{C}$). We observed no signal for direct slice transfer to a diamond preheated by the laser at 1 or 2 W, attributable to thermal shock on placing it on the warm diamond. Ideally, the foil/Kapton layers could be replaced with thin glass or polymer (to be more robust against pressure from above) coated with Al to form a mirror. It should be noted that standard commercial glass coverslips are too thick for this purpose (type #0 are $85\text{--}105\ \mu\text{m}$ thick).

One additional way of achieving good thermal dissipation is to have the diamond in contact with a SiC wafer [11]. Another method we utilize in this work was to use plates of aluminum

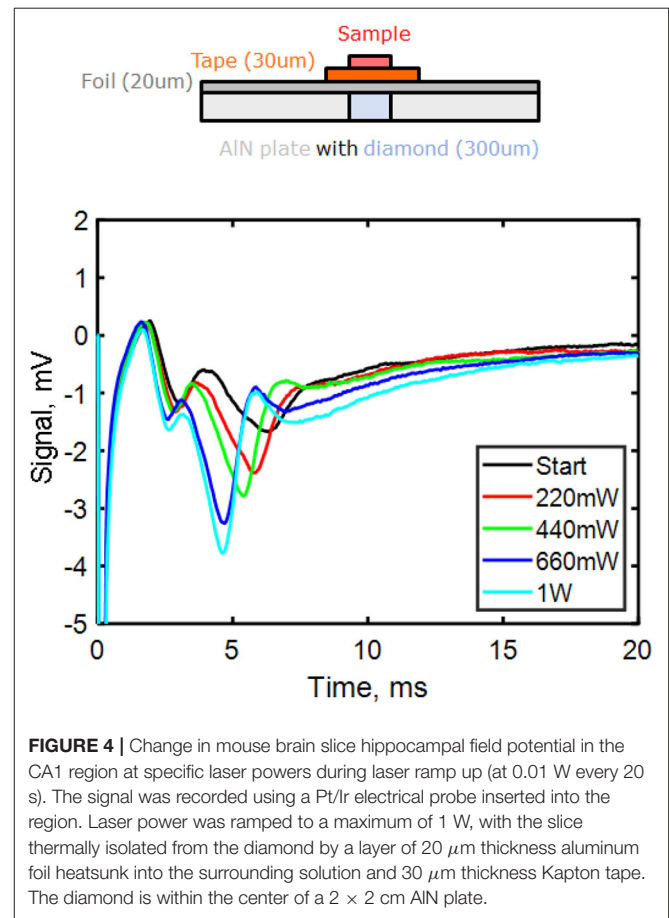
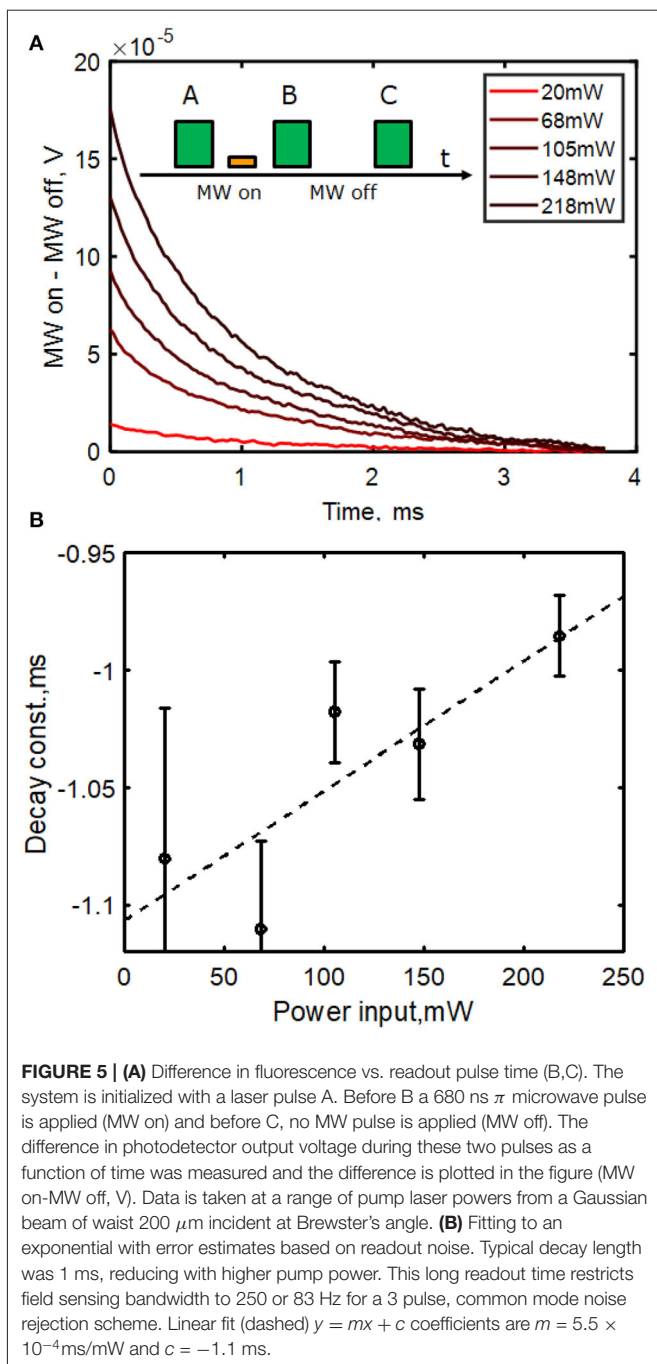


FIGURE 4 | Change in mouse brain slice hippocampal field potential in the CA1 region at specific laser powers during laser ramp up (at 0.01 W every 20 s). The signal was recorded using a Pt/Ir electrical probe inserted into the region. Laser power was ramped to a maximum of 1 W, with the slice thermally isolated from the diamond by a layer of $20\ \mu\text{m}$ thickness aluminum foil heatsunk into the surrounding solution and $30\ \mu\text{m}$ thickness Kapton tape. The diamond is within the center of a $2 \times 2\ \text{cm}$ AlN plate.

nitride (AlN) with a precision laser cut hole for the diamond. AlN is cheaper to purchase, easier to machine and has a good thermal conductivity while being an electrical insulator. This allowed heat to be dissipated out from the side facets of the diamond. We note from our previous work that thermal effects on the magnetometry can be canceled by driving two $m_s = \pm 1$ hyperfine transitions, although at a factor $2 \times$ cost in sensitivity [39].

Although we present electrophysiology measurements from the hippocampal slice here, we were unable to observe these signals in the magnetometer readout. Our previous estimates (detailed methodology in Karadas et al. [22]) had indicated that reaching $\text{nT}/\sqrt{\text{Hz}}$ sensitivity along with signal filtering and averaging would be sufficient to resolve signals from a brain slice. We speculate that this failure was due to magnetic field cancellation at the diamond. We consider that this occurs due to current propagation in other directions in the slice than the desired direction we impose using the permanent magnet DC bias field to maximize the magnetic field along the most sensitive NV axis. We found it extremely difficult to position the slice (in a solution bath) correctly to direct the current in the hippocampus. Higher spatial resolution and/or vector magnetometry is required in order to probe the cause of the absence of magnetic signal. In our setup this could not be achieved without reducing ensemble size, fluorescence collection and excessively reducing sensitivity.



Although widefield imaging microscopy cannot resolve pT-level signals at the present time, this or scanning either the sample or the diamond on a probe over the biological sample may prove a method to overcome this issue in the future.

3.3. Pulsed Measurement

Substantial effort in recent years has gone into developing pulsed laser/microwave schemes for field detection and imaging. These have been very successful in improving sensitivity to high frequency AC fields (>10 kHz) via dynamical decoupling

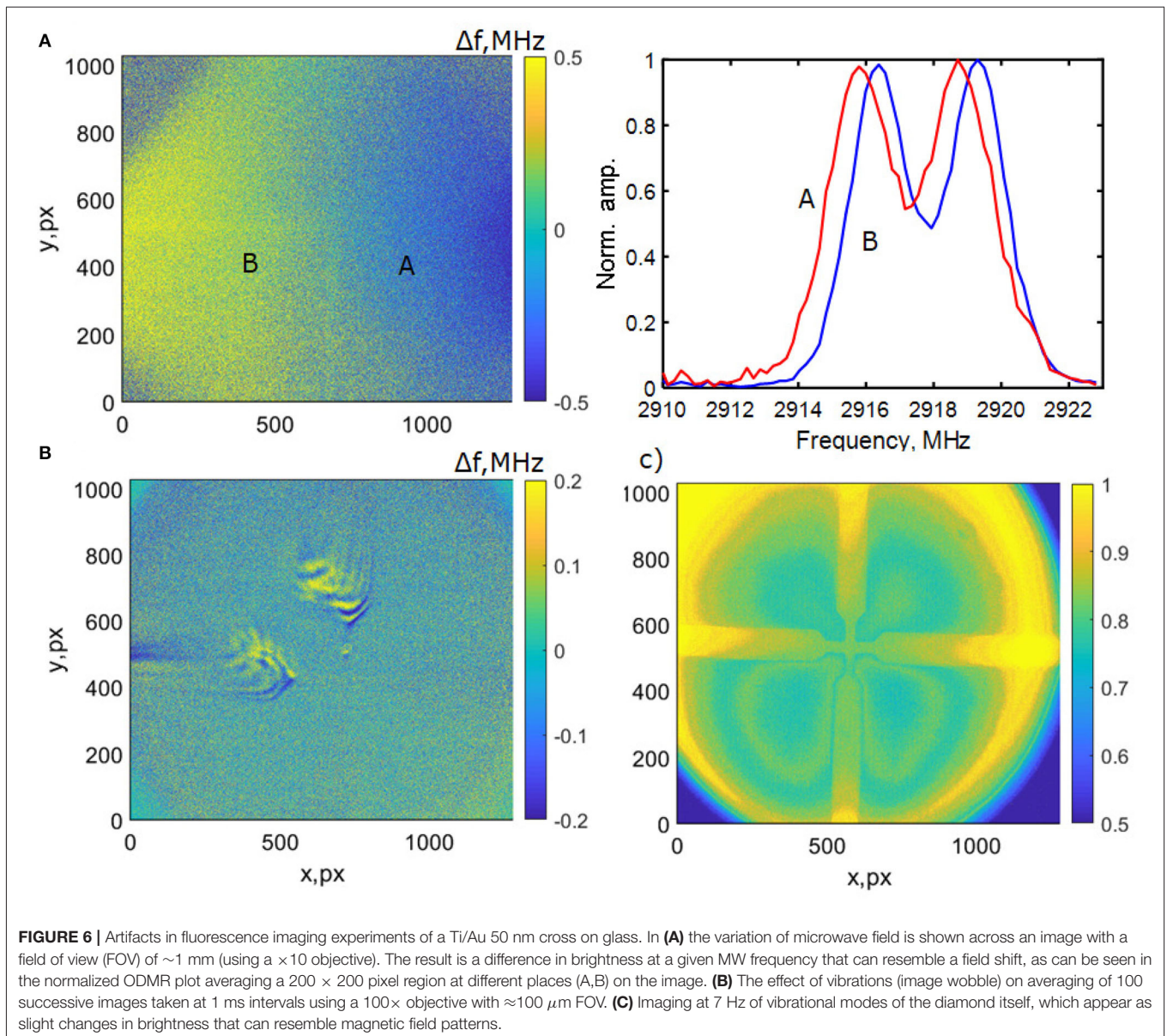
methods, rather than in the limit of low frequency and DC signals. A significant problem for DC sensing is the time required to read a large ensemble of NV centers required to achieve a high level of sensitivity. This can limit the measurement bandwidth to below that required for many biological sensing applications, particularly if laser power must be limited in order to protect the biological sample from damage.

Here we measured the ensemble readout time for our diamond. We used a long (100 ms) initialization laser pulse (A) to ensure that as many NVs as possible were initialized in the $m_s = 0$ ground state. We then sent a microwave pulse (on resonance at 2.91 GHz) of variable length τ (MW on) This was followed by a second laser readout pulse (B), followed by a repeat of this sequence without the microwave pulse (MW off), finishing with a second readout pulse (C) (see schematic, **Figure 5A**). We measured the difference in fluorescence output between the readout pulse with MW on (A) and MW off (B) as a function of time, as would be necessary in a measurement scheme, such as Ramsey interferometry. We varied the length of the microwave pulse τ to maximize this difference, which was found at $\tau = 680$ ns. For a single NV, this would correspond to a π -pulse. For our large ensemble, this corresponds to an approximate π -pulse for the most number (far from all) NVs. **Figure 5** shows the result of these measurements, measuring the difference in fluorescence (detected photovoltage) as a function of readout laser pulse time and averaging over 1,000 repetitions of the pulse sequence. We find a readout (reinitialization) time with a decay time on the order of 1 ms, fitting using a single exponential function. We estimate the error bars on the exponential fit in **Figure 5B**) based on the maximum deviation in fit parameter produced by the peak to peak readout noise on the photodetector voltage, which decreased with higher laser power (more fluorescence signal). Within error bounds, the decay time could be decreased by 200–300 μs by increasing laser power from 20 to 218 mW, the maximum possible using this measurement configuration due to power limitations imposed by our acousto-optic modulator. We estimate the laser power intensity at the diamond to be 1.5 kW/cm^2 . Assuming a linear extrapolation to the higher power density used, our readout time is comparable to the 150 μs in the work by Wolf et al. [13]. This is likely due to the reason given in their work, related to Gaussian spread of pump laser power, but also due to variations in strain and local field across the diamond and NV ensemble.

We note that for a large ensemble, a constant amplitude and phase microwave pulse will not correctly address all NVs, either as a π -pulse in this example or as a $\pi/2$ -pulse for a sensing scheme based on Ramsey interferometry [10]. A prospect to overcome this and enhance sensitivity in the pulsed regime may be microwave pulse shaping, using an arbitrary waveform generator and optimal control methods to boost readout fidelity [40].

3.4. Widefield Imaging

The camera limitations of NV center widefield fluorescence imaging are discussed in detail in our recent work [39]. A key problem with NV ensemble widefield imaging is bit depth. The majority of digital cameras in general and used for microscopy



work in only 8 or 10 bit depth (since the human eye cannot distinguish a greater color or monochrome palette). With a large background fluorescence brightness, this can result in the on MW resonance contrast being spread across too few digitization levels. We therefore use more specialized 12 and 16 bit cameras (Imaging Development Systems GmbH) in order to avoid artifacts associated with low bit depth. An ideal camera would be one with an initial analog black level correction stage, that can spread the contrast across the full digitization range.

Such a high level of background brightness means shot noise will significantly exceed readout noise or dark noise on each pixel. Based on ODMR measurements and from technical specifications, we can estimate the best sensitivity possible. Assuming a detection area of $5 \times 5 \text{ mm}^2$ with $3.5 \mu\text{m}^2$ pixel size (~ 2 Mpixels) and a diamond with a ODMR linewidth of 1 MHz,

contrast of 2% and collecting a fluorescence output of $\approx 6 \text{ mW}$, we calculate the best per pixel shot noise limited sensitivity of an imaging system to be $\sim 50 \text{ nT}/\sqrt{\text{Hz}}$. This presently restricts imaging of biological signals to specific, low bandwidth cases rather than imaging of pT-level signals, such as those from neural activity.

A key issue we address in this work is imaging artifacts that can easily resemble magnetic fields. From our measurements, we demonstrate a number of these in **Figure 6**. Variation in microwave power and resonance frequency across the image width can be more significant than the shift resulting from local changes in magnetic field (**Figure 6A**), which can in turn be mistaken for localized magnetic field imaging. Jitter or wobble in repeated averaged images can produce patterns that appear to be localized to electrodes or areas where a field is

expected (**Figure 6B**). In addition, low frequency vibration of the diamond itself in the typical frequency range of biological signals can be observed in a magnetic-field like pattern of fluorescence brightness change (**Figure 6C**). Finally, magnetic field-resembling diffraction patterns can arise from imperfect interfaces and air or solution gaps between diamond and sample.

4. DISCUSSION

Improved sensitivity is key for biosensing, since this would allow greater diamond-sample separation while still being able to detect the signal, would allow more comprehensive measurement and filtering of background noise and would permit biological magnetic field imaging of even weaker signals (i.e., sub-pT to fT level for MEG). Substantial work in the field has focused on using pulse sequences to improve sensitivity [10]. This method appears challenging for DC/low frequency sensing, due to the bandwidth limitations of slow readout times for large ensembles, although microwave pulse shaping and optimal control techniques common in nuclear magnetic or electron spin resonance experiments (NMR/ESR) may help here. A number of novel sensing techniques are currently being pursued which are suitable for sensing in this low frequency regime. This includes experiments using an optical cavity and infrared or green absorption [41, 42] or the very recent work by Fescenko et al. [43] promising sub-pT/ $\sqrt{\text{Hz}}$ sensitivity using flux concentrators. Novel techniques at an early stage, such as laser threshold magnetometry [44, 45] also appear promising. Such laser threshold experiments can potentially work with other materials beyond diamond, avoiding the problem of the large shot noise background from spin triplet fluorescence emission. Another possibility we suggest here is that pump light absorption may be exploited using interferometry techniques, such as by placing the diamond with the sample in one arm of a Mach-Zehnder configuration and detecting magnetic field through the effect of the field-dependent absorption of the diamond on the interference pattern generated at the output. This requires minimizing reflective losses and good stable transmission through the diamond in order to be realized.

It should be noted that many of these schemes pose problems for positioning the biological sample near the diamond yet out of the beam path. However, with sufficient sensitivity, the stand-off distance between the sample and the diamond can be increased (as is already necessary and possible for SQUID and atomic magnetometers), allowing it to be displaced laterally from the diamond while maintaining an orientation that directs the magnetic field along a sensitive NV axis. Many of these novel schemes are at an early stage and require further experiments to test their viability before applications to biosensing can be considered.

In this work, we have demonstrated methods that avoid damage to biological samples. Further work is however required in terms of improving dissipation of heat away from the diamond and away from the sample. This is challenging since any heatsink must be thin to minimize sample-diamond separation and also electrically insulating. We note that there has been important

parallel effort in constructing integrated miniaturized sensors [46–48]. Although their reported sensitivity is several orders of magnitude worse, it is possible that by using techniques from semiconductor fabrication (particularly efficient heatsinking) that these devices may have a significant role to play in future NV biosensing.

Finally, it is hoped that advances in diamond material processing may drive future development. In particular, improvements in CVD growth, nitrogen levels and conversion to NV⁻ centers, optimization of irradiation and dealing with material strain. Patterning of the diamond may allow a greater fraction of the fluorescence to escape, boosting efficiency [49].

5. CONCLUSION

Sensing of biological signals via their magnetic fields using diamond NV centers provides a potential route to better measure and understand them, whether in an electrophysiology-style microscopy configuration or from MEG-style sensing of inaccessible tissues in a living subject. Previous work has shown the technique to be biocompatible and widely applicable to a number of different systems, in both a bulk sensing and imaging configuration. There are, however, challenges in realizing such measurements, both in general from material limitations and the need to filter out unwanted noise, to specific demands unique to biosensing, such as maintaining temperature stability. In the coming years, further advances in sensitivity are required in order to realize ambitious sensing goals. A number of promising ideas are currently under development, particularly using pulsed schemes and in improving diamond material quality.

DATA AVAILABILITY STATEMENT

The datasets generated for this study are available on request to the corresponding author.

ETHICS STATEMENT

The animal study was reviewed and approved by AH, UA, and J-FP. Research was conducted according to applicable national laws and guidelines and local rules at DTU/KU.

AUTHOR CONTRIBUTIONS

JLW, NH, and LT performed the experiments for which data is shown as figures in this work. JLW wrote the manuscript with input from AH, KB-S, UA, J-FP, and NH. All authors contributed to the article and approved the submitted version.

FUNDING

The work presented here was funded by the Novo Nordisk Foundation through the synergy grant bioQ (NNF17OC0028086) and the Center for Macroscopic Quantum States-bigQ (bigQDNRF142) funded by the Danish National Research Foundation (DNRF).

ACKNOWLEDGMENTS

We acknowledge the assistance of Kristian Hagsted Rasmussen for fabrication and diamond processing and Axel Thielscher,

Mursel Karadas (current and former DTU Heath Tech), and Adam Wojciechowski (former DTU Physics, currently Jagiellonian University, Krakow) for contributions and prior experimental and theoretical modeling work.

REFERENCES

- Körber R, Storm JH, Seton H, Mäkelä JP, Paetau R, Parkkonen L, et al. SQUIDS in biomagnetism: a roadmap towards improved healthcare. *Supercond Sci Technol.* (2016) **29**:113001. doi: 10.1088/0953-2048/29/11/113001
- Li M, Matyushov A, Dong C, Chen H, Lin H, Nan T, et al. Ultra-sensitive NEMS magnetoelectric sensor for picotesla DC magnetic field detection. *Appl Phys Lett.* (2017) **110**:143510. doi: 10.1063/1.4979694
- Zuo S, Heidari H, Farina D, Nazarpour K. Miniaturized magnetic sensors for implantable magnetomyography. *Adv Mater Technol.* (2020) **5**:2000185. doi: 10.1002/admt.202000185
- Boto E, Holmes N, Leggett J, Roberts G, Shah V, Meyer SS, et al. Moving magnetoencephalography towards real-world applications with a wearable system. *Nature.* (2018) **555**:657–61. doi: 10.1038/nature26147
- Taylor JM, Cappellaro P, Childress L, Jiang L, Budker D, Hemmer PR, et al. High-sensitivity diamond magnetometer with nanoscale resolution. *Nat Phys.* (2008) **4**:810–6. doi: 10.1038/nphys1075
- McGuinness LP, Yan Y, Stacey A, Simpson DA, Hall LT, Maclaurin D, et al. Quantum measurement and orientation tracking of fluorescent nanodiamonds inside living cells. *Nat Nanotechnol.* (2011) **6**:358–63. doi: 10.1038/nnano.2011.64
- Acosta VM, Jarmola A, Bauch E, Budker D. Optical properties of the nitrogen-vacancy singlet levels in diamond. *Phys Rev B.* (2010) **82**:201202. doi: 10.1103/physrevb.82.201202
- Rondin L, Tetienne JB, Hingant T, Roch JF, Maletinsky P, Jacques V. Magnetometry with nitrogen-vacancy defects in diamond. *Rep Prog Phys.* (2014) **77**:056503. doi: 10.1088/0034-4885/77/5/056503
- Schirhagl R, Chang K, Loretz M, Degen CL. Nitrogen-vacancy centers in diamond: nanoscale sensors for physics and biology. *Annu Rev Phys Chem.* (2014) **65**:83–105. doi: 10.1146/annurev-physchem-040513-103659
- Barry JF, Schloss JM, Bauch E, Turner MJ, Hart CA, Pham LM, et al. Sensitivity optimization for NV-diamond magnetometry. *Rev Mod Phys.* (2020) **92**:015004. doi: 10.1103/RevModPhys.92.015004
- Barry JF, Turner MJ, Schloss JM, Glenn DR, Song Y, Lukin MD, et al. Optical magnetic detection of single-neuron action potentials using quantum defects in diamond. *Proc Natl Acad Sci USA.* (2016) **113**:14133–8. doi: 10.1073/pnas.1601513113
- Hall LT, Hill CD, Cole JH, Hollenberg LCL. Ultrasensitive diamond magnetometry using optimal dynamic decoupling. *Phys Rev B.* (2010) **82**:045208. doi: 10.1103/physrevb.82.045208
- Wolf T, Neumann P, Nakamura K, Sumiya H, Ohshima T, Isoya J, et al. Subpicotesla diamond magnetometry. *Phys Rev X.* (2015) **5**:041001. doi: 10.1103/physrevx.5.041001
- Masuyama Y, Mizuno K, Ozawa H, Ishiwata H, Hatano Y, Ohshima T, et al. Extending coherence time of macro-scale diamond magnetometer by dynamical decoupling with coplanar waveguide resonator. *Rev Sci Instrum.* (2018) **89**:125007. doi: 10.1063/1.5047078
- Zheng H, Xu J, Iwata GZ, Lenz T, Michl J, Yavkin B, et al. Zero-field magnetometry based on nitrogen-vacancy ensembles in diamond. *Phys Rev Appl.* (2019) **11**:064068. doi: 10.1103/physrevapplied.11.064068
- Zheng H, Sun Z, Chatzidrosos G, Zhang C, Nakamura K, Sumiya H, et al. Microwave-free vector magnetometry with nitrogen-vacancy centers along a single axis in diamond. *Phys Rev Appl.* (2020) **13**:044023. doi: 10.1103/PhysRevApplied.13.044023
- Clevenson H, Trusheim ME, Teale C, Schröder T, Braje D, Englund D. Broadband magnetometry and temperature sensing with a light-trapping diamond waveguide. *Nat Phys.* (2015) **11**:393–7. doi: 10.1038/nphys3291
- Zhao B, Guo H, Zhao R, Du F, Li Z, Wang L, et al. High-sensitivity three-axis vector magnetometry using electron spin ensembles in single-crystal diamond. *IEEE Magn Lett.* (2019) **10**:1–4. doi: 10.1109/lmag.2019.2891616
- Schloss JM, Barry JF, Turner MJ, Walsworth RL. Simultaneous broadband vector magnetometry using solid-state spins. *Phys Rev Appl.* (2018) **10**:034044. doi: 10.1103/physrevapplied.10.034044
- Hall LT, Beart GCG, Thomas EA, Simpson DA, McGuinness LP, Cole JH, et al. High spatial and temporal resolution wide-field imaging of neuron activity using quantum NV-diamond. *Sci Rep.* (2012) **2**:401. doi: 10.1038/srep00401
- Hall LT, Simpson DA, Hollenberg LCL. Nanoscale sensing and imaging in biology using the nitrogen-vacancy center in diamond. *MRS Bull.* (2013) **38**:162–7. doi: 10.1557/mrs.2013.24
- Karadas M, Wojciechowski AM, Huck A, Dalby NO, Andersen UL, Thielscher A. Feasibility and resolution limits of opto-magnetic imaging of neural network activity in brain slices using color centers in diamond. *Sci Rep.* (2018) **8**:4503. doi: 10.1038/s41598-018-22793-w
- Sage DL, Arai K, Glenn DR, DeVience SJ, Pham LM, Rahn-Lee L, et al. Optical magnetic imaging of living cells. *Nature.* (2013) **496**:486–9. doi: 10.1038/nature12072
- Glenn DR, Lee K, Park H, Weissleder R, Yacoby A, Lukin MD, et al. Single-cell magnetic imaging using a quantum diamond microscope. *Nat Methods.* (2015) **12**:736–8. doi: 10.1038/nmeth.3449
- Davis HC, Ramesh P, Bhatnagar A, Lee-Gosselin A, Barry JF, Glenn DR, et al. Mapping the microscale origins of magnetic resonance image contrast with subcellular diamond magnetometry. *Nat Commun.* (2018) **9**:131. doi: 10.1038/s41467-017-02471-7
- Kazi Z, Shelby I, Brunelle N, Watanabe H, Itoh KM, Wiggins P, et al. Wide-field magnetic imaging of sub-50 nm ferromagnetic nanoparticles for time-resolved bio-mechanical orientation measurements. In: *Conference on Lasers and Electro-Optics*. San Jose, CA (2019). doi: 10.1364/cleo_at.2019.am4i.1
- Glenn DR, Fu RR, Kehayias P, Sage DL, Lima EA, Weiss BP, et al. Micrometer-scale magnetic imaging of geological samples using a quantum diamond microscope. *Geochem Geophys Geosyst.* (2017) **18**:3254–67. doi: 10.1002/2017gc006946
- Schlüssel Y, Lenz T, Rohner D, Bar-Haim Y, Bougas L, Groswasser D, et al. Wide-field imaging of superconductor vortices with electron spins in diamond. *Phys Rev Appl.* (2018) **10**:034032. doi: 10.1103/physrevapplied.10.034032
- Lee M, Jang B, Yoon J, Mathpal MC, Lee Y, Kim C, et al. Magnetic imaging of a single ferromagnetic nanowire using diamond atomic sensors. *Nanotechnology.* (2018) **29**:405502. doi: 10.1088/1361-6528/aad2fe
- Jahnke KD, Naydenov B, Teraji T, Koizumi S, Umeda T, Isoya J, et al. Long coherence time of spin qubits in ¹²C enriched polycrystalline chemical vapor deposition diamond. *Appl Phys Lett.* (2012) **101**:012405. doi: 10.1063/1.4731778
- Edmonds AM, Hart CA, Turner MJ, Colard PO, Schloss JM, Olsson K, et al. Generation of nitrogen-vacancy ensembles in diamond for quantum sensors: optimization and scalability of CVD processes. *arXiv [Preprint]*. arxiv:2004.01746.
- Trusheim ME, Englund D. Wide-field strain imaging with preferentially aligned nitrogen-vacancy centers in polycrystalline diamond. *New J Phys.* (2016) **18**:123023. doi: 10.1088/1367-2630/aa5040
- El-Ella HAR, Ahmadi S, Wojciechowski AM, Huck A, Andersen UL. Optimised frequency modulation for continuous-wave optical magnetic resonance sensing using nitrogen-vacancy ensembles. *Opt Express.* (2017) **25**:14809. doi: 10.1364/oe.25.014809
- Bauch E, Hart CA, Schloss JM, Turner MJ, Barry JF, Kehayias P, et al. Ultralong dephasing times in solid-state spin ensembles via quantum control. *Phys Rev X.* (2018) **8**:031025. doi: 10.1103/physrevx.8.031025
- Dréau A, Lesik M, Rondin L, Spinicelli P, Arcizet O, Roch JF, et al. Avoiding power broadening in optically detected magnetic resonance of single NV

- defects for enhanced dc magnetic field sensitivity. *Phys Rev B*. (2011) **84**:195204. doi: 10.1103/physrevb.84.195204
36. Bougas L, Wilzewski A, Dumeige Y, Antypas D, Wu T, Wickenbrock A, et al. On the possibility of miniature diamond-based magnetometers using waveguide geometries. *Micromachines*. (2018) **9**:276. doi: 10.3390/mi9060276
37. Sasaki K, Monnai Y, Saijo S, Fujita R, Watanabe H, Ishi-Hayase J, et al. Broadband, large-area microwave antenna for optically detected magnetic resonance of nitrogen-vacancy centers in diamond. *Rev Sci Instrum*. (2016) **87**:053904. doi: 10.1063/1.4952418
38. Webb JL, Clement JD, Troise L, Ahmadi S, Johansen GJ, Huck A, et al. Nanotesla sensitivity magnetic field sensing using a compact diamond nitrogen-vacancy magnetometer. *Appl Phys Lett*. (2019) **114**:231103. doi: 10.1063/1.5095241
39. Wojciechowski AM, Karadas M, Osterkamp C, Jankuhn S, Meijer J, Jelezko F, et al. Precision temperature sensing in the presence of magnetic field noise and vice-versa using nitrogen-vacancy centers in diamond. *Appl Phys Lett*. (2018) **113**:013502. doi: 10.1063/1.5026678
40. Nöbauer T, Angerer A, Bartels B, Trupke M, Rotter S, Schmiedmayer J, et al. Smooth optimal quantum control for robust solid-state spin magnetometry. *Phys Rev Lett*. (2015) **115**:190801. doi: 10.1103/physrevlett.115.190801
41. Chatzidrosos G, Wickenbrock A, Bougas L, Leefer N, Wu T, Jensen K, et al. Miniature cavity-enhanced diamond magnetometer. *Phys Rev Appl*. (2017) **8**:044019. doi: 10.1103/physrevapplied.8.044019
42. Ahmadi S, El-Ella HAR, Wojciechowski AM, Gehring T, Hansen JOB, Huck A, et al. Nitrogen-vacancy ensemble magnetometry based on pump absorption. *Phys Rev B*. (2018) **97**:024105. doi: 10.1103/physrevb.97.024105
43. Fescenko I, Jarmola A, Savukov I, Kehayias P, Smits J, Damron J, et al. Diamond magnetometer enhanced by ferrite flux concentrators. *Phys Rev Res*. (2020) **2**:023394. doi: 10.1103/PhysRevResearch.2.023394
44. Jeske J, Cole JH, Greentree AD. Laser threshold magnetometry. *New J Phys*. (2016) **18**:013015. doi: 10.1088/1367-2630/18/1/013015
45. Dumeige Y, Roch JF, Bretenaker F, Debuisschert T, Acosta V, Becher C, et al. Infrared laser threshold magnetometry with a NV doped diamond intracavity etalon. *Opt Express*. (2019) **27**:1706. doi: 10.1364/oe.27.001706
46. Ibrahim MI, Foy C, Englund DR, Han R. 29.2 A scalable quantum magnetometer in 65 nm CMOS with vector-field detection capability. In: *2019 IEEE International Solid-State Circuits Conference (ISSCC)* (San Francisco, CA: IEEE) (2019). doi: 10.1109/isscc.2019.8662434
47. Kim D, Ibrahim MI, Foy C, Trusheim ME, Han R, Englund DR. A CMOS-integrated quantum sensor based on nitrogen-vacancy centres. *Nat Electron*. (2019) **2**:284–9. doi: 10.1038/s41928-019-0275-5
48. Stürner FM, Brenneis A, Kassel J, Wostradowski U, Röfver R, Fuchs T, et al. Compact integrated magnetometer based on nitrogen-vacancy centres in diamond. *Diamond Relat Mater*. (2019) **93**:59–65. doi: 10.1016/j.diamond.2019.01.008
49. Huang TY, Grote RR, Mann SA, Hopper DA, Exarhos AL, Lopez GG, et al. A monolithic immersion metalens for imaging solid-state quantum emitters. *Nat Commun*. (2019) **10**:2392. doi: 10.1038/s41467-019-10238-5

Conflict of Interest: The authors declare that the research was conducted in the absence of any commercial or financial relationships that could be construed as a potential conflict of interest.

Copyright © 2020 Webb, Troise, Hansen, Achara, Brinza, Staacke, Kieschnick, Meijer, Perrier, Berg-Sørensen, Huck and Andersen. This is an open-access article distributed under the terms of the Creative Commons Attribution License (CC BY). The use, distribution or reproduction in other forums is permitted, provided the original author(s) and the copyright owner(s) are credited and that the original publication in this journal is cited, in accordance with accepted academic practice. No use, distribution or reproduction is permitted which does not comply with these terms.

Chapter 6

Detection of biological signals from a live mammalian muscle using an early stage diamond quantum sensor

6.1 Introduction

Sensing electrical signals generated by action potentials passively and non-invasively is crucial in biomedicine. Current techniques for passive sensing such as magnetoencephalography and magnetocardiography make use of complex magnetometers that can detect magnetic fields generated deep within the tissues. Although extremely sensitive, these magnetometers such as SQUID or SERF, have the disadvantages of being bulky, expensive as well as having limited bandwidth and poor spatial resolution.

In the next section, following the experimental methods described in Chapters 3 and 5, the first demonstration of magnetic sensing of action potential in mammalian muscles is carried out. By employing a cw-ODMR scheme in a wide-field configuration, action potentials in Extensor Digitorum Longus (EDL) muscle in mice are sensed simultaneously with a diamond NV sensor as well as probe electrodes. Pulsed blue LED light is used to trigger muscle fibers to fire action potentials in mice that have been genetically modified to express Channelrhodopsin-2, a light-activated cation channel.

The described methods are not limited to optogenetics studies and the measured signals can be easily recovered with digital signal processing techniques. Despite the

need for high-power green laser pump, it is shown that the sample can be kept alive and in close contact with the diamond sensor for many hours. By chemically inhibiting the muscle contraction, while retaining the action potential propagation, it is ensured that the measured signals are free from movement artifacts. The averaged magnetic signals shows a noise level of ~ 20 pT (Standard Deviation) and an action potential peak amplitude of 300 pT, resulting in a signal-to-noise ratio of ~ 15 .

Although uncompetitive in terms of SNR with probe electrophysiology, this proof-of-principle bulk experiment paves the way towards high-resolution imaging of electrical activity in biological specimens.

6.2 Publication

This section was published in Scientific Report with the title of “Detection of biological signals from a live mammalian muscle using an early stage diamond quantum sensor” as follows:



OPEN

Detection of biological signals from a live mammalian muscle using an early stage diamond quantum sensor

James Luke Webb^{1✉}, Luca Troise¹, Nikolaj Winther Hansen², Christoffer Olsson³, Adam M. Wojciechowski⁴, Jocelyn Achard⁵, Ovidiu Brinza⁵, Robert Staacke⁶, Michael Kieschnick⁶, Jan Meijer⁶, Axel Thielscher^{3,7}, Jean-François Perrier², Kirstine Berg-Sørensen¹, Alexander Huck¹ & Ulrik Lund Andersen¹

The ability to perform noninvasive and non-contact measurements of electric signals produced by action potentials is essential in biomedicine. A key method to do this is to remotely sense signals by the magnetic field they induce. Existing methods for magnetic field sensing of mammalian tissue, used in techniques such as magnetoencephalography of the brain, require cryogenically cooled superconducting detectors. These have many disadvantages in terms of high cost, flexibility and limited portability as well as poor spatial and temporal resolution. In this work we demonstrate an alternative technique for detecting magnetic fields generated by the current from action potentials in living tissue using nitrogen vacancy centres in diamond. With $50 \text{ pT}/\sqrt{\text{Hz}}$ sensitivity, we show the first measurements of magnetic sensing from mammalian tissue with a diamond sensor using mouse muscle optogenetically activated with blue light. We show these proof of principle measurements can be performed in an ordinary, unshielded lab environment and that the signal can be easily recovered by digital signal processing techniques. Although as yet uncompetitive with probe electrophysiology in terms of sensitivity, we demonstrate the feasibility of sensing action potentials via magnetic field in mammals using a diamond quantum sensor, as a step towards microscopic imaging of electrical activity in a biological sample using nitrogen vacancy centres in diamond.

Sensing of signals produced by living tissue is an essential tool for both medical diagnostics and for advancing the fundamental understanding of the structure and functioning of biological systems. Such signals, generated by propagating action potentials, are of particular importance in excitable cells such as neurons and muscle cells, allowing the cell-to-cell communication and movement that is essential for the functioning of the tissue and the organism as a whole¹. Action potential can be measured to high precision and sensitivity using electrical probes, including by non-contact methods in proximity to neural pathways². However, electrical probes are difficult to use for measurements of activity within tissue. Here the electrodes must pass through the tissue and any protective layer (e.g. the bone of the skull for a living subject), with a high risk of inducing damage. In the case of dissected samples for microscopy, insertion of electrodes can produce erroneous results or kill neurons near the probe³. For living subjects, this can have a severe impact on health, arising either from direct damage or secondary infection, particularly those arising from breaching the blood-brain barrier⁴. A further disadvantage is limited spatial resolution offered by a single point or multielectrode arrays⁵. Correctly positioning thin, flexible probes to reach a precise measurement site inside tissue is very difficult, with multielectrode arrays further adding to the invasiveness of the technique.

¹Center for Macroscopic Quantum States (bigQ), Department of Physics, Technical University of Denmark, Kgs. Lyngby, Denmark. ²Department of Neuroscience, University of Copenhagen, Copenhagen, Denmark. ³Department of Health Technology, Technical University of Denmark, Kgs. Lyngby, Denmark. ⁴Jagiellonian University, Krakow, Poland. ⁵Laboratoire des Sciences des Procédés et des Matériaux, Université Sorbonne Paris Nord, 93430 Villetaneuse, France. ⁶Division Applied Quantum System, Felix Bloch Institute for Solid State Physics, Leipzig University, 04103 Leipzig, Germany. ⁷Danish Research Centre for Magnetic Resonance, Centre for Functional and Diagnostic Imaging and Research, Copenhagen University Hospital Hvidovre, Copenhagen, Denmark. ✉email: jaluwe@fysik.dtu.dk

Magnetic field sensing provides an alternative route towards noninvasive, high resolution, high speed sensing. Here the magnetic field from electrical activity in any part of the tissue, including deep within it, can be detected to high precision and spatially localised without contact, from outside the specimen or subject and without the need to insert invasive probes. To date, techniques for sensing biological magnetic fields, for example magnetoencephalography (MEG) of the living brain, have been primarily based on superconducting quantum interference devices (SQUIDs)^{6–9}. This approach requires bulky magnetic shielding and cryogenic cooling, thus preventing proximity studies of living tissue and delivering poor spatial resolution. These disadvantages have also limited the use of the technique for dissected tissue microscopy.

Noninvasive detection of magnetic fields in an unshielded, ambient environment can instead be realized by using nitrogen vacancy (NV) centres in diamond for magnetic field sensing^{10–12}. NV centers are quantum defects that can provide broadband vector magnetic field sensing^{13–16} and imaging with high spatial resolution under ambient conditions using the technique of optically detected magnetic resonance (ODMR)^{17,18}. It has broad applicability in life science^{19,20} particularly due to the high biocompatibility of diamond, which can be placed in contact or even within biological specimens^{21,22}. Thus far NV sensing has focused on static or slow processes, such as imaging magnetotactic bacteria^{23,24}. As yet there has been limited demonstration of sensing biological electrophysiological signals via magnetic field using diamond, with the most notable work being that by Barry et al.²⁵ for invertebrates. Difficulties have included reaching sufficient sensitivity, keeping the sample alive and undamaged during measurement, interference from stimulation artifacts and the presence of background magnetic noise.

In this work, we report the first use of a diamond quantum sensor to measure action potentials *in vitro* from a live mammalian specimen via their magnetic field. We detect the induced field from the dissected leg muscle of a genetically modified mouse, using optogenetic stimulation of channelrhodopsin to induce the action potential through blue light stimulation. We achieve a magnetic field sensitivity of 50 pT/ $\sqrt{\text{Hz}}$ and demonstrate methods that allow the specimen to remain alive under continuous measurement by the sensor. By using advanced data post-processing and filtering, we are able to demonstrate the first example of sensing of magnetic field from optogenetic stimulation using such a sensor under ambient conditions in a noisy, unshielded laboratory. Although as yet uncompetitive with probe electrophysiology in terms of sensitivity at this early stage, we consider these measurements an early but important step towards the goal of *in vivo* biosensing from living specimens using diamond quantum sensing, with the particular end goal of demonstrating sensing and imaging of signals in neural networks in the mammalian brain^{26,27}.

Results

We used an inverted microscope containing a diamond magnetic field sensor, consisting of a single crystalline diamond sample with a 20 μm layer comprising a high density of NV centers at the top facet (Fig. 1, see “Methods” section). The biological specimen was placed near the NV surface separated only by a foil/insulator layer, thereby ensuring high proximity of the specimen to the sensing NV layer. Laser light at 532 nm and frequency swept microwaves were applied to the NV sensor, while the induced fluorescence from the NV centers was imaged onto a photodetector. The time-varying magnetic field from the specimen was then detected using the protocol of optically detected magnetic resonance (ODMR) magnetometry.

Dynamic range and background noise. The diamond sensor was capable of measuring all the ambient background noise up to the kHz frequency range while maintaining maximum sensitivity without the sensor signal output saturating. An example of the raw magnetometer signal measured can be seen in Fig. 2a,b. Assuming an ODMR linewidth of 1 MHz, the approximate dynamic range without loss of sensitivity was estimated as 42 μT , comfortably above the 600 nT level of the predominant 50 Hz and 150 Hz background noise.

We first measured the background noise detected by the magnetometer with deionised water in the chamber but without a muscle. Figure 2c shows the amplitude spectral density, measured at microwave frequency on resonance (magnetically sensitive). Our noise floor was approximately 50 pT/ $\sqrt{\text{Hz}}$, defined by contributions from the electronic noise of the amplifiers and photodetector and the shot noise of the detected fluorescence. Here the shot noise limited sensitivity was approximately 8 pT/ $\sqrt{\text{Hz}}$. To characterise the noise, we measured the magnetometer output over many hours. The result can be seen in the spectrogram in Fig. 2d, showing the range (< 1 kHz) where we expected to observe a biological signal. The two largest noise peaks can be seen at 50 Hz and 150 Hz, as expected from magnetic field detection of the fundamental mains frequency and from field produced by equipment transformers, each peak broadened by variable phase drift. Aside from mains harmonics, we observe a number of broad and narrowband noise sources. The majority of these we attribute to variable load airconditioning and water pumps in the building where the experiment was located, including some equipment from United States manufacturers that produced 60 Hz fields. We consider this background typical for a research lab or clinical environment.

Muscle electrophysiology. Figure 3a shows a sketch of the fundamental biological process to be measured, where stimulation with light triggers a cascading opening of ion channels, generating an action potential (producing current flow and magnetic field) along the muscle. Further details on this process are given in Supplementary Information. Prior to the magnetometry experiment, this optogenetic stimulation was tested in a preliminary investigation in a separate setup capable of measuring action potential and muscle extension force. An example of a stimulation, measuring action potential using electrical probes and by measuring the force resulting from subsequent muscle contraction can be seen in Fig. 3b. This test setup was used to determine the intensity of light required for good stimulation. No saturation in the electrical probe signal was observed up to the maximum intensity the light source could deliver.

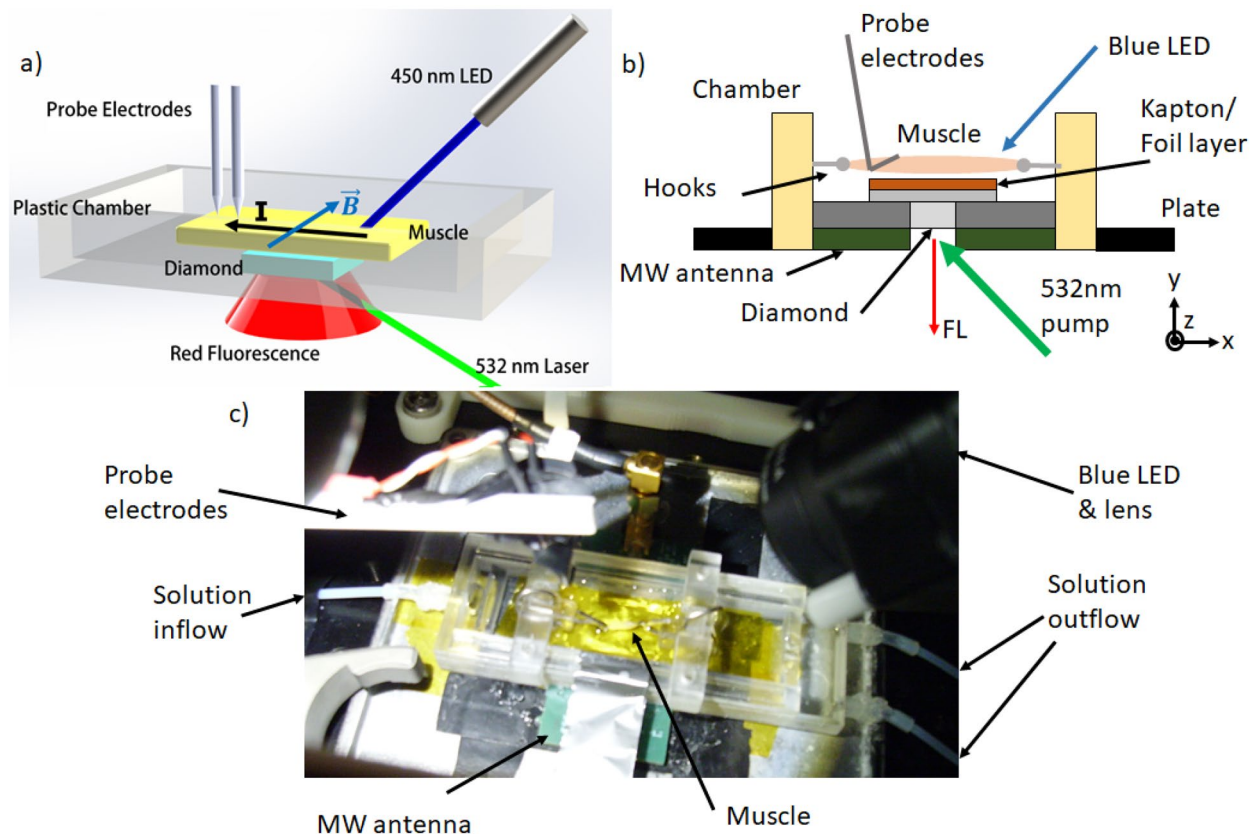


Figure 1. Experiment schematic and photograph. (a) Simplified 3D schematic of the magnetometer setup, showing the laser and blue LED illumination and fluorescence (FL) collection directions and sample chamber orientation, the direction of maximum magnetic field sensitivity (B) and the direction of current flow (I) in the muscle. (b) Side view schematic (not to scale) of the chamber/diamond sensor/MW antenna stack, joined and affixed to a movable plate with silicone. (c) Photograph from above of the chamber, showing solution inflow connections and the mouse muscle, below which the diamond lies separated by a layer of Kapton tape and aluminium foil acting as a heatsink.

Figure 3c shows the response measured using an electrical probe contact to a stimulated muscle in the magnetometer sample chamber. We measured both the diamond sensor output and the electrical probe contact simultaneously, to give a complete picture of the muscle behaviour. The maximum biological signal amplitude as measured by the electrical probes versus time is given in Fig. 3d. The signal strength decreased over time as the muscle fatigued. This meant that after a certain time, a maximum signal to noise ratio was reached where further averaging would not help resolve the biological signal in the magnetic data. To find this point, we calculated the signal to noise ratio of the signal as a function of number of iterations during postprocessing. The rate of fatigue varied between different muscles, ranging from 8 h in Fig. 3 up to 16–18 h. We note that our electrical probe data was taken purely as a reference to compare to the magnetic readout. It was measured via a simple DC measurement using a home-built amplifier, making it far noisier than specially designed RF shielded, state of the art electrophysiology setups.

Filtering process. Figure 4a shows the amplitude spectral density from Fast Fourier transforming the electrical probe data. The majority of the signal can be found in a frequency range from DC up to hundreds of Hz (blue histogram plot), thus unfortunately overlapping with the majority of the background magnetic noise. We make the reasonable assumption that the magnetic readout resembles the electrical probe readout since they originate from the same biological process. Therefore to filter the magnetic data, we limited the bandwidth to the range in which we expect a signal, thereby rejecting the majority of the background noise. Postprocessing the data collected, we imposed a digital bandpass filter from $f_{low} = 20$ Hz to a range of upper cutoff frequencies to determine the minimum at which the filter begins to corrupt the electrical probe data. This can be seen in Fig. 4b in the inset and as a percentage deviation from the raw signal in the main figure. We chose an upper cutoff of $f_{up} = 1.5$ kHz, to include as many of the signal frequencies as possible. It can be seen clearly from the spectrum in Fig. 4a that this was more than sufficient to resolve the signal while excluding a significant amount of background noise.

In order to remove the background noise within the measurement bandwidth, we Fourier transformed each 60 s iteration dataset, selectively applied frequency domain notch filters corresponding to the noise peaks and then inverse Fourier transformed the data to recover the a filtered version of the timeseries. Due to the frequency

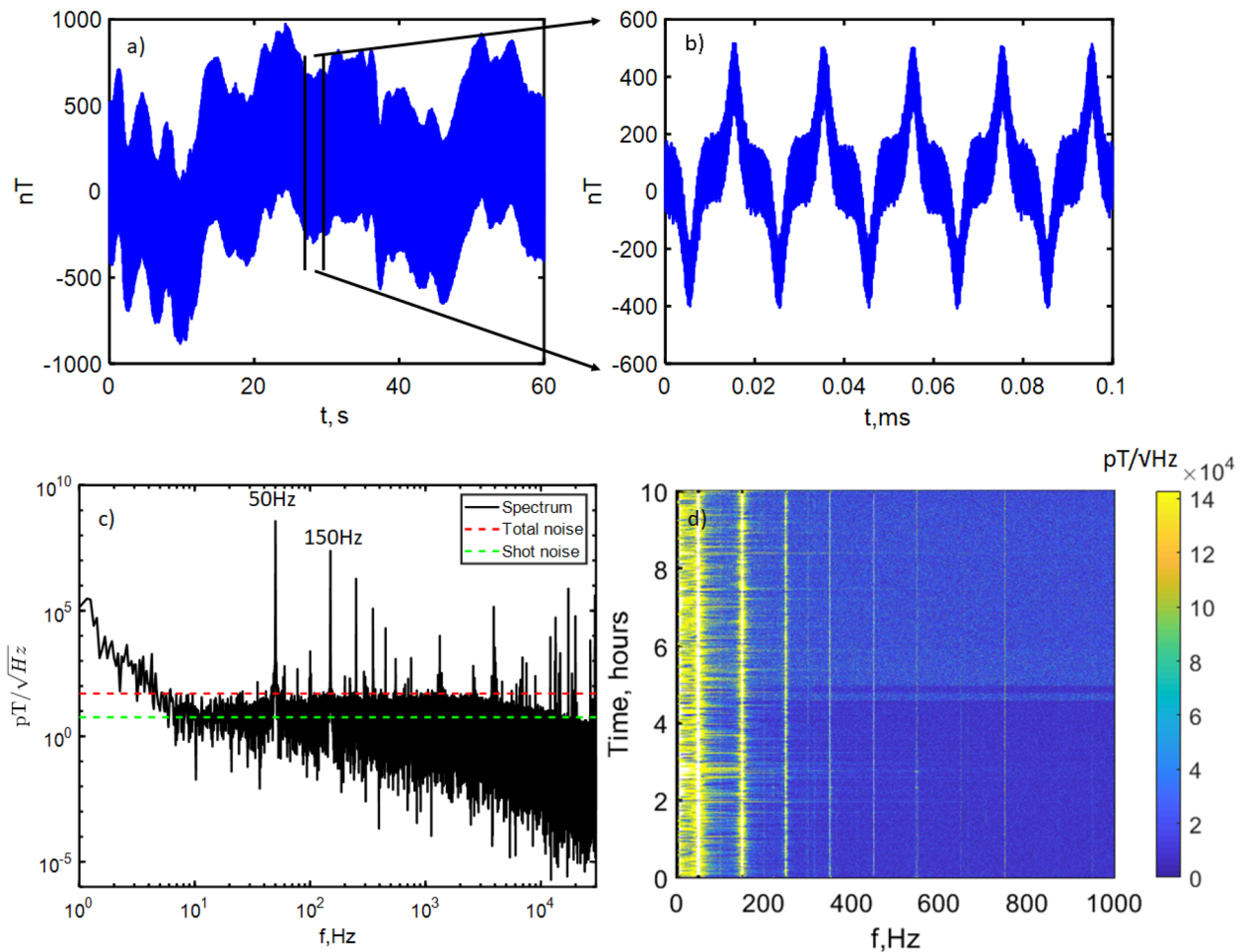


Figure 2. Demonstration of high dynamic range, bandwidth and sensitivity to magnetic field. (a) The raw unfiltered magnetic signal for a full 60 s iteration and (b) a zoomed 0.1 s segment of the same iteration. The signal was dominated by low frequency and DC laser power drift (< 5 Hz), 50 Hz and 150 Hz noise from mains electricity and higher frequency (> 10 kHz) noise and ranges between $\pm 1 \mu\text{T}$, well within the dynamic range of the magnetometer. (c) Spectral density in $\text{pT}/\sqrt{\text{Hz}}$ for a single 60 s iteration and (d) a spectrogram of repeated 60 s acquisitions over 10 h. The sensitivity floor is approximately $50 \text{ pT}/\sqrt{\text{Hz}}$ with $f(-3 \text{ dB}) = 4.8 \text{ Hz}$ defined by the lock-in amplifier low pass filter. Also indicated are calculations of the total noise, which includes electronic and shot noise, and of the estimated shot noise level alone. Many sources of background magnetic noise can be seen to peak well above this floor.

overlap between signal and noise, it was critical to remove only parts of the signal that met two strict conditions: (1) to be clearly defined as noise (peak sufficiently above the white noise floor) and (2) only at those frequencies that did not distort the sought biological signal (on applying the same filter to the electrical probe data). Meeting only condition 1 would minimise noise while also removing the sought biological signal, whereas meeting only condition 2 would artificially recover the biological signal in the magnetic data by selection.

We met these conditions by using two threshold values. The first, n_{th} we define as the multiple above the median spectral amplitude a peak must exceed to be classed as noise. To apply this, we divided the spectrum into 40 Hz wide windows, taking the median in each window m_v , and removed only those frequencies in each window that peaked above $m_v \times n_{th}$. By windowing, we avoided an excessive biasing of the filtering towards lower frequencies, due to the background $1/f^x$ spectral slope. The second threshold value, m_{th} , we define as the percentage change in electrical probe signal relative to the unfiltered signal over a 40 ms window which starts at the time of stimulation ($t = 0$). These methods are clarified further in Supplementary Information.

We first removed those frequency components with the largest spectral amplitude (most likely to be noise) and continued until the SNR for each 60 s iteration was maximised, requiring between 60–200 notched frequencies. In the Supplementary Information, we show how this process can be simplified by first removing the broad 50/150 Hz mains noise through time domain filtering, flattening the spectrum in the < 200 Hz range²⁸. We note that excluding the noise at < 5 Hz due to laser power fluctuations, 84 percent of the magnetic noise (4.8 kHz bandwidth) was confined to 50 Hz and 150 Hz harmonics. As an aside, we show in the Supplementary Information that it is possible to significantly reduce the noise and recover a signal through use of a $(n \times 50 \text{ Hz})$ comb of fixed-width notch filters. This configuration could be easily implemented in hardware for a sensor device for practical applications.

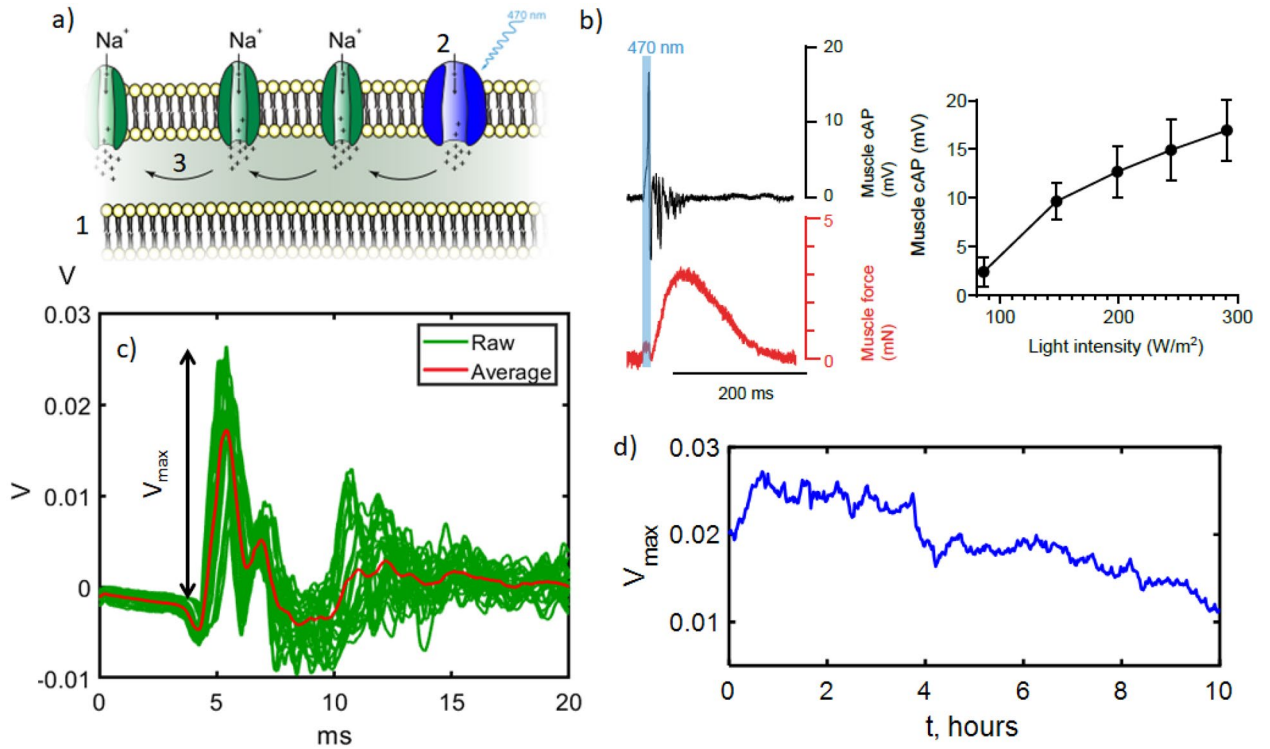


Figure 3. Mouse muscle electrophysiology and signal variation over time (a) Sketch of the biological signal generation process. In the muscle cell bi-lipid membrane (1) channelrhodopsin (2) opening triggers influx of Na^+ ions (3), creating an action potential running along the muscle. (b) Preliminary measurements taken on a separate setup of a single stimulation and readout via electrical probes (mV) and via muscle contraction force (mN). The strength of the signal as a function of light intensity is also shown. (c) Example of the readout of the biological signal in the magnetometer setup from a muscle (Muscle 1) by the electrical contact probe. Here $t = 0$ ms is when the stimulation light is applied. The red trace shows the average signal observed over all stimulations. (d) (left axis) Maximum size of the initial peak in the signal, which steadily drops by a factor of 2 over time as the muscle becomes fatigued.

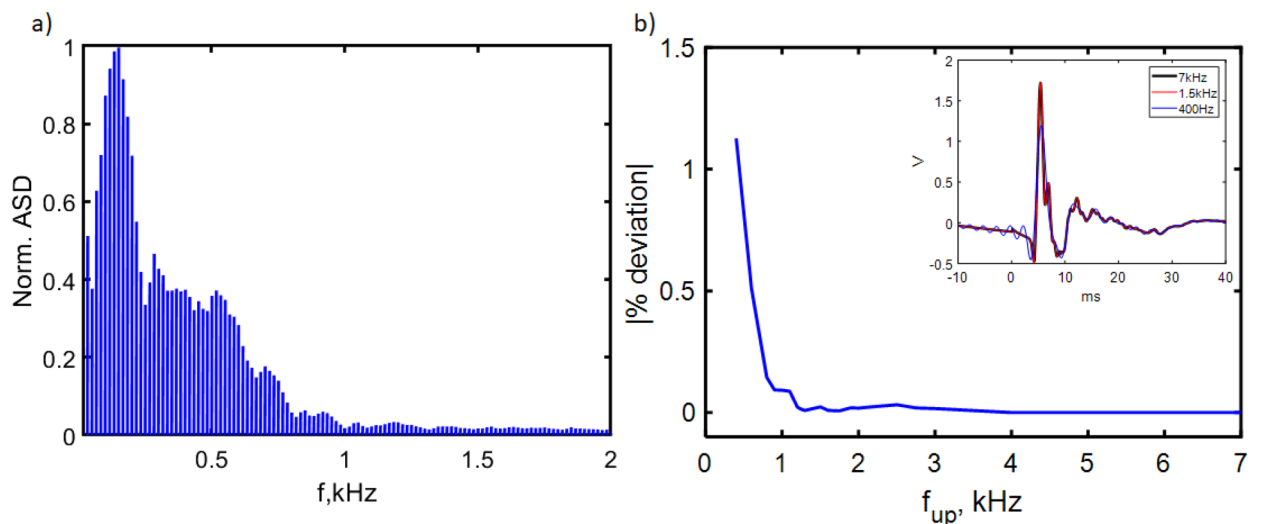


Figure 4. Frequency spectrum of the biological signal and defining optimum filter thresholding. (a) Spectrogram of the normalised Fourier transform amplitudes of the electrical probe voltage data, showing that the majority of the signal frequency components (shaded blue region) are under 1.5 kHz. (b) Percentage deviation from the unfiltered signal as a function of upper bandpass cutoff frequency f_{up} . The signal begins to be significantly corrupted below 1.5 kHz, as can be seen in the inset example for $f_{up} = 400$ Hz where $t = 0$ is the stimulation time.

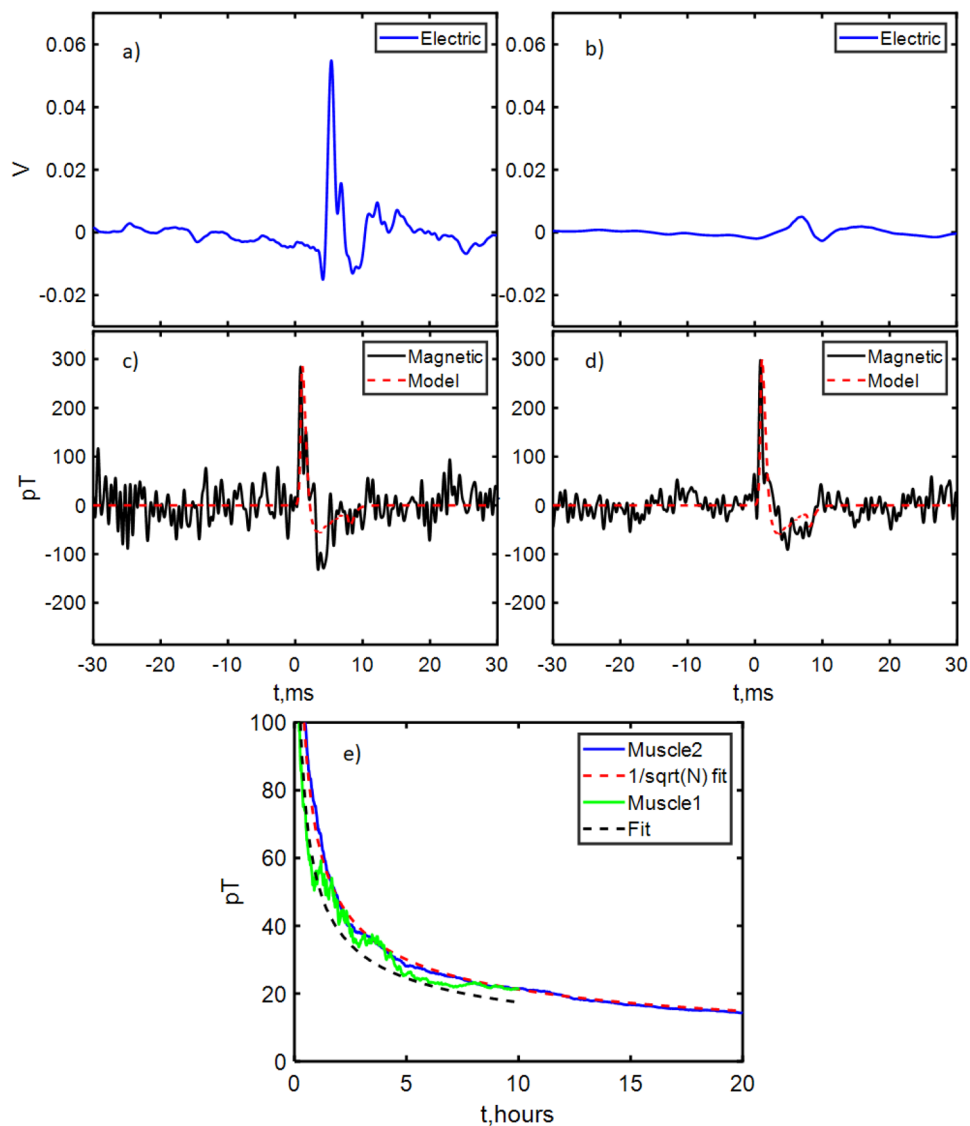


Figure 5. Simultaneous electrical and magnetometer readout of the biological signal. Here the blue traces in (a,b) are the scaled electrical probe data, with with black traces in (b,c) the simultaneous magnetometer readout for LED stimulation of two muscles: Muscle 1 (a,c left panes), averaged for 8 h (30×425 stimulations) and Muscle 2 (b,d right panes), averaged for 16 h (30×837 stimulations). The maximum signal strength was approximately 250 pT. (e) Noise on the filtered magnetic data as a function of time for Muscle 1 and Muscle 2, showing $1/\sqrt{N}$ dependence with the number of measurements taken (increasing time).

Biological signal via magnetic field. The timeseries for $N \times 60$ s iterations for both electrical probe and magnetic data was then averaged. Data was obtained separately from two muscles. The results for Muscle 1 can be seen in Fig. 5a,c and for Muscle 2 in Fig. 5b,d. We observe $1/\sqrt{N}$ scaling (Fig. 5e) reaching an ultimate (rms) noise level of 22 pT for Muscle 1 and 16 pT for Muscle 2. The improved sensitivity for Muscle 2 was obtained with 12 h more measurement averaging. For the second muscle, 2,3-Butanedione monoxime was added to the solution bath in order to inhibit movement without affecting the action potential. For Muscle 1, this compound was absent. A signal was observed in the magnetic data for both muscles typical of an action potential propagating along the muscle. This signal was present with and without muscle inhibitor, ruling out the signal being an artifact arising from muscle motion. For Muscle 2, a signal to noise ratio of 1 was reached after 32 iterations (30×32 simulations, 36 min measurement time), defining SNR as the averaged signal strength divided by the standard deviation of the averaged background magnetic noise. We phenomenologically modeled the expected action potential magnetic signal, full details of which are given in the Supplementary Information. The model parameters were within the range provided by literature and yield good agreement to the experimental data^{29–31}.

We note that for Muscle 1 the diamond was placed approximately $2\text{mm} \pm 1\text{ mm}$ closer to the stimulation position along the muscle length than the electrical probes. This gap was not present for Muscle 2. The biological signal in the magnetic data for Muscle 1 was therefore consistently observed $1.5\text{ms} \pm 0.5\text{ ms}$ ahead of the electrical

probe readout. This gives a crude estimate of propagation velocity in the muscle of 0.5–3 m/s³². The observed delay rules out that the recorded magnetic signal could stem from crosstalk pickup from the simultaneously measured electric probe circuit.

The difference in the shape and magnitude of the electrical readout between Muscle 1 and Muscle 2 arises from differences in contact quality between the muscles and the silver chloride probe electrodes. As a result of a reduced contact quality to Muscle 2, the signal strength was lowered and additional capacitance was introduced leading to distortions of the signal probed by the electrodes. This effect is not present on the magnetometer readout where we saw a sharp response, thus representing an advantage of the magnetic sensing over conventional electrophysiology.

Discussion

Using a diamond quantum sensor with pT-scale sensitivity to magnetic field and kHz measurement bandwidth, this work provides the first demonstration of sensing of the magnetic field from a signal generated by a living, mammalian biological specimen. We show that the sample can be kept alive for many hours while being measured using the quantum sensor, despite the current need for high laser power. The signal resembles that typical of action potentials measured by conventional electrical probes, without the drawbacks of poor electrical contact adding capacitive distortion. We measure a time delay between magnetic and electrical probe signal consistent with signal propagation along the muscle. Using optogenetic activation and comparison to a muscle where motion had been inhibited ensured the signal we measure was free of artifacts. The magnetometry technique is not dependent on optogenetic stimulation and is widely applicable to conventional electrical probe stimulation, or where stimulation originates from the living specimen itself.

Using digital signal processing techniques, we show that a weak magnetic signal can be recovered in a noisy background without magnetic shielding, even in an ordinary laboratory environment with a significant degree of background magnetic noise typical of that in a large, busy building at a university or a hospital. Unlike alternative methods for high-sensitivity magnetometry, the high dynamic range of the diamond sensor allows the background noise to be recorded without saturation. Since the sensor does not saturate, the background noise can be directly detected and can thus be removed by adaptive windowed notch filtering. Future advances in sensitivity will only help improve the clear identification of the different sources of background noise, aiding filtering and noise reduction and could eventually allow active cancellation of magnetic noise in a small volume using a second sensor.

We obtain a peak-to-peak noise of between 200–300 pT on a single 60 s iteration after filtering. Such a noise level would allow a single stimulation event of 1–1.5 nT (with SNR ≥ 5) to be clearly observed in realtime. As the majority of action potentials only drive sufficient current to produce a field in the sub-nanotesla range, some improvement is therefore required to reach single shot readout. However, if high proximity between the sample and sensor is achieved (as is possible in our setup) then nanotesla-level signals may be observed. Our previous theoretical calculations (Karadas et al.²⁷) show signals of 1 nT from the hippocampus of mice and previous work using invasive probes close to neurons in living subjects has shown similar field strength³³.

We show that filtering can also be done to a reasonable degree using fixed-width notch filters at mains harmonics frequencies. This could be implemented in hardware for realtime filtering in a portable sensor device to be used in a research or clinical environment. Using a higher quality, isotopically purified diamond would allow significant improvement in sensitivity over our previous work in this direction (see³⁴). Although it may not be desirable or necessary to minaturise the setup for microscopy in order to maintain mechanical stability and ease of access for users, a portable handheld diamond sensor would allow recording of signals from living whole organisms, in particular for faster signals (kHz bandwidth and above) that cannot be easily detected by competing technology. As discussed in our previous work, feeding multiple diamond sensors from the same central laser via fibre optic coupling would be highly desirable, particularly in terms of spatially resolving the location of signals within tissue and to perform gradiometry to reduce common mode noise³⁵. An alternative direction is full minaturisation and integration of the sensor using semiconductor nanofabrication techniques, although as yet this has yet to deliver the necessary sensitivity^{36,37}.

The capability to operate in an ordinary lab or clinical environment without relying on superconducting technology, would open the door to many new research and diagnostic possibilities. A number of competing technologies seek to do this, most notably atomic vapour magnetometers^{38–41}. Although they are thus far superior in sensitivity, compared to diamond NV sensing, they have a number of disadvantages such as lack of biocompatibility, low dynamic range, inability to perform vector sensing in a single sensor, the need to screen from the Earth's magnetic field to achieve maximum sensitivity and low bandwidth at maximum sensitivity (< 100 Hz for a recent commercial atomic vapour sensor from QuSpin, Inc.⁴² used for biosensing) that can be insufficient to achieve the micro to few-millisecond (kHz) time resolution needed to sense many biological signals.

We note that the measurements we present in this work could be easily performed with existing electrical probe electrophysiology techniques, to a far higher degree of sensitivity than via our magnetic measurements. However, it is not our intention for our method to be competitive with state of the art electrical probes, but to be a step towards offering new, noninvasive capabilities they cannot deliver, while having advantages over alternative magnetic sensing methods such as high bandwidth and room temperature operation. Our results represent an important proof of concept experiment, demonstrating that a diamond quantum sensor in a very early stage of development can sense mammalian biological signals. The end goal, for which this experiment represents an early step, is to use the diamond sensor to perform microscopic imaging of magnetic field, to give noninvasive high spatial resolution of electrical activity²⁶. This would offer a new capability to map electrical activity, important for example in studying the structure in the brain and linking this with whole organism behaviour. Our setup is designed to eventually be capable of this imaging via widefield microscopy from dissected tissue

slices. Alternative microscopy techniques are also being pursued towards this goal, in particular fluorescence microscopy from nanodiamonds within the biosample^{22,43} and non-contact scanning sensors⁴⁴. Scanning sensor technology is currently limited to atomically flat surfaces, however advances in diamond probes, potentially arising from work on boron doped diamond probes used for invasive electrochemical sensing, may be of use in developing a non-invasive scanning NV bioprobe^{45,46}. It is hoped that further advances in diamond materials development and through novel sensing schemes that a level of sensitivity can be reached to allow imaging using these methods in the coming years, with sufficient spatial resolution ($< 10 \mu\text{m}$) to resolve signals along individual neural pathways⁴⁷.

Methods

Inverted microscope. Figure 1a shows a simplified 3D schematic of our inverted microscope incorporating the diamond biosensor. For optical pumping, up to 2 W of horizontally polarised 532 nm green laser (Coherent Verdi G2) illumination could be delivered from below a raised platform at Brewster's angle for diamond (67 deg). Polarisation was controlled before incidence on the diamond using a half wave plate to ensure maximum power transmission. Red fluorescence from the diamond was collected separately from the incident green light using an aspheric, anti-reflective coated 12 mm diameter condenser lens (Thorlabs ACL1210). Fluorescence light was directed onto an electronically balanced photodetector (New Focus Inc.). 6 mW was the typical power of collected fluorescence for 2 W of green laser light. A reference beam for the photodetector was obtained by splitting off a few-mW portion of the input beam using a polarising beamsplitter.

Diamond preparation. The diamond used in this work was a [100] oriented electronic-grade single crystal from Element Six with dimensions $2 \times 2 \times 0.5 \text{ mm}^3$ overgrown by a $20 \mu\text{m}$ thick nitrogen doped layer using chemical vapor deposition (CVD). Nitrogen content in the gas phase was optimised during the growth to reach a level of 5 ppm of nitrogen-14. The diamond was then 2.25 MeV proton irradiated with a fluence of 3×10^{15} protons/cm² followed by annealing at 800 °C for 4 h. This gave a NV⁻ density ranging between 0.1 and 1 ppm. The diamond was mounted into a central hole of a laser cut aluminum nitrate heatsink plate of dimensions $3 \times 3 \times 0.05 \text{ cm}^3$. We measured an ODMR linewidth of 1 MHz with a contrast of approximately 1.5 percent for each nitrogen-14 hyperfine transition.

Sensor geometry. The diamond and aluminium nitride plate were attached using watertight aquarium-safe silicone to a custom built broadband microwave antenna fabricated onto a printed circuit board with a hole for fluorescence collection from below (see schematic Fig. 1b). On top of both antenna and plate was silicone mounted a rectangular 3D-printed, custom designed rectangular plastic sample chamber, which can be seen in Fig. 1c, that could hold a flow bath of solution, fed using a peristaltic pump. The chamber was fully accessible from above, allowing biological samples to be introduced and probe electrodes to contact the sample using micromanipulators. The sample was held on a pair of sliding hooks within the bath, directly above the top surface of the diamond. To protect the biological sample from laser heating, a $16 \mu\text{m}$ thick layer of aluminum foil was placed on the top surface of the diamond, attached by $50 \mu\text{m}$ Kapton tape in order to electrically insulate the foil and diamond from the sample. The resulting tens of micrometer separation between sample and diamond was undesirable due to reduction in magnetic field strength, but was taken as a precaution against sample heat damage based on previous experimental experience. We note that this layer is not waterproof, meaning the sample and diamond sensor are in indirect contact via the solution bath. Here the biocompatibility and robustness of the diamond sensor is an advantage, since it will not degrade or otherwise contaminate the solution which could ultimately kill or damage the biological sample to be studied. The layer could be reduced in thickness and ultimately eliminated by better conduction of heat away from the diamond and the use of lower laser power without compromising sensitivity via future diamond material development.

Control and readout. The microwave field was generated using a three-frequency drive scheme⁴⁸ using two radiofrequency (RF) generators (Stanford SG394) feeding a balanced mixer and then amplified (Minicircuits ZHL-16W-43+). One generator drove the transition between the $m_s = 0$ and $m_s = \pm 1$ of the ground state of the NVs with a frequency in the range of 2.7–3 GHz and frequency modulated at 33 kHz to implement lock-in detection. The second generator provided a fixed frequency of 2.16 MHz to drive multiple hyperfine transitions. Two rare-earth magnets were aligned parallel to the (110) direction in the diamond and perpendicular to the main direction of signal current propagation, generating a DC bias field of $\sim 1.5 \text{ mT}$. These directions are labelled on Fig. 1a and the field axis corresponds to their z-axis on Fig. 1b. We used a continuous wave (CW) scheme with constant microwave and laser power ensuring a stable (temperature) environment. Magnetometer sensitivity was optimised by adjusting the power of the reference beam to the balanced photodetector and by independently sweeping the power on the two RF signal generators to optimise microwave drive.

Finally, the output voltage from the balanced detector was passed to a lock-in amplifier (Stanford SR850), from which the output was digitised by an analogue to digital converter (ADC, model NI PCI-6221) at 80 kSa/s. We term this channel the *magnetic data*. We used a lock-in time constant of 30 μs , giving a magnetic field measurement bandwidth of approximately 4.8 kHz. The muscle was surface contacted by an electrical probe consisting of two L-shaped AgCl coated silver wires positioned 3 mm apart under the muscle mounted on a micromanipulator. The recording electrode voltage was amplified (Axon Cyberamp 320). This was then digitised at the same rate and simultaneously with the magnetic data. We term this channel the *electrical probe data*.

Specimen preparation. The muscle was stimulated optogenetically using blue light from a 470 nm LED. Experiments were performed on genetically modified mice in which Channelrhodopsin 2 (ChR2), a light-gated

cation channel, was used to create an action potential in the muscle. Animals were euthanized by cervical dislocation and extensor digitorum longus (EDL) muscles from both hind limbs were dissected in carbogen-saturated (95% O₂/5% CO₂) cold artificial cerebrospinal fluid (ACSF). Small suture loops were tied on distal and proximal tendons for later suspension in the recording chamber. Until use, EDL muscles were stored in a holding chamber continuously bubbled with carbogen. For some muscles, the myosin ATPase inhibitor 2,3-Butanedione monoxime (5 mM in ACSF; Sigma) was added in order to uncouple excitation from contraction, ensuring that we measure only action potential and removing any possible artifacts arising from sample motion. Full details of the biological preparation are given in Supplementary Information with this work.

Prior to the experiment, the sample chamber and connecting tubing were cleaned by pumping heavily diluted household bleach through the system, followed by flushing with deionised water. This was then replaced with ACSF solution, carbogenated in a 500 ml bottle and forming a closed circuit with the sample chamber. Temperature was measured in the chamber as 34 °C with laser and microwave power on. The mouse muscle was held in the chamber by suture loops on hooks just above (but not in contact with) the diamond.

Stimulation protocol. The muscle was optically stimulated every 2 s, with a light pulse length of 5 ms. The absence of contamination of the recording by a photovoltaic effect (Becquerel effect) induced by light was confirmed by taking traces recorded with the same protocols in the absence of muscle. Data from the magnetometer and from the electrodes was recorded from the ADC for 60 s data acquisition iterations during stimulation, giving 30 stimulations per iteration. The full data from both magnetic and electrical probe channels (2 × 80kSa/s × 60 s) was stored for postprocessing. Many hours of data acquisition was possible. Postprocessing ensured that unexpected transient noise could be captured. A random delay time was implemented between 60 s iterations (length between 10–30 s), ensuring each iteration began with a different mains phase to assist averaging. The absolute start time of each iteration was recorded and this measurement timeseries is used in the relevant plots in the results section. A fast ODMR sweep for selecting the optimal MW frequency was performed every 5 min during the measurement to compensate for any thermal drift.

Ethical statement. All methods in this work were carried out in compliance with the ARRIVE guidelines according to relevant Danish national guidelines and regulations. Experimental protocols were approved where required by the Technical University of Denmark, the University of Copenhagen and the Danish National Committee on Health Research Ethics (DNVK).

Received: 14 August 2020; Accepted: 28 December 2020

Published online: 28 January 2021

References

- Kandel, E. R., Schwartz, J. H., Jessell, T. M., Hudspeth, A. J. & Mack, S. Principles of Neural Science, fifth edition (2013).
- Scanziani, M. & Häusser, M. Electrophysiology in the age of light. *Nature* **461**, 930–939 (2009).
- Hong, G. & Lieber, C. M. Novel electrode technologies for neural recordings. *Nat. Rev. Neurosci.* **20**, 330–345. <https://doi.org/10.1038/s41583-019-0140-6> (2019).
- Fiáth, R. *et al.* Slow insertion of silicon probes improves the quality of acute neuronal recordings. *Sci. Rep.* <https://doi.org/10.1038/s41598-018-36816-z> (2019).
- Lee, W. & Someya, T. Emerging trends in flexible active multielectrode arrays. *Chem. Mater.* **31**, 6347–6358. <https://doi.org/10.1021/acs.chemmater.9b00165> (2019).
- Jaklevic, R. C., Lambe, J., Silver, A. H. & Mercereau, J. E. Quantum interference effects in josephson tunneling. *Phys. Rev. Lett.* **12**, 159–160 (1964).
- Clarke, J., Lee, Y.-H. & Schneiderman, J. Focus on SQUIDS in biomagnetism. *Supercond. Sci. Technol.* **31**, 080201 (2018).
- Hämäläinen, M., Hari, R., Ilmoniemi, R. J., Knuutila, J. & Lounasmaa, O. V. Magnetoencephalography—theory, instrumentation, and applications to noninvasive studies of the working human brain. *Rev. Mod. Phys.* **65**, 413–497. <https://doi.org/10.1103/RevModPhys.65.413> (1993).
- Cohen, D. Magnetic fields around the torso: Production by electrical activity of the human heart. *Science* **156**, 652–654 (1967).
- Gruber, A. Scanning confocal optical microscopy and magnetic resonance on single defect centers. *Science* **276**, 2012–2014 (1997).
- Doherty, M. W. *et al.* The nitrogen-vacancy colour centre in diamond. *Phys. Rep.* **528**, 1–45 (2013).
- Taylor, J. M. *et al.* High-sensitivity diamond magnetometer with nanoscale resolution. *Nat. Phys.* **4**, 810–816 (2008).
- Schloss, J. M., Barry, J. F., Turner, M. J. & Walsworth, R. L. Simultaneous broadband vector magnetometry using solid-state spins. *Phys. Rev. Appl.* **10**, 034044 (2018).
- Fescenko, I. *et al.* Diamond magnetometer enhanced by ferrite flux concentrators. *Phys. Rev. Res.* **2**, 023394 (2020).
- Wolf, T. *et al.* Subpicotesla diamond magnetometry. *Phys. Rev. X* **5**, 041001 (2015).
- Chatzidrosos, G. *et al.* Miniature cavity-enhanced diamond magnetometer. *Phys. Rev. Appl.* **8**, 044019 (2017).
- Delaney, P., Greer, J. C. & Larsson, J. A. Spin-polarization mechanisms of the nitrogen-vacancy center in diamond. *Nano Lett.* **10**, 610–614 (2010).
- Wojciechowski, A. M. *et al.* Precision temperature sensing in the presence of magnetic field noise and vice-versa using nitrogen-vacancy centers in diamond. *Appl. Phys. Lett.* **113**, 013502 (2018).
- Schirhagl, R., Chang, K., Lorez, M. & Degen, C. L. Nitrogen-vacancy centers in diamond: Nanoscale sensors for physics and biology. *Annu. Rev. Phys. Chem.* **65**, 83–105 (2014).
- Wu, Y., Jelezko, F., Plenio, M. B. & Weil, T. Diamond quantum devices in biology. *Angew. Chem. Int. Ed.* **55**, 6586–6598 (2016).
- McGuinness, L. P. *et al.* Quantum measurement and orientation tracking of fluorescent nanodiamonds inside living cells. *Nat. Nanotechnol.* **6**, 358–363 (2011).
- Kucsko, G. *et al.* Nanometre-scale thermometry in a living cell. *Nature* **500**, 54–58. <https://doi.org/10.1038/nature12373> (2013).
- Sage, D. L. *et al.* Optical magnetic imaging of living cells. *Nature* **496**, 486–489 (2013).
- Davis, H. C. *et al.* Mapping the microscale origins of magnetic resonance image contrast with subcellular diamond magnetometry. *Nat. Commun.* **9**, 1–9 (2018).

25. Barry, J. F. *et al.* Optical magnetic detection of single-neuron action potentials using quantum defects in diamond. *Proc. Nat. Acad. Sci.* **113**, 14133–14138 (2016).
26. Hall, L. T. *et al.* High spatial and temporal resolution wide-field imaging of neuron activity using quantum NV-diamond. *Sci. Rep.* **2**, 401 (2012).
27. Karadas, M. *et al.* Feasibility and resolution limits of opto-magnetic imaging of neural network activity in brain slices using color centers in diamond. *Sci. Rep.* **8**, 1–14 (2018).
28. Webb, J. *et al.* Sensing of magnetic fields from biological signals using diamond nitrogen vacancy centres. arXiv:2004.02279 (2020).
29. Cannon, S., Brown, R. & Corey, D. Theoretical reconstruction of myotonia and paralysis caused by incomplete inactivation of sodium channels. *Biophys. J.* **65**, 270–288 (1993).
30. Nikolic, K. *et al.* Photocycles of channelrhodopsin-2. *Photochem. Photobiol.* **85**, 400–411 (2009).
31. Yizhar, O., Fenno, L. E., Davidson, T. J., Mogri, M. & Deisseroth, K. Optogenetics in neural systems. *Neuron* **71**, 9–34 (2011).
32. Juel, C. Muscle action potential propagation velocity changes during activity. *Muscle Nerve* **11**, 714–719 (1988).
33. Caruso, L. *et al.* In vivo magnetic recording of neuronal activity. *Neuron* **95**, 1283–1291.e4. <https://doi.org/10.1016/j.neuron.2017.08.012> (2017).
34. Webb, J. L. *et al.* Nanotesla sensitivity magnetic field sensing using a compact diamond nitrogen-vacancy magnetometer. *Appl. Phys. Lett.* **114**, 231103 (2019).
35. Sulai, I. A. *et al.* Characterizing atomic magnetic gradiometers for fetal magnetocardiography. *Rev. Sci. Instrum.* **90**, 085003. <https://doi.org/10.1063/1.5091007> (2019).
36. Kim, D. *et al.* A CMOS-integrated quantum sensor based on nitrogen-vacancy centres. *Nat. Electron.* **2**, 284–289. <https://doi.org/10.1038/s41928-019-0275-5> (2019).
37. Bougas, L. *et al.* On the possibility of miniature diamond-based magnetometers using waveguide geometries. *Micromachines* **9**, 276. <https://doi.org/10.3390/mi9060276> (2018).
38. Boto, E. *et al.* A new generation of magnetoencephalography: Room temperature measurements using optically-pumped magnetometers. *NeuroImage* **149**, 404–414 (2017).
39. Boto, E. *et al.* Moving magnetoencephalography towards real-world applications with a wearable system. *Nature* **555**, 657–661 (2018).
40. Jensen, K. *et al.* Magnetocardiography on an isolated animal heart with a room-temperature optically pumped magnetometer. *Sci. Rep.* **8**, 1–9 (2018).
41. Jensen, K. *et al.* Non-invasive detection of animal nerve impulses with an atomic magnetometer operating near quantum limited sensitivity. *Sci. Rep.* **6**, 1–7 (2016).
42. QuSpin. Technical documentation on QZFM Gen-2 OPM sensor, QuSpin Inc (2020).
43. Zhang, T. *et al.* Hybrid nanodiamond quantum sensors enabled by volume phase transitions of hydrogels. *Nat. Commun.* <https://doi.org/10.1038/s41467-018-05673-9> (2018).
44. Fernández-Rossier, J. Imaging magnetic 2d crystals with quantum sensors. *Science* **364**, 935. <https://doi.org/10.1126/science.aax6598> (2019).
45. Einaga, Y., Foord, J. S. & Swain, G. M. Diamond electrodes: Diversity and maturity. *MRS Bull.* **39**, 525–532. <https://doi.org/10.1557/mrs.2014.94> (2014).
46. Cobb, S. J., Ayres, Z. J. & Macpherson, J. V. Boron doped diamond: A designer electrode material for the twenty-first century. *Annu. Rev. Anal. Chem.* **11**, 463–484. <https://doi.org/10.1146/annurev-anchem-061417-010107> (2018).
47. Barry, J. F. *et al.* Sensitivity optimization for NV-diamond magnetometry. *Rev. Mod. Phys.* <https://doi.org/10.1103/revmodphys.92.015004> (2020).
48. El-Ella, H. A. R., Ahmadi, S., Wojciechowski, A. M., Huck, A. & Andersen, U. L. Optimised frequency modulation for continuous-wave optical magnetic resonance sensing using nitrogen-vacancy ensembles. *Opt. Express* **25**, 14809 (2017).

Acknowledgements

We would like to thank Carmelo Bellardita for helping us do the immunohistochemistry. We acknowledge the Core Facility for Integrated Microscopy, Faculty of Health and Medical Sciences, University of Copenhagen for using their confocal microscope for immunohistochemistry image acquisition. We acknowledge the assistance of Kristian Hagsted Rasmussen for fabrication and diamond processing and Mursel Karadas (former DTU Heath Technology, currently New York University) for contributions and prior experimental and theoretical modeling work.

Author contributions

The project was conceived by A.H. and U.L.A. Methodology development, investigation and analysis were performed by J.L.W., L.T., N.W.H. and A.M.W. N.W.H. performed all animal dissections. Modeling work was performed by C.O. Diamond growth and irradiation was performed by J.A., O.B., R.S., M.K. and J.M. This manuscript was written by J.L.W. with editing and review contribution by all other authors. The overall supervision was performed by A.T., J.F.P., K.B.S., A.H. and U.L.A.

Competing interests

The authors declare no competing interests.

Additional information

Supplementary Information The online version contains supplementary material available at <https://doi.org/10.1038/s41598-021-81828-x>.

Correspondence and requests for materials should be addressed to J.L.W.

Reprints and permissions information is available at www.nature.com/reprints.

Publisher's note Springer Nature remains neutral with regard to jurisdictional claims in published maps and institutional affiliations.



Open Access This article is licensed under a Creative Commons Attribution 4.0 International License, which permits use, sharing, adaptation, distribution and reproduction in any medium or format, as long as you give appropriate credit to the original author(s) and the source, provide a link to the Creative Commons licence, and indicate if changes were made. The images or other third party material in this article are included in the article's Creative Commons licence, unless indicated otherwise in a credit line to the material. If material is not included in the article's Creative Commons licence and your intended use is not permitted by statutory regulation or exceeds the permitted use, you will need to obtain permission directly from the copyright holder. To view a copy of this licence, visit <http://creativecommons.org/licenses/by/4.0/>.

© The Author(s) 2021



Chapter 7

Laser stimulation of muscle activity with simultaneous detection using a diamond colour centre biosensor

7.1 Introduction

Following the work described in the previous chapter, which employed LED light to activate action potentials in genetically modified mice, the experimental results obtained by combining focused laser stimulation with simultaneous magnetic field sensing will be illustrated next. Based on these results, it is demonstrated that highly localized and high intensity laser excitation of action potential can be achieved without interfering with the sensing apparatus. Using this type of excitation could be an essential tool for developing technologies for mapping neural activity and conducting intracellular nanodiamond experiments.

It is shown that focused optogenetic stimulation can lead to stronger muscle contraction in EDL muscles in mice and the resulting movement can be detected as an artifact in the optical readout. This contraction artifact could be suppressed by adding 2,3-Butanedione monoxime (BDM) to the bath chamber without affecting the propagation of the compound action potential. The magnetic signal was recovered with a spectral whitening algorithm used to remove the correlated noise produced by environmental sources. Finally, by using computer simulation and modeling of the

examined system, new insights about the behavior of Channelrodopsin under intense light stimulation are illustrated.

7.2 Publication

This manuscript was submitted to Biosensors and Bioelectronics with the title of “Laser stimulation of muscle activity with simultaneous detection using a diamond colour centre biosensor” as follows:

Laser stimulation of muscle activity with simultaneous detection using a diamond colour centre biosensor

Luca Troise^a, Nikolaj W. Hansen^b, Christoffer Olsson^c, James L. Webb^{a,*}, Leo Tomasevic^d, Jocelyn Achard^e, Ovidiu Brinza^e, Robert Staacke^f, Michael Kieschnick^f, Jan Meijer^f, Axel Thielscher^{c,d}, Hartwig Siebner^d, Kirstine Berg-Sørensen^c, Jean-François Perrier^b, Alexander Huck^{a,**} and Ulrik Lund Andersen^{a,***}

^aCenter for Macroscopic Quantum States (bigQ), Department of Physics, Technical University of Denmark, 2800 Kgs. Lyngby, Denmark

^bDepartment of Neuroscience, University of Copenhagen, Copenhagen, Denmark

^cDepartment of Health Technology, Technical University of Denmark, 2800 Kgs. Lyngby, Denmark

^dDanish Research Centre for Magnetic Resonance (DRCMR), Hvidovre Hospital, 2650 Hvidovre, Copenhagen, Denmark

^eLaboratoire des Sciences des Procédés et des Matériaux, Université Sorbonne Paris Nord, 93430 Villetaneuse, France

^fDivision Applied Quantum System, Felix Bloch Institute for Solid State Physics, Leipzig University, 04103, Leipzig, Germany

ARTICLE INFO

Keywords:
diamond
nitrogen vacancy
optogenetics
magnetometry
biosensing

ABSTRACT

The detection of biological activity at the microscopic level, including electrical signals or heat flow, is key for understanding the function of biosystems and relating this to physical structure. Conventional sensing methods often rely on invasive probes to stimulate and detect activity, with significant potential to induce damage in the target system. In recent years, a new type of biosensor based on colour centres in diamond has raised the possibility of instead passively sensing and imaging living biological systems. In this work we use such a sensor to record the magnetic field generated by a strong, highly localised electrical biosignal in mammalian tissue kept alive *in vitro*, generated by focused, high intensity pulsed laser optogenetic stimulation. We observe a compound action potential response and a slow signal component which we seek to explain using a detailed model of the biological system. Our sensor is capable of recording from the stimulation site, without photovoltaic or fluorescence artifacts associated with alternative techniques. We demonstrate sensor operation in an ordinary unshielded lab environment through novel application of spectral whitening filtering, to overcome background noise from common electromechanical sources including electrical mains. Our work represents a step towards selective induction of localised activity while performing passive sensing and imaging with diamond sensors, opening the way to future applications including mapping of neural activity and intracellular processes.

1. Introduction

Sensing biological activity at the microscopic level, including the flow of heat or electrical charge, is of fundamental importance for understanding processes in living organisms, relating this to structure and behaviour and for disease diagnosis, such as identifying the early stages of neurodegenerative disorders, including peripheral nerve damage and muscle atrophy (McDonald, 2012). Of particular interest is the biological response to a stimulus, such as a pulse of electrical current or light, and being able to detect this response with high spatial and temporal resolution (Scanziani and Häusser, 2009). Many different biosensor approaches have been developed for microscopic direct detection of activity, in particular recording of electrical activity using probe electrodes (electrophysiology) and by sensing using fluorescent biomarkers (Grienberger and Konnerth, 2012; Lin and Schnitzer, 2016). However, such methods are highly invasive, particularly to record deep within tissue. This entails the risk of tissue damage, through mechanical action, toxicity or infection, which could be detrimental for living organisms and might adversely affect the sought after activity (Gechev et al., 2016; Mahajan et al., 2020).

*jaluwe@fysik.dtu.dk

**alexander.huck@fysik.dtu.dk

***ulrik.andersen@fysik.dtu.dk

✉ jaluwe@fysik.dtu.dk (J.L. Webb); alexander.huck@fysik.dtu.dk (A. Huck); ulrik.andersen@fysik.dtu.dk (U.L. Andersen)

ORCID(s):

An alternative method is to indirectly detect activity, passively using a sensor outside of the sample or subject. For electrical activity in the brain or nervous system, this can be achieved by monitoring the magnetic field induced by the signal, which can freely penetrate biological tissue. Field sensing has been demonstrated for larger scale tissue sensing in established techniques such as magnetoencephalography (MEG) and magnetocardiography (MCG), using superconducting quantum interference device (SQUID) sensors (Clarke et al., 2018; Hämäläinen et al., 1993). However, these sensors have significant disadvantages, requiring special shielding from background magnetic field (e.g. geomagnetic, mains electricity) and cryogenic cooling, limiting these valuable techniques to very few facilities and applications.

In recent years, new biosensor approaches without these drawbacks have been actively pursued (Arlett et al., 2011; Baselt et al., 1998; Boto et al., 2018). In this work, we focus on an approach utilising colour centres, defect sites in a solid state material with optical properties highly sensitive to their local environment. In particular, interest has focused on the negatively charged nitrogen vacancy (NV) centres in diamond, consisting of a nitrogen substitutional dopant paired with a lattice vacancy. NV centres have been used for sensing of magnetic field (Taylor et al., 2008), electric field (Dolde et al., 2011), temperature (Neumann et al., 2013) and strain (pressure/force) (Kehayias et al., 2019) via optically detected magnetic resonance (ODMR) spectroscopy (Neumann et al., 2009; Steinert et al., 2010). Diamond NV sensors offer advantages including high sensitivity (Fescenko et al., 2020; Wolf et al., 2015), room temperature operation and high spatial (Mizuno et al., 2020; Sage et al., 2013) and temporal (Barry et al., 2020) resolution. Diamond is highly biocompatible, with biosensors based on NV centres able to operate in solution at a wide range of temperatures (Toyli et al., 2012), both remotely and in close contact (even within) a biological specimen (Barry et al., 2016; Wu et al., 2021)

Sensors based on NV centres in diamond are particularly suited to microscopy applications in either widefield or confocal configurations (Sage et al., 2013; Horsley et al., 2018; Gruber et al., 1997), in a manner SQUIDS or other alternative sensors cannot easily achieve. NV sensors can sense a small volume region, containing single (neuron) cells and down to the few or single molecule level. A desirable goal is to simultaneously sense while selectively and precisely optically stimulating activity within the sensing region, without suffering from measurement artifacts existing sensors can suffer (Kozai and Vazquez, 2015; Cardin et al., 2010; Packer et al., 2013). Achieving this goal is key to realising applications including nanoscale nuclear magnetic resonance (Staudacher et al., 2013), radical pair sensing for avian magnetoreception (Xu et al., 2021), intracellular nanodiamond studies (Kucsko et al., 2013; Fujiwara et al., 2020; McGuinness et al., 2011) and stimulation of neurons in brain tissue (Hall et al., 2012; Karadas et al., 2018; Price et al., 2020). Due to the confinement required, focused laser stimulation is preferable for these applications, with the higher laser optical intensity ideal for for stimulation well within tissue.

In this work, we seek to demonstrate the viability of such focused laser stimulation combined with simultaneous microscopic sensing from biological tissue using a diamond NV sensor, located in proximity to the stimulation site. Building on our previous work (Webb et al., 2021), we use living *extensor digitorum longus* (EDL) muscles from mice *in vitro*, genetically modified to contain channelrhodopsin (ChR2). We stimulate the muscle tissue using focused pulsed laser light, of a specific wavelength and intensity, generating highly localised ($\approx 150\mu\text{m}$) stimulation and activation of the muscle response. We then record the response of the muscle via the magnetic field induced by ionic current associated with compound action potentials in the muscle. We seek to 1) demonstrate artifact-free recording of activity using our diamond NV sensor with high temporal resolution, 2) explore the biological response recorded under laser stimulation, 3) derive new insight into the behavior of the biological system and response via the use of computer modelling and 4) employ new methodology including spectral whitening filtering of background noise to enhance biosensor signal recovery in an ordinary lab environment without magnetic shielding.

2. Material and Methods

We performed *in vitro* studies of EDL muscles dissected from mice, expressing the light sensitive cation channel Channelrhodopsin2 (ChR2) in muscle cells to achieve optogenetic triggering of electrical activity in the muscle using blue light. Muscles were placed in a solution chamber directly above our diamond NV sensor (Figure 1). Stimulation was performed using a 488nm laser diode with the beam directed in free space and focused using a long working distance lens into the sample chamber. The electrical response (*electric data* in this work) was measured using an AgCl electrode in light surface contact with the muscle 2-2.5 millimeters away from the laser stimulation site, and the induced magnetic field recorded simultaneously by the diamond NV sensor (*magnetic data* below).

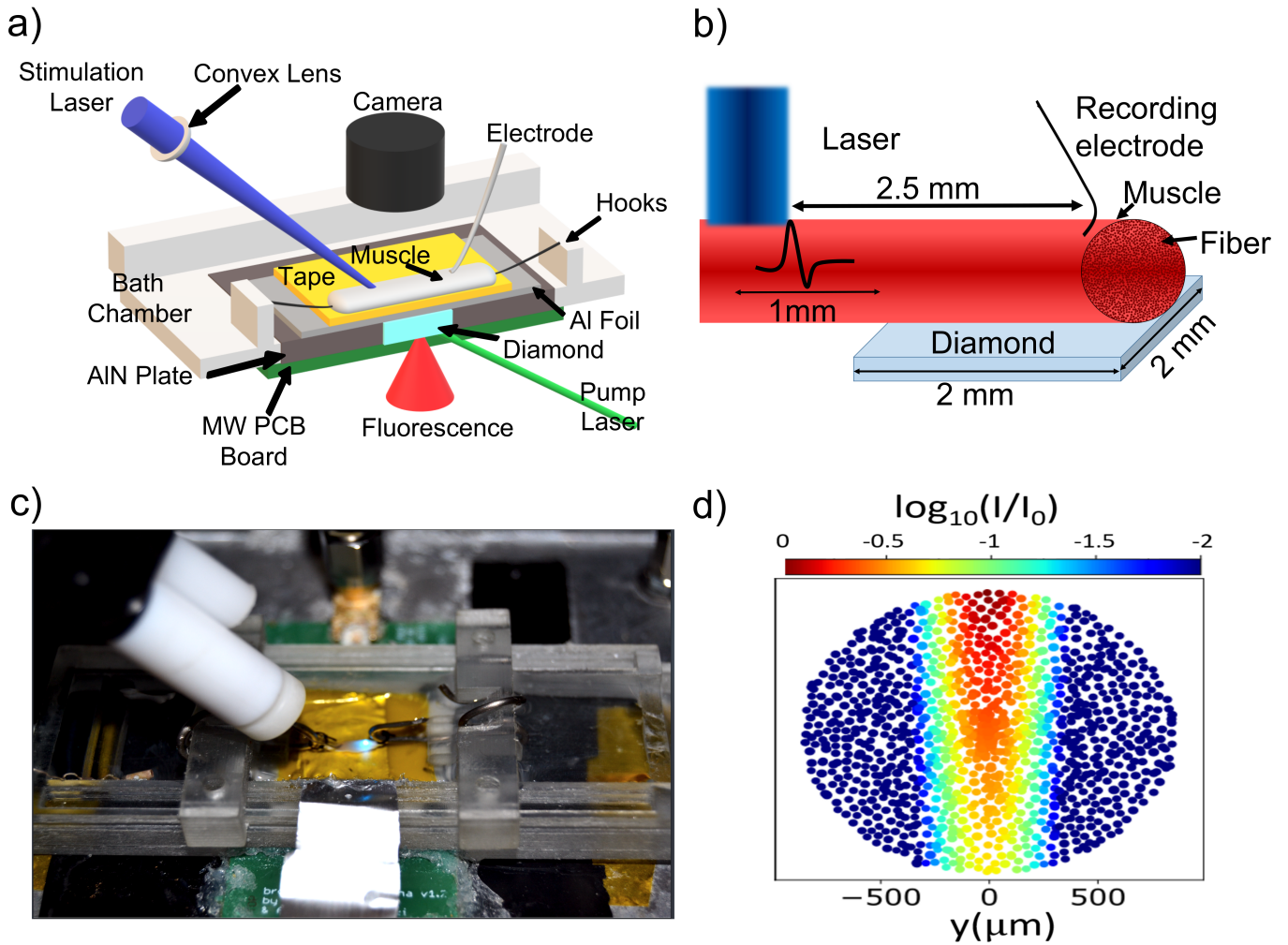


Figure 1: Experimental setup and muscle cross section used for modelling a) Schematic of the experimental setup and b) picture of the muscle in the solution chamber with a 488nm blue stimulation laser spot incident on the muscle surface. The laser spot could be placed with high precision anywhere within the sample chamber in a 2x2cm area using mechanical mirror mounts. c) Schematic illustration of experimental setup, as used in the modelling. d) Simulated cross-section of muscle showing the light intensity (I/I_0) distribution on the muscle fibers with laser stimulation.

2.1. Diamond NV Sensor

We used a [100] oriented electronic-grade diamond (Element Six), of dimensions $2 \times 2 \times 0.5 \text{ mm}^3$, overgrown via chemical vapour deposition (CVD) with a $20 \mu\text{m}$ thick diamond layer with a doping concentration of $\approx 5 \text{ ppm}$ of ^{14}N . NV centres were generated by 2.8MeV proton irradiation and subsequent annealing at 800°C . We measured an ODMR microwave resonance linewidth of 1 MHz and a resonance contrast of 1.5%. The diamond was mounted into an aluminum nitride plate heatsink, with the top surface of the diamond covered by a $16 \mu\text{m}$ thick layer of aluminium foil to reflect stray laser light back into the diamond and to prevent the stimulation laser from reaching it (Figure 1). The aluminium foil was covered by a layer of Kapton tape ($50 \mu\text{m}$) to electrically insulate the diamond from the biological sample. The aluminum nitride plate holding the diamond was mounted on top of a microwave antenna printed on a PCB board. On top of the diamond, we mounted a 3D printed plastic chamber for holding a solution bath, sealed using aquarium silicone.

2.2. Sensor Operation

We optically pumped our diamond with 1.4W of 532nm green laser light (Coherent Verdi G2), linearly polarised and coupled to the diamond on its bottom surface at Brewster's angle (67°). Red fluorescence from the NV centres was collected using a 12mm diameter condenser lens (Thorlabs ACL 1210) and passed through an optical filter (FEL0600). Magnetic field at the diamond was recorded as a modulation of the intensity of the red fluorescence emission recorded

using an auto-balanced optical receiver (Nirvana 2007, New Focus Inc.). We measure only the magnetic field response in the direction perpendicular to the electrical current propagation direction inside the muscle, with this single axis response maximised by applying a static bias field of 1.5 mT parallel to the [110] crystallographic direction in the diamond. A continuous wave scheme was implemented with fixed laser power and a three-frequency microwave driving scheme (El-Ella et al., 2017) using two microwave generators (Stanford SG394) to drive the triplet ground state transition (2.7-3GHz) and the ^{14}N hyperfine transitions (2.16 MHz). The two RF signals were delivered to the diamond via a printed circuit board nearfield antenna. The microwaves were modulated at 23.3 kHz for lock-in detection (Stanford SR850), using a time constant of $30\mu\text{s}$ giving a sensor measurement bandwidth of 4.8kHz. The output of the lock-in amplifier was digitised at a rate of 80 kSa/s using an analog to digital converter (NI PCI-6221) and recorded using custom-written software.

2.3. Muscle Preparation

We used mice expressing the light sensitive cation channel Channelrhodopsin2 (ChR2) in muscle cells expressing Parvalbumin (PV) by crossing Gt(ROSA)26Sor^{tm32}(CAG-COP4*H134R/EYFP)^{Hze} (stock no.: 024109; Jackson Laboratory) mice with Pvalb^{tm1(cre)Arbr} mice (stock no.: 017320; Jackson Laboratory) (Webb et al., 2021). Adult PV-Cre::ChR2 mice were dissected as described previously (Webb et al., 2021). Quickly following euthanasia by cervical dislocation, EDL muscles were dissected in carbogen (95% O₂/5% CO₂) saturated ice-cold artificial cerebrospinal fluid (ACSF) containing (in mM): NaCl (111), NaHCO₃ (25), glucose (11), KCl (3), CaCl₂ (2.5), MgCl₂ (1.3) and KH₂PO₄ (1.1). Small suture loops were tied on proximal and distal tendons. The dissected mouse muscle was kept in a solution bath of artificial cerebrospinal fluid (ACSF), chilled by passing a recycled feed of ACSF into the solution chamber through plastic tubing submerged in ice to maintain a bath temperature between 18°C and 20°C. The ACSF was bubbled with carbogen gas to oxygenate the muscle and allow survival for up to 20 hours of measurement.

2.4. Laser Stimulation and Recording

The muscle was gently stretched on top of the diamond NV sensor by two adjustable hooks and a probe electrode (AgCl coated silver wire) mounted on a micromanipulator placed in contact with the muscle top surface. The electric data from this probe electrode was recorded via a differential amplifier (Axon Cyberamp 320) relative to the grounded solution bath. Muscles were stimulated to produce compound action potentials (AP) using a TTL triggered 488nm blue laser (OdicForce Ltd.). Laser light was directed through free space to the muscle and focused onto the muscle using an $f=400$ mm plano-convex lens, giving a $1/e^2$ laser spot size of $\approx 150\mu\text{m}$, measured using a microscope camera mounted above the sample chamber. This beam waist could be further reduced by additional lenses in the beam path as required. Using optomechanical mirror mounts, the laser spot could be moved at sub-millimeter precision to any position on the muscle, with a travel of 2×2 cm² across the chamber. This represents an improvement over a confocal/inverted widefield microscopy configuration where stimulation is limited only to the centre of the objective field of view (Mrózek et al., 2015; Bernardi et al., 2020). We positioned the stimulation laser spot approximately 0.5 mm (Figure 1,b) along the muscle away from the diamond, to ensure we recorded signal propagation in only one direction (towards one end of the muscle). Control measurements were taken of the photovoltaic effect from laser stimulation incident to the probe electrode (see Supplementary Information) and for laser stimulation directly on the diamond NV sensor. For the latter, no detectable artifact was observed in the magnetic data, measuring using 5ms pulses at 50mW directly onto the Kapton layer above the diamond for up to 10 hours.

To ensure the stray field from the high current at laser turn-on was not recorded, the blue laser head was placed 3.5m away from the diamond NV sensor and the TTL trigger decoupled using a custom-built optocoupler. Optimal blue laser power was found by initially stimulating the muscle with low input laser power (5 mW), and then slowly increasing the power until a maximal response of the muscle was observed in the electric data. Optical stimulation was performed at a frequency of 0.5 Hz and with a pulse length of 5 ms. For this length, stimulation power was found to be in the range of 20-50 mW, varying between different muscles. Signals were recorded using 60s continuous time traces, giving the high spectral resolution necessary to filter and remove background magnetic noise. Many hours of recording could be acquired (up to 20), limited only by the lifespan of the muscle in the solution bath.

2.5. Filtering by Spectral Whitening

Without magnetic shielding, it was necessary to remove a substantial amount of magnetic noise from our sensor readout, including stationary mains noise at harmonics of 50Hz and non-stationary noise from building pumps and compressors. In our previous work, we demonstrated that this was possible using windowed notch filtering (Webb

et al., 2020). However this noise removal is relatively slow and suboptimal, due to the use of serially generated fixed frequency windows and a single global threshold value to identify noise peaks, constraints imposed by computational time. Here, we instead implemented a Linear Time-Invariant (LTI) spectral whitening filter. This method has been used extensively for a range of applications, including radar and detection of gravitational waves (Gabbard et al., 2018; Chatziioannou et al., 2019; Roman et al., 2000). To implement the filter, the power spectral density (PSD) of each 60s time traces was used to estimate the noise spectrum and to derive the transfer function for whitening the signals. The double-sided PSD was calculated with Welch's periodogram method with a segment length of 3.5s and 50% overlap. The input signals were whitened in the range from 20Hz-40kHz; the lower frequency bound was chosen in order to avoid high-pass filter artifacts, the high frequency bound was set by the Nyquist frequency of the digitisation. Following whitening, an additional 3rd order Butterworth lowpass filter was applied with a cutoff frequency chosen at 650Hz, the expected upper frequency of the muscle electrical signal. Baseline wander was removed from the trials using robust detrending (de Cheveigné and Arzounian, 2018). Further details of the filter method and optimisation are supplied in Supplementary Information.

2.6. Simulation and Modelling Method

In order to verify and analyze the detected signal we performed a numerical simulation of the biosensor and muscle biosystem. We use the NEURON software package (Hines and Carnevale, 2001) to simulate the signal propagation in a muscle. The ion channel mechanisms were modified in accordance with a previous muscle model on EDL muscles in mice (Cannon et al., 1993) (full details in Supplementary Information). The optogenetic stimulation current was modelled with the use of a biophysical model developed by Foutz et al. (Foutz et al., 2012), which is based on the four-state model described by Nikolic et al. (Nikolic et al., 2009).

We modelled the individual muscle fibers in a cylindrical geometry with a cylinder radius of 845 μm and an individual fiber radius given by a uniform distribution of $22.5 \pm 3.5 \mu\text{m}$ (Augusto et al., 2017). The fibers started at the back end of the laser stimulation spot and extended straight across the laser beam, and over across the NV diamond (Figure 1,b and c). The light distribution inside the muscle was calculated according to the Kubelka-Munk model. The diamond was divided into 20x20 individual pixels with side-lengths of 100 μm , and the magnetic field was calculated at each pixel, and then averaged across the whole diamond. The local field potential (LFP) was calculated as a monopolar readout approximately at the site of the electrical recording tip (Figure 1,c). The magnetic and electrical field calculation were based on calculations performed in (Karadas et al., 2018), using the LFPy software package (Lindén et al., 2014).

3. Results and Discussion

3.1. Movement Inhibition

The strong contraction of the muscle after laser stimulation was found to produce a movement-induced artifact in our diamond NV sensor. This artifact arose due to a slight shift in microwave resonance frequency resulting from a motion-induced change in coupling between the nearfield antenna and the diamond and tissue above it. In order to remove this artifact, we pharmacologically suppressed movement using the myosin ATPase inhibitor 2,3-Butanedione monoxime (BDM), without affecting compound action potential propagation. To determine the necessary concentration, we gradually increased the concentration of BDM in the recycled ACSF pumped through the solution bath, starting a 2.5 mM and increasing in steps of 2.5 mM at 10 minute intervals.

Figure 2,a) shows the measured NV sensor response (magnetic data) for a laser stimulated muscle at a range of different concentrations of BDM. With no or low concentration of BDM, we observed a significant movement artifact, equivalent to a 15nT magnetic field signal, followed by a decaying response lasting over 200ms. This artifact completely masked the sought action potential signal from the muscle. The motion artifact was considerably larger for laser stimulation than observed in our previous work using LED stimulation. We attribute this to significantly more effective stimulation of the muscle with the higher intensity laser than the weaker LED light, with the stronger movement clearly visible even by eye.

By increasing the concentration of BDM from 2.5 to 20mM in the ACSF solution, we observed a clear reduction in the movement artifact, with complete elimination above 15mM. This could also be observed in the electric signal from the surface electrode, with oscillations reflecting the movement of the electrode on the muscle eliminated in favour of the electrical response in the muscle (Figure 2, a). In order to confirm the absence of movement, we used a white light microscope and camera mounted above the sample, recording the movement of the muscle edge as a function of time

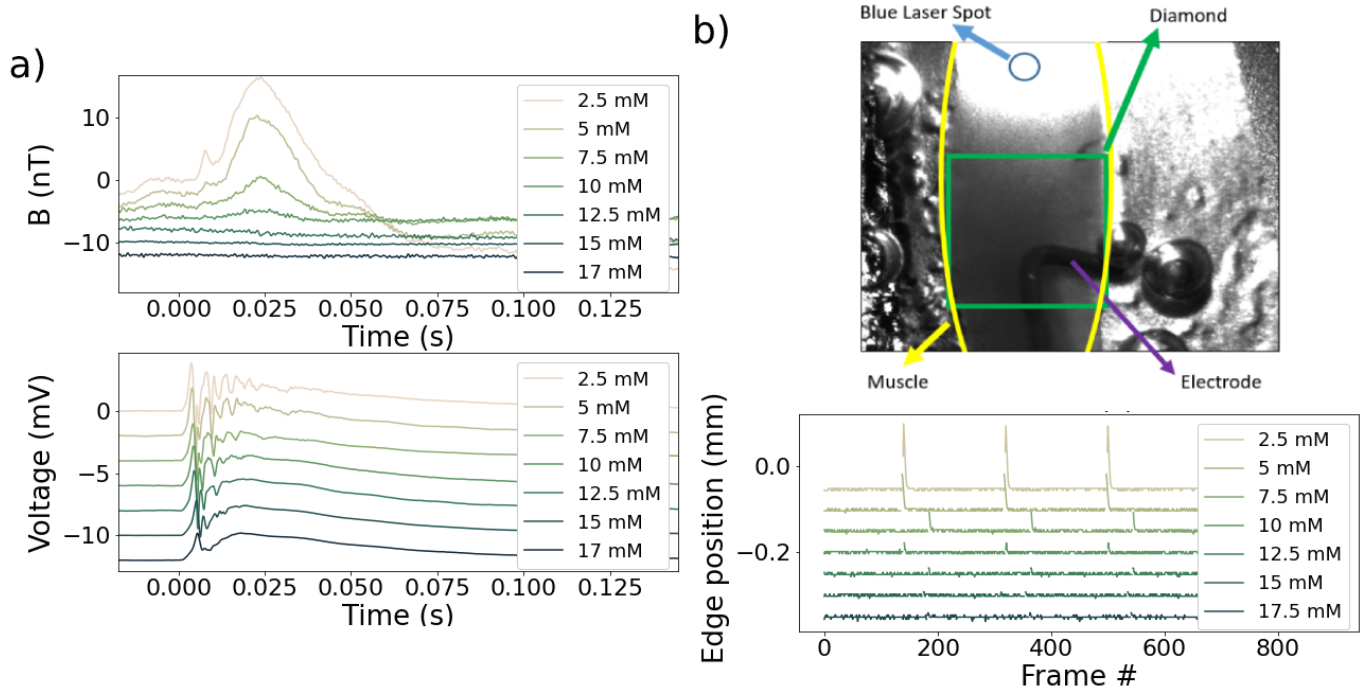


Figure 2: The diamond NV sensor and optical response to stimulation as a function of increasing BDM concentration. a) NV sensor response to stimulation - with low concentrations of BDM a large artifact associated with muscle movement was observed; this was eliminated at concentrations above 15mM. Bottom: Electric data for the same muscle. Here, oscillations arising from movement of the electrode on the moving muscle can be seen to vanish in favour of the biosignal of the electrical activity in the muscle. b) To fully confirm the suppression of movement, we used white light microscopy, imaging the muscle edge during stimulation with a camera at 90fps. Above 15mM, spikes associated with muscle movement are completely eliminated.

while stimulating with the blue laser. With low concentrations of BDM, clear jumps in position could be observed post-stimulation as the muscle moved (Figure 2,b). Above 15mM of BDM, these were completely suppressed, with no movement detectable anywhere along the muscle.

3.2. Noise Filtering

In Figure 3,a) and b) we show the unfiltered power spectral density (PSD) from data recorded using our diamond NV sensor, containing significant noise from background magnetic field sources. We show the effect of our whitening filter algorithm in Figure 3,c) and b). As can be observed in the spectrum and the post-filtered timeseries, the filter significantly reduced the noise level. The PSD used to derive the filter was calculated using Welch's method with time intervals of 3.5s, 50% overlap and Hanning window. In Supplementary Information, we outline the process by which we optimise the parameters of the whitening filter to remove noise, while retaining sufficient frequency components of the biosignal. We also directly compare the whitening filter performance against that derived using notch filtering and clarify how real absolute magnetic field units (Tesla) can be recovered from the relative PSD of the whitened data. Overall, we found the performance of the whitening filter in terms of noise removal was not significantly better than by using the notch filter method. However, it was significantly faster ($\times 2.5$ speedup) and easier to implement, requiring only the calculation of the PSD for each 60s time trace compared to a serial algorithm needed to sweep through and build the notch filter mask. For the majority of biological applications, the signal shape and relative amplitude is of main concern, making the whitening method a fast and effective option.

3.3. Biosignal Readout

In Figure 4,a) we show examples of the biological signal measured by the diamond NV sensor (*magnetic data*) and simultaneously recorded electrically using the AgCl contact electrode (*electric data*) for 3 different muscles (M1-3), each recorded in a separate experimental run. For each muscle, we observed both a fast response peak (AP) at ~ 5 ms and a slower response (CH) at ~ 10 ms after the stimulation trigger. We attribute the first peak (AP) to the compound

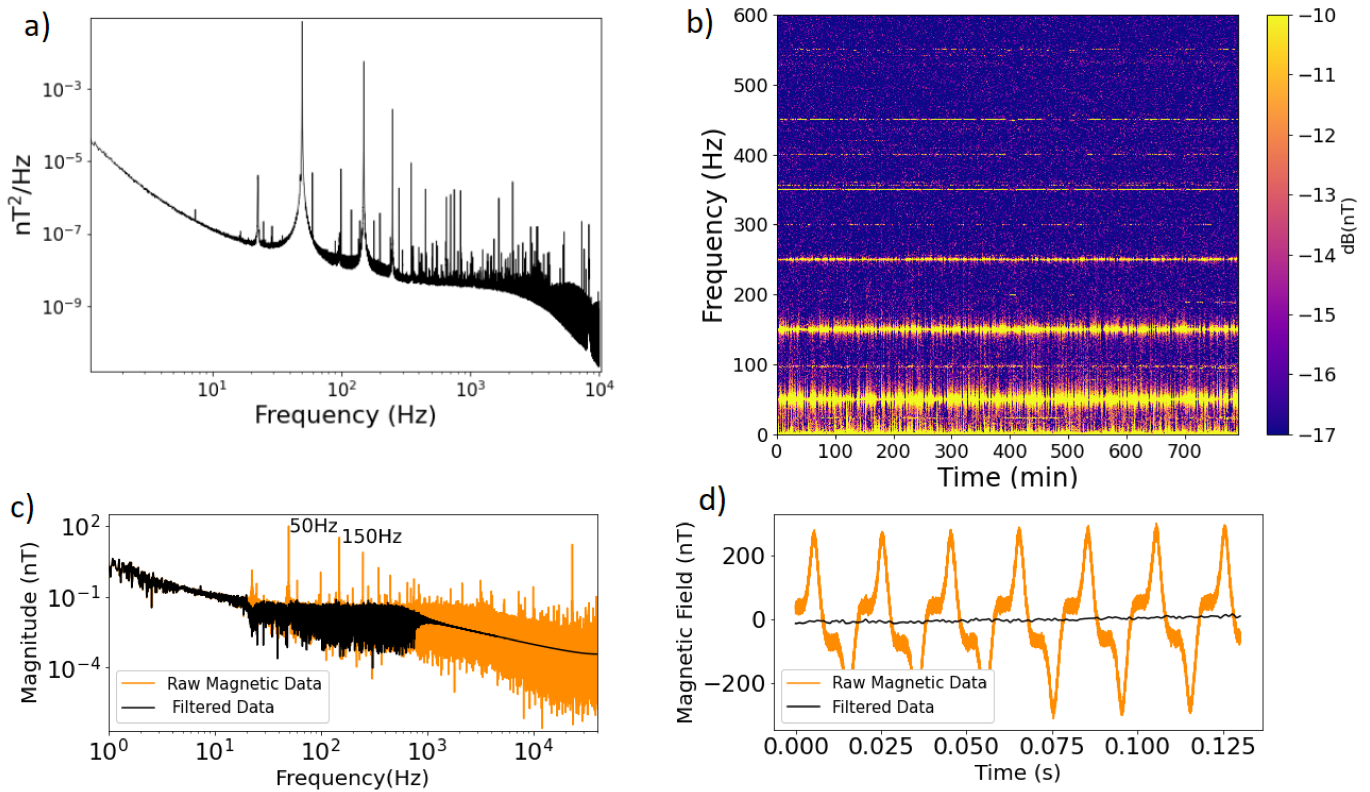


Figure 3: The noise spectrum of the diamond NV sensor, before and after post-processing filtering. a) Averaged spectrum of the background magnetic noise as measured by the sensor and b) spectrogram of the same noise taken over 13 hours. We observe significant noise arising from sources such as mains electricity in the $<1\text{kHz}$ region that contains the majority of the components of the ms-scale biological signal. c) Comparison of the amplitude spectrum before and after the application of the whitening filter, with a significant amount of noise identified and removed. This is reflected in the example timeseries shown in d), showing a 0.5sec trace before and after the filter is implemented. Filtering reduces the noise from peak-to-peak of 400nT to less than 1nT on a single 60sec trace.

action potential response and the second slower peak (CH) to the response from channelrhodopsin activity. Both signals decayed in amplitude over many stimulations while retaining a similar shape, with the AP signal decaying more rapidly and begin subsumed into the CH signal after 4-6 hours of measurement (Figure 5). A slight delay in time was observed between the electric and magnetic data, arising from the positioning of the probe electrode away from the stimulation site, but still within 0.2-0.5 mm of the $2 \times 2 \text{ mm}^2$ diamond sensor. We use a compromise upper cutoff frequency of 650Hz, minimising distortion to both AP and CH signals (see Supplementary Information), but acting to smooth the AP signal in the magnetic data. We note that the biological signal we observe using laser stimulation is significantly different from that previously observed for LED stimulation. The AP peak amplitude was weaker by a factor of 2 and in both the electric and magnetic data and recording shown in Figure 2, a), we observed a non-negative refractory period followed by a slowly (tens of milliseconds) decaying response (CH). Furthermore, we observe a difference in the relative height of the AP and CH peaks between the magnetic and electrical readouts. We attribute this to the channelrhodopsin channels opening faster and remaining open for longer under higher intensity laser light, allowing ionic current to flow for longer and generating the strong CH signal.

The peak magnetic field observed for muscle M2 was a factor of 5 stronger than for M1 and M3. We consider this likely to arise due to unexpected variability in sensor response across the $2 \times 2 \text{ mm}^2$ diamond area. Due to the high level of internal reflection in high refractive index diamond, that we collect light from the full diamond volume and that the diamond had a relatively uniform density of NV centres, we expected sensor output to not vary significantly depending on muscle position, so long as the muscle was positioned approximately above the sensor. However, we found this not to be the case. Later investigations using a scanned electrified probe tip across the diamond surface, recording the magnetic field it induced, determined an area approximately $0.5 \times 0.5 \text{ mm}$ to be a factor 16 better sensitivity than the lowest response elsewhere on the diamond (see Supplementary Information). This region corresponded approximately

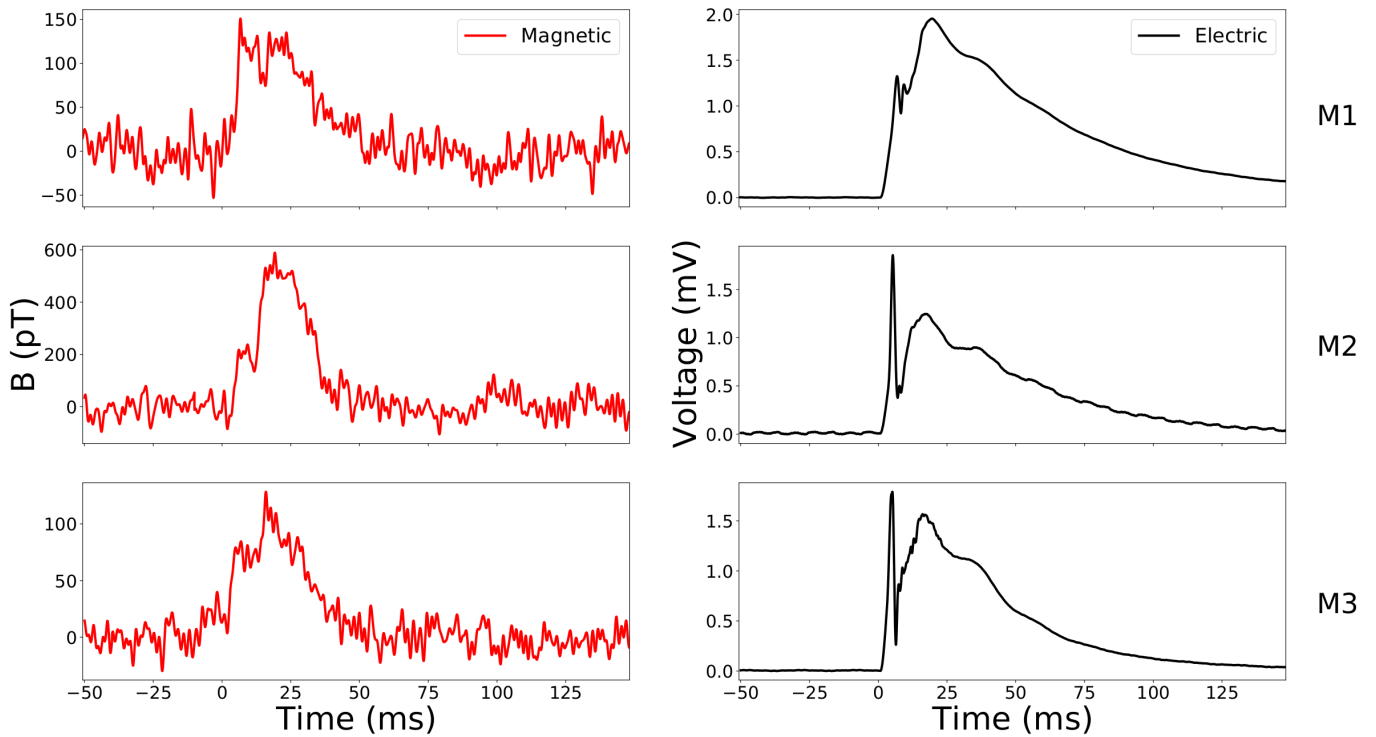


Figure 4: Measuring the muscle biological response electrically and magnetically. Magnetic and electric data recorded for 3 different muscles (M1-M3). The data shown is the average response over 15000, 13500 and 540 stimulations for M1-3 respectively. The action potential (AP) peak and the channelrhodopsin (CH) are clearly distinguishable on all three muscles. On all subfigures, time $t=0$ corresponds to the instant laser stimulation is triggered.

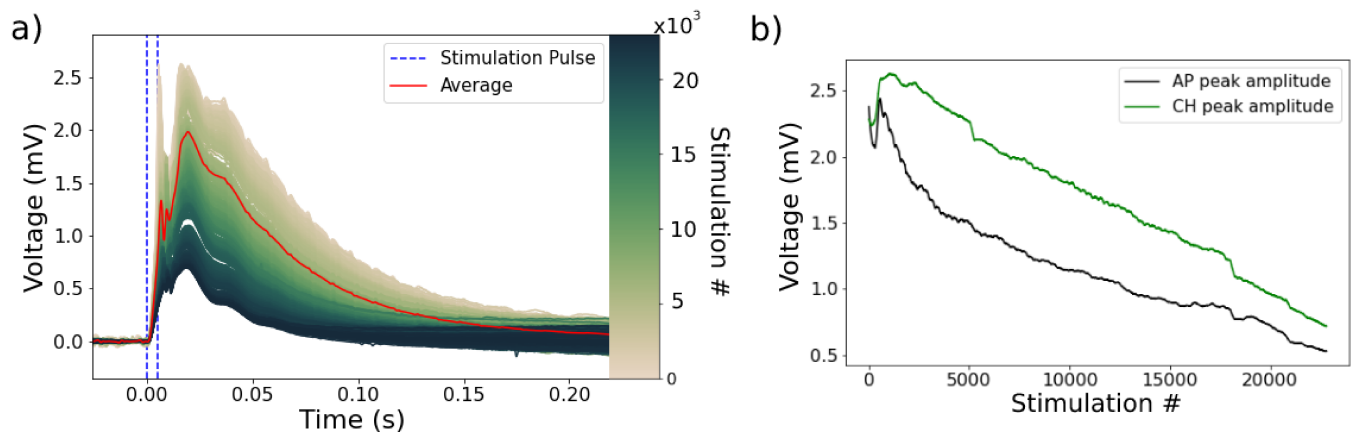


Figure 5: Stability of the measured biological response over time. a) Variations in electric data recording versus number of stimulations for muscle M1. The amplitude of the signal gradually decreased over time as the muscle fatigued. We observed both a fast response peak from the action potential at ~ 5 ms and a second slower peak from channelrhodopsin at ~ 20 ms. b) Scaling of the standard deviation of the 60s timeseries (measuring noise) as a function of number of stimulations for both notch and whitening filtering, showing the decay of the AP and CH peaks.

to where the pump laser beam struck the diamond, receiving the maximum laser intensity.

Although we cannot directly confirm the precise positioning, in the case of M2 it is likely the muscle was located optimally at the most sensitive region. For M1 and M2, the location was suboptimal but enough to yield a signal. For a number of other muscles, likely located away from this region, we recorded no biosignal in the magnetic data. We consider the positional response a particularly important result for this type of sensor, highlighting the need to correctly position the biosamples and spatially map sensor response. We also highlight that this potentially offers a novel route to spatially resolve and image signals well below the physical dimensions of the sensor using a scanned, highly focused

pump laser beam. Further investigations of these aspects are called for, but are beyond the scope of this work.

3.4. Simulation and Modeling

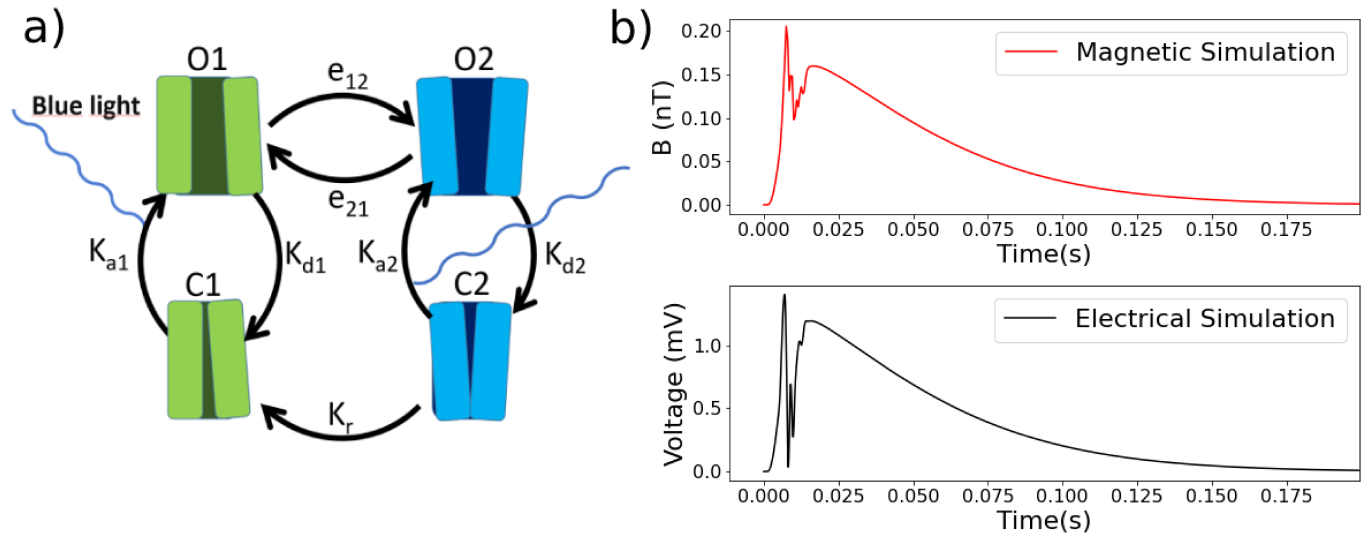


Figure 6: Channelrhodopsin model as related to our recorded response. a) Depiction of the different stages of the four-state model of a ChR2 molecule. Blue light can transition the ChR2 from closed (C1 and C2) to open (O1 and O2). b) Upper figure show simulated magnetic signal as detected by averaging over the whole diamond. Lower figure show simulated LFP as detected by an electrode positioned as in Figure 1,c.

In order to explore the origin of the observed signal features, we modelled the muscle system to calculate the response under laser stimulation. In both electric and magnetic data, we observed a signal (CH) with a slow decay (Figure 4). We attribute this signal to the activation of channelrhodopsin, with such a signal previously observed for optogenetically stimulated muscle signals (Bruegmann et al., 2015; Magown et al., 2015). When trying to model this response, we found that the original biophysical models of ChR2, developed for stimulation of neurons rather than muscle, could not describe the length of the CH signal we observe. Modelling the dynamics of ChR2 in neurons for a large span of different scenarios, including covering the range of current and intensity in this work, predict that any signal should decay within 15 ms of the stimulation (Nikolic et al., 2009).

The four-state ChR2 model (Grossman et al., 2011) for this process is shown in Figure 6,a). The ChR2-proteins are mainly populated at rest in the closed fast state (C1), which, when illuminated, transitions to the open fast state (O1) with transition rate K_{a1} (stimulation laser intensity dependent) thus allowing influx of ions to the fiber. The O1 is unstable and decays mainly to C1 (with transition rate K_{d1}) as long as short excitation pulses (≈ 5 ms) are used. This typically results in a single action potential without any pronounced secondary prolonged current.

With longer pulse duration, C1 can also transition to the slow opened state (O2). This transition is characterised with the irradiance dependent transition rates e_{12} and e_{21} . The O2 state relaxes relatively slow to the closed slow state (C2) with a transition rate of K_{d2} , which in turn can either transition back to O2 given an excitation, with transition rate K_{a2} , or return to C1 with transition rate K_r . As the O2 state stays open for a longer time period after the stimulation pulse, it also creates a longer decay of the signal. This was experimentally observed for neuron stimulation for excitation pulses exceeding 50ms (Nikolic et al., 2009).

However, we observe our slowly decaying CH signal at a shorter stimulation period of 5 ms. This implied that the ChR2 in the studied muscle has transitioned into the O2 configuration at a greater degree than it would occur in neurons. We therefore modified the four-state model to account for this behaviour (see Supplementary Information for full details). Briefly, we modeled the induction of a secondary long-lasting current at a stimulation period of 5 ms by allowing for a stronger transition to the O2 configuration in ChR2, decaying more slowly to the closed state. This was done by setting the e_{12} and e_{21} parameters higher during illumination, and then letting e_{12} remain high after illumination, whereas e_{21} returned to a low value (Table SI1). Furthermore, the conductivity of the O2 state was also set higher than in previous models (from about 2-5fS to 25fS). These alternative values for the ChR2 model can be justified by considering the higher intensity of the stimulation laser light compared to that in the original ChR2

model and that we experiment on muscle rather than neuronal structures, with a different environment in the muscle sarcolemma compared to neural cell membrane. These alternative values for the ChR2 model can be justified by considering and the . Modification of these few parameters gives a modelled signal (Figure 6, b) highly representative of the magnetic and electric data recorded experimentally (Figure 4).

4. Conclusions

In this work, we demonstrate the viability of a diamond nitrogen-vacancy (NV) colour centre biosensor for recording biosignals while stimulating activity in high proximity to the sensor with focused pulsed laser light. Although we use simple muscle tissue, which could be easily probed electrically, our results show that highly localised, high intensity, selective excitation of specific biological processes in more complex systems can be done while passively sensing in the same localised region. This is essential for realising proposals such as to mapping neural activity in networks in the brain (Alivisatos et al., 2012) and experiments using intracellular nanodiamonds (Schirhagl et al., 2014).

We show that laser optogenetic stimulation of mouse muscle has a stronger physical response than our previous investigations using much lower intensity LED stimulation (Webb et al., 2021). This resulted in a significant movement artifact in the biosensor readout. We were able to fully suppress this artifact using a muscle movement inhibitor, although suppression was more challenging with higher intensity laser illumination than low intensity LED light. These results highlight the importance of understanding and eliminating unwanted artifacts in biosensing experiments. Although in this work the motion artifact represented a disadvantage, it could be exploited in a novel type of diamond NV sensor for force/motion detection, such as vector sensing of force/movement in a biological sample (Cohen et al., 2020).

Using a filter algorithm based on spectral whitening we shown similar noise reduction performance as for using a notched filter, but with an improvement in terms of post-processing filter time (≈ 2.5 times faster), especially where recovery of precise field units are not required. This represents a step forward in terms of realising real-time biological signal recovery in an ordinary, unshielded lab environment Further advances in filtering may be obtained by implementing artificial intelligence techniques in filter design, in particular by supplying synthetic known biosignals to the sensor.

We observe both short period (AP) and long period (CH) signals in the magnetic data recorded by our NV sensor. Through modeling, we attribute these signals to muscle action potential (AP) and to current flow through channel-rhodopsin (CH), with more muscle fibres addressed by the deeply penetrating laser beam and the channel opened for longer by the higher laser intensity. Although not ideal, with the channelrodopsin activation obscuring the action potential signal, the result exemplifies the usefulness of our diamond NV sensor in gaining new insight into a biological system close to the optical stimulation site. Using alternative techniques, artifacts arising from photovoltaic effects (for electrical probes) or optical bleaching (for fluorescent biomarkers) would entirely mask the biosignal. The muscle position variability of the strength of our magnetic response highlights the need to properly characterise the sensor, and the potential to record strong signals if this process is well optimised. These results also potentially point to a way to achieve spatial resolution below the physical dimensions of the diamond, while still maintaining the same optical collection and excitation scheme. Such spatial resolution is key to fully, microscopically resolve and identify the origin of activity in living biological samples.

5. Competing Interests

The authors declare that they have no known competing interests that would influence the work reported here.

6. Ethical Statement

The work described in this article has been carried out in accordance with Directive 86/609/EEC for animal experiments and all relevant national legislation in Denmark.

7. Author Statement

LT, NWH, JLW: Conceptualization, Methodology, Software, Investigation, Validation, Data Curation, Formal Analysis, Writing - original draft and editing. CO: Conceptualization, Methodology, Analysis, Writing - original draft and editing. AH,ULA,JFP,KBS: Conceptualization, Supervision, Funding Acquisition, Writing - editing.

8. Funding

The work presented here was funded by the Novo Nordisk foundation through the synergy grant bioQ (Grant Number: NNF17OC0028086) and the Center for Macroscale Quantum States (bigQ) funded by the Danish National Research Foundation (Grant number:DNRF142).

References

- Alivisatos, A. P., Chun, M., Church, G. M., Greenspan, R. J., Roukes, M. L., and Yuste, R. (2012). The brain activity map project and the challenge of functional connectomics. *Neuron*, 74(6):970–974.
- Arlett, J., Myers, E., and Roukes, M. (2011). Comparative advantages of mechanical biosensors. *Nature nanotechnology*, 6(4):203–215.
- Augusto, V., Padovani, C. R., and Campos, G. E. R. (2017). Skeletal muscle fiber types in C57BL6J mice. *Journal of Morphological Sciences*, 21(2):0.
- Barry, J. F., Schloss, J. M., Bauch, E., Turner, M. J., Hart, C. A., Pham, L. M., and Walsworth, R. L. (2020). Sensitivity optimization for NV-diamond magnetometry. *Reviews of Modern Physics*, 92(1).
- Barry, J. F., Turner, M. J., Schloss, J. M., Glenn, D. R., Song, Y., Lukin, M. D., Park, H., and Walsworth, R. L. (2016). Optical magnetic detection of single-neuron action potentials using quantum defects in diamond. *Proceedings of the National Academy of Sciences*, 113(49):14133–14138.
- Baselt, D. R., Lee, G. U., Natesan, M., Metzger, S. W., Sheehan, P. E., and Colton, R. J. (1998). A biosensor based on magnetoresistance technology. *Biosensors and Bioelectronics*, 13(7-8):731–739.
- Bernardi, E., Moreva, E., Traina, P., Petrini, G., Tchernij, S. D., Forneris, J., Pastuović, Ž., Degiovanni, I. P., Olivero, P., and Genovese, M. (2020). A biocompatible technique for magnetic field sensing at (sub)cellular scale using nitrogen-vacancy centers. *EPJ Quantum Technology*, 7(1).
- Boto, E., Holmes, N., Leggett, J., Roberts, G., Shah, V., Meyer, S. S., Muñoz, L. D., Mullinger, K. J., Tierney, T. M., Bestmann, S., Barnes, G. R., Bowtell, R., and Brookes, M. J. (2018). Moving magnetoencephalography towards real-world applications with a wearable system. *Nature*, 555(7698):657–661.
- Bruegmann, T., van Bremen, T., Vogt, C. C., Send, T., Fleischmann, B. K., and Sasse, P. (2015). Optogenetic control of contractile function in skeletal muscle. *Nature Communications*, 6(1).
- Cannon, S., Brown, R., and Corey, D. (1993). Theoretical reconstruction of myotonia and paralysis caused by incomplete inactivation of sodium channels. *Biophysical Journal*, 65(1):270–288.
- Cardin, J. A., Carlé, M., Meletis, K., Knoblich, U., Zhang, F., Deisseroth, K., Tsai, L.-H., and Moore, C. I. (2010). Targeted optogenetic stimulation and recording of neurons in vivo using cell-type-specific expression of channelrhodopsin-2. *Nat. Protoc.*, 5(2):247–254.
- Chatziioannou, K., Haster, C.-J., Littenberg, T. B., Farr, W. M., Ghonge, S., Millhouse, M., Clark, J. A., and Cornish, N. (2019). Noise spectral estimation methods and their impact on gravitational wave measurement of compact binary mergers. *Physical Review D*, 100(10).
- Clarke, J., Lee, Y.-H., and Schneiderman, J. (2018). Focus on SQUIDS in biomagnetism. *Superconductor Science and Technology*, 31(8):080201.
- Cohen, D., Nigmatullin, R., Kenneth, O., Jelezko, F., Khodas, M., and Retzker, A. (2020). Utilising NV based quantum sensing for velocimetry at the nanoscale. *Scientific Reports*, 10(1).
- de Cheveigné, A. and Arzounian, D. (2018). Robust detrending, rereferencing, outlier detection, and inpainting for multichannel data. *NeuroImage*, 172:903–912.
- Dolde, F., Fedder, H., Doherty, M. W., Nöbauer, T., Rempp, F., Balasubramanian, G., Wolf, T., Reinhard, F., Hollenberg, L. C. L., Jelezko, F., and Wrachtrup, J. (2011). Electric-field sensing using single diamond spins. *Nature Physics*, 7(6):459–463.
- El-Ella, H. A. R., Ahmadi, S., Wojciechowski, A. M., Huck, A., and Andersen, U. L. (2017). Optimised frequency modulation for continuous-wave optical magnetic resonance sensing using nitrogen-vacancy ensembles. *Optics Express*, 25(13):14809.
- Fescenko, I., Jarmola, A., Savukov, I., Kehayias, P., Smits, J., Damron, J., Ristoff, N., Mosavian, N., and Acosta, V. M. (2020). Diamond magnetometer enhanced by ferrite flux concentrators. *Physical Review Research*, 2(2).
- Foutz, T. J., Arlow, R. L., and McIntyre, C. C. (2012). Theoretical principles underlying optical stimulation of a channelrhodopsin-2 positive pyramidal neuron. *Journal of Neurophysiology*, 107(12):3235–3245.
- Fujiwara, M., Sun, S., Dohms, A., Nishimura, Y., Suto, K., Takezawa, Y., Oshimi, K., Zhao, L., Sadzak, N., Umehara, Y., Teki, Y., Komatsu, N., Benson, O., Shikano, Y., and Kage-Nakadai, E. (2020). Real-time nanodiamond thermometry probing in vivo thermogenic responses. *Science Advances*, 6(37):eaba9636.
- Gabbard, H., Williams, M., Hayes, F., and Messenger, C. (2018). Matching matched filtering with deep networks for gravitational-wave astronomy. *Physical Review Letters*, 120(14).
- Gechev, A., Kane, N., Koltzenburg, M., Rao, D., and van der Star, R. (2016). Potential risks of iatrogenic complications of nerve conduction studies (ncs) and electromyography (emg). *Clinical Neurophysiology Practice*, 1:62–66.
- Grienberger, C. and Konnerth, A. (2012). Imaging calcium in neurons. *Neuron*, 73(5):862–885.
- Grossman, N., Nikolic, K., Toumazou, C., and Degenaar, P. (2011). Modeling study of the light stimulation of a neuron cell with channelrhodopsin-2 mutants. *IEEE Transactions on Biomedical Engineering*, 58(6):1742–1751.
- Gruber, A., Dräbenstedt, A., Tietz, C., Fleury, L., Wrachtrup, J., and von Borczyskowski, C. (1997). Scanning confocal optical microscopy and magnetic resonance on single defect centers. *Science*, 276(5321):2012–2014.
- Hall, L. T., Beart, G. C. G., Thomas, E. A., Simpson, D. A., McGuinness, L. P., Cole, J. H., Manton, J. H., Scholten, R. E., Jelezko, F., Wrachtrup, J., Petrou, S., and Hollenberg, L. C. L. (2012). High spatial and temporal resolution wide-field imaging of neuron activity using quantum NV-diamond. *Scientific Reports*, 2(1).
- Hämäläinen, M., Hari, R., Ilmoniemi, R. J., Knuutila, J., and Lounasmaa, O. V. (1993). Magnetoencephalography—theory, instrumentation, and applications to noninvasive studies of the working human brain. *Reviews of Modern Physics*, 65(2):413–497.
- Hines, M. L. and Carnevale, N. T. (2001). Neuron: A tool for neuroscientists. *The Neuroscientist*, 7(2):123–135.

- Horsley, A., Appel, P., Wolters, J., Achard, J., Tallaire, A., Maletinsky, P., and Treutlein, P. (2018). Microwave device characterization using a widefield diamond microscope. *Phys. Rev. Applied*, 10:044039.
- Karadas, M., Wojciechowski, A. M., Huck, A., Dalby, N. O., Andersen, U. L., and Thielscher, A. (2018). Feasibility and resolution limits of opto-magnetic imaging of neural network activity in brain slices using color centers in diamond. *Scientific Reports*, 8(1).
- Kehayias, P., Turner, M. J., Trubko, R., Schloss, J. M., Hart, C. A., Wesson, M., Glenn, D. R., and Walsworth, R. L. (2019). Imaging crystal stress in diamond using ensembles of nitrogen-vacancy centers. *Physical Review B*, 100(17).
- Kozai, T. D. Y. and Vazquez, A. L. (2015). Photoelectric artefact from optogenetics and imaging on microelectrodes and bioelectronics: new challenges and opportunities. *J. Mater. Chem. B Mater. Biol. Med.*, 3(25):4965–4978.
- Kucsko, G., Maurer, P. C., Yao, N. Y., Kubo, M., Noh, H. J., Lo, P. K., Park, H., and Lukin, M. D. (2013). Nanometre-scale thermometry in a living cell. *Nature*, 500(7460):54–58.
- Lin, M. Z. and Schnitzer, M. J. (2016). Genetically encoded indicators of neuronal activity. *Nat. Neurosci.*, 19(9):1142–1153.
- Lindén, H., Hagen, E., Leski, S., Norheim, E. S., Pettersen, K. H., and Einevoll, G. T. (2014). LFPy: a tool for biophysical simulation of extracellular potentials generated by detailed model neurons. *Frontiers in neuroinformatics*, 7:41.
- Magown, P., Shettar, B., Zhang, Y., and Rafuse, V. F. (2015). Direct optical activation of skeletal muscle fibres efficiently controls muscle contraction and attenuates denervation atrophy. *Nature Communications*, 6(1).
- Mahajan, S., Hermann, J. K., Bedell, H. W., Sharkins, J. A., Chen, L., Chen, K., Meade, S. M., Smith, C. S., Rayyan, J., Feng, H., Kim, Y., Schiefer, M. A., Taylor, D. M., Capadona, J. R., and Ereifej, E. S. (2020). Toward standardization of electrophysiology and computational tissue strain in rodent intracortical microelectrode models. *Frontiers in Bioengineering and Biotechnology*, 8:416.
- McDonald, C. M. (2012). Clinical approach to the diagnostic evaluation of hereditary and acquired neuromuscular diseases. *Physical Medicine and Rehabilitation Clinics of North America*, 23(3):495–563. *Neuromuscular Disease Management and Rehabilitation, Part I: Diagnostic and Therapy Issues*.
- McGuinness, L. P., Yan, Y., Stacey, A., Simpson, D. A., Hall, L. T., Maclaurin, D., Praver, S., Mulvaney, P., Wrachtrup, J., Caruso, F., Scholten, R. E., and Hollenberg, L. C. L. (2011). Quantum measurement and orientation tracking of fluorescent nanodiamonds inside living cells. *Nature Nanotechnology*, 6(6):358–363.
- Mizuno, K., Ishiwata, H., Masuyama, Y., Iwasaki, T., and Hatano, M. (2020). Simultaneous wide-field imaging of phase and magnitude of AC magnetic signal using diamond quantum magnetometry. *Scientific Reports*, 10(1).
- Mrózek, M., Rudnicki, D., Kehayias, P., Jarmola, A., Budker, D., and Gawlik, W. (2015). Longitudinal spin relaxation in nitrogen-vacancy ensembles in diamond. *EPJ Quantum Technology*, 2(1).
- Neumann, P., Jakobi, I., Dolde, F., Burk, C., Reuter, R., Waldherr, G., Honert, J., Wolf, T., Brunner, A., Shim, J. H., Suter, D., Sumiya, H., Isoya, J., and Wrachtrup, J. (2013). High-precision nanoscale temperature sensing using single defects in diamond. *Nano Letters*, 13(6):2738–2742.
- Neumann, P., Kolesov, R., Jacques, V., Beck, J., Tisler, J., Batalov, A., Rogers, L., Manson, N. B., Balasubramanian, G., Jelezko, F., and Wrachtrup, J. (2009). Excited-state spectroscopy of single NV defects in diamond using optically detected magnetic resonance. 11(1):013017.
- Nikolic, K., Grossman, N., Grubb, M. S., Burrone, J., Toumazou, C., and Degenaar, P. (2009). Photocycles of channelrhodopsin-2. *Photochemistry and Photobiology*, 85(1):400–411.
- Packer, A. M., Roska, B., and Häusser, M. (2013). Targeting neurons and photons for optogenetics. *Nat. Neurosci.*, 16(7):805–815.
- Price, J. C., Mesquita-Ribeiro, R., Dajas-Bailador, F., and Mather, M. L. (2020). Widefield, spatiotemporal mapping of spontaneous activity of mouse cultured neuronal networks using quantum diamond sensors. *Frontiers in Physics*, 8.
- Roman, J., Rangaswamy, M., Davis, D., Zhang, Q., Himed, B., and Michels, J. (2000). Parametric adaptive matched filter for airborne radar applications. *IEEE Transactions on Aerospace and Electronic Systems*, 36(2):677–692.
- Sage, D. L., Arai, K., Glenn, D. R., DeVience, S. J., Pham, L. M., Rahn-Lee, L., Lukin, M. D., Yacoby, A., Komeili, A., and Walsworth, R. L. (2013). Optical magnetic imaging of living cells. *Nature*, 496(7446):486–489.
- Scanziani, M. and Häusser, M. (2009). Electrophysiology in the age of light. *Nature*, 461:930–939.
- Schirhagl, R., Chang, K., Loretz, M., and Degen, C. L. (2014). Nitrogen-vacancy centers in diamond: nanoscale sensors for physics and biology. *Annual review of physical chemistry*, 65:83–105.
- Staudacher, T., Shi, F., Pezzagna, S., Meijer, J., Du, J., Meriles, C. A., Reinhard, F., and Wrachtrup, J. (2013). Nuclear magnetic resonance spectroscopy on a (5-nanometer)³ sample volume. *Science*, 339(6119):561–563.
- Steinert, S., Dolde, F., Neumann, P., Aird, A., Naydenov, B., Balasubramanian, G., Jelezko, F., and Wrachtrup, J. (2010). High sensitivity magnetic imaging using an array of spins in diamond. *Review of Scientific Instruments*, 81(4):043705.
- Taylor, J. M., Cappellaro, P., Childress, L., Jiang, L., Budker, D., Hemmer, P. R., Yacoby, A., Walsworth, R., and Lukin, M. D. (2008). High-sensitivity diamond magnetometer with nanoscale resolution. *Nature Physics*, 4(10):810–816.
- Toyli, D., Christle, D., Alkauskas, A., Buckley, B., Van de Walle, C., and Awschalom, D. (2012). Measurement and control of single nitrogen-vacancy center spins above 600 k. *Physical Review X*, 2(3):031001.
- Webb, J. L., Troise, L., Hansen, N. W., Achard, J., Brinza, O., Staacke, R., Kieschnick, M., Meijer, J., Perrier, J.-F., Berg-Sørensen, K., Huck, A., and Andersen, U. L. (2020). Optimization of a diamond nitrogen vacancy centre magnetometer for sensing of biological signals. *Frontiers in Physics*, 8.
- Webb, J. L., Troise, L., Hansen, N. W., Olsson, C., Wojciechowski, A. M., Achard, J., Brinza, O., Staacke, R., Kieschnick, M., Meijer, J., Thielscher, A., Perrier, J.-F., Berg-Sørensen, K., Huck, A., and Andersen, U. L. (2021). Detection of biological signals from a live mammalian muscle using an early stage diamond quantum sensor. *Scientific Reports*, 11(1).
- Wolf, T., Neumann, P., Nakamura, K., Sumiya, H., Ohshima, T., Isoya, J., and Wrachtrup, J. (2015). Subpicotesla diamond magnetometry. *Physical Review X*, 5(4).
- Wu, Y., Alam, M. N. A., Balasubramanian, P., Ermakova, A., Fischer, S., Barth, H., Wagner, M., Raabe, M., Jelezko, F., and Weil, T. (2021). Nanodiamond theranostic for light-controlled intracellular heating and nanoscale temperature sensing. *Nano Lett.*, 21(9):3780–3788.
- Xu, J., Jarocho, L. E., Zollitsch, T., Konowalczyk, M., Henbest, K. B., Richert, S., Golesworthy, M. J., Schmidt, J., Déjean, V., Sowood, D. J. C.,

Short Title of the Article

Bassetto, M., Luo, J., Walton, J. R., Fleming, J., Wei, Y., Pitcher, T. L., Moise, G., Herrmann, M., Yin, H., Wu, H., Bartölke, R., Käsehagen, S. J., Horst, S., Dautaj, G., Murton, P. D. F., Gehrckens, A. S., Chelliah, Y., Takahashi, J. S., Koch, K.-W., Weber, S., Solov'yov, I. A., Xie, C., Mackenzie, S. R., Timmel, C. R., Mouritsen, H., and Hore, P. J. (2021). Magnetic sensitivity of cryptochrome 4 from a migratory songbird. *Nature*, 594(7864):535–540.

Supplementary Information: Laser stimulation of muscle activity with simultaneous detection using a diamond colour centre biosensor

Luca Troise¹, Nikolaj Winther Hansen², Christoffer Olsson³, James Luke Webb¹, Leo Tomasevic⁴, Jocelyn Achard⁵, Ovidiu Brinza⁵, Robert Staacke⁶, Michael Kieschnick⁶, Jan Meijer⁶, Axel Thielscher^{3,4}, Hartwig Siebner⁴, Kirstine Berg-Sørensen³, Jean-François Perrier², Alexander Huck¹, and Ulrik Lund Andersen¹

¹*Center for Macroscopic Quantum States (bigQ), Department of Physics, Technical University of Denmark, Kgs. Lyngby, Denmark*

²*Department of Neuroscience, University of Copenhagen, Copenhagen, Denmark*

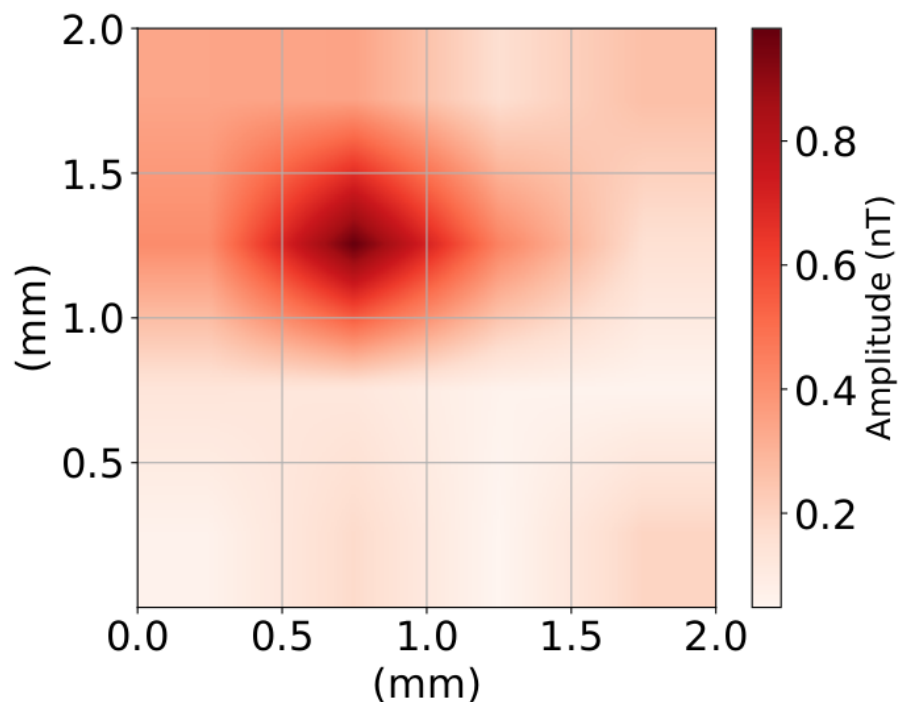
³*Department of Health Technology, Technical University of Denmark, Kgs. Lyngby, Denmark*

⁴*Danish Research Centre for Magnetic Resonance, Centre for Functional and Diagnostic Imaging and Research, Copenhagen University Hospital Hvidovre, Denmark*

⁵*Laboratoire des Sciences des Procédés et des Matériaux, Université Sorbonne Paris Nord, 93430 Villetaneuse, France*

⁶*Division Applied Quantum System, Felix Bloch Institute for Solid State Physics, Leipzig University, 04103, Leipzig, Germany*

1 Mapping of Diamond Sensitivity

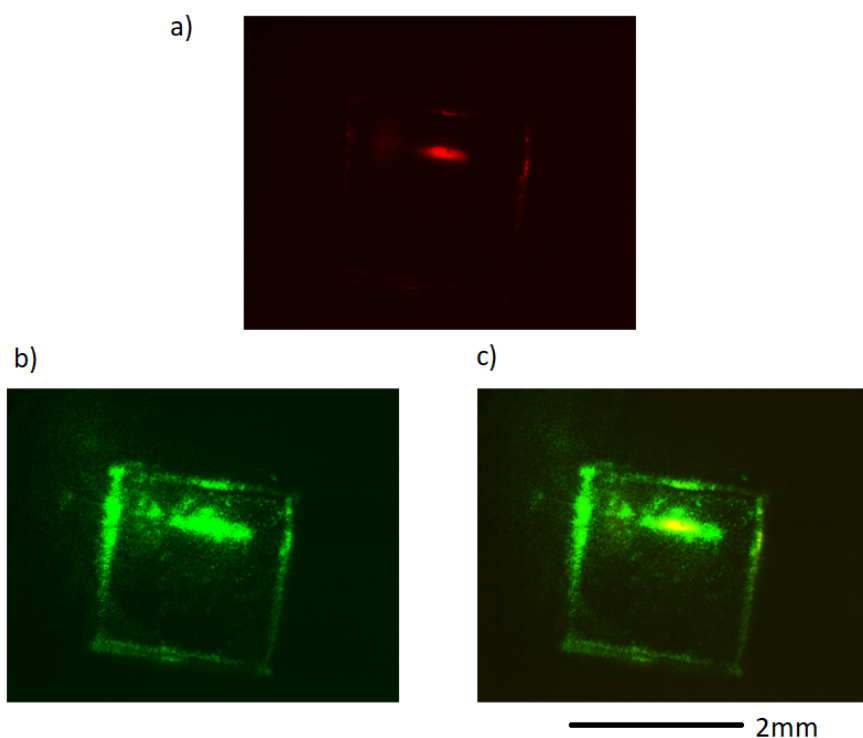


Supplementary Figure 1: Strength of the response in nT measured by the sensor to a wire electrode carrying a 20Hz, 10mA current scanned manually across the surface of the diamond sensor. Maximum sensor sensitivity corresponds to the point of maximum response to the electrode (darkest red).

Although we collected light from the entire diamond (within the numerical aperture of our condenser lens), and therefore did not expect significant nonuniformity of sensing across the 2x2mm diamond area, it was found during the course of later experiments that sensitivity did in fact vary. We found higher sensitivity at the point directly adjacent to where the 532nm pump laser strikes the underside of the diamond. As we did not account for this, we only positioned the muscle correctly on this sensitive region by chance.

To identify this point for better sample positioning, we mounted a thin Cu wire on a glass rod, in turn mounted to a (x,y) micrometer stage. This wire was then connected to a current source producing a 20Hz, 10mA AC signal. This signal induced a sharp magnetic field gradient at the wire tip, which would then generate a response from NV centres in the part of the diamond directly below it. We could then record the amplitude of this 20Hz signal relative to the white noise floor by monitoring our NV sensor output, giving us a measure of sensitivity at a given point. We divided our sensor area into 4×4 squares, manually driving the Cu wire to each square approximately 0.1mm above the diamond surface using a translation stage, with the top mounted white light microscope for guidance.

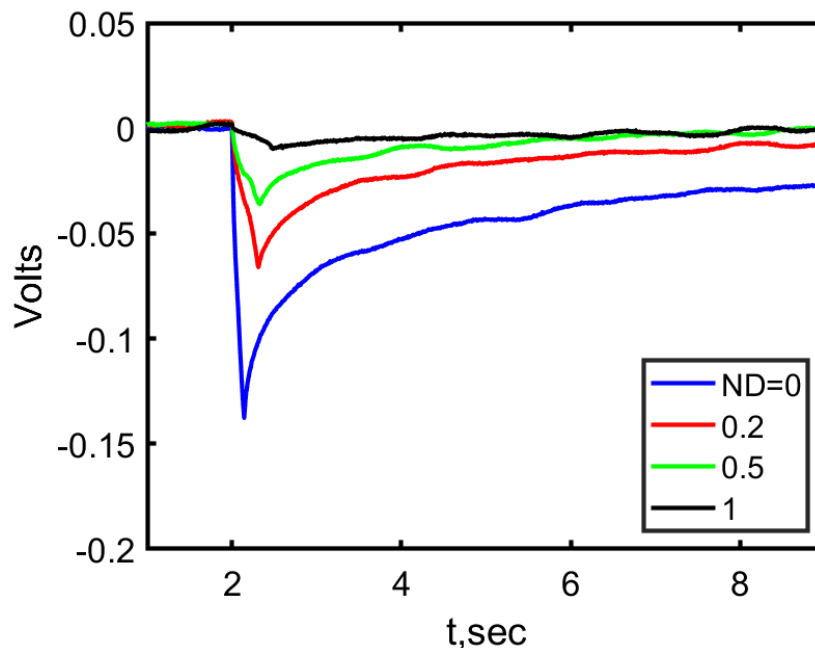
This map of signal amplitude (where higher amplitude = greater sensitivity) is shown in Supplementary Figure 1. By removing the top Kapton tape and foil layers, we could image the



Supplementary Figure 2: Imaging through the diamond using the white light microscope above the sample chamber, with the foil and Kapton cover layer removed such that the point at which the pump laser strikes the diamond can be seen. In a) we use an optical filter to show only the region of maximum fluorescence emission and in b) and c) the maximum green pump laser and green/red overlaid. (Note - image is flipped horizontally with respect to the signal map in the previous figure)

position where the pump laser reaches the diamond, generating the most fluorescence. This is shown in Supplementary Figure 2 approximately coinciding with the position of maximum sensitivity. Recognising this issue allowed us to better position future samples to maximise the strength of magnetic field recorded.

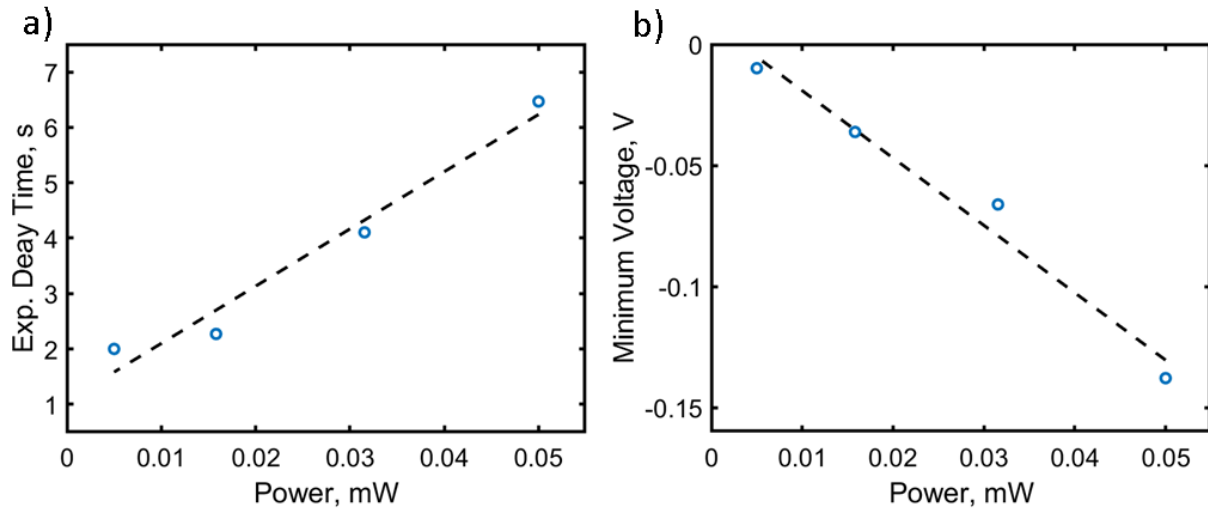
2 Photovoltaic Effect



Supplementary Figure 3: Photovoltaic effect resulting from a 5ms stimulation laser pulse (at $t=2\text{sec}$) directed at the stimulation electrode. We attenuate the power of the 50mW laser light by using neutral density filters placed in the beam path ($\text{ND}=0-1$). The strength of the effect we record from the electrodes (V) is significantly higher than the strength of the recorded biosignal (mV), and would entirely mask it for any recording near the stimulation site.

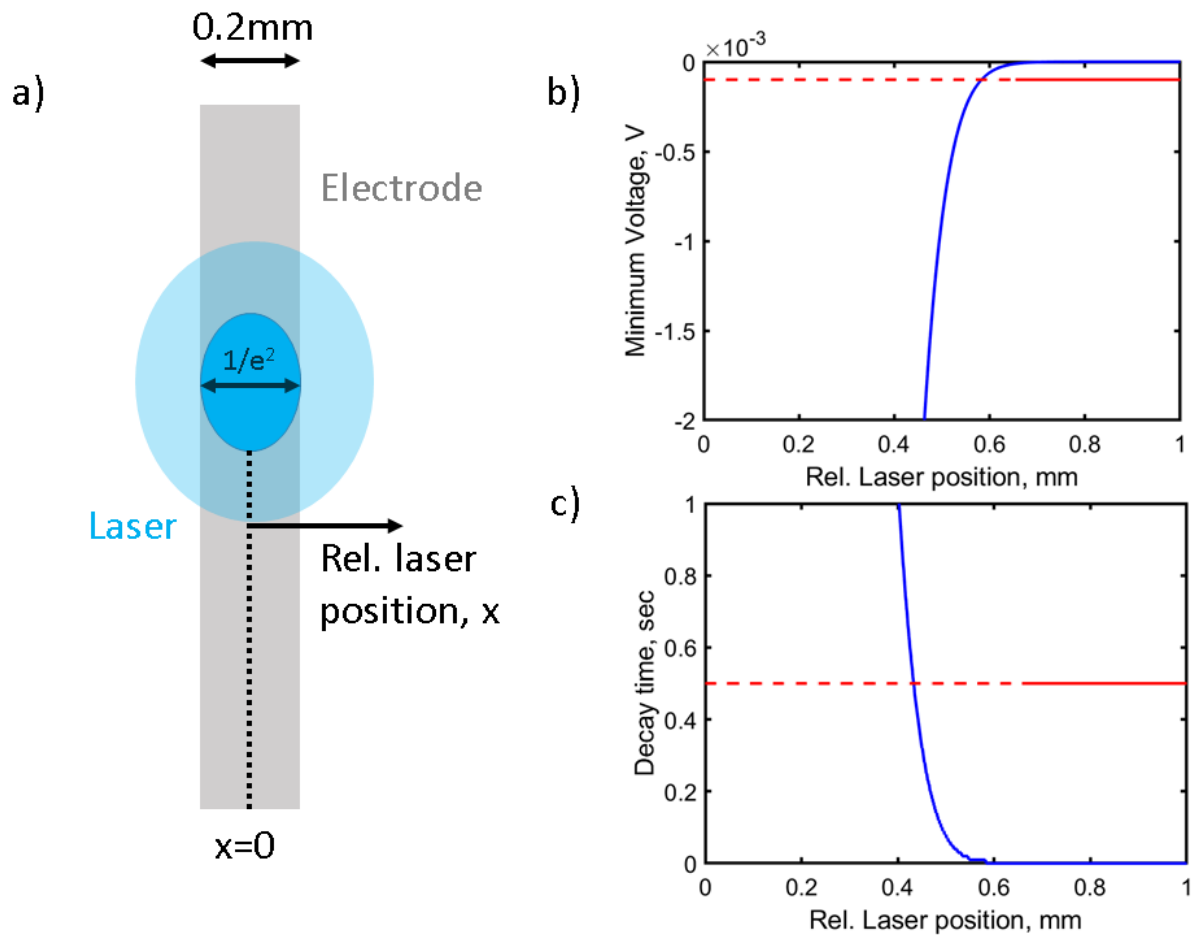
We recorded and modelled the photovoltaic effect arising from the stimulation laser shining on the electrical probe electrode. These artifacts were recorded by triggering a stimulation laser pulse during a 10sec recording, with a range of neutral density filters introduced to vary the stimulation laser power between 5-50mW. A strong artifact was observed in the electric data (Supplementary Figure 3 and 4), with the absolute magnitude of the single shot voltage peaking at 0.14Vm decaying on the order of many seconds, was measured when laser stimulation at 50mW was aimed directly at the electrode. The decay of this signal was far slower than the stimulation rate, potentially leading to artifact compounding and hysteresis effects. Even with a manual optomechanical translation stage, we found it challenging experimentally to precisely position the beam at a number of set distances from the electrode. However, using this data and modeling the laser as a Gaussian beam with $1/e^2=200\mu\text{m}$ (approximately the same width as the electrode), we could extrapolate the effect of stimulating away from the electrode. This is shown in Supplementary Figure 5. We find that the stimulation cannot occur within 0.5mm of the electrode without introducing a significant artifact (here defined as 10% of the $\approx 2\text{mV}$ single shot peak biosignal). We consider this estimate to be optimistic, and in practice even smaller artifacts would be desired, especially when averaging over many stimulations.

Such photovoltaic artifacts exemplify how it is extremely challenging to recover a weak



Supplementary Figure 4: Extrapolated parameters for the photovoltaic effect from the experimental data in Supplementary Figure 3. In a) we fit an exponential of the form $\exp(-1/\tau)$ to the decay after the minimum voltage is reached and plot the decay constant τ as a function of stimulation laser power after the ND filter. In b) we plot the minimum artifact voltage, again as a function of laser power. We fit both parameters as a linear function of laser power (dashed line).

biological signal at or close to the optical stimulation site using electrical probes - a drawback the diamond NV sensor does not suffer. We note that for electric data measurements in the main text, we located the probe electrode on the muscle surface well away from the stimulation site and shielded it from the stimulation laser using black tape. This eliminated any prospect of artifact pickup.



Supplementary Figure 5: a) Model of the stimulation laser ($1/e^2=200\mu\text{m}$ as in the experiment) on a 0.2mm width recording electrode. We model the expected minimum voltage and decay time as a function of laser position in x , where $x=0$ has the laser centred on the electrode as in the experimental data in Supplementary Figure 3. By calculating the total integrated power the electrode receives and using the linear fits in Supplementary Figure 4, we can estimate the strength of the artifact (peak absolute voltage) and the decay time. In b) we plot the minimum voltage, showing the distance required to reach 1/10th of the size of the biosignal. In c) we plot the time required to decay to this voltage, showing the distance required for decay to occur before the next stimulation (within 0.5s).

3 Optimization of Whitening Filter

Using spectral whitening is ideal for the magnetic data from our sensor, as the SNR of the biosignal is $\ll 1$, meaning that all peaks in the power spectrum significantly above the white noise floor are entirely noise. By using the method outlined in the main text, this allows these noise peaks to be eliminated by dividing by a suitable approximation of the PSD, without having to specifically identify each noise peak (as is required for notch filtering) and without requiring any knowledge about the sought biosignal.

However, for eliminating lower amplitude noise near the white noise floor, this simple whitening method suffers the drawback that in minimising the noise on the signal by estimating a PSD ever closer to the actual PSD of the signal, it may begin to remove frequencies that are part of the desired biosignal. This can lead to a corruption of the recovered signal from the magnetic data, either through distortion of the shape of the signal or introduction of filter artifacts. In the extreme case where the estimated PSD entirely matches the actual PSD, the noise will be zero, but the signal will be completely eliminated.

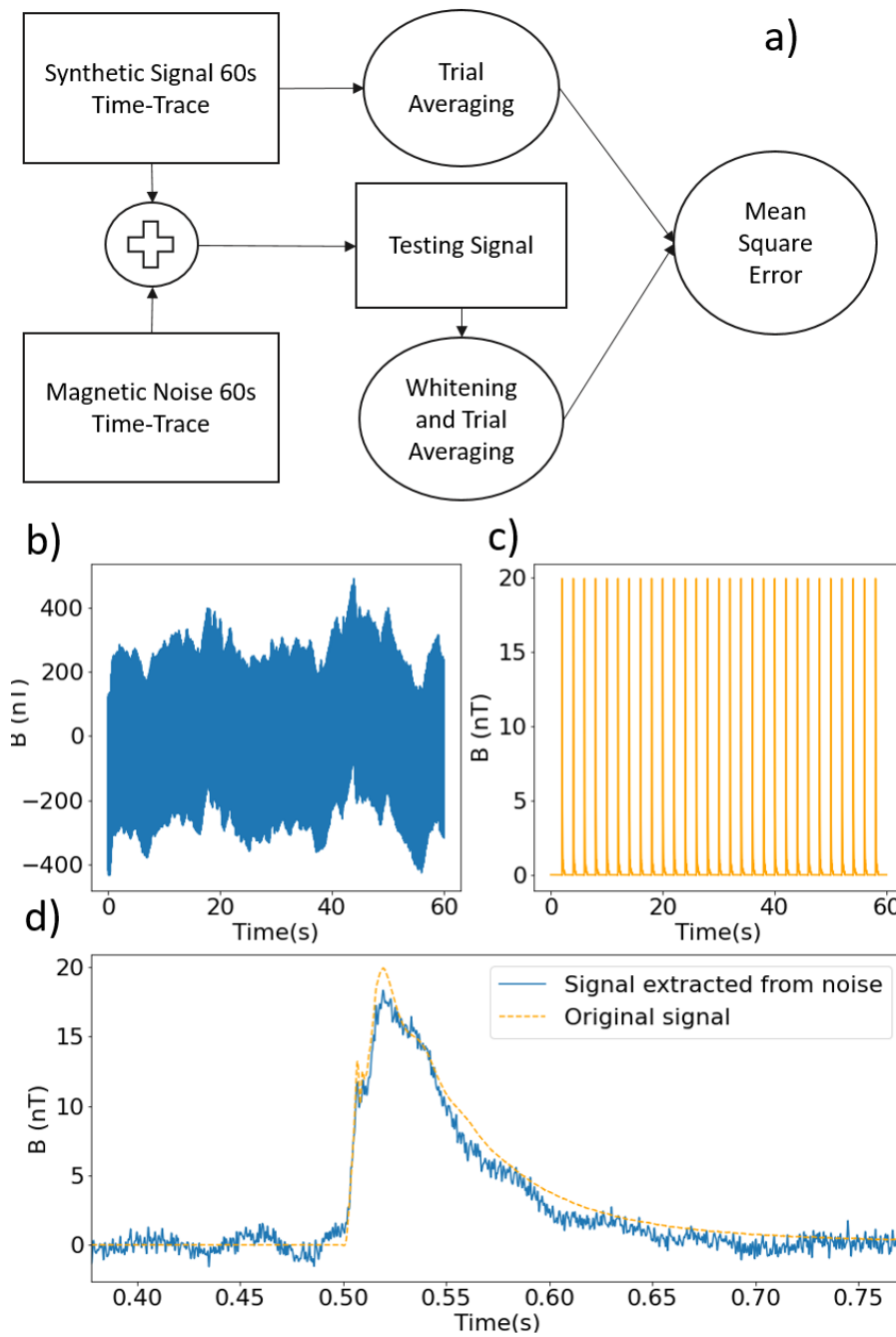
Here, that the SNR of the biosignal is $\ll 1$ presents a problem: we cannot from a single 60sec iteration timeseries determine the degree of corruption of the biosignal in the magnetic data. We cannot see the biosignal in a single timeseries, nor can we see the components of the signal in the frequency spectrum. These could be resolved by averaging over many 60sec iterations corresponding to thousands of stimulations. However, this would be extremely time consuming - the datasets are many tens of gigabytes and therefore too large to hold in PC memory, wherefore they would need to be reloaded from an external disk for each of the hundreds of iterations of the whitening parameters. Furthermore, using this mean power spectrum would not necessarily allow us to effectively filter out transient noise present in each 60sec iteration dataset, or cope with frequency and phase drift in the mains noise.

The solution we use here is to provide a test signal that has a higher SNR that puts the signal components above the white noise floor, but crucially still below the majority of the noise peaks. This can be done in two ways. The first is to generate a test signal (such as square pulses or a synthetic biosignal) in a field coil adjacent to the diamond NV sensor, recording this signal plus the background noise, then applying the filter to the magnetic data recorded from the sensor. The second, which we use in this work, is to separately record the electric data from a probe on the muscle, to scale this as a replica magnetic field signal of $\approx 1-20$ nT strength and then mix this signal with a recording of magnetic data which is purely the background noise (no muscle in the chamber). This process is outlined in Supplementary Figure 6.

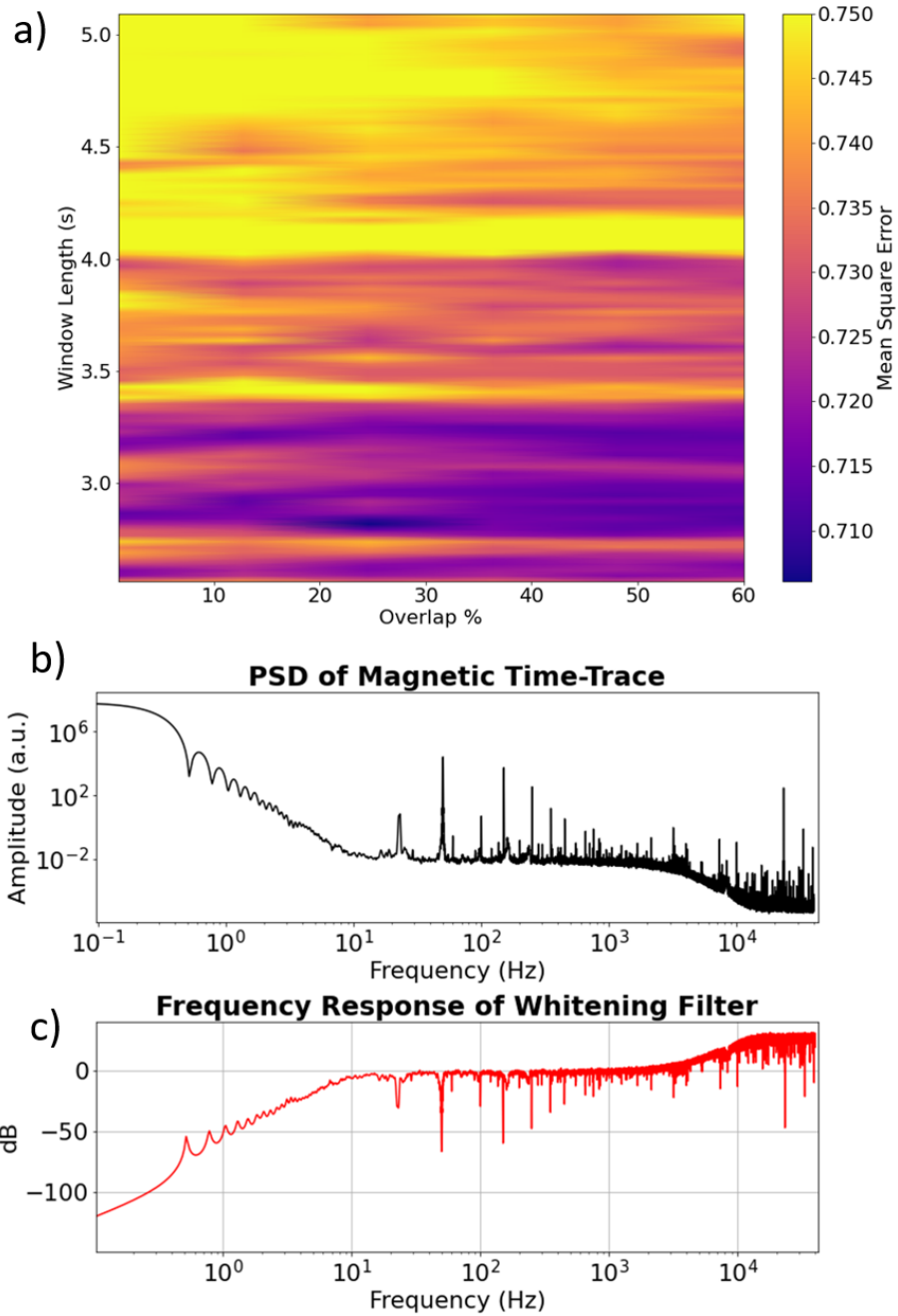
The parameters chosen for the optimization of the whitening filter were respectively the size and the number of overlapping points of the windows used to calculate the PSD with Welch's method. To optimize these parameters the following routine was implemented with the goal of minimizing the mean square error (MSE) between the filtered signal in the magnetic data and the replica test signal defined below:

1. A 60s time trace containing a train of measured electrical data from the electrode on the muscle was generated (Figure 6) and converted into a scaled equivalent magnetic field signal(c))
2. A 60s magnetic time trace containing only magnetic noise was measured (Figure 6(b))
3. The two time-traces from 1) and 2) were added together to create a composite signal.
4. The whitening filter was applied to the composite signal.
5. The whitened testing signal was divided into trials of 29 trials of 1s and the latter were averaged
6. The MSE was computed between the averaged trial obtained in 5) and the replica signal in 1) ((Figure 6(d))

Supplementary Figure 3, a) shows an example of the results obtained from the optimization routine. The MSE was minimized in the chosen parameter space by using with a window length of 2.8 s and 30% overlap. With these parameters it was possible to compute the PSD of the magnetic time traces Figure 7(b) and derive their corresponding whitening filter Figure 7(c).

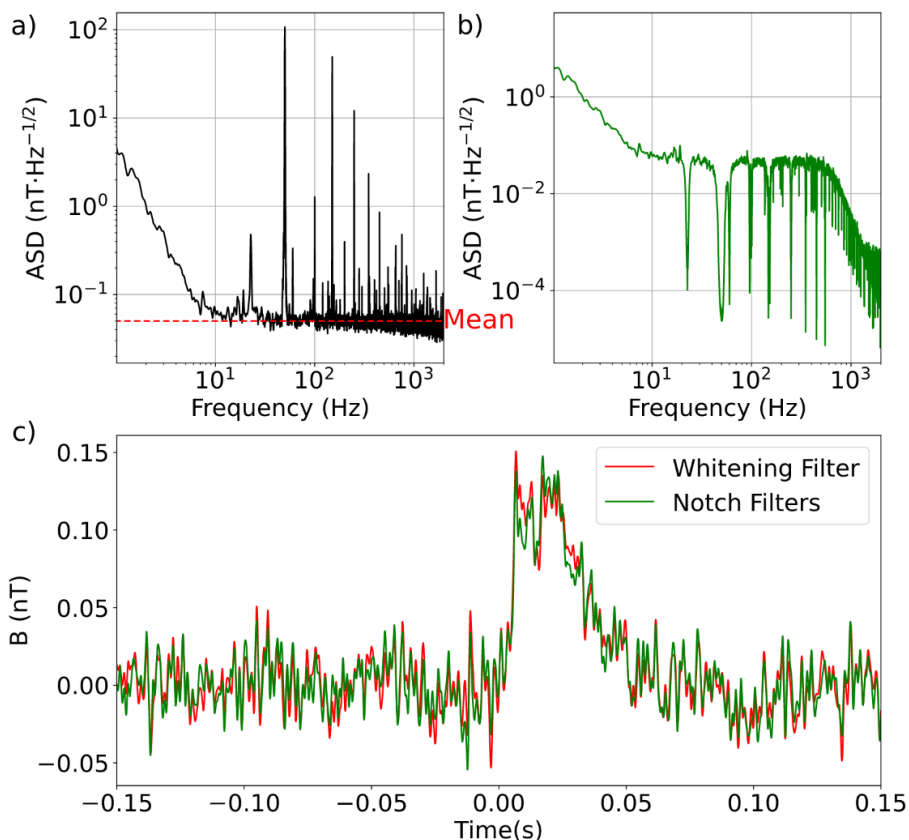


Supplementary Figure 6: a) Diagram illustrating the Whitening filter parameters optimization routine. b) Example of pure noise time-trace from magnetic readout c) Synthetic signal recreated from the measured electric data recorded from the response from the mouse muscle d) Comparison between original synthetic signal (orange) and signal extracted from noise with the whitening filter after averaging the trials.



Supplementary Figure 7: a) Results From the Whitening Filter Optimization a) Color map of the MSE with varying parameters b) Example of PSD calculated from the magnetic data with optimized parameters c) Whitening Filter frequency response derived from the PSD in b).

4 Whitening Unit Recovery



Supplementary Figure 8: a) Method for restoring units to the unitless whitened data by taking the PSD mean, assuming the PSD is relatively flat across the measurement bandwidth. b) The PSD from notch filtering, removing the majority of noise peaks while retaining the (Tesla) units. The equivalent for whitening is shown in the main text. c) Comparison of the magnetic data for Muscle 1 filtered using the whitening method and scaled by the method in a),b) and by using the notch method. Recovery of units could also be achieved by scaling the whitened signal to match the notch filtered signal in the time domain.

By performing the whitening filter procedure, we lose the real (Tesla) magnetic field units of the measurement, by effectively dividing the power spectra density by an approximated version of itself with the same units. To convert the whitened signal back into Tesla units with reasonable accuracy, as we do in the main text, we must use a recalibration factor. We can obtain this in two ways:

1. We can take the mean white noise floor of the unfiltered PSD over the measurement bandwidth, identifying and ignoring the major noise peaks above the floor (e.g. 50/150Hz). This is illustrated in Supplementary Figure 8. Here our chosen upper cutoff frequency is 650Hz and lower cutoff (to eliminate low frequency laser technical noise) was 20Hz. We can then multiply our unitless whitened filtered signal by this mean value to restore the magnetic field units. Although this procedure is relatively simple, it relies on the PSD being flat over the bandwidth and the correct identification of noise peaks above the white noise floor for masking.

For higher bandwidths, the former criteria is not met, due to the rolloff imposed by lock-in amplification.

2. We can perform the filtering using the slower notch method (detailed in our previous work, see citation in main text). This method retains the Tesla units in the filtered output signal. We can then scale in the time domain our unitless signal from the whitening process to the notch filtered signal to recover the units. This scaling could be done with either the raw filtered output data, by using the biosignal or by using a known test signal applied using a field coil to the diamond NV sensor.

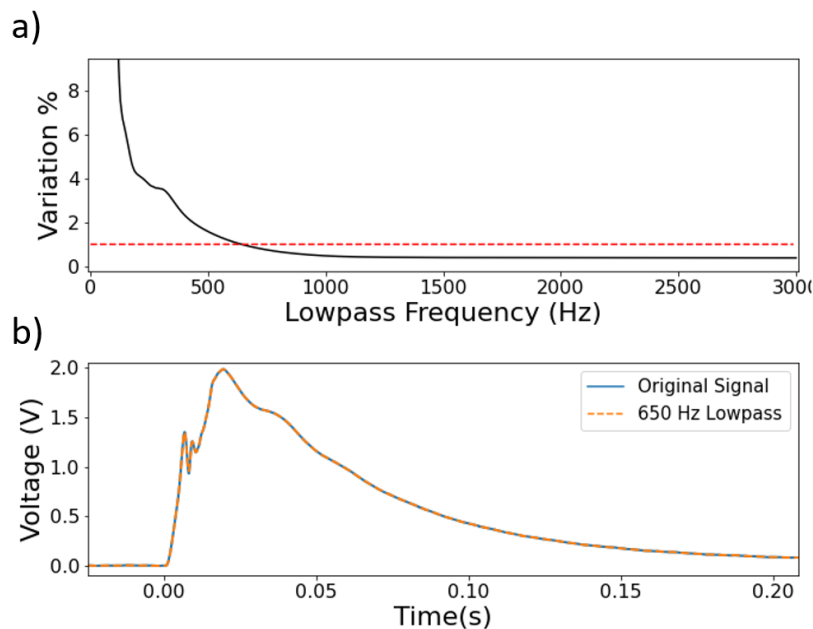
Supplementary Figure 8 shows a comparison of an example biosignal with the units recovered, filtered by both notch and whitening filtering, with good agreement between them. We note that using the notch method to recover the units effectively defeats the purpose of the whitening (faster, no need to identify manually every noise peak). However, we note that for most applications - especially in biosensing - only the shape and relative size of the signal matters and the absolute units for magnetic field may not be required. Such a relative signal can be obtained more simply and quickly by the whitening filter.

5 Determination of Low-Pass Filter Cutoff Frequency

To determine the low pass cutoff frequency for filtering the magnetic time traces, the averaged signal in the electric data recorded using the AgCl probe electrode was filtered using a 3rd order Butterworth filter with varying cutoff frequency, and the variation percentage between the original signal and the filtered signal was computed at each step (Figure 9(a)). The definition of percentage variation used was the following:

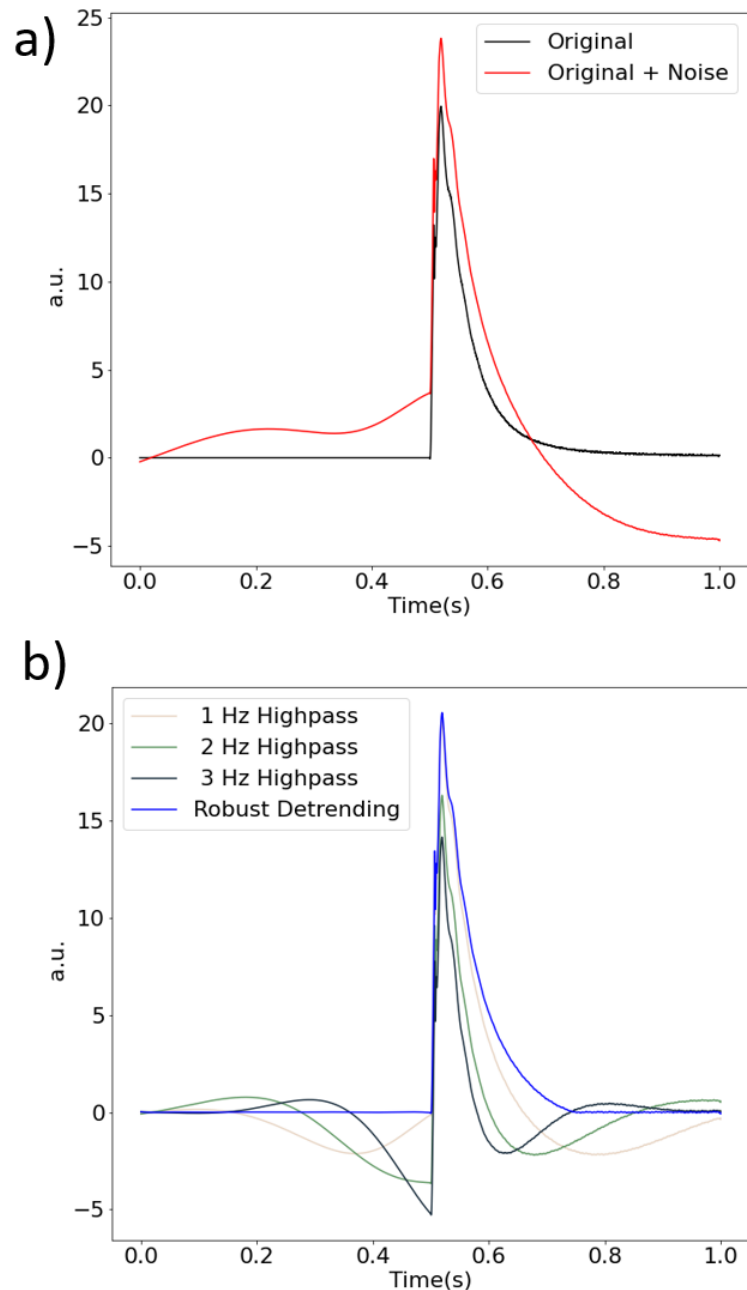
$$\text{Variation}\% = \frac{1}{N} \sum \frac{|x_i - x'_i|}{|x_i|} \quad (1)$$

where x and x' are respectively the original and the filtered signal. The threshold for the percentage variation was deliberately chosen to be at 1% at which there was no visible distortion of the biological signal (Figure 9(b)). The cutoff frequency for the low-pass filter corresponding to the chosen threshold was 650 Hz.



Supplementary Figure 9: a) Variation percentage between the filtered signal and the original signal with varying lowpass cutoff frequency, red dashed line indicated the chosen threshold at 1% . b) Comparison between the original electrical response and the filtered one.

6 Robust Detrending



Supplementary Figure 10: a) Measured electrophysiological response (black) and measured electrophysiological response with artificially added low frequency drift (red). 2) Comparison of robust detrending method and standard high-pass filtering with varying cutoff frequencies.

Robust detrending allows the removal of slow baseline drift while avoiding the distorting effects of high-pass filter artifacts. The presence of deflections before the stimulation that triggered the biological signal can easily lead to misinterpretation of the signal itself. In *detrending*, the drift is removed by fitting and subtracting a polynomial to the time trace. Unfortunately, detrending is still subject to artifacts due to the signal being present in the fitting process. This problem is readily solved with *robust detrending*: the portion of time-

trace containing the biological signal is masked before the polynomial is fit to the data. For demonstrational purposes, low frequency noise was added to the measured electrical response from the mouse muscle (Figure 10(a)) and removed both with standard Butterworth high-pass filtering and with robust detrending (Figure 10(b)). High-pass filtering with cutoff frequencies <1 Hz is not sufficient to completely eliminate the low frequency drift, while cutoff frequencies >1 Hz create deflection artifacts before the biological signal. In this case, to implement robust detrending, the time-trace was masked in the time interval between 0.5-0.8 s in which the biological signal is present. A high order polynomial (10th) was used to fit the remaining data points and subsequently subtracted from them. The results clearly shows that the biological signal obtained with robust detrending is free from deflection artifacts and highly resembles the original signal from Figure 10(a) .

7 Modeling

7.1 Ion Channels

The muscle action potential was simulated with the use of NEURON. The model parameters for this simulation was based on the models for mammalian skeletal muscles described in Cannon et al. (citation in main text). This was implemented as a simple version of the Hodgkin-Huxley model with the following ion currents:

$$I_{ion} = g_{Na}(V_m - E_{Na}) + g_K(V_m - E_K) + g_{leak}(V_m - E_{leak}) \quad (2)$$

where the sodium and potassium conductance is derived from their gating parameters m, n and h , which determine the amount of opened ion channels, such that:

$$g_{Na} = \bar{g}_{Na}m^3h \quad (3)$$

$$g_K = \bar{g}_Kn^4 \quad (4)$$

Where \bar{g}_{ion} is the maximum conductance of a particular ion channel. The gating parameters is calculated by solving the following set of differential equations:

$$\frac{dy}{dt} = \alpha_y \times (1 - y) - \beta_y \times y; y \in m, n, h \quad (5)$$

And:

$$\alpha_m = \frac{\bar{\alpha}_m(V_m - \bar{V}_m)}{1 - \exp(-\frac{V_m - \bar{V}_m}{K_{\alpha m}})}, \quad \beta_m = \bar{\beta}_m \exp(-\frac{V_m - \bar{V}_m}{K_{\beta m}}) \quad (6)$$

$$\alpha_h = \bar{\alpha}_h \exp(-\frac{V_m - \bar{V}_h}{K_{\alpha h}}), \quad \beta_h = \frac{\bar{\beta}_h}{1 + \exp(-\frac{V_m - \bar{V}_h}{K_{\beta h}})} \quad (7)$$

$$\alpha_n = \frac{\bar{\alpha}_n(V_m - \bar{V}_n)}{1 - \exp(-\frac{V_m - \bar{V}_n}{K_{\alpha n}})}, \quad \beta_n = \bar{\beta}_n \exp(-\frac{V_m - \bar{V}_n}{K_{\beta n}}) \quad (8)$$

The final ion channel term, the leak conductance, is a steady state variable, and thus the conductance is constant set to $0.75\text{mS}/\text{cm}^2$.

We also added a current due to the presence of the T-tubuli in the sarcolemma (I_t), reflecting that the membrane potential of the sarcoplasmic surface may be different than the membrane potential inside the T-tubuli. Given an extracellular resistance of R_a , and with the membrane

potential of the T-tubule denoted as V_t , then the current contribution from the T-tubuli are:

$$I_t = \frac{V_m - V_t}{R_a} \quad (9)$$

V_t is calculated using the same Hodgkin-Huxley model as for the sarcolemma, however, since the ion channel densities of the T-tubuli are lower, each of these have to be scaled with a corresponding ratio η_{ion} , i.e. the ratio of ion channel density in the tubular space to the ion channel density in the sarcoplasmic regions.

$$I_{t,ion} = \eta_{Na}g_{Na}(V_t - E_{Na}) + \eta_Kg_K(V_t - E_K) + \eta_{leak}g_{leak}(V_t - E_{leak}) \quad (10)$$

| $Cm(\mu F/cm^2)$ | $R_s(\Omega cm)$ | $R_a(\Omega cm^2)$ | $\bar{g}_{Na}(mS/cm^2)$ | $\bar{g}_K(mS/cm^2)$ | $g_l(mS/cm^2)$ |
|---------------------------|---------------------------|---------------------------|--------------------------|--------------------------|--------------------------|
| 1 | 125 | 250 | 150 | 21.6 | 0.75 |
| $\bar{\alpha}_m(ms^{-1})$ | $\bar{\alpha}_h(ms^{-1})$ | $\bar{\alpha}_n(ms^{-1})$ | $\bar{\beta}_m(ms^{-1})$ | $\bar{\beta}_h(ms^{-1})$ | $\bar{\beta}_n(ms^{-1})$ |
| 0.288 | 0.0081 | 0.0131 | 1.38 | 4.38 | 0.067 |
| $K_{\alpha m}(mV)$ | $K_{\beta m}(mV)$ | $K_{\alpha h}(mV)$ | $K_{\beta h}(mV)$ | $K_{\alpha n}(mV)$ | $K_{\beta n}(mV)$ |
| 10 | 18 | 14.7 | 9 | 7 | 40 |
| $\bar{V}_m(mV)$ | $\bar{V}_h(mV)$ | $\bar{V}_n(mV)$ | η_{Na} | η_K | η_{leak} |
| -46 | -45 | -40 | 0.1 | 0.4 | 0.5 |

Table 1: Model parameters for the muscle fibre channel dynamics

7.2 Channelrhodopsin 2 model

Here we outline the implemented channelrhodopsin 2 four-state model (ChR2) based on the works by Grossman et al. and Nikolic et al. (citation in main text)

If O_1 , O_2 , C_1 , and C_2 are the fraction of ChR2 molecules in a cell section which is in the fast open, slow open, fast closed, and slow closed state respectively, then the instantaneous rate of change of these states can be defined by a set of rate equations:

$$\frac{dO_1}{dt} = K_{a1}C_1 - (K_{d1} + e_{12})O_1 + e_{21}O_2 \quad (11)$$

$$\frac{dO_2}{dt} = K_{a2}C_2 + e_{12}O_1 - (K_{d2} + e_{21})O_2 \quad (12)$$

$$\frac{dC_2}{dt} = K_{d2}O_2 - (K_{a2} + K_r)C_2 \quad (13)$$

$$C_1 + C_2 + O_1 + O_2 = 1 \quad (14)$$

Here e_{12} and e_{21} are the transition rates between O_1 and O_2 , from $1 \rightarrow 2$ and $2 \rightarrow 1$ respectively. These two parameters depend on light illumination and attains different values e_{ij}^{Light} and e_{ij}^{Dark} depending on whether light is on or not. The rate constants K_{d1} and K_{d2} are the closing rates from the open to the closed state of the fast and slow opened state respectively while K_r is the transition rate between the closed slow state and the closed open state.

Finally, K_{a1} and K_{a2} are the transition rates from the closed to the open states, they depend on the light illumination according to the following equations:

$$K_{ai} = \begin{cases} \varepsilon_i \varphi (1 - e^{-(t-t_{ON})/\tau}), & \text{Light ON} \\ \varepsilon_i \varphi_0 (e^{-(t-t_{OFF})/\tau} - e^{-(t-t_{ON})/\tau}), & \text{Light OFF} \end{cases} \quad (15)$$

where ε is the quantum efficiency of channelrhodopsin, φ is the photon flux per area, τ is the time constant of channel. The stimulating current when the light is on is then calculated as:

$$I_{ChR2} = I_{Max}(O_1 + \gamma O_2) \quad (16)$$

with γ the ratio between the conductivities of the O_2 and O_1 states ($\gamma = g_2/g_1$), and I_{Max} the maximum stimulation current. I_{Max} is calculated for the case of when all ChR2 are in the O_1 state, thus allowing maximum current:

$$I_{max} = (V - E_{ChR2})g_{Max,ChR2} \quad (17)$$

where E_{ChR2} is the reversal potential (set to 0 mV) and g_{ChR2} is the channel conductance per area ($g_{Max,ChR2} = g_1 \rho_{ChR2}$), where ρ_{ChR2} is the density of the channelrhodopsin in the membrane. The parameters for the laser model can be seen in Table 2.

7.3 Light model

To obtain an accurate model of the experimental data, it is necessary to also know the light distribution in the muscle tissue. One common method of fitting light propagating in biological tissue, which was used in the present study, is the Kubelka-Munk (KM) model for diffuse scattering media. It is a method that provides a relatively simple analytical expression for the irradiance at all points in the tissue (see Fig. 2b in the main text). It should however be noted that this is an approximation, as the KM model assumes isotropic scattering and isotropic illumination.

The irradiance at a point in the tissue can be expressed in cylindrical coordinates, as (see Foutz et al. 10.1152/jn.00501.2011):

$$I(r, z) = I_0 G(r, z) C(z) M(r, z) \quad (18)$$

where I_0 is the irradiance of the light source, G is the Gaussian distribution of the emitted light, C is the spreading of unfocused light, and M describes the lights scattering and absorption behavior. The Gaussian distribution (G) can be calculated as:

$$G(r,z) = \frac{1}{\sqrt{2\pi}} \exp[-2(\frac{r}{R(z)})^2] \quad (19)$$

Where the $R(z)$ is the radius of the light cone at depth of z starting from R_0 emission. The spread function (C) is:

$$C(z) = \frac{R_0}{R(z)} \quad (20)$$

And the spreading (M) can be calculated by:

$$M(r,z) = \frac{b}{a \sinh(b\mu_s \sqrt{r^2 + z^2}) + b \cosh(b\mu_s \sqrt{r^2 + z^2})} \quad (21)$$

with a and b being respectively:

$$a = 1 + \frac{\mu_a}{\mu_s} \text{ and } b = \sqrt{a^2 - 1} \quad (22)$$

where μ_s is the scatter coefficient per unit thickness (in $[\text{mm}^{-1}]$), and μ_a is the absorption coefficient per unit thickness (in $[\text{mm}^{-1}]$).

Laser light, in contrast to light from an LED, is collimated around a given direction of propagation, and over the distances investigated in the present experimental setup, we approximated this as completely collimated, focused beam ($C=1$). The irradiance at all segments in the muscle fiber model was calculated using the above equations with Python.

| | Description | Value Laser Model |
|---|--------------------------------|----------------------|
| <i>Channelrhodopsin-2 properties</i> | | |
| $K_{d1}(s^{-1})$ | Decay Rate | 117 |
| $K_{d2}(s^{-1})$ | Decay Rate | 36 |
| $e_{12}(s^{-1})$ | Transition rate: light | 265 |
| | Transition rate: dark | 265 |
| $e_{21}(s^{-1})$ | Transition rate: light | 46 |
| | Transition rate: dark | 23 |
| $K_r(s^{-1})$ | Recovery rate | 0.4 |
| $g_1(\text{fS})$ | O1 state conductivity | 50 |
| $g_2(\text{fS})$ | O2 state conductivity | 25 |
| $\sigma_{ret}(\mu\text{m}^{-2})$ | Retinal cross section | 1.2×10^{-8} |
| ϵ_1 | Quantum efficiency | 0.5 |
| ϵ_2 | Quantum efficiency | 0.1 |
| $\tau(\text{ms})$ | ChR2 time constant | 6.5 |
| $\rho_{ChR2^*}(\mu\text{m}^{-2})$ | ChR2 density | 200 |
| <i>Fiber optic-Tissue Properties</i> (Aravanis et al., 2007) | | |
| $\mu_a(\text{mm}^{-1})$ | Absorbance coefficient, Muscle | 0.45 |
| $\mu_s(\text{mm}^{-1})$ | Scattering coefficient, Muscle | 2.9 |
| η_{tissue} | Muscle index of refraction | 1.41 |

Table 2: LED and laser stimulation model parameters

7.4 Muscle Geometry

The geometry of the muscle was approximated as a bundle of close-packed fibers in a circular geometry (see Fig. 2a in the main text). The radius of the entire muscle was set to $845 \mu\text{m}$, as estimated from the smallest radius seen in Fig. 2b in the main text, and the radius of an individual fiber was set to a uniform distribution of $22.5 \pm 3.5 \mu\text{m}$, as the most common fiber types in an EDL mouse muscle. The position and diameter of an individual fiber, as simulated by NEURON, was then set according to this geometry. The simulated laser spot was positioned at one end of the muscle, such that the full width of the laser spot ($500 \mu\text{m}$ in diameter) hit the top center side of the muscle. The LFP was recorded from a simulated electrode 2.5 mm from the laser center spot, at a 70° angle from the diamond plane. The diamond was placed below the muscle, 1 mm from the laser spot center, as estimated from Fig. 3b in the main text.

7.5 Extracellular Field Calculations

The LFP was calculated based on the membrane and axial currents provided from the NEURON simulation. This calculation was performed using the python package LFPy. These were calculated for each fiber individually, and then superimposed for the total LFP signal. Similarly, the magnetic field signal was calculated by dividing the $2 \times 2 \text{ mm}$ diamond into a 20×20 grid, and the magnetic field strength from each fiber was superimposed to each grid position. For a fiber divided into N segments of length Δs_n , the magnetic field from that fiber at a radial distance r_n from the segment center can be calculated as:

$$B(r, t) = \frac{\mu_0}{4\pi} \sum_{n=1}^N \frac{I_{ax}^n(t) \times r_n}{r_n} \left[\frac{h_n}{\sqrt{h_n^2 + r_n^2}} - \frac{l_n}{\sqrt{l_n^2 + r_n^2}} \right] \quad (23)$$

where the axial current in segment n , I_{ax}^n , can be calculated from the membrane potential (V_m), and the intracellular resistivity, R_a , as $I_{ax}^n(t) = \frac{V_m^n - V_m^{n-1}}{\Delta s_n R_a}$. Further, h_n is the longitudinal distance from the segment end and $l_n = h_n + \Delta s_n$ is the longitudinal distance from the beginning of the segment (see cited work in the main text by Karadas et al. for more detail).

The magnetic field strength in a nerve bundle exhibit cancellation effects, which results in a scaling factor of the magnetic field. This was implemented by scaling the magnetic field strength by a factor of $s(d) = 0.25 + \frac{42.6}{d+52}$.

7.6 Model Alterations

As explained in the main text, when increasing the stimulating irradiance on a muscle by several hundreds of times compared to that of previous experiments, the signal produces a secondary peak which is on the same order of magnitude as the AP and which also extends for about 100ms. At a first attempt, we modeled this behavior by implementing a model presented by Nikolic et al. and Grossman et al. However, this failed to reproduce a sufficiently strong secondary peak, as

experimentally obtained. The model was originally created for modeling neuronal dynamics using light intensities in the order of magnitude similar to that of an LED source, and thus has not been optimized for the present experimental purpose. This discrepancy is most likely due to the fact that several (unknown) parameters change with the irradiance level. Nikolic et al. and Grossman et al. explored the intensity dependencies of several parameters in their studies, and Nikolic provides a function for how e_{12} and e_{21} depend on the light flux:

$$e_{12}(\varphi) = e_{12,dark} + c_1 \log(1 + \varphi/\varphi_0) \quad (24)$$

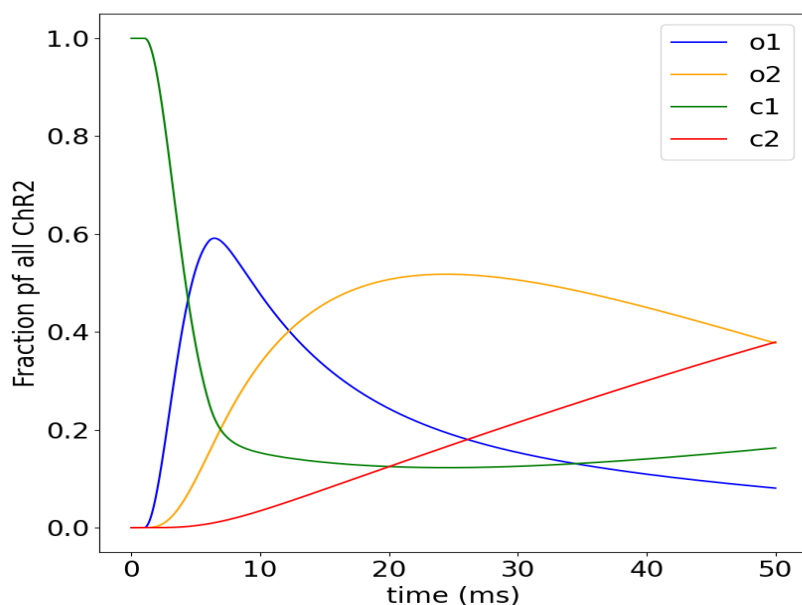
Where c_1 and φ_0 are constants, and φ is the light flux. In the present model, this light dependency function was however insufficient to reproduce the large secondary peak. Although Eq. (??) may introduce a more direct transition to the O2 state, it cannot change the magnitude of the O2 current. To accommodate the much stronger intensity of our laser experiment, we had to additionally include a higher conductivity to the O2 state than what has been previously reported.

To summarize, in the present study, we have used the four-state model, with certain parameter modifications (see section on Channelrhodopsin-2 modeling above and Table 2), and separately modified the parameters of the four-state model to fit for the much stronger intensity case of the laser experiment. The parameters in either of these models are independent on the intensity. The dependency of the different important ChR2 parameters on light intensity in this scenario should in future studies be investigated further with more extensive experimental support. These separate models should thus only be seen as a qualitative fit of the experimental curves, and not as predictive models.

7.7 Model sensitivity

In this section we investigate briefly how the presented model behaves at different situations to examine how sensitive the resulting detected LFP signal is to different factors, such as the position of the recording electrode. In Supplementary Figure 12 we see that by moving the electrode closer to the stimulation site, the secondary peak becomes stronger in comparison to the first peak. This is expected, since the first peak originates from the current flows from the action potential which propagates throughout the whole muscle, whereas the secondary peak originates from saltatory conduction due to the prolonged opening of the ChR2 molecules, which strength is directly proportional to the distance from the stimulation site. The first peak also decreases in peak strength as one records further away from the stimulation site, but this is due to that the AP:s closer to the stimulation site are more synchronized, and drift apart across the muscle due to differences in conduction velocities.

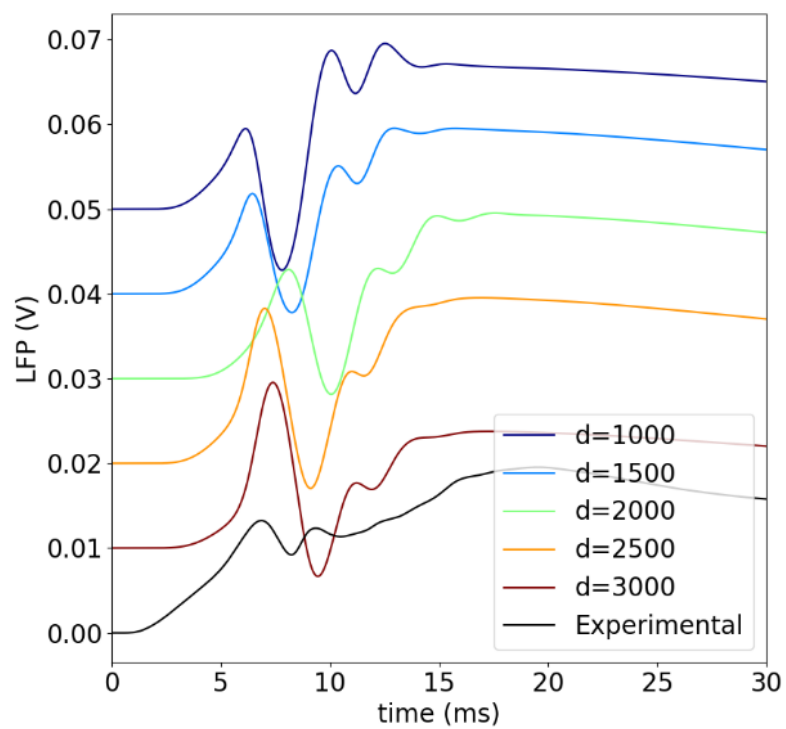
We also investigated how the present model behaved with respect to stimulations from different laser powers (see Supplementary Figure 13). By decreasing the laser power from the experimentally used one (50mW), the first peak in the LFP shifts to longer delay times. This



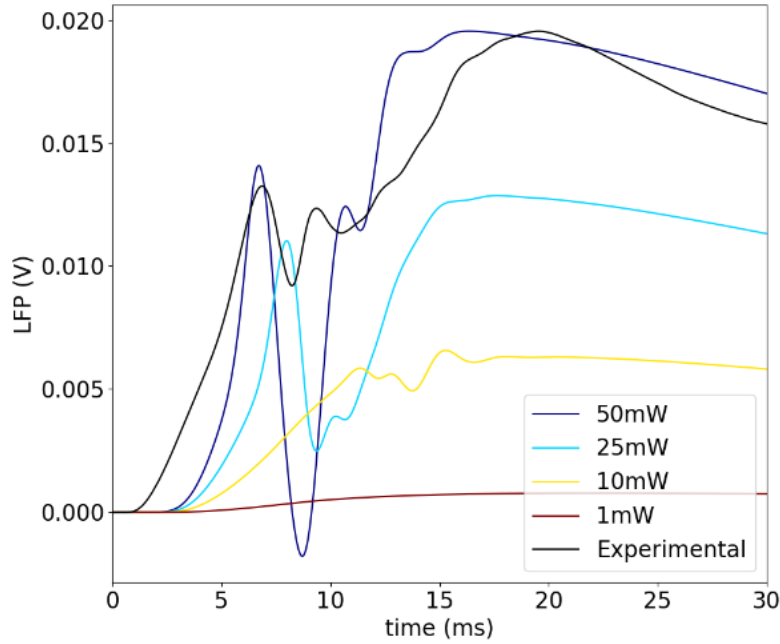
Supplementary Figure 11: Fraction of ChR2 molecules in a segment in the different states (O1, O2, C1, and C2) over time. Stimulation occurs after 1ms.

is expected, as the number of opened ChR2 molecules, and thus the stimulating current, is proportional to the irradiance. The lower intensity furthermore mean that there are fewer fibers activated, and thus the action potential signal (first peak) decreases.

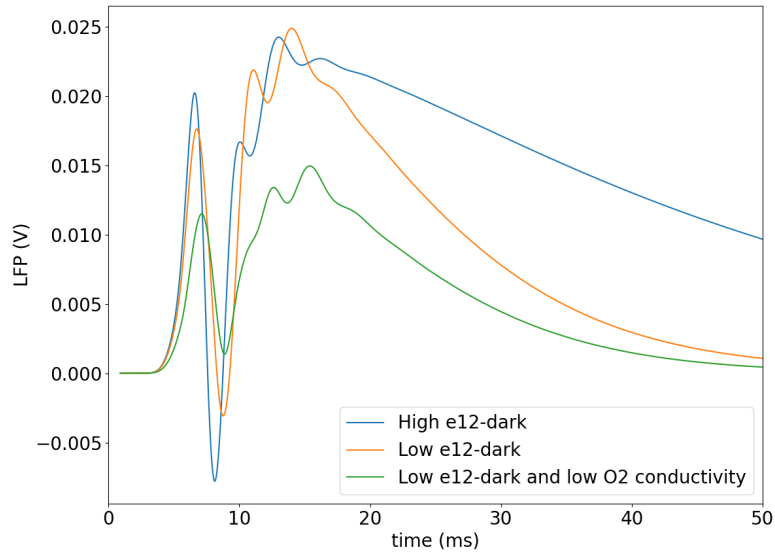
Finally, we show in Supplementary Figure 14 how the current changes due to differing transition rate parameters of e_{12} and e_{21} , and due to alternating O2-conductivity. As can be seen from the figure, the secondary peak decreases with both decreasing e_{21} -dark rate, and with decreasing O2-conductivity.



Supplementary Figure 12: Simulated and experimentally obtained LFP signals as recorded at different distances (d) from the center of the laser stimulation point.



Supplementary Figure 13: LFP at different laser powers, with the same spot size of 50m. The 50mW signal is scaled such that its maximum equals the experimental maximum, and the other signals are scaled with that same scaling factor to show how the total signal decreases with decreasing laser power.



Supplementary Figure 14: LFP vs time for different values of transition parameters to qualitatively highlight their effect. “High e12 dark” corresponds to e_{12} and $e_{12}^{Dark}=265$, $e_{21}=46$. and $e_{21}^{Dark}=23$. “Low e12 dark” corresponds to e_{12} and $e_{12}^{Dark}=2.65$, $e_{21}=46$. and $e_{21}^{Dark}=23$. “Low e12-dark and low O2 conductivity” corresponds to the same values for the transition rates e_{ij} and e_{ij}^{Dark} as “Low e12 dark” while the conductivity of the O2 state was lowered from 25fS to 2.5fS.

Chapter 8

High speed microcircuit and synthetic biosignal widefield imaging using nitrogen vacancies in diamond

8.1 Introduction

For applications ranging from microscopic electronic circuit inspection to sensing of biological signals, the ability to image electrical currents with high spatial and temporal resolution without damaging the sample is essential. Nano-scale resolution of electrical signals with bandwidth up to the kHz range can be accomplished by utilizing NV centers in diamond, which can operate as a high density array of separate sensors. In the following section, imaging of electrical currents in a lithographically patterned circuit using a camera with integrated lock-in amplifier is demonstrated. The current-induced magnetic fields generated both from a 130 Hz alternated current and from a synthetic signal that replicates the shape of dendritic currents (Inhibitory Postsynaptic Potentials, IPSP) in a mouse hippocampus are spatially resolved as a function of time with a frame rate up to 3500 FPS. Although the sensor used in this study is not sensitive enough to spatially resolve real biological signals, the given methodologies, in combination with enhanced pulsed laser protocols and optimized diamond material, could be a useful tool for mapping neural pathways.

8.2 Publication

This manuscript was submitted to Applied Physics Reviews with the title of “High speed microcircuit and synthetic biosignal widefield imaging using nitrogen vacancies in diamond” as follows:

High speed microcircuit and synthetic biosignal widefield imaging using nitrogen vacancies in diamond

James L. Webb,^{1,*} Luca Troise,¹ Nikolaj W. Hansen,² Louise F. Frellsen,¹
Christian Osterkamp,³ Fedor Jelezko,³ Steffen Jankuhn,⁴ Jan Meijer,⁴ Kirstine
Berg-Sørensen,⁵ Jean-François Perrier,² Alexander Huck,^{1,†} and Ulrik Lund Andersen^{1,‡}

¹*Center for Macroscopic Quantum States (bigQ), Department of Physics,
Technical University of Denmark, 2800 Kgs. Lyngby, Denmark*

²*Department of Neuroscience, Copenhagen University, 2200 Copenhagen, Denmark*

³*Institute for Quantum Optics and Center for Integrated Quantum Science and Technology (IQST),
Ulm University, Albert-Einstein-Allee 11, 89081, Ulm, Germany.*

⁴*Division Applied Quantum System, Felix Bloch Institute for Solid State Physics, Leipzig University, 04103, Leipzig, Germany*

⁵*Department of Health Technology, Technical University of Denmark, 2800 Kgs. Lyngby, Denmark*

(Dated: July 30, 2021)

The ability to measure the passage of electrical current with high spatial and temporal resolution is vital for applications ranging from inspection of microscopic electronic circuits to biosensing. Being able to image such signals passively and remotely at the same time is of high importance, to measure without invasive disruption of the system under study or the signal itself. A new approach to achieve this utilises point defects in solid state materials, in particular nitrogen vacancy (NV) centres in diamond. Acting as a high density array of independent sensors, addressable opto-electronically and highly sensitive to factors including temperature and magnetic field, these are ideally suited to microscopic widefield imaging. In this work we demonstrate such imaging of signals from a microscopic lithographically patterned circuit at the micrometer scale. Using a new type of lock-in amplifier camera, we demonstrate sub-millisecond (up to 3500 frames-per-second) spatially resolved recovery of AC and pulsed electrical current signals, without aliasing or undersampling. Finally, we demonstrate as a proof of principle the recovery of synthetic signals replicating the exact form of signals in a biological neural network: the hippocampus of a mouse.

I. INTRODUCTION

Microscopic electrical transport underpins both synthetic systems such as integrated circuits as well as biological processes including the functioning of the human brain and nervous system. Operating at high speed and relying on transport down to single electronic charges, these systems require advanced inspection tools, in order to monitor transport performance and diagnose fault. In the case of a synthetic circuit, faults arising from factors including poor insulation and electromigration [1] can reduce device lifetime, requiring intervention before failure. Equivalently in a biological system, faults at the microscopic level arising from disease (e.g. Alzheimer's) can have serious consequences if left undetected.

Key to microscopic inspection are techniques capable of spatially and temporally resolving electrical transport in both synthetic or biological systems. Presently, this is difficult to achieve noninvasively without causing damage to the circuit or surrounding packaging - a factor especially important for biological tissue. Existing methods for integrated circuit inspection such as laser voltage probing [2], electron microscopy [3], THz spectroscopy[4] and electrophysiology probes[5] or fluorescence microscopy [6] for biosystems require unimpeded

local access. Furthermore, these existing techniques are all active, requiring direct interaction with the target system. This active sensing has the potential to interfere with the target signal or at worst induce damage in the system under study.

What is desirable is an inspection tool that is passive, remote and noninvasive. In recent years, a new technique has emerged for this purpose utilising point defects in solid state materials. Located in a solid material at a distance from the signal source under study, these can act as atomic scale (quantum) sensors to remotely and passively probe factors including electric field[7], temperature[8], pressure/strain[9], motion [10, 11] and in particular magnetic field[12–14]. State of the art measurements are based on negative charged nitrogen-vacancy centres (NVs) in diamond [15]. Consisting of a substitutional nitrogen dopant paired with a lattice vacancy, these defects have an energy level structure highly sensitive to environmental factors. Sensing using NV centres can be performed by monitoring fluorescence output of a single or NV ensemble in a diamond under green laser and microwave irradiation via optically detected magnetic resonance (ODMR) spectroscopy [16, 17]. Acting as a high density array of independent sensors, NVs are ideally suited for widefield imaging using fluorescence emission, particularly imaging of magnetic field arising from electrical circuits[18, 19], electronic transport in graphene[20, 21], ferromagnetic geological samples[22] and in biological systems[23–25].

A particular goal of widefield NV sensing is to image

* jaluwe@fysik.dtu.dk

† alexander.huck.dtu.dk

‡ ulrik.andersen@fysik.dtu.dk

and record the passage of signals in a living biological neural network [26]. A realisation of this idea would give key new physiological insight. However, state of the art imaging with NV centres suffers from two disadvantages. The first is that the level of per-pixel sensitivity is as yet insufficient to resolve the picotesla-level signals from neurons[27]. This is compounded by limitations in field-of-view as well as artifacts and background noise [28]. The second is that limitations in measurement methods, in particular low camera frame rates, prohibit the temporal resolution of the desired signals. Imaging has therefore been limited to slow or static measurements (of e.g. temperature [19, 29] or DC magnetic field from ferromagnetic materials[30–32]) or relying on signal aliasing [33], unsuitable for accurate time resolved signal recovery.

In this work, we address the second of these limitations. We use a novel type of lock-in amplifier camera (Helicam, Heliotis AG [34–36]), imaging NV centres in diamond to spatially resolve the absolute magnitude of the magnetic field induced by current flow in a lithographically patterned microcircuit. We demonstrate the viability of our technique to map current flow in the circuit with a wide field of view (mm scale) and micrometer-level resolution, limited only by choice of microscope objective. We show this can be done with a simple constant laser and microwave (continuous wave) method and non-uniform laser illumination of the diamond at Brewster’s angle. This optical coupling method allows us to maximise coupling of laser pump light into the diamond, key to increasing overall fluorescence emission and hence improving overall sensitivity. We demonstrate imaging of AC current signals of frequencies up to 1.5kHz and recover pulsed signals replicating digital and analog signals in integrated circuits with sub-millisecond resolution. This is significantly faster than current state of the art experiments in the field. We demonstrate signal recovery above the noise floor at the single pixel level, using image regions of the diamond both directly adjacent to and well away from the patterned wire. Finally, we generate and demonstrate the detection of a signal precisely replicating the shape of current signals (field excitatory postsynaptic potentials, fEPSPs) as measured from the hippocampus in the living brain of a mouse, as a proof of principle demonstration towards biological neural network imaging.

II. METHODS

A simplified schematic of our setup is shown in Figure 1. We use a 2x2mm electronic grade diamond (Element 6) with a top 1 μ m CVD overgrown layer with approximately 99.99% ^{12}C and 10ppm ^{15}N doping. The diamond was irradiated with He^+ at 1.8MeV with a dose of 10^{15} cm^{-2} , followed by annealing at 900°C. We measured the NV concentration to be in the range 0.1-1ppm. The fluorescence emission of this diamond, measured using a photodiode power meter (Thorlabs S120C) in place of the

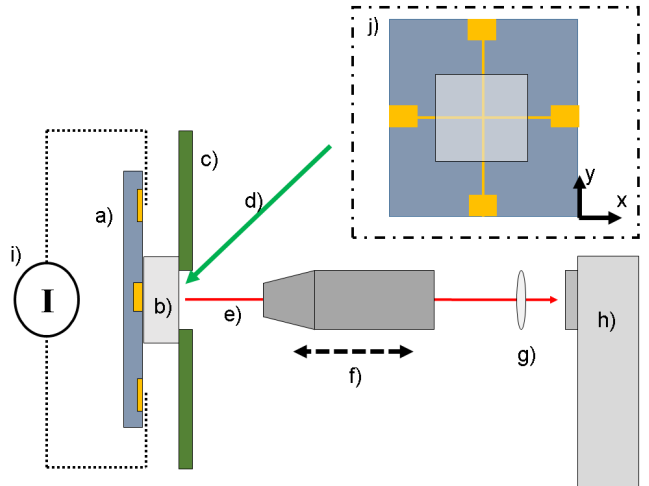


FIG. 1. Simplified schematic of the experimental setup (not to scale). The lithographically patterned circuit cross on a Si or glass substrate (a) is placed adjacent to the diamond (b) and affixed using either acrylic glue or a 3D printed plastic holder. The diamond and circuit is then affixed to a PCB microwave antenna (c) with a hole to allow pump laser (d) to reach the diamond at Brewster’s angle and fluorescence collection (e) via a translatable microscope objective (f). The fluorescence is focused (g) into the lock-in camera (h) to produce an image of the circuit. Current is applied through the circuit (h) using soldered contacts to the circuit chip. The view from the perspective of the camera is detailed in (j), with the diamond on the centre of the cross tracks.

camera was measured to be $152\mu\text{W}$ under 1.8W of green pump laser power, a relatively low level as compared to state of the art schemes[37].

We fabricated the circuit on either Si or glass substrate, patterned using ultraviolet mask aligned photolithography and metallised by deposition of Ti/Au. Track widths were $10\mu\text{m}$, decreasing to $5\mu\text{m}$ in a $15\times 15\mu\text{m}$ square region at the centre of the cross. We mounted the diamond and circuit on a printed circuit board (PCB) microwave antenna with a hole through which laser light could be directed into the diamond, which was mounted directly onto the PCB using Kapton tape. We mounted the diamond with the NV centre layer at the surface adjacent to that where we attached the circuit, using a small amount of acrylic glue or a 3D printed plastic holder.

Up to 1.8W of green pump light could be supplied to the diamond at Brewster’s angle using a diode pumped solid state laser (Cobolt Samba). Light was directed to the diamond via a focusing lens (Thorlabs LB1676), defocused slightly in order to achieve more uniform illumination across a large part of the diamond. Fluorescence collection was achieved using a 10x microscope objective (Nikon) placed approximately 10mm from the diamond NV layer and mounted on a micrometer translation stage ($\pm 5\text{mm}$ travel) to achieve focus control, with a second coarse adjustment stage to control lateral optical alignment and a screw post for vertical alignment. Light col-

lected by the objective was passed through a long wavelength pass filter (Thorlabs FELH0600) mounted in a beamtube to remove the 532nm pump laser light, leaving only the emitted diamond fluorescence. A second lens (Thorlabs) placed 20cm behind the objective focused this light into the aperture of the camera.

For fluorescence detection we used a lock-in amplifier camera (Heliotis Helicam C3), running at a rate of up to 3500 frames per second (fps). Although heatsunk to the optical table and capable of 3800fps, we ran the camera at a reduced framerate due to concerns regarding overheating during long period acquisitions. The camera produced a trigger signal which was supplied to a microwave generator (Stanford SG380). This was used to frequency modulate microwaves (at ± 4 MHz) which were then delivered to the PCB antenna and diamond via a microwave amplifier (Minicircuits ZHL-16W-43+). When on NV microwave resonance, this modulation produced the same frequency modulation of the fluorescence light emitted by the NV centres. This could be detected and demodulated by the camera, following the same basic principle as a standard lock-in detection measurement for each camera pixel, allowing significant rejection of noise, particularly pump laser DC and low frequency technical noise. Our field of view projected onto the 300x300 pixel sensor area (292x280 useable) with a 10x objective was approximately 450x450 μ m. Magnification could be increased if required by the simple replacement of the microscope objective and eyepiece lens.

To maximise sensitivity, we required the maximum change in measured pixel value p_v recorded by the camera. Here we define p_v as the amplitude derived from the in-phase(I) and quadrature (Q) camera-digitised values for each pixel, with a value ranging from 0-1024 (10 bits). Maximum change in p_v could be obtained by measuring at a single microwave frequency f on the point of greatest slope dp_v/df in the ODMR spectrum. To identify this frequency of maximum sensitivity and to enable conversion back into real (Tesla) units of magnetic field, we performed a reference ODMR spectrum. Here we swept microwave frequency $f=2700$ -3100MHz, simultaneously imaging using the camera in lock-in mode while adjusting a static magnetic field to split the resonances along the 4 NV crystallographic axes. This field was applied using a 1-inch square neodymium permanent magnet behind the diamond circuit assembly, with the majority of field out of the circuit plane. We then selected the resonance with the maximum resonance frequency shift produced by the static offset field. Magnetic field imaging was then performed in this resonance, at the microwave frequency f_{max} delivering the maximum ODMR slope (dp_v/df) averaged over all image pixels. To precisely identify the point of maximum sensitivity, we then performed a high frequency resolution ODMR reference centred on microwave frequency $f_{max} \pm 0.5$ -2MHz.

This procedure allowed us to either recover the full ODMR for all NV resonances (a time consuming process) or to more simply determine the ODMR slope for each

pixel for a single NV axis just at the microwave frequency giving the maximum magnetic field response. Knowing this slope for a given single NV axis allowed recovery of the magnetic field in Tesla units using the conversion factor $df/dB=28$ Hz/nT [38].

Measurements were performed at different modulation frequencies (2.5KHz to 14kHz) and frame rates (650-3500fps). For each measurement we took 500 continuous frames (the maximum memory capacity of the camera), giving either a single intensity value or a timeseries for each camera pixel. Data was then transferred to PC via USB2.0, taking up to 8sec per 500 frame acquisition. Each timeseries could then be examined individually, to show the presence of the desired pulsed signal, or fast Fourier transformed to recover the frequency and magnitude of the AC signal. Either AC magnitude, pulse magnitude or fluorescence intensity could then be plotted to generate an image of the total magnetic field seen by the NV centres across the field of view. Although our technique also allowed recovery of signal phase by extracting pixel I and Q values separately, for the results in this work we avoid this by using a voltage trigger (NI-DAQ 6221) that set a constant (zero) phase at the start of each 500 frame acquisition. Reference images were taken off microwave resonance and with the circuit grounded through a switchbox in order to subtract camera pixel offset values.

Signals were generated in the cross circuit using a current source (Keithley 6221), supplying leads soldered to 4 pads patterned on the circuit substrate. The current source was used to generate AC square wave signals as well as pulsed and synthetic biosignals using an inbuilt arbitrary waveform generation (AWG) capability. Currents ranging from 1mA up to 100mA were applied to the circuit. By examining the ODMR traces, no visible drift in resonance frequency associated with temperature increase due to resistive heating was observed.

To provide the hippocampus biosignal to be replicated in our circuit, brain slices were obtained from adult (4-8 weeks) C57BL/6 mice (Janvier, France). Briefly, following Isoflurane anesthesia mice were decapitated and their brains dissected submerged in ice-cold, carbogen (95% O₂/5% CO₂) saturated sucrose substituted artificial cerebrospinal fluid (sACSF) containing (in mM): Sucrose (200), NaHCO₃ (25), glucose (11), KCl (3), CaCl₂ (0.1), MgCl₂ (4), KH₂PO₄ (1.1), Sodium pyruvate (2), myoinositol (3) and ascorbic acid (0.5). 300 μ m thick sagittal brain slices were cut in ice-cold sACSF using a VT1200s Vibratome (Leica, Germany). Slices were allowed to recover for at least 90 minutes in an interface type holding chamber, continuously bubbled with carbogen, kept at 28°C and filled with regular ACSF containing (in mM): NaCl (111), NaHCO₃ (25), glucose (11), KCl (3), CaCl₂ (2.5), MgCl₂ (1.3) and KH₂PO₄ (1.1). Individual slices containing the hippocampus was transferred to a custom made submerged type recording chamber continuously perfused with carbogen-saturated ACSF. Field excitatory post synaptic potentials (fEP-

SPs) were evoked by stimulating the Schaffer Collaterals at 0.05Hz using 0.05ms current pulses delivered through a twisted Pt/Ir wire electrode, connected to an A365 stimulus isolator (WPI, USA) and placed in the Stratum Radiatum at the border between the CA3-CA1 regions. fEPSPs were recorded by an ACSF filled glass electrode (4-6 MOhm), connected to a CV-7B headstage (Molecular Devices, USA) and placed in the Stratum Radiatum region of CA1. fEPSP signals were amplified using a 700B amplifier (Molecular Devices, USA) and digitized for recording (NI-DAQ 6221).

III. RESULTS

A. Intensity and ODMR

We first aligned and focused the camera and collection optics to give a clear, centred image of the circuit. This was achieved by a simple recording of the NV fluorescence intensity at 50fps while adjusting alignment. Figure 2a,a) shows the circuit imaged through the diamond in intensity mode, with the conductive Ti/Au tracks of the circuit brighter due to reflecting more of the fluorescence generated in the adjacent NV layer. By performing ODMR spectroscopy in intensity mode, we estimated the all-pixel average contrast on microwave resonance to be 1.2-1.6%. As detailed in Methods, we then used the lock-in capability of the camera, with frequency modulation of the microwaves supplied to the diamond, to perform ODMR spectroscopy. Selecting a single microwave resonance with the strongest response (greatest frequency shift) to the majority out of plane static offset magnetic field, we then performed a detailed step scan (50kHz, 500frames/point) across the frequencies with the maximum ODMR spectrum slope dp_v/df for each pixel. The response averaging all pixels for this spectrum can be seen in Figure 2,b). For each pixel, a slightly different ODMR spectrum was recorded due to local broadening effects including strain or variations in offset field, resulting in the less than smooth slope in the figure. Examples of measured single pixel ODMR spectra can be seen in Supplementary Information. The degree of resonance frequency variation was $<0.2\text{MHz}$ across the image. This allowed us to extract dp_v/df for each pixel using an ODMR scan of 1-2MHz across the resonance, and to remain sensitive (close the maximum slope) for the majority of pixels using only a single fixed microwave frequency ($f=2758.7\text{MHz}$).

We selected a single resonance in this manner due to the significant amount of time required to capture the full ODMR spectrum covering all NV microwave resonances via the relatively slow data transfer rate of the camera. Were faster transfer speeds available, it would be possible to perform vector sensing in the manner similar to that outlined in the work by Schloss et al. [39] by recording from each microwave resonance in turn. However, using a single NV axis gave a simple and useful measure of

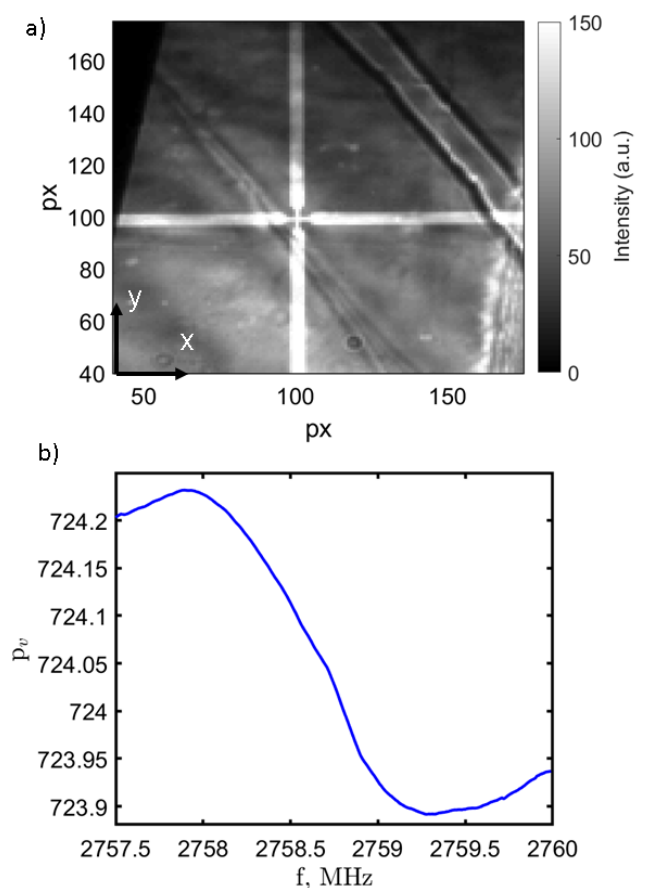


FIG. 2. a) Image of the intensity of fluorescence from the diamond in a region zoomed in around the cross circuit centre. Throughout this work, 1 pixel \approx $\pm 1.5 \times 1.5 \mu\text{m}$. The edge of the diamond can be seen as the black area in the upper left of the image. The feature across the upper right is a surface contamination artifact (residual glue on the circuit substrate). b) ODMR spectroscopy as pixel value average across the whole image p_v versus microwave drive frequency centred on a single microwave resonance (single NV axis). This reference trace could be used to convert into real (Tesla) units of magnetic field.

the magnitude of the magnetic field at that point in the image and hence the magnitude of current flow in the adjacent circuit. We note that the ODMR spectrum is only required for magnetic field unit conversion. For the majority of relevant applications often only the relative signal (shape, current path, on/off) is necessary. This can be achieved more simply by taking a fast ODMR trace to find the point of maximum sensitivity at maximum slope dp_v/df and recording the relative response in terms of unitless change in p_v .

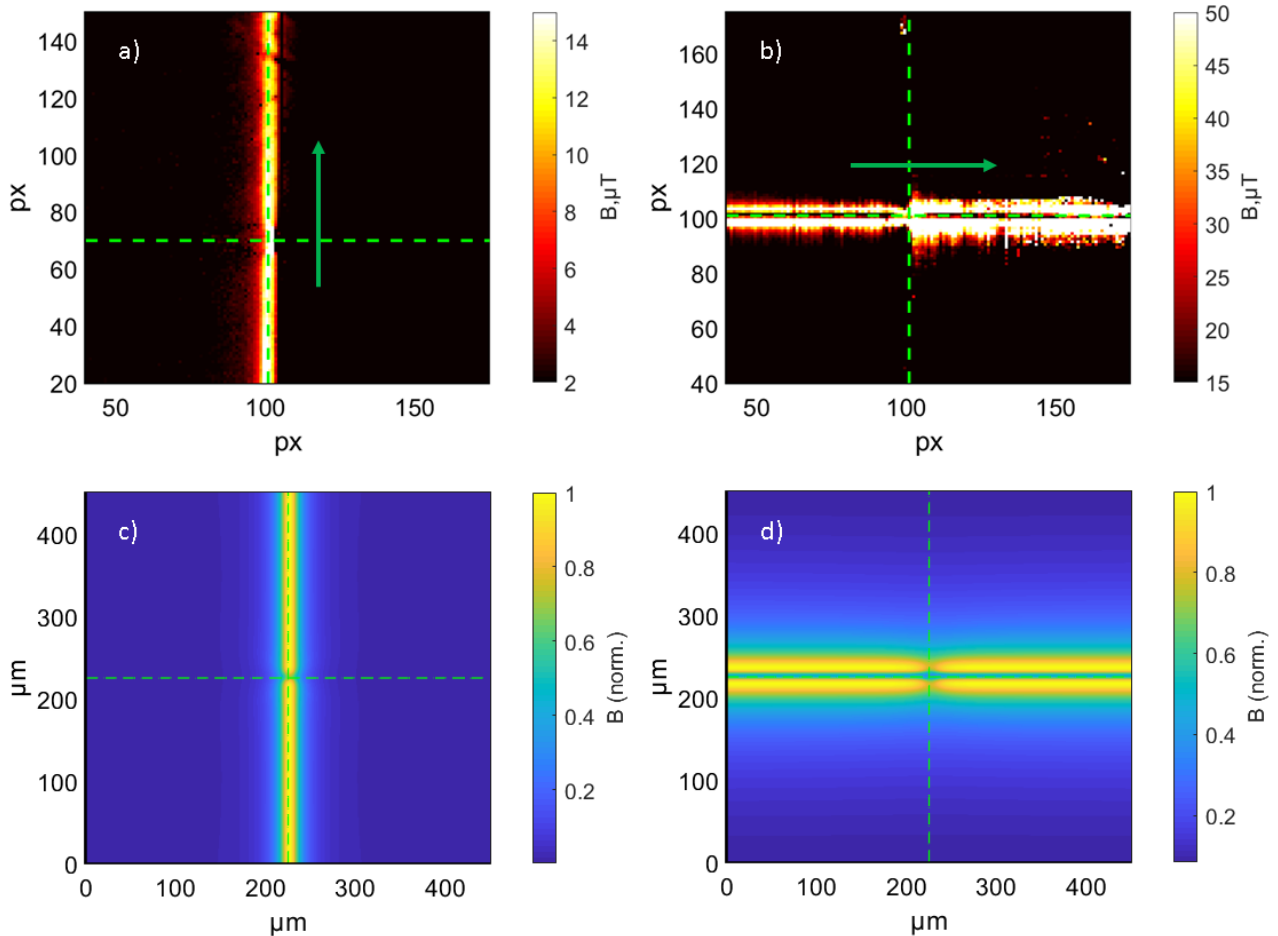


FIG. 3. a) Imaged magnetic field resulting from a 130Hz, 4mA alternating current in the vertical (y-axis) cross direction marked with a green arrow, and b) from 130Hz, 20mA current in the horizontal (x-axis) direction. We plot the response only from pixels with a signal $\text{SNR} > 3$, in order to clearly distinguish the signal from background noise in the images. A strong response was imaged from the NVs directly adjacent to the current-carrying wire tracks, that could be qualitatively replicated by first-principles modeling of the expected field strength (c and d). The location of the cross is shown as a dashed line. The higher noise to the right hand side of the cross in b) as compared to the left is an artifact from higher noise from a block of camera pixels in this region.

B. Alternating Current Imaging

In Figure 3,a) and b) we show example images of the magnetic field, arising from a constant 130Hz alternating current passed through the cross circuit either in the vertical (y) or horizontal (x) direction. This current replicates lower frequency current typical of transmission in power lines i.e. 50/60Hz and odd inductive harmonics e.g. 150/180Hz. We use a microwave modulation rate of 2.5kHz, close to the slowest possible camera modulation rate, and framerate of 650fps, delivering the best average per-pixel SNR for the target signal. As expected, we observed the strongest response from the NV centres directly adjacent to the circuit, dropping rapidly away from the wire position. This response was only observed in the directions through the cross where current flowed, indicated in the figures by green arrows. We observed clearly

the change in magnetic field resulting from track width reduction in the cross centre, in both current directions. As we imaged a projection of field along a single (out of circuit plane) NV axis, field response was much greater in the vertical (y) current direction, which allowed higher SNR signal recovery at lower current than with current in the horizontal (x) direction.

In order to validate our images, we calculated the relative strength of the field covering the entire camera field of view ($300 \times 300 \text{px}$, approximately $450 \times 450 \mu\text{m}$). Modeling as an infinitely long wire of elements dl carrying current I (full details in Supplementary Information) we calculated the field strength projected along an NV axis best aligned with the predominantly out of plane (z direction) DC offset field. Figure 3c,d) shows these plots of the calculated relative magnetic field, normalised to the maximum in the modeled field of view, assuming a

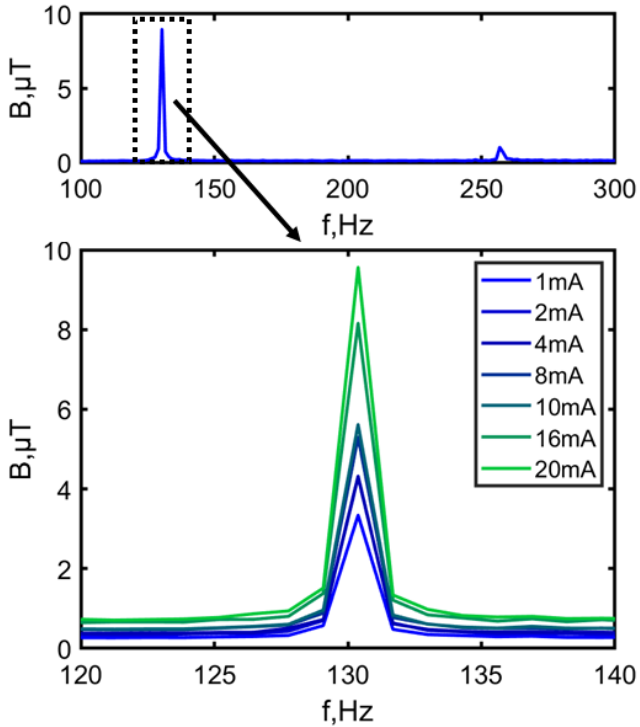


FIG. 4. Spectrum of the current signal extracted from the FFT of a 500 frame length timeseries, averaging spectra taken from all useable pixels (292x280). Both the 130Hz primary and 260Hz second harmonic are visible. The signal was observed to reduce in strength with lower current, as expected for magnetic field from a current carrying wire.

circuit-NV separation of $10\mu\text{m}$. The modelled images strongly replicate the experimental images, particularly the central narrowing and strip of relatively low magnetic field near the wire track with current in the horizontal (x) direction, where the magnetic field vector at the NV layer points away from the sensitive NV axis.

To further test magnetic field recording, we imaged the cross at a range of different applied current values between 1-20mA. In Figure 4 the amplitude spectrum of the signal can be seen, extracted from a 500 frame timeseries for each pixel then averaged across the image. Examples of the spectra for individual pixels across the image are given in Supplementary Information. The primary (130Hz) and second (260Hz) harmonic of the current signal are both observed and the change in signal amplitude at 130Hz as a function of current can be seen in Figure 5. The AC signal was observed to scale linearly with current, as would be expected from a measurement of magnetic field from a current carrying wire. By increasing the camera modulation rate and framerate, we were able to acquire similar data for AC current signals of frequency up to 490Hz (6kHz microwave modulation, 1000fps) and up to 1.51kHz (14kHz microwave modulation, 3500fps). This can be seen in the Supplementary Information.

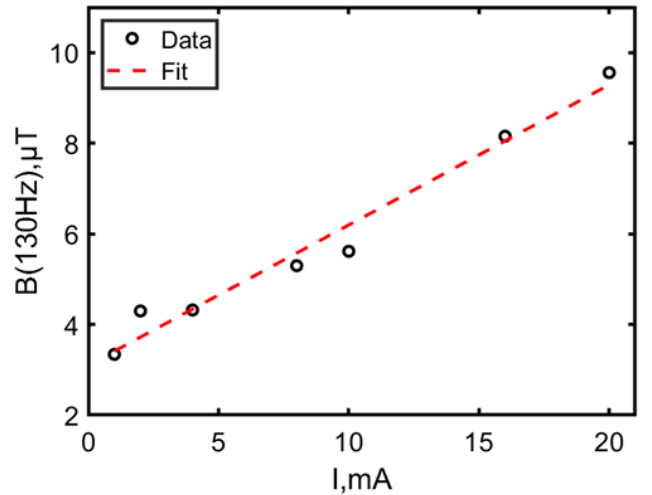


FIG. 5. Maximum strength of the 130Hz signal from the averaged spectra in Figure 4 as a function of current. As expected, the measured magnetic field linearly with current (dashed fit).

C. Pulsed Current

In order to demonstrate detection of a digital signal as typical for an integrated circuit, we applied a series of 20mA current pulses of 1ms/1ms forward/reverse polarity current as detailed in Figure 6,a), separated by 20ms intervals. In order to record such short period signals, we increased the camera frame rate to 3500fps and microwave modulation rate to 14kHz, while still capturing 500 image frames, giving a 142ms timeseries for each pixel covering a set of 6 applied pulses. We acquired 2500x500 frame image sets, extracting an average 500 frame timeseries for each pixel.

The relative strength of the forward current 1ms pulses are shown in the image in Figure 6, b). As a consequence of the higher sensing bandwidth (higher frame rate) we captured more noise, giving a lower image SNR. We also noted a reduction in signal strength, which we attribute to loss of modulation synchronicity between the camera and our microwave generator, arising from trigger incompatibility at modulation rates above approximately 3kHz. Although this technical issue compromised imaged signal strength, we clearly observed the applied pulsed signal in our magnetic field image, directly adjacent to the current carrying track, indicated by a green arrow in Figure 6,b).

The recorded magnetic field from the applied pulses is shown in the timeseries in Figure 7, from a) averaging all pixels with a signal $\text{SNR} > 3$ and b) for a single example pixel in the image on the circuit track. The 1ms/1ms pulses can be clearly detected, with magnetic field amplitude up to $50\mu\text{T}$. Notably, detection is possible with $\text{SNR} > 3$ using data from just a single pixel receiving fluorescence from NVs directly adjacent to the circuit track. Although the signal was strongest along the current path,

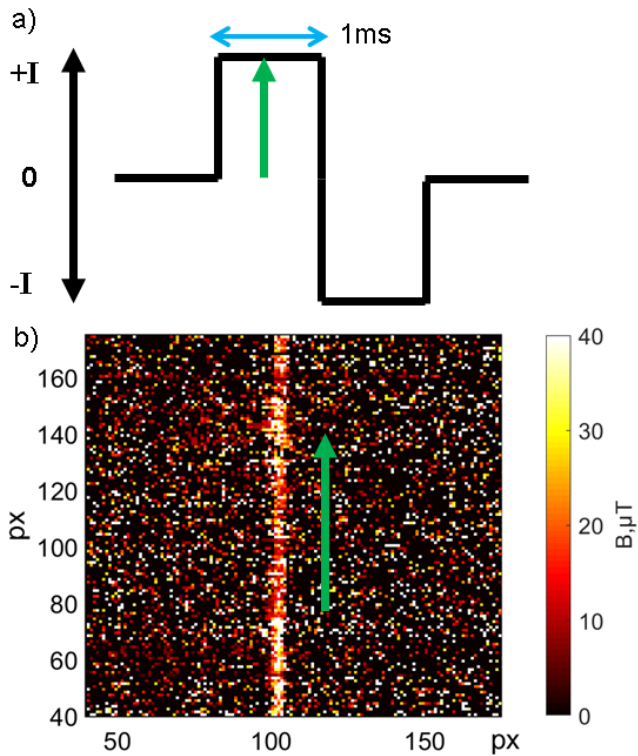


FIG. 6. a) Schematic of the 1ms/1ms forward/reverse polarity pulsed current signal. The signal is repeated every 20ms. b) Image map of the strength of the 1ms forward component of the pulsed signal extracted from the pixel timeseries over 500 frames (at 3500fps), averaging the 6 pulses captured within the acquisition. For clarity, only pixel values with a signal $\text{SNR} > 3$ are shown, with the remainder set to zero. The direction of the current through the cross circuit is indicated by a green arrow.

we could still observe the pulses within the images away from this region. This is demonstrated in Figure 7,c) plotting the recorded timeseries for 20000 pixels in a region centered on the current track. Although having a lower SNR, the pulsed signal was still observable when imaging NV centre fluorescence up to at a distance of at least $53\mu\text{m}$ away from the current path.

D. Detection of a Synthetic Biosignal

Finally, we demonstrate the acquisition of a signal with the same form as a neuronal signal, as may be found in the brain or nervous system of a living person or animal. We replicated the shape of a typical signal acquired from a prior electrical recordings of fEPSPs in the hippocampus of a mouse obtained from living dissected tissue slices. We applied the signal using the arbitrary waveform generator mode of our current source, with a maximum forward current amplitude of 20mA. We note that this current is significantly more than the current

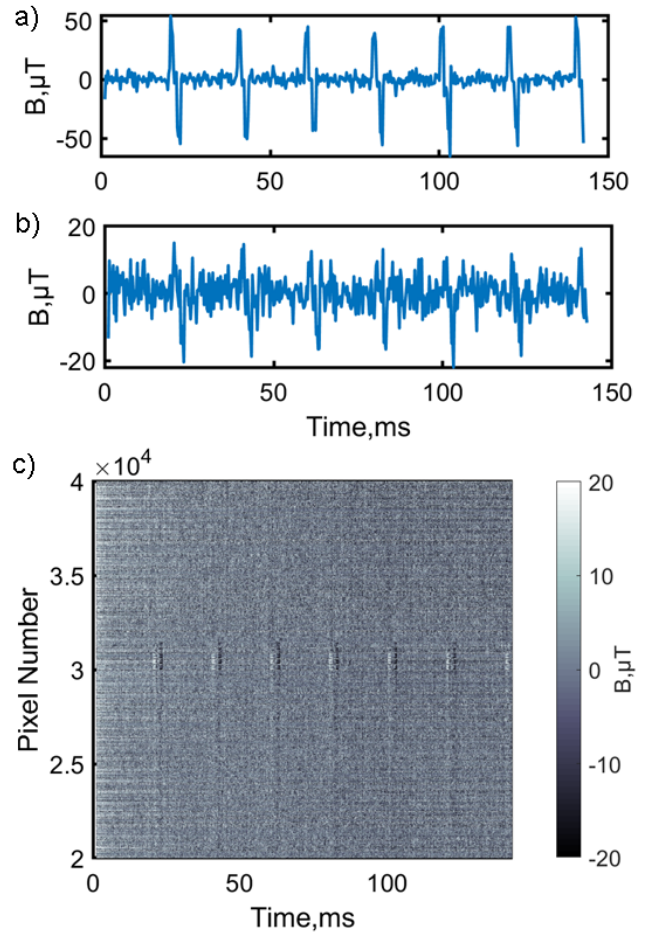


FIG. 7. Timeseries of the acquired signal for the acquisition period (142ms at 3500fps), taking the average over 1000 repeated 500 frame acquisitions. In a) the average of all pixels with a $\text{SNR} > 3$ is shown, with the signal clearly resolved. In b) an example timeseries is given for a single pixel in a region of the image close to the current path, where despite the higher noise level the signal could still be observed. c) A sequence of timeseries for pixels 20000-40000 covering a region centred on the cross current path. The strongest signal is observed for recording from pixels receiving fluorescence from NVs adjacent to the current carrying track, however the pulsed signal is still observable (with a decreasing SNR) away from it.

generated by a voltage signal in a neuron (low-nA to pA[40]). However, in this work we purely seek to demonstrate a proof of principle demonstration of lock-in camera acquisition recovery of a signal the same shape and length, for which our choice of amplitude gives a clear visible signal within the sensitivity limitations imposed by our diamond.

The strength of the detected signal is demonstrated in Figure 8,a) and b), mirroring the equivalent Figure 6 and 7 for the pulsed current, with the strongest signal again imaged closest to the current carrying track. We extracted the synthetic hippocampus signal from averaging the timeseries from 2500×500 frame acquisitions for

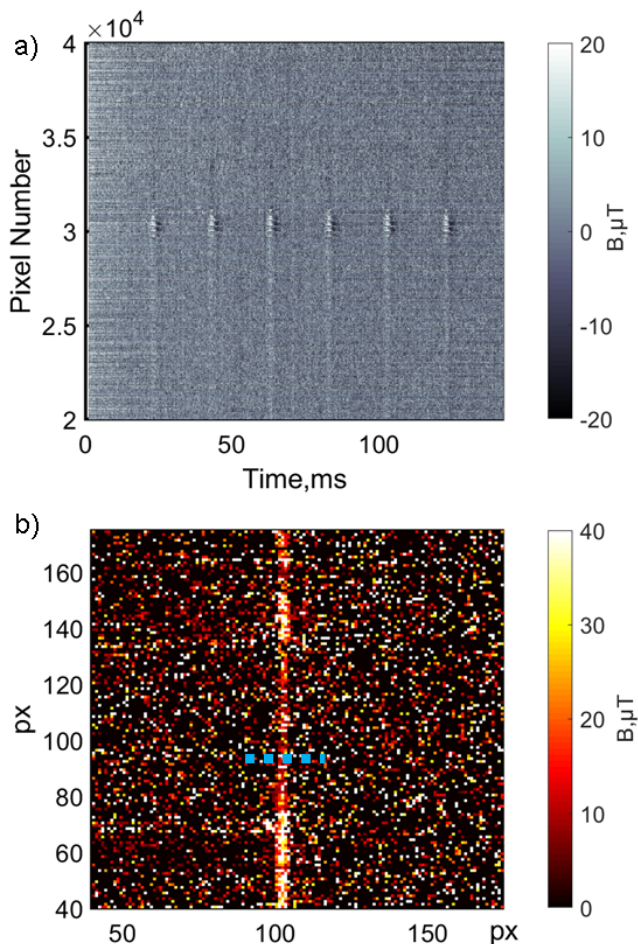


FIG. 8. The equivalent of plots in Figure 6 and Figure 7 for the synthetic biosignal. As for the 1ms pulses, the signal can be observed clearly for pixels recording fluorescence from NVs directly adjacent to the current carrying track, but can also be observed at a lower SNR away from this region. The blue dashed line represents the track of pixels for the data presented in Figure 9.

each pixel. A plot of this signal as compared to the applied current signal can be seen in Figure 9,a) for 5 pixel steps across the current track (blue dashed line in Figure 8,b). In pixels recording fluorescence from NVs adjacent to the current track we observed a strong signal, highly representative of the applied synthetic signal at a peak magnetic field strength of $15\text{-}20\mu\text{T}$, with the signal decaying in strength in the image away from this path. In Figure 8,b) we plot the average signal acquired for all pixels with a signal $\text{SNR}>3$. This signal also replicated the applied current signal, as shown in the red dashed trace.

A key feature we note in all our data is the constant reduction in noise with continual averaging (scaling as \sqrt{N} , with N the number of 500 frame acquisitions). This is demonstrated in Figure 10,a), where we calculate the all-pixel average standard deviation of the magnetic field

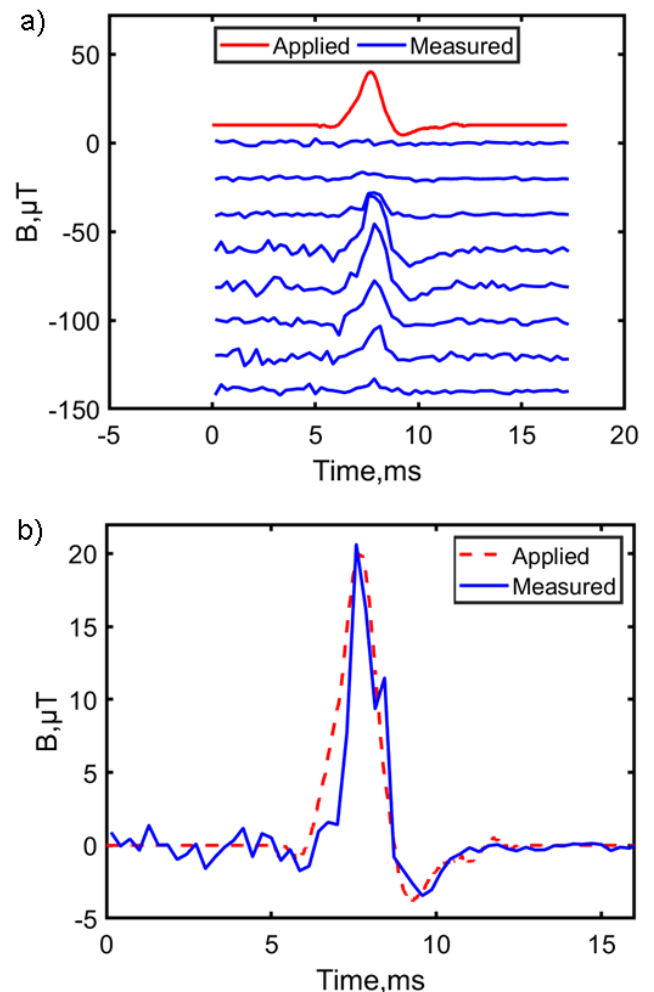


FIG. 9. a) Magnetic field signal measured from individual pixels taking 5 pixel steps along the blue dashed line indicated in Figure 8. For each step we add an offset from the previous by $-20\mu\text{T}$ for clarity, with the (scaled) applied synthetic biosignal shown in red at the top. As expected is most clearly observed in the image region closest to the current path, dropping in strength to either side. b) The signal recorded from averaging the response of all pixels with a signal $\text{SNR}>3$, overlaid onto the (scaled) generated signal (red, dashed). The signal recovered via the magnetic field imaging matches well with the applied signal, with no distortion or artifacts.

in the timeseries, taken with zero applied signal in a 5ms period between the current pulses. After 2500 acquisitions, we reach a noise level of approximately 200nT ($6.8\text{nT}/\sqrt{Hz}$ on a 1.75kHz acquisition bandwidth at 3500fps), averaging over all 292×280 useable pixels in the image. A histogram of the noise on the individual pixels after 1000 acquisitions is given in Figure 10,b), peaking at approximately $2.5\text{-}3\mu\text{T}$ ($84\text{-}100\text{nT}/\sqrt{Hz}$). The noise follows a Poisson distribution, as would be expected due to fluorescence shot noise with a non-uniform laser illumination of the diamond. In previous experiments using

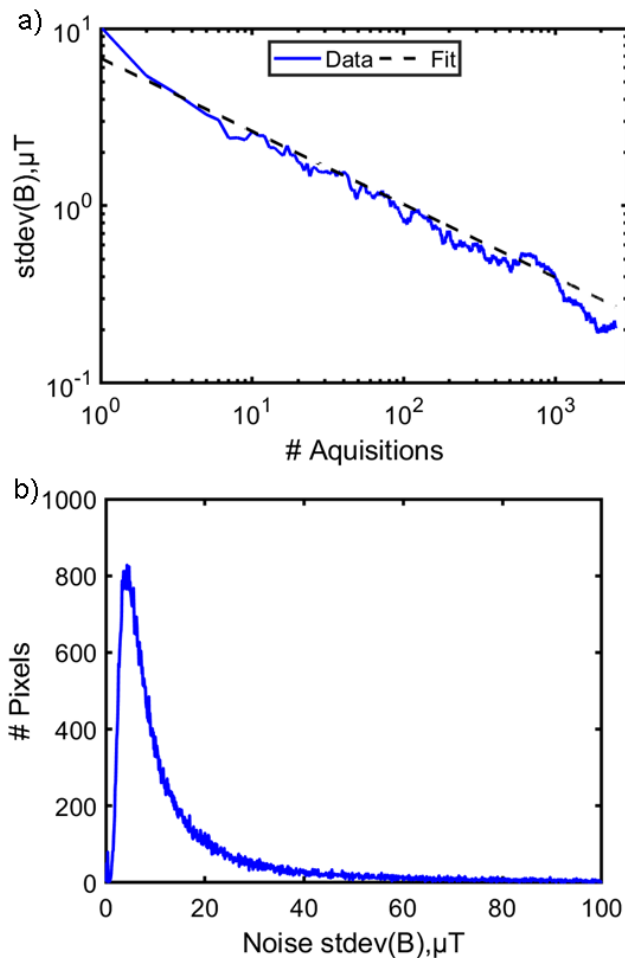


FIG. 10. a) Scaling of the standard deviation of the magnetic field signal between the current pulses as a function of number of 500 frame acquisitions $N=0-2500$, as a measure of readout noise. The noise continually reduces with a \sqrt{N} trend, without reaching a plateau. b) Histogram of the individual pixel noise after 1000 acquisitions, with the majority of pixels in the low- μT noise range.

a conventional camera where DC noise is included in the images, we found the noise level to plateau well before the number of frames acquired by the lock-in camera[28]. We attribute this inclusion of a high level of laser technical noise, in particular fluctuations in laser power. The lock-in camera thus offers the possibility to reach far lower noise levels through continual averaging, with available time the only limitation. The scaling we observe in Figure 10 is the same as for our experiments using a DC-noise rejecting balanced photodetector[41].

We note that it was necessary to apply a far larger synthetic biosignal current than would be realistically produced, allowing us to demonstrate in principle the signal acquisition and imaging, but without the necessary noise level to resolve the real signal. As yet, state of the art performance in NV sensing can only resolve real biosignals

on the pT-nT level through integrating total fluorescence emission from a mm-scale diamond. Previous theoretical calculations such as the works by Karadas et al. [42, 43] and Wojciechowski et al. [35] have explored the expected current and magnetic field strength and camera requirements to image a real biosignal, which have yet to be reached experimentally, as well as the absolute necessity of spatial resolution to avoid cancellation from regions of opposing field polarity.

The diamond we used in this work has characteristics well below these requirements, with low fluorescence emission and relatively low ODMR contrast (1.2-1.6%). This is significantly worse than state of the art diamonds in the literature, where total emissions in the mW range at comparable (1-2W) pump laser power is possible and where contrast of up to 30% can be reached in preferentially aligned samples[44–46]. To generate sufficient contrast, it was also necessary to supply a relatively high microwave power (-5dBm input with 45dB amplifier gain), eliminating the ^{15}N hyperfine resonances in the ODMR spectrum through power broadening[47], further reducing the maximum achievable dp_v/df slope and hence sensitivity.

We highlight that although we do not have the diamond to reach the necessary levels of sensitivity for real biosensing in this work, no aspect of the measurement method of the synthetic replica signal utilising the lock-in camera is incompatible with future material improvement. In particular, the level of fluorescence from the diamond collected by the camera (a maximum of $152\mu\text{W}$ full sensor or $1.7\text{nW}/\text{pixel}$) and the level of the demodulated signal are three orders of magnitude below the lock-in camera limits of up to $2.5-3\mu\text{W}/\text{pixel}$ or $250-270\text{mW}$ across the sensor area [35, 48].

IV. CONCLUSION

In this work we demonstrate proof of principle passive and remote imaging of propagating electrical current in a circuit, using a novel type of lock-in amplifier camera. We image the current-induced magnetic field detected via variations in fluorescence emission from nitrogen vacancy (NV) centres in diamond. Using a simple continuous wave method without aliasing or undersampling, we demonstrate imaging of low frequency alternating current (as typical in electrical power distribution systems), rapid pulsed current (as typical in integrated circuits) and a representation of a biosignal (as generated in a neural network in the living brain). We show that each of these types of signal can be observed and mapped, both spatially and as a function of time, at a high frame rate (up to 3500fps) significantly faster than previously achieved in the literature.

We consider the reduction in noise with continual averaging to be a significant lock-in camera advantage over conventional cameras, where DC and correlated noise from in particular pump laser power fluctuations can

cause the noise to plateau after a relatively low number of averaged frames. We consider this feature to be particularly useful in either mapping repeated, consistent fast signals such as transport or magnetism in 2D materials [31] or biological neural networks or for slowly varying long period measurements e.g. temperature measurement in living cells via nanodiamond experiments [49].

The method we demonstrate can be readily adapted to a typical inverted microscope setup used for NV sensing and imaging, including for biological samples [41, 50]. Although our diamond does not allow us to reach the necessary level of sensitivity to directly observe and image signals in a real biosample, with improvements in material growth and optimisation and the potential for implementation of pulsed laser and microwave protocols (recently demonstrated during the production of this work by Hart et al. [51]), the methods we demonstrate here represent a clear means by which such signals could be resolved in future.

During the preparation of our manuscript, we became aware of contemporary work by Parashar et al. [52], independently following a similar procedure as we outline in this work, resolving AC signals from a bulk magnetic field applied across the diamond using a field coil rather than a microcircuit. Both their work and ours highlight the key advantages of the simplicity of the lock-in camera based technique and the limitations, particularly in terms of the possibility of significantly higher sensitivity through improved diamond growth and irradiation.

V. ACKNOWLEDGMENTS

The work presented here was funded by the Novo Nordisk foundation through the synergy grant bioQ and the bigQ Center funded by the Danish National Research Foundation (DNRF). We acknowledge the assistance of Kristian Hagsted Rasmussen for microfabrication.

-
- [1] R. Hoffmann-Vogel, *Applied Physics Reviews* **4**, 031302 (2017), URL <https://doi.org/10.1063/1.4994691>.
- [2] U. Kindereit, in *2014 IEEE International Reliability Physics Symposium* (IEEE, 2014), URL <https://doi.org/10.1109/irps.2014.6860635>.
- [3] K. Nakamae, *Measurement Science and Technology* **32**, 052003 (2021), URL <https://doi.org/10.1088/1361-6501/abd96d>.
- [4] J. True, C. Xi, N. Jessurun, K. Ahi, and N. Asadizanjani, *Optical Engineering* **60** (2021), URL <https://doi.org/10.1117/1.oe.60.6.060901>.
- [5] A. V. Ulyanova, C. Cottone, C. D. Adam, K. G. Gagnon, D. K. Cullen, T. Holtzman, B. G. Jamieson, P. F. Koch, H. I. Chen, V. E. Johnson, et al., *Frontiers in Neuroscience* **13** (2019), URL <https://doi.org/10.3389/fnins.2019.00397>.
- [6] K. Ohki, S. Chung, Y. H. Ch'ng, P. Kara, and R. C. Reid, *Nature* **433**, 597 (2005), URL <https://doi.org/10.1038/nature03274>.
- [7] F. Dolde, H. Fedder, M. W. Doherty, T. Nöbauer, F. Rempp, G. Balasubramanian, T. Wolf, F. Reinhard, L. C. L. Hollenberg, F. Jelezko, et al., *Nature Physics* **7**, 459 (2011), URL <https://doi.org/10.1038/nphys1969>.
- [8] P. Neumann, I. Jakobi, F. Dolde, C. Burk, R. Reuter, G. Waldherr, J. Honert, T. Wolf, A. Brunner, J. H. Shim, et al., *Nano Letters* **13**, 2738 (2013), URL <https://doi.org/10.1021/nl401216y>.
- [9] S. Knauer, J. P. Hadden, and J. G. Rarity, *npj Quantum Information* **6** (2020), URL <https://doi.org/10.1038/s41534-020-0277-1>.
- [10] D. Cohen, R. Nigmatullin, O. Kenneth, F. Jelezko, M. Khodas, and A. Retzker, *Scientific Reports* **10** (2020), URL <https://doi.org/10.1038/s41598-020-61095-y>.
- [11] Y. Liu, H. Guo, W. Zhang, Z. Zhang, Z. Li, Y. Li, J. Tang, Z. Ma, and J. Liu, *Physics Letters A* **384**, 126832 (2020), URL <https://doi.org/10.1016/j.physleta.2020.126832>.
- [12] J. M. Taylor, P. Cappellaro, L. Childress, L. Jiang, D. Budker, P. R. Hemmer, A. Yacoby, R. Walsworth, and M. D. Lukin, *Nature Physics* **4**, 810 (2008), URL <https://doi.org/10.1038/nphys1075>.
- [13] S. Hong, M. S. Grinolds, L. M. Pham, D. L. Sage, L. Luan, R. L. Walsworth, and A. Yacoby, *MRS Bulletin* **38**, 155 (2013), URL <https://doi.org/10.1557/mrs.2013.23>.
- [14] T. Wolf, P. Neumann, K. Nakamura, H. Sumiya, T. Ohshima, J. Isoya, and J. Wrachtrup, *Physical Review X* **5** (2015), URL <https://doi.org/10.1103/physrevx.5.041001>.
- [15] A. Gruber, *Science* **276**, 2012 (1997), URL <https://doi.org/10.1126/science.276.5321.2012>.
- [16] P. Delaney, J. C. Greer, and J. A. Larsson, *Nano Letters* **10**, 610 (2010), URL <https://doi.org/10.1021/nl903646p>.
- [17] E. V. Levine, M. J. Turner, P. Kehayias, C. A. Hart, N. Langellier, R. Trubko, D. R. Glenn, R. R. Fu, and R. L. Walsworth, *Nanophotonics* **8**, 1945 (2019), URL <https://doi.org/10.1515/nanoph-2019-0209>.
- [18] A. Horsley, P. Appel, J. Wolters, J. Achard, A. Tal-laire, P. Maletinsky, and P. Treutlein, *Physical Review Applied* **10** (2018), URL <https://doi.org/10.1103/physrevapplied.10.044039>.
- [19] Y. Chen, Z. Li, H. Guo, D. Wu, and J. Tang, *EPJ Quantum Technology* **8** (2021), URL <https://doi.org/10.1140/epjqt/s40507-021-00097-9>.
- [20] J.-P. Tetienne, N. Donschuk, D. A. Broadway, A. Stacey, D. A. Simpson, and L. C. L. Hollenberg, *Science Advances* **3**, e1602429 (2017), URL <https://doi.org/10.1126/sciadv.1602429>.
- [21] M. J. H. Ku, T. X. Zhou, Q. Li, Y. J. Shin, J. K. Shi, C. Burch, L. E. Anderson, A. T. Pierce, Y. Xie, A. Hamo, et al., *Nature* **583**, 537 (2020), URL <https://doi.org/10.1038/s41586-020-2507-2>.
- [22] D. R. Glenn, R. R. Fu, P. Kehayias, D. L. Sage, E. A. Lima, B. P. Weiss, and R. L. Walsworth, *Geochemistry, Geophysics, Geosystems* **18**, 3254 (2017), URL <https://doi.org/10.1002/2017gc006946>.

- [23] J. C. Price, R. Mesquita-Ribeiro, F. Dajas-Bailador, and M. L. Mather, *Frontiers in Physics* **8** (2020), URL <https://doi.org/10.3389/fphy.2020.00255>.
- [24] D. L. Sage, K. Arai, D. R. Glenn, S. J. DeVience, L. M. Pham, L. Rahn-Lee, M. D. Lukin, A. Yacoby, A. Komeili, and R. L. Walsworth, *Nature* **496**, 486 (2013), URL <https://doi.org/10.1038/nature12072>.
- [25] R. Schirhagl, K. Chang, M. Loretz, and C. L. Degen, *Annual Review of Physical Chemistry* **65**, 83 (2014), URL <https://doi.org/10.1146/annurev-physchem-040513-103659>.
- [26] L. T. Hall, G. C. G. Beart, E. A. Thomas, D. A. Simpson, L. P. McGuinness, J. H. Cole, J. H. Manton, R. E. Scholten, F. Jelezko, J. Wrachtrup, et al., *Scientific Reports* **2** (2012), URL <https://doi.org/10.1038/srep00401>.
- [27] M. Parashar, K. Saha, and S. Bandyopadhyay, *Communications Physics* **3** (2020), URL <https://doi.org/10.1038/s42005-020-00439-6>.
- [28] J. L. Webb, L. Troise, N. W. Hansen, J. Achard, O. Brinza, R. Staacke, M. Kieschnick, J. Meijer, J.-F. Perrier, K. Berg-Sørensen, et al., *Frontiers in Physics* **8** (2020), URL <https://doi.org/10.3389/fphy.2020.522536>.
- [29] R. Tanos, W. Akhtar, S. Monneret, F. F. de Oliveira, G. Seniutinas, M. Munsch, P. Maletinsky, L. le Gratiet, I. Sagnes, A. Dréau, et al., *AIP Advances* **10**, 025027 (2020), URL <https://doi.org/10.1063/1.5140030>.
- [30] D. A. Simpson, J.-P. Tetienne, J. M. McCoey, K. Ganesan, L. T. Hall, S. Petrou, R. E. Scholten, and L. C. L. Hollenberg, *Scientific Reports* **6** (2016), URL <https://doi.org/10.1038/srep22797>.
- [31] D. A. Broadway, S. C. Scholten, C. Tan, N. Dontschuk, S. E. Lillie, B. C. Johnson, G. Zheng, Z. Wang, A. R. Oganov, S. Tian, et al., *Advanced Materials* **32**, 2003314 (2020), URL <https://doi.org/10.1002/adma.202003314>.
- [32] Z. Kazi, I. M. Shelby, H. Watanabe, K. M. Itoh, V. Shutthanandan, P. A. Wiggins, and K.-M. C. Fu, *Physical Review Applied* **15** (2021), URL <https://doi.org/10.1103/physrevapplied.15.054032>.
- [33] K. Mizuno, H. Ishiwata, Y. Masuyama, T. Iwasaki, and M. Hatano, *Scientific Reports* **10** (2020), URL <https://doi.org/10.1038/s41598-020-68404-5>.
- [34] P. Lambelet, in *Optical Measurement Systems for Industrial Inspection VII*, edited by P. H. Lehmann, W. Osten, and K. Gasteringer (SPIE, 2011), URL <https://doi.org/10.1117/12.889390>.
- [35] A. M. Wojciechowski, M. Karadas, A. Huck, C. Osterkamp, S. Jankuhn, J. Meijer, F. Jelezko, and U. L. Andersen, *Review of Scientific Instruments* **89**, 031501 (2018), URL <https://doi.org/10.1063/1.5010282>.
- [36] R. Patel, S. Achamfuo-Yeboah, R. Light, and M. Clark, *Optics Express* **19**, 24546 (2011), URL <https://doi.org/10.1364/oe.19.024546>.
- [37] J. F. Barry, J. M. Schloss, E. Bauch, M. J. Turner, C. A. Hart, L. M. Pham, and R. L. Walsworth, *Reviews of Modern Physics* **92** (2020), URL <https://doi.org/10.1103/revmodphys.92.015004>.
- [38] A. Cooper, E. Magesan, H. N. Yum, and P. Cappellaro, *Nature Communications* **5** (2014), URL <https://doi.org/10.1038/ncomms4141>.
- [39] J. M. Schloss, J. F. Barry, M. J. Turner, and R. L. Walsworth, *Physical Review Applied* **10** (2018), URL <https://doi.org/10.1103/physrevapplied.10.034044>.
- [40] J. Mitterdorfer and B. P. Bean, *The Journal of Neuroscience* **22**, 10106 (2002), URL <https://doi.org/10.1523/jneurosci.22-23-10106.2002>.
- [41] J. L. Webb, L. Troise, N. W. Hansen, C. Olsson, A. M. Wojciechowski, J. Achard, O. Brinza, R. Staacke, M. Kieschnick, J. Meijer, et al., *Scientific Reports* **11** (2021), URL <https://doi.org/10.1038/s41598-021-81828-x>.
- [42] M. Karadas, A. M. Wojciechowski, A. Huck, N. O. Dalby, U. L. Andersen, and A. Thielscher, *Scientific Reports* **8** (2018), URL <https://doi.org/10.1038/s41598-018-22793-w>.
- [43] M. Karadas, C. Olsson, N. W. Hansen, J.-F. Perrier, J. L. Webb, A. Huck, U. L. Andersen, and A. Thielscher, *Frontiers in Neuroscience* **15** (2021), URL <https://doi.org/10.3389/fnins.2021.643614>.
- [44] C. Osterkamp, M. Mangold, J. Lang, P. Balasubramanian, T. Teraji, B. Naydenov, and F. Jelezko, *Scientific Reports* **9** (2019), URL <https://doi.org/10.1038/s41598-019-42314-7>.
- [45] P. Balasubramanian, C. Osterkamp, Y. Chen, X. Chen, T. Teraji, E. Wu, B. Naydenov, and F. Jelezko, *Nano Letters* **19**, 6681 (2019), URL <https://doi.org/10.1021/acs.nanolett.9b02993>.
- [46] L. M. Pham, N. Bar-Gill, D. L. Sage, C. Belthangady, A. Stacey, M. Markham, D. J. Twitchen, M. D. Lukin, and R. L. Walsworth, *Physical Review B* **86** (2012), URL <https://doi.org/10.1103/physrevb.86.121202>.
- [47] A. Dréau, M. Lesik, L. Rondin, P. Spinicelli, O. Arcizet, J.-F. Roch, and V. Jacques, *Physical Review B* **84** (2011), URL <https://doi.org/10.1103/physrevb.84.195204>.
- [48] J. Schloss, *Optimizing nitrogen-vacancy diamond magnetic sensors and imagers for broadband sensitivity* (2011), PhD Thesis, MIT.
- [49] M. Fujiwara, S. Sun, A. Dohms, Y. Nishimura, K. Suto, Y. Takezawa, K. Oshimi, L. Zhao, N. Sadzak, Y. Ume-hara, et al., *Science Advances* **6**, eaba9636 (2020), URL <https://doi.org/10.1126/sciadv.aba9636>.
- [50] J. F. Barry, M. J. Turner, J. M. Schloss, D. R. Glenn, Y. Song, M. D. Lukin, H. Park, and R. L. Walsworth, *Proceedings of the National Academy of Sciences* **113**, 14133 (2016), URL <https://doi.org/10.1073/pnas.1601513113>.
- [51] C. A. Hart, J. M. Schloss, M. J. Turner, P. J. Scheidegger, E. Bauch, and R. L. Walsworth, *Physical Review Applied* **15** (2021), URL <https://doi.org/10.1103/physrevapplied.15.044020>.
- [52] M. Parashar, D. Shishir, A. Bathla, A. Gokhale, S. Bandyopadhyay, and K. Saha, *Lock-in detection based dynamic widefield magnetometry using quantum defects in diamond* (2021), arXiv, 2107.12232.



Chapter 9

Sensing of Action Potentials from Corpus Callosum in Mice

9.1 Introduction

The corpus callosum is the largest nerve tract in the brain, forming the principal connection between the left and right cerebral hemispheres and it consists of more than 200 million myelinated and unmyelinated nerve fibers. Myelinated axons are larger and faster conducting than unmyelinated axons, which are more compact and slower conducting [93].

A recent study on the agenesis of the corpus callosum in humans, a rare congenital disorder characterized by the absence of the corpus callosum, has suggested that this particular nerve plays a crucial role in problem solving and verbal processing speed [94]. Furthermore, a number of studies have demonstrated that structural abnormalities of the corpus callosum in multiple sclerosis (MS) are associated with attention deficits, limited information processing, memory decline, and impaired executive functions [95, 96].

From a clinical and diagnostic perspective, the corpus callosum harbors excellent properties such as well-defined fiber orientation and borders, which limit the mixing of different tissue types. Such properties are essential for the evaluation of injuries in normal appearing white matter, abnormal areas of white matter which cannot be detected with conventional MRI techniques [97, 98]. Due to these factors, being able to

image the electrical activity of the corpus callosum in a quantitative and non-invasive way could be crucial for early diagnosis of MS. NV centers in diamonds may prove to be an essential tool for quantitatively imaging these anomalies in the corpus callosum due to their great biocompatibility and high spatial and temporal resolution.

In the next section, preliminary results regarding sensing of action potentials from corpus callosum in mice will be presented.

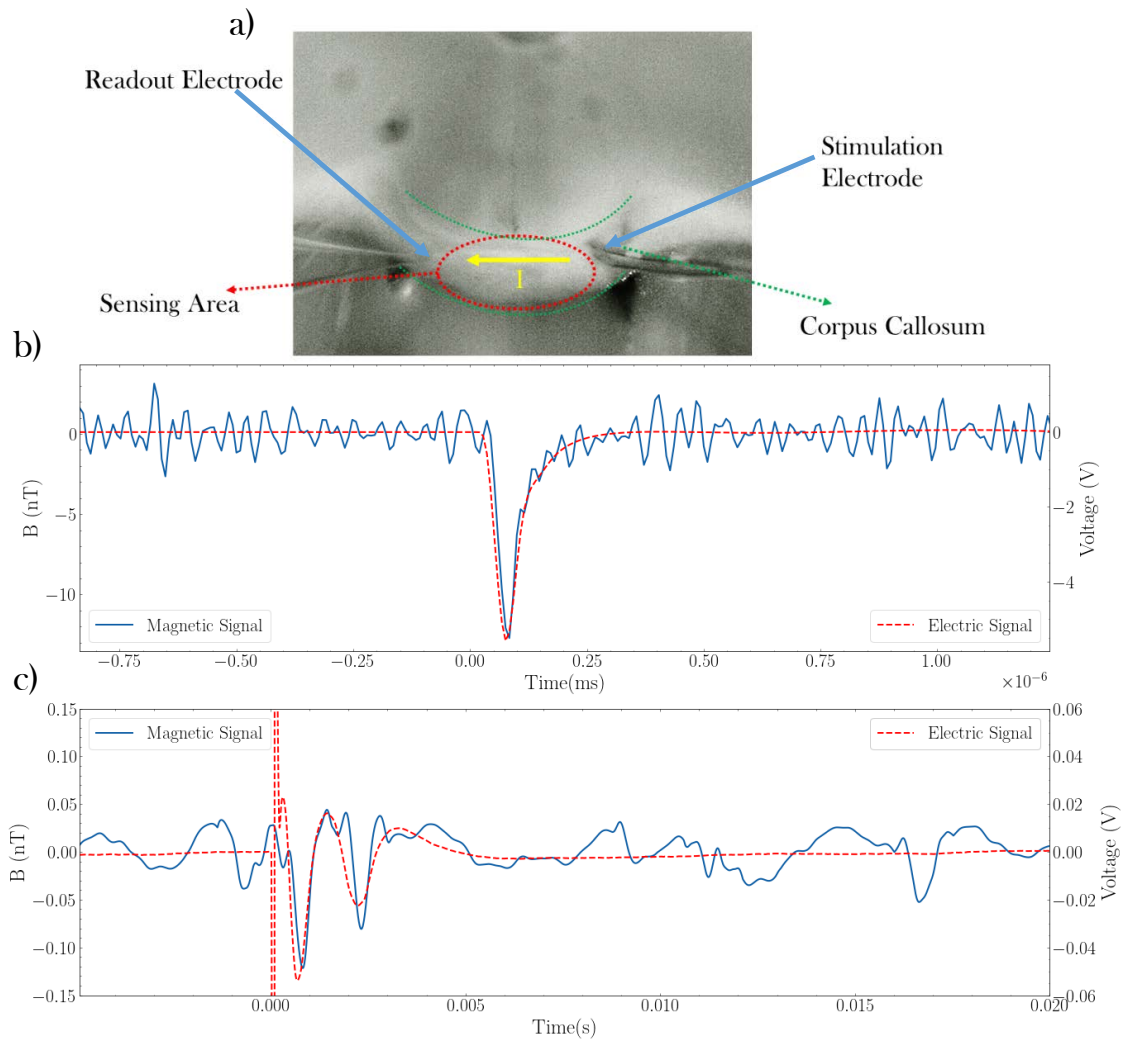


Figure 9.1: a) White light microscopy image of brain slice during a recording. The red dashed line indicates a $\sim 0.1 \times 0.3 \text{ mm}^2$ region of the diamond (underneath the slice) where the pump laser couples to the diamond, generating the most fluorescence. Green dashed lines indicate the well-define borders of the corpus callosum. b) Stimulation artifacts generated by a $50 \mu\text{s}$ current pulse in the magnetic (blue line) and electric (dashed red line). c) Averaged magnetic and electric signals after data post-processing. The two features labeled as 1 and 2 represent the compound action potential generated by the myelinated and unmyelinated axons.

9.2 Preliminary Investigation

Coronal slices of 400 μm of thickness were obtained from wild-type mice (C57BL-6) using a vibratome. After dissection, the slices were kept for one hour in a resting chamber filled with ACSF at 28°C. By adopting the same sensing methodology described in Chapter 3, brain slices were positioned in the custom-made sample chamber containing ACSF solution by carefully aligning the corpus callosum on the most sensitive region of the diamond (Supp. Info, Chapter 7).

A white-light microscope image taken from the top of the sample chamber is shown in Fig. 9.1a: a platinum-iridium twisted wire electrode was employed to trigger the compound action potential in the corpus callosum while a AgCl probe electrode measured the electric response. Action potentials were triggered by a current pulse train with amplitudes in the range of 0.4-0.5 mA at a frequency of 2 Hz with pulse length of 50 μs . The sample could be kept alive in the solution bath for many hours (>12 hrs) by keeping the ACSF solution constantly oxygenated and at a temperature in the range of 15°-17° C.

Magnetic and electric signals were recorded simultaneously with an acquisition rate of 125 kHz, the time constant of the lock-in was set to 10 μs allowing a bandwidth of \sim 10 kHz with a 6 dB/Octave filter roll-off. These particular settings were necessary for reaching the largest bandwidth allowed with our current lock-in amplifier, a crucial step for correctly identifying and removing the large stimulation artifact in the magnetic data.

While the magnetic response from the compound action potentials was expected to be in the order of a few hundred picotesla, the stimulation artifact was detected in the magnetic time-traces as a fast-pulse in the nanotesla range (Fig. 9.1b). To avoid the distorting artifact caused by low-pass filtering such a large and fast spike, the stimulation artifact was removed in the magnetic time-traces by common spline interpolation before noise filtering.

Due to the relatively fast stimulation rate, it was possible to acquire 10^4 epochs in \sim 90 minutes of recordings, allowing a final RMS noise in the magnetic data of \sim 10 pT after filtering and averaging. By using the same method illustrated in Chapter 3 for determining the bandwidth of the underlying biological signal, the low-pass filter cutoff frequency was set to 3 kHz.

The resulting averaged magnetic signal appeared in good agreement with the electric reference Fig. 9.1c. The two features (labeled as 1 and 2), present in both signals can be interpreted as the compound action potential response from myelinated and unmyelinated axons respectively [99]. In this example, the conduction velocities could be estimated from the electrical readout to be \sim 0.13 m/s for peak 1 and \sim 0.38 m/s for peak 2, assuming a stimulation-probe electrode distance of 300 μm . While one would expect that the electric response would be delayed compared to the magnetic response in the present configuration, we attribute the time overlap of the signals to

the delay on the magnetic signal imposed by the filtering process and by the imperfect alignment on the sensing area.

One of the most important factors worth noticing when comparing electric and magnetic detection is that the NV sensor requires fields in the μT range to saturate, and in our experience these fields cannot be produced by the current pulses required to trigger biological responses ($<1\text{ mA}$) without damaging the sample. This is not true for commercially available voltage amplifiers even at low gain settings (10x, 100x). When amplifiers saturate after a stimulation spike, they can take several milliseconds to recover, which delays the time it takes to reproduce signals accurately [100]. This issue can be resolved only by lowering the gain on the voltage amplifier, at the expense of possibly noisier readouts.

The mechanical stress imposed by the electrode stimulation as implemented in this experiment does not allow for excitation of AP in multiple spots of the corpus callosum. The tissue surrounding the stimulation electrode tends to relax after a few minutes of recording, making it very difficult to extract and re-position the electrode without causing serious damage. An interesting possibility that could be explored would be combining optogenetics techniques on corpus callosum with magnetic imaging for mapping of neural activity. Similar measurements have been conducted with functional MRI (fMRI) and with calcium imaging [101] techniques, with limited spatial and temporal resolution.

Although improvements in sensitivity are needed for spatially resolving such signals in the hundreds of pT range, it is possible to envision how NV centers imaging, in conjunction with optogenetics, could one day be applied to the mapping of electrical activity within brain slices.

Chapter 10

Summary and Outlook

In this thesis, continuous-wave wide-field sensing of biomagnetic signals with NV centers in diamonds was discussed. The first chapter introduced the field of magnetometry and it was followed by a brief description of the the properties of the NV centers in the second chapter. An illustration of the experimental framework was presented in the third chapter. Finally, the experimental results and current research pursuits were described.

In Chapter 4 we have presented a miniaturized fiber-coupled NV magnetometer that employed off-the-shelf components and a specially cut diamond to achieve a sensitivity of $7 \text{ nT}/\sqrt{\text{Hz}}$. The main limitations for the size of the sensor were given by the size of the internal optics, which could be further miniaturized. The diamond used in this work was a commercially available crystal (Element Six) with low NV concentration (0.2 ppb). By employing a ^{12}C purified diamond with increased defect density via optimized doping, irradiation and annealing it would have been possible to boost the NV absorption and therefore sensitivity. Balanced detection was achieved with optical (manual) balancing of the fluorescence and reference powers, this could have been improved with a custom-made electronically balanced photodetector. Due to leakage of stray green pump light in the photodetector, further improvements in shot-noise limited sensitivity could have been achieved by improving the optical filtering. Overall, the sensitivity demonstrated by our sensor could allow a wide range of applications, especially due to its portability and to the biocompatibility of the diamond that allows high proximity to the investigated sample. Other successful attempts to miniaturize fiber-coupled NV magnetometers have seen the creation of portable sen-

sors with sub-nanotesla sensitivity and full integration of components [102] or with a cavity-enhanced absorption-based scheme [103].

With the methodology described in Chapters 3 and 5, the first demonstrations of magnetic sensing with NV centers of action potentials in mammal tissue was presented. Action potentials in Extensor Digitorum Longus (EDL) muscle in mice were triggered via blue LED light (Chapter 6) and focused laser light (Chapter 7) stimulation using optogenetics techniques. In Chapter 9, it was proved that this methodology is not limited to optogenetically modified mice muscles but it can be extended to other biological samples such as mouse brain slices.

The induced magnetic field was detected in a passive and non-invasive fashion while the samples were kept alive for many hours (>10hrs). This was accomplished despite the need for high-power laser pump required to achieve a sensitivity of $50 \text{ pT}/\sqrt{\text{Hz}}$.

Although the experiments were conducted in an unshielded environment with the presence of strong correlated magnetic noise, the underlying magnetic signal was recovered using simple digital processing techniques.

With a peak SNR of ~ 15 , the resulting magnetic signals were similar to those measured by standard electrical probes without the disadvantages of capacitive distortion and mechanical stress caused by probe contact.

A single-shot readout noise of 300 pT (RMS) with a 1 kHz bandwidth after noise filtering was observed, and with the measured action potential induced fields in the subnanotesla range, it was still difficult to observe such signals in real time. Improving sensitivity to reach a single shot readout with sub-picotesla noise (RMS) would allow more comprehensive measurements by reducing the recording time and allowing easier filtering of background magnetic noise.

Finally, in Chapter 8 the imaging of magnetic fields induced by currents propagating in a micrometer scale circuit was demonstrated using NV centers in diamond. By employing a cw-ODMR scheme and a camera with integrated lock-in amplifier, it was shown that different types of low-frequency signals could be spatially resolved as a function of time with a high acquisition rate (up to 3500 fps). While our diamond sensor was not sensitive enough to directly observe and image signals in a real biosample, with improved diamond material and optimized pulsed protocols [104] the methods presented here represent a clear way to resolve such signals in the future.

Although the majority of the work in the field has focused on using pulse sequences to achieve higher sensitivities [32], those methods can result challenging for wide-field, low frequency sensing due to slow polarization and readout times of large NV ensembles. Few novel sensing techniques are being explored which could be suitable for sensing at low frequencies such as using magnetic flux concentrators [81], optical cavities and infrared or green light absorption [103, 105]. A possible way to increase contrast for NV ensembles would be using CVD diamonds with preferentially aligned NV- along a single crystallographic axis. Several researches have demonstrated preferential alignment in the order of 94-99% [51, 106, 107]. Despite being a promising

route, a number of aspects need to be further investigated, such as how irradiation and annealing cannot increase N-to-NV⁻ conversion efficiency without compromising the preferential alignment [107].

Bibliography

- [1] Kirstine Bjerrum Meyer and Hans Christian Ørsted. *Scientific life and works of HC Ørsted*. AF Høst, 1920.
- [2] Michael Faraday. *Experimental researches in electricity: reprinted from the Philosophical Transactions of 1831-1843, 1846-1852*. Vol. 2. R. and JE Taylor, 1839.
- [3] James Clerk Maxwell. *A treatise on electricity and magnetism*. Vol. 1. Clarendon press, 1873.
- [4] J Vrba. “Magnetoencephalography: the art of finding a needle in a haystack”. In: *Physica C: Superconductivity* 368.1-4 (2002), pp. 1–9.
- [5] Peter Hansen, Morten Kringelbach, and Riitta Salmelin. *MEG: an introduction to methods*. Oxford university press, 2010.
- [6] Pavel Ripka. *Magnetic sensors and magnetometers*. Artech house, 2021.
- [7] Fritz Primdahl. “The fluxgate magnetometer”. In: *Journal of Physics E: Scientific Instruments* 12.4 (1979), p. 241.
- [8] Zheng You. *Space Microsystems and Micro/Nano Satellites*. Butterworth-Heinemann, 2017.
- [9] Didier Robbes. “Highly sensitive magnetometers—a review”. In: *Sensors and Actuators A: Physical* 129.1-2 (2006), pp. 86–93.
- [10] C Dolabdjian et al. “Spatial resolution of SQUID magnetometers and comparison with low noise room temperature magnetic sensors”. In: *Physica C: Superconductivity* 368.1-4 (2002), pp. 80–84.
- [11] Kai-Mei C Fu et al. “Sensitive magnetometry in challenging environments”. In: *AVS Quantum Science* 2.4 (2020), p. 044702.
- [12] I Mateos et al. “Noise characterization of an atomic magnetometer at sub-millihertz frequencies”. In: *Sensors and Actuators A: Physical* 224 (2015), pp. 147–155.

- [13] Xiao Wang and KV Kamenev. “Review of modern instrumentation for magnetic measurements at high pressure and low temperature”. In: *Low Temperature Physics* 40.8 (2014), pp. 735–746.
- [14] DM Toyli et al. “Measurement and control of single nitrogen-vacancy center spins above 600 K”. In: *Physical Review X* 2.3 (2012), p. 031001.
- [15] M Schmelz et al. “Field-stable SQUID magnetometer with sub-fT Hz- 1/2 resolution based on sub-micrometer cross-type Josephson tunnel junctions”. In: *Superconductor Science and Technology* 24.6 (2011), p. 065009.
- [16] John Clarke, John Clarke, and Alex I Braginski. *The SQUID Handbook: Fundamentals and Technology of SQUIDs and SQUID Systems*. Vol. 1. Wiley-Vch, 2003.
- [17] Antti I Ahonen et al. “122-channel SQUID instrument for investigating the magnetic signals from the human brain”. In: *Physica Scripta* 1993.T49A (1993), p. 198.
- [18] JC Allred et al. “High-sensitivity atomic magnetometer unaffected by spin-exchange relaxation”. In: *Physical review letters* 89.13 (2002), p. 130801.
- [19] Dmitry Budker and Michael Romalis. “Optical magnetometry”. In: *Nature physics* 3.4 (2007), pp. 227–234.
- [20] IK Kominis et al. “A subfemtotesla multichannel atomic magnetometer”. In: *Nature* 422.6932 (2003), pp. 596–599.
- [21] Jundi Li et al. “SERF atomic magnetometer—recent advances and applications: A review”. In: *IEEE Sensors Journal* 18.20 (2018), pp. 8198–8207.
- [22] HB Dang, Adam C Maloof, and Michael V Romalis. “Ultrahigh sensitivity magnetic field and magnetization measurements with an atomic magnetometer”. In: *Applied Physics Letters* 97.15 (2010), p. 151110.
- [23] Guiying Zhang, Shengjie Huang, and Qiang Lin. “Magnetoencephalography using a compact multichannel atomic magnetometer with pump-probe configuration”. In: *AIP Advances* 8.12 (2018), p. 125028.
- [24] JM Taylor et al. “High-sensitivity diamond magnetometer with nanoscale resolution”. In: *Nature Physics* 4.10 (2008), pp. 810–816.
- [25] L Childress et al. “Coherent dynamics of coupled electron and nuclear spin qubits in diamond”. In: *Science* 314.5797 (2006), pp. 281–285.
- [26] Jeronimo R Maze et al. “Nanoscale magnetic sensing with an individual electronic spin in diamond”. In: *Nature* 455.7213 (2008), pp. 644–647.
- [27] Gopalakrishnan Balasubramanian et al. “Nanoscale imaging magnetometry with diamond spins under ambient conditions”. In: *Nature* 455.7213 (2008), pp. 648–651.
- [28] Victor M Acosta et al. “Diamonds with a high density of nitrogen-vacancy centers for magnetometry applications”. In: *Physical Review B* 80.11 (2009), p. 115202.
- [29] CL Degen. “Scanning magnetic field microscope with a diamond single-spin sensor”. In: *Applied Physics Letters* 92.24 (2008), p. 243111.

-
- [30] Francesco Casola, Toeno Van Der Sar, and Amir Yacoby. “Probing condensed matter physics with magnetometry based on nitrogen-vacancy centres in diamond”. In: *Nature Reviews Materials* 3.1 (2018), pp. 1–13.
- [31] Romana Schirhagl et al. “Nitrogen-vacancy centers in diamond: nanoscale sensors for physics and biology”. In: *Annual review of physical chemistry* 65 (2014), pp. 83–105.
- [32] John F Barry et al. “Optical magnetic detection of single-neuron action potentials using quantum defects in diamond”. In: *Proceedings of the National Academy of Sciences* 113.49 (2016), pp. 14133–14138.
- [33] Igor Lovchinsky et al. “Nuclear magnetic resonance detection and spectroscopy of single proteins using quantum logic”. In: *Science* 351.6275 (2016), pp. 836–841.
- [34] HJ Mamin et al. “Nanoscale nuclear magnetic resonance with a nitrogen-vacancy spin sensor”. In: *Science* 339.6119 (2013), pp. 557–560.
- [35] David R Glenn et al. “Micrometer-scale magnetic imaging of geological samples using a quantum diamond microscope”. In: *Geochemistry, Geophysics, Geosystems* 18.8 (2017), pp. 3254–3267.
- [36] Marcus W Doherty et al. “Electronic properties and metrology applications of the diamond NV- center under pressure”. In: *Physical review letters* 112.4 (2014), p. 047601.
- [37] Victor M Acosta et al. “Temperature dependence of the nitrogen-vacancy magnetic resonance in diamond”. In: *Physical review letters* 104.7 (2010), p. 070801.
- [38] Eric Van Oort and Max Glasbeek. “Electric-field-induced modulation of spin echoes of NV centers in diamond”. In: *Chemical Physics Letters* 168.6 (1990), pp. 529–532.
- [39] M Block et al. “Optically enhanced electric field sensing using nitrogen-vacancy ensembles”. In: *Physical Review Applied* 16.2 (2021), p. 024024.
- [40] Jennifer M Schloss et al. “Simultaneous broadband vector magnetometry using solid-state spins”. In: *Physical Review Applied* 10.3 (2018), p. 034044.
- [41] M Loretz, T Rosskopf, and CL Degen. “Radio-frequency magnetometry using a single electron spin”. In: *Physical review letters* 110.1 (2013), p. 017602.
- [42] J-P Tetienne et al. “Spin relaxometry of single nitrogen-vacancy defects in diamond nanocrystals for magnetic noise sensing”. In: *Physical Review B* 87.23 (2013), p. 235436.
- [43] V Vijayanthimala et al. “The long-term stability and biocompatibility of fluorescent nanodiamond as an in vivo contrast agent”. In: *Biomaterials* 33.31 (2012), pp. 7794–7802.
- [44] Nitin Mohan et al. “In vivo imaging and toxicity assessments of fluorescent nanodiamonds in *Caenorhabditis elegans*”. In: *Nano letters* 10.9 (2010), pp. 3692–3699.
- [45] KiranJ van der Laan et al. “Nanodiamonds for in vivo applications”. In: *Small* 14.19 (2018), p. 1703838.

- [46] Laura Moore et al. “Comprehensive interrogation of the cellular response to fluorescent, detonation and functionalized nanodiamonds”. In: *Nanoscale* 6.20 (2014), pp. 11712–11721.
- [47] RC Burns et al. “HPHT growth and x-ray characterization of high-quality type IIa diamond”. In: *Journal of Physics: Condensed Matter* 21.36 (2009), p. 364224.
- [48] A Lenef and SC Rand. “Electronic structure of the N-V center in diamond: Theory”. In: *Physical Review B* 53.20 (1996), p. 13441.
- [49] Michael Lurie Goldman et al. “Phonon-induced population dynamics and intersystem crossing in nitrogen-vacancy centers”. In: *Physical review letters* 114.14 (2015), p. 145502.
- [50] Marcus W Doherty et al. “The nitrogen-vacancy colour centre in diamond”. In: *Physics Reports* 528.1 (2013), pp. 1–45.
- [51] Hitoshi Ishiwata et al. “Perfectly aligned shallow ensemble nitrogen-vacancy centers in (111) diamond”. In: *Applied Physics Letters* 111.4 (2017), p. 043103.
- [52] Peter J Mohr, Barry N Taylor, and David B Newell. “CODATA recommended values of the fundamental physical constants: 2006”. In: *Journal of Physical and Chemical Reference Data* 80.3 (2008), pp. 633–1284.
- [53] Michael E Wieser and Willi A Brand. “Isotope ratio studies using mass spectrometry”. In: *Reference Module in Chemistry, Molecular Sciences and Chemical Engineering*. Elsevier, 2013.
- [54] MW Doherty et al. “Theory of the ground-state spin of the NV- center in diamond”. In: *Physical Review B* 85.20 (2012), p. 205203.
- [55] John F Barry et al. “Sensitivity optimization for NV-diamond magnetometry”. In: *Reviews of Modern Physics* 92.1 (2020), p. 015004.
- [56] Chang S Shin et al. “Room-temperature operation of a radiofrequency diamond magnetometer near the shot-noise limit”. In: *Journal of Applied Physics* 112.12 (2012), p. 124519.
- [57] Nabeel Aslam et al. “Nanoscale nuclear magnetic resonance with chemical resolution”. In: *Science* 357.6346 (2017), pp. 67–71.
- [58] Norman F Ramsey. “A molecular beam resonance method with separated oscillating fields”. In: *Physical Review* 78.6 (1950), p. 695.
- [59] Erwin L Hahn. “Spin echoes”. In: *Physical review* 80.4 (1950), p. 580.
- [60] G De Lange et al. “Universal dynamical decoupling of a single solid-state spin from a spin bath”. In: *Science* 330.6000 (2010), pp. 60–63.
- [61] A Dréau et al. “Avoiding power broadening in optically detected magnetic resonance of single NV defects for enhanced dc magnetic field sensitivity”. In: *Physical Review B* 84.19 (2011), p. 195204.
- [62] Andreas FL Poulsen et al. “Investigation and comparison of measurement schemes in the low frequency biosensing regime using solid-state defect centers”. In: *arXiv preprint arXiv:2109.13028* (2021).
- [63] Elke Neu et al. “Single photon emission from silicon-vacancy colour centres in chemical vapour deposition nano-diamonds on iridium”. In: *New Journal of Physics* 13.2 (2011), p. 025012.

-
- [64] Takayuki Iwasaki et al. “Germanium-vacancy single color centers in diamond”. In: *Scientific reports* 5.1 (2015), pp. 1–7.
- [65] Gergő Thiering and Adam Gali. “Color centers in diamond for quantum applications”. In: *Semiconductors and Semimetals*. Vol. 103. Elsevier, 2020, pp. 1–36.
- [66] Yafei Zhang et al. “HPHT synthesis of large single crystal diamond doped with high nitrogen concentration”. In: *Diamond and Related Materials* 17.2 (2008), pp. 209–211.
- [67] Ulrika FS D’Haenens-Johansson et al. “Large Colorless HPHT-Grown Synthetic Gem Diamonds from New Diamond Technology, Russia”. In: *Gems & Gemology* 51.3 (2015).
- [68] Michael Schwander and Knut Partes. “A review of diamond synthesis by CVD processes”. In: *Diamond and related materials* 20.9 (2011), pp. 1287–1301.
- [69] Element Six. “The Element Six CVD Diamond Handbook”. In: ().
- [70] Kenichi Ohno et al. “Engineering shallow spins in diamond with nitrogen delta-doping”. In: *Applied Physics Letters* 101.8 (2012), p. 082413.
- [71] S Pezzagna et al. “Creation efficiency of nitrogen-vacancy centres in diamond”. In: *New Journal of Physics* 12.6 (2010), p. 065017.
- [72] J Achard, Vincent Jacques, and A Tallaire. “Chemical vapour deposition diamond single crystals with nitrogen-vacancy centres: a review of material synthesis and technology for quantum sensing applications”. In: *Journal of Physics D: Applied Physics* 53.31 (2020), p. 313001.
- [73] Joonhee Choi et al. “Depolarization dynamics in a strongly interacting solid-state spin ensemble”. In: *Physical review letters* 118.9 (2017), p. 093601.
- [74] Amiram Grinvald et al. “Functional architecture of cortex revealed by optical imaging of intrinsic signals”. In: *Nature* 324.6095 (1986), pp. 361–364.
- [75] Micha E Spira and Aviad Hai. “Multi-electrode array technologies for neuroscience and cardiology”. In: *Nature nanotechnology* 8.2 (2013), pp. 83–94.
- [76] Chi-Cheng Fu et al. “Characterization and application of single fluorescent nanodiamonds as cellular biomarkers”. In: *Proceedings of the National Academy of Sciences* 104.3 (2007), pp. 727–732.
- [77] Vadym N Mochalin et al. “The properties and applications of nanodiamonds”. In: *Nature nanotechnology* 7.1 (2012), pp. 11–23.
- [78] A Ermakova et al. “Detection of a few metallo-protein molecules using color centers in nanodiamonds”. In: *Nano letters* 13.7 (2013), pp. 3305–3309.
- [79] LT Hall et al. “High spatial and temporal resolution wide-field imaging of neuron activity using quantum NV-diamond”. In: *Scientific reports* 2.1 (2012), pp. 1–9.
- [80] Kasper Jensen et al. “Non-invasive detection of animal nerve impulses with an atomic magnetometer operating near quantum limited sensitivity”. In: *Scientific reports* 6.1 (2016), pp. 1–7.
- [81] Ilja Fescenko et al. “Diamond magnetometer enhanced by ferrite flux concentrators”. In: *Physical review research* 2.2 (2020), p. 023394.

- [82] Kento Sasaki et al. “Broadband, large-area microwave antenna for optically detected magnetic resonance of nitrogen-vacancy centers in diamond”. In: *Review of Scientific Instruments* 87.5 (2016), p. 053904.
- [83] Catalin P Constantin et al. “Biocompatibility of polyimides: A mini-review”. In: *Materials* 12.19 (2019), p. 3166.
- [84] Haitham AR El-Ella et al. “Optimised frequency modulation for continuous-wave optical magnetic resonance sensing using nitrogen-vacancy ensembles”. In: *Optics express* 25.13 (2017), pp. 14809–14821.
- [85] Stanford Research Systems. “MODEL SR850 DSP Lock-In Amplifier Manual”. In: ().
- [86] Nir Grossman et al. “Modeling study of the light stimulation of a neuron cell with channelrhodopsin-2 mutants”. In: *IEEE Transactions on Biomedical Engineering* 58.6 (2011), pp. 1742–1751.
- [87] Lisa A Gunaydin et al. “Ultrafast optogenetic control”. In: *Nature neuroscience* 13.3 (2010), pp. 387–392.
- [88] Hunter Gabbard et al. “Matching matched filtering with deep networks for gravitational-wave astronomy”. In: *Physical review letters* 120.14 (2018), p. 141103.
- [89] Katerina Chatziioannou et al. “Noise spectral estimation methods and their impact on gravitational wave measurement of compact binary mergers”. In: *Physical Review D* 100.10 (2019), p. 104004.
- [90] Jaime R Roman et al. “Parametric adaptive matched filter for airborne radar applications”. In: *IEEE Transactions on Aerospace and Electronic Systems* 36.2 (2000), pp. 677–692.
- [91] Alain de Cheveigné and Israel Nelken. “Filters: when, why, and how (not) to use them”. In: *Neuron* 102.2 (2019), pp. 280–293.
- [92] Alain de Cheveigné and Dorothee Arzounian. “Robust detrending, rereferencing, outlier detection, and inpainting for multichannel data”. In: *NeuroImage* 172 (2018), pp. 903–912.
- [93] Kimberley A Phillips et al. “The corpus callosum in primates: processing speed of axons and the evolution of hemispheric asymmetry”. In: *Proceedings of the Royal Society B: Biological Sciences* 282.1818 (2015), p. 20151535.
- [94] Leighton BN Hinkley et al. “The role of corpus callosum development in functional connectivity and cognitive processing”. In: (2012).
- [95] Eric B Larson, Debra S Burnison, and Warren S Brown. “Callosal function in multiple sclerosis: bimanual motor coordination”. In: *Cortex* 38.2 (2002), pp. 201–214.
- [96] Ivar Reinvang et al. “Dichotic listening performance in relation to callosal area on the MRI scan.” In: *Neuropsychology* 8.3 (1994), p. 445.
- [97] Stephen M Rao et al. “Correlation of magnetic resonance imaging with neuropsychological testing in multiple sclerosis”. In: *Neurology* 39.2 (1989), pp. 161–161.
- [98] DJ Werring et al. “Diffusion tensor imaging of lesions and normal-appearing white matter in multiple sclerosis”. In: *Neurology* 52.8 (1999), pp. 1626–1626.

-
- [99] Lijun Li et al. “A novel approach for studying the physiology and pathophysiology of myelinated and non-myelinated axons in the CNS white matter”. In: *PLoS One* 11.11 (2016), e0165637.
- [100] KL Venkatachalam, Joel E Herbrandson, and Samuel J Asirvatham. “Signals and signal processing for the electrophysiologist: part II: signal processing and artifact”. In: *Circulation: Arrhythmia and Electrophysiology* 4.6 (2011), pp. 974–981.
- [101] Yi Chen et al. “Mapping the brain-wide network effects by optogenetic activation of the corpus callosum”. In: *Cerebral Cortex* 30.11 (2020), pp. 5885–5898.
- [102] Felix M Stürner et al. “Integrated and Portable Magnetometer Based on Nitrogen-Vacancy Ensembles in Diamond”. In: *Advanced Quantum Technologies* 4.4 (2021), p. 2000111.
- [103] Georgios Chatzidrosos et al. “Miniature cavity-enhanced diamond magnetometer”. In: *Physical Review Applied* 8.4 (2017), p. 044019.
- [104] Connor A Hart et al. “N-V-Diamond Magnetic Microscopy Using a Double Quantum 4-Ramsey Protocol”. In: *Physical Review Applied* 15.4 (2021), p. 044020.
- [105] Sepehr Ahmadi et al. “Nitrogen-vacancy ensemble magnetometry based on pump absorption”. In: *Physical Review B* 97.2 (2018), p. 024105.
- [106] M Lesik et al. “Perfect preferential orientation of nitrogen-vacancy defects in a synthetic diamond sample”. In: *Applied Physics Letters* 104.11 (2014), p. 113107.
- [107] Takahiro Fukui et al. “Perfect selective alignment of nitrogen-vacancy centers in diamond”. In: *Applied Physics Express* 7.5 (2014), p. 055201.